Development of a fault detection and diagnosis approach for a binary ice system

Yuxuan Liu

A thesis submitted for the degree of Doctor of Philosophy in the Department of Mechanical Engineering, University College London,

University of London

March 2015

DECLARATION

I, Yuxuan Liu, confirm that the work presented in this thesis is my own. Where information has been derived from other sources, I confirm that this has been indicated in the thesis.

_____

Yuxuan Liu

March 2015

Abstract

Fault detection and diagnosis (FDD) is an important part to maintain the performance, improve the reliability and prevent energy wastage of the refrigeration systems. Binary ice systems, which have become more commonly employed in both industry and domestic applications, are essentially refrigeration systems using water-ice slurry mixture as a secondary refrigerant. The existence of the ice makes binary ice systems different from conventional liquid chillers, leading to the requirement of a specified FDD method. Therefore, the current research focuses on developing a model based dynamic FDD approach that can capture the unique features of binary ice systems in order to detect some pre-selected faults, including binary ice flow restriction, cooling water flow restriction, incorrect solution concentration, ice generator scraper fault and ice generator motor failure.

To provide fault free predictions for the FDD, a dynamic hybrid model of the binary ice system was proposed. The model consisted of an analytical sub-model of the scraped surface ice generator, which was an essential component of the binary ice system that produced ice, and an artificial neural network (ANN) sub-model of the primary refrigeration circuit. The two sub-models were coupled by using two of the ANN model's outputs as the inputs to the analytical model, namely the evaporating temperature and the compressor power consumption, as well as sharing some of the input parameters. The coupled model was validated with data from a 2.5kW laboratory binary ice test rig.

The FDD was carried out by monitoring the changes of the residuals of some carefully chosen parameters, using CUmulative SUM (CUSUM) test. Two parameters, namely cooling water temperature difference and evaporating temperature, were monitored for fault detection purpose, and condenser outlet temperature, cooling water temperature difference, discharge temperature and binary ice outlet temperature were observed for fault diagnosis function. An ANN fault classifier was developed to identify the type of the fault by analysing the combinations of the fault diagnosis parameter variations. This FDD method was found to be able to detect and diagnose successfully the pre-selected faults without raising any false alarm, and in addition it was capable of diagnosing three pairs of double fault.

Acknowledgements

First of all, I would like to thank my supervisor, Dr William K. O. Suen, for his constant support and encouragement throughout my PhD research and thesis producing. This thesis would not have been completed or written without his help.

William's research group members/ex-students have all been helpful, and I would particularly thank Dr Daniel Colbourne and Dr Rotchana Prapainop who had been spending time for discussion of my experiments, showing me techniques and offering help, and Mr Jones Katoh for his initial suggestions.

Furthermore, I would like to thank all my colleges in Department of Mechanical Engineering, UCL, who kindly let me to use their tools, help installing instruments for my experiments and so on.

Most importantly, none of this would have been possible without the love and support from my parents, my husband and my lovely coming baby who have brightened my lives. This thesis is dedicated to them.

List of content

Nomenclature

A	area [m^2]
ANN	artificial neural network
b	bias
B	the number of blades per 360 degrees
C	concentration by weight (weight of the ethanol divided by the total solution weight) [%wt]
C_p	specific heat capacity [kJ/(kgK)]
CUSUM	cumulated sum
C_v	concentration by volume [%]
FDD	fault detection and diagnosis
h	heat transfer coefficient [W/(m^2 K)]
H	specific enthalpy [J/kg]
HVAC	heating, ventilation, and air conditioning
k	thermal conductivity [W/(m K)]
L	length [m]
L_{ice}	specific latent heat of the ice [J/kg]
m	mass flowrate [kg/s]
MLP	multilayer perceptron
N	rotation speed [rev/s]
NARX	nonlinear autoregressive exogenous
Nu	Nusselt number
PCS	phase change slurry
p	pressure [bar]
PO	oil pressure [kPa]
Q	capacity [kW]
Q_{leak}	equivalent heat loss from the chiller [kW]

r	radius [m]
R	thermal resistance of the heat exchangers [K/kW]
R^2	coefficients of determination
RBF	radial basis function
Re_a	axial Reynolds number
Re_r	rotational Reynolds number
S	sensitivity factor
SSIG	scraped surface ice generator
ΔS_T	internal irreversibility [kW/K]
t	time [s]
T	temperature [℃]
ΔT	temperature difference [℃]
TDL	tapped delay line
TO	oil temperature [℃]
TXV	thermostatic expansion valve
u	volume flowrate [L/min]
U	overall heat transfer coefficient [W/(m^2 K)]
$\boldsymbol{w}$	weight matrix
W	power consumption [kW]

Greek letters

β	regression coefficient
δ	threshold
ε	error
$\eta_{chiller}$	chiller efficiency [%]
η_{isen}	isentropic efficiency [%]
λ	statistical threshold
μ	dynamic viscosity [Pa s]

μ_B	dynamic viscosities for Bingham fluid [Pa s]
μ_N	dynamic viscosities for Newtonian fluid [Pa s]
ρ	density [kg/m^3]
σ	standard deviation
τ_0	yield stress [MPa]

Subscripts

I	Section I
II	Section II
bi	binary ice
c	condenser
ca	condenser approach
cf	carrier fluid
com	compressor
dis	discharge
e	evaporator
ea	evaporator approach
f	freezing point or freezing front
fluid	secondary fluid
i	inner
ice	ice properties
in	inlet
l	fluid
latent	latent heat
max	maximum value
min	minimum value
nor	normalised value
o	original or outer

out	outlet
r	refrigerant
sec	secondary fluid
sc	subcooling
sh	superheat
shaft	rotating shaft
suc	suction
tank	solution tank
w	cooling water
wall	wall
water	cooling water

List of Tables

List of Figures

1. Introduction

Refrigeration and Air Conditioning (RAC) systems have become an essential part of our daily lives, serving a wide range of domestic, commercial and industrial applications. As in many other thermal and electro-mechanical systems, faults could develop in the systems, causing system malfunction and leading to energy wastage, poor temperature/capacity control, unsafe operation, and in some cases, even catastrophic component failure (Stouppe and Lau 1989; Isermann 1997; Gertler 1998). Over the years, various fault detection and diagnosis (FDD) techniques/methodologies have been researched, developed, and implemented for RAC systems (Katipamula and Brambley 2005) in particular vapour compression systems (Rossi 1995; Breuker and Braun 1998b). Essentially, FDD is a process monitoring technique used for detecting abnormal working conditions of a system and deducing the sources of the faults by monitoring specific system parameters (Chiang et al. 2001).

Over the past two decades, RAC industry has been developing and applying alternative refrigerants to replace the ozone depleting CFC/HCFC refrigerants (Sekiya and Misaki 2000; Spatz and Yana Motta 2004). However, many of these alternatives are still considered as threats to the environment or to human safety as they either have high global warming potentials (GWPs), e.g. R507, R404A, or high flammability/toxicity, e.g. R717 (Ammonia), R290 (Propane), R30 (methylene chloride). Therefore it is important to ensure there is minimal or no escape of refrigerant to the environment or into occupied space due to leakage which is a typical/common fault in RAC systems. In addition, some of the alternative refrigerants are also quite expensive, especially the synthetic ones (e.g. R507 is ten times more expensive than R22, and R1234yf is around £160/kg), it would be sensible to reduce total system refrigerant charge quantity and leakage possibility by improving the design of the system.

One conventional approach employed to reduce the total refrigerant charge quantity, the possibility of refrigerant leakage and the potential hazardous impact on occupants is to confine the main refrigeration circuit, commonly referred as the primary circuit, and the primary refrigerant in a plant room, and use a heat transfer fluid (HTF) to distribute the cooling to the remote loads. The distribution system is

commonly referred as the secondary system (Arora 2010) and the heat transfer fluid as the secondary refrigerant. For conventional secondary systems, single phase fluids such as water are often employed as the secondary refrigerants (Riffat et al. 1997). For sub-zero temperature applications, where the water cannot be used, other secondary fluids such as brine or glycol solutions (Melinder 2007) are often employed instead. However, their concentrations need to be increased to depress their freezing point for lower temperature applications (Melinder 1997); this correspondingly increases their viscosities significantly, resulting in rather high pumping costs.

Phase change slurries (PCSs)[1], as a relatively new kind of secondary refrigerant, benefit from the high latent heat absorbed during the melting the solid phase (Egolf and Kauffeld 2005). The solid part of PCSs is generated as very small particles, and when suspended in the liquid phase, becomes a pumpable binary mixture. Among various PCSs, binary ice, also known as ice slurry, is receiving much attention in recent years (Wang and Kusumoto 2001; Davies 2005; Hägg 2005; Tamasauskas et al. 2012; Yeo et al. 2012). As defined by Egolf and Kauffeld (2005), binary ice is a homogenous mixture of aqueous solution and fine ice particles with diameters smaller than 1mm. It possesses unique thermal-physical properties and flow characteristics due to the presence of ice particles in the carrier fluid (Knodel et al. 2000). Its advantages include high cooling capacity per unit flow rate, small temperature change, low pumping power requirement, etc. (Lee et al. 2006; Kauffeld et al. 2010; Kumano et al. 2010b), when compared to traditional single phase secondary fluids. The applications of binary ice include comfort cooling for multi-function buildings, food processing and preservations, mining, fire-fighting, etc. (Kauffeld et al. 2010).

Binary ice systems possess unique operation characteristics, which may mean the existing FDD approaches are not applicable to binary ice refrigeration systems. In this thesis, the development of a FDD approach for binary ice system is presented.

[1] Phase change slurry is a mixture of dispersed phase change particles and a continuous carrier fluid.

1.1 Fault detection and diagnosis (FDD)

1.1.1 FDD methods and procedures

Faults, which can be caused by design error, aging, incorrect operation setting, human error, etc., result in system malfunction or/and performance degradation (Chiang et al. 2001). Even small faults could lead to substantial energy wastage, increase in maintenance cost and system down time (Isermann 2005). Some faults could potentially cause a complete system breakdown. As a result, fault detection and diagnosis techniques are introduced to detect the abnormal operation behaviour, so that problems can be identified and rectified in an effectively and timely manner.

Figure 1.1 shows the typical structure of a FDD approach which essentially consists of three main steps: fault detection, fault diagnosis and fault evaluation. The first step, fault detection, is to determine whether a fault exists in the system or whether everything is working correctly. It is carried out by comparing certain measured (or derived) system parameters with fault-free data. The fault-free data can be obtained from model predictions or from historical/log data (Schein and Bushby 2006). If the residual, which represents their difference, fails to fall within a pre-defined 'fault-free' threshold, a fault is registered. The next step is to identify the fault and isolate its source.

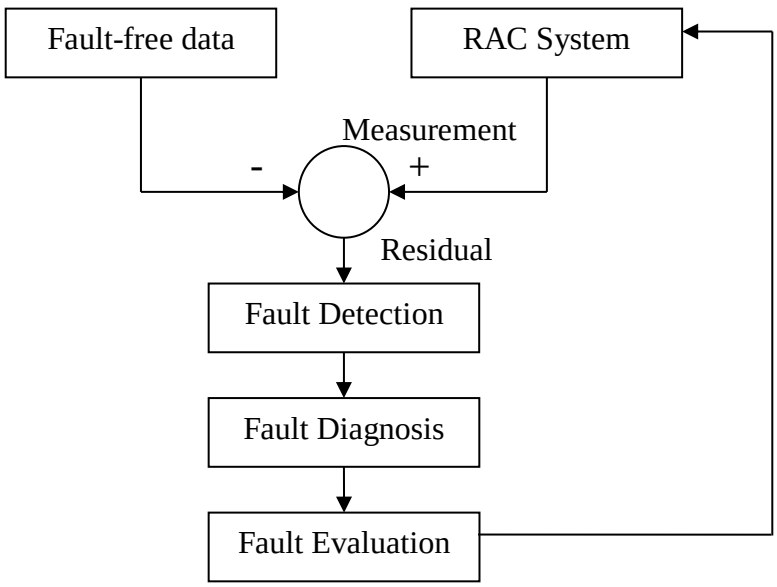

Figure 1.1 Flow chart of a typical FDD process

Different faults have different influences/impacts on the system behaviours, often referred to as fault signatures. For examples, condenser fouling will increase the evaporating temperature (Cui and Wang 2005), while refrigerant leakage will reduce it (Assawamartbunlue and Brandemuehl 2006). By analysing the combinations of the changes of various selected system parameters, faulty component(s) or types of faults can be isolated (Braun 1999). Their influences on system performance and operating conditions, safety, environment, energy penalty and repair cost can then be evaluated (Braun 2003); appropriate actions can then be taken accordingly.

The previous three steps are usually followed by decision making to decide how to deal with the fault. If the fault may cause a severe problem, like damaging the system or being related to safety issues, the system should be shut down immediately. For less serious faults, the FDD system can choose whether to report the fault or to tolerate it without stopping its operation, but the fault has to be continuously monitored and eventually get rectified.

Many kinds of FDD modelling techniques have been developed or studied for various systems including RACs. They can be put into three main groups: physical model-based (also referred as white box models or analytical models) (Koury et al. 2001), process history based FDDs (i.e. black box models) (Swider et al. 2001; Ertunc and Hosoz 2006) and a combination of the two which often called hybrid or grey box models (Katipamula and Brambley 2005).

For the physical model-based methods, a mathematical model, which has been properly validated, is to simulate the physical process of the system. This method is based on establishing physical relationships which require a thorough understanding of the physical process involved. The simulated outputs are then compared with the measured values. Although it may be more computationally intensive, it is capable of showing the transient state of a system in details and it can be utilised to simulate both normal and faulty working conditions. However, physical models are relatively hard to develop, especially for complicated systems, and sometimes when assumptions are made to simplify the calculations, the simulation accuracies could be compromised, which may generate unreliable FDD results (Chiang et al. 2001). In this case, extra calibrations using experimental data are necessary, resulting in the formation of some kind of grey box models (Ding et al. 2009).

Models based on process history show advantages when sufficient amount of historical data are available. The data, which can be divided into input and output data groups, are employed to train the model (Yegnanarayana 2004). The training process is to determine the correlations that can relate the inputs with the outputs, but they unfortunately cannot reflect the physical relationships between the two groups (Swider 2003). When applied to fault detection, the model uses a set of measured data as model input to generate predicted output data which are then compared with measured output data. This can be applied regardless of whether the physical processes involved are clearly understood or not, making it easier to develop when compared with the physical models. Artificial neural networks and regression algorithms (Sreedharan and Haves 2001) are some of the commonly used history data based FDD models.

A grey box model is a combination of the physical and process history models, based on physical principles of the systems but with some of the modelling parameters obtained by black box models (Gordon and Ng 2000; Saththasivam and Ng 2008).

It is unlikely a single FDD modelling technique can deal with all types of faults, as individual FDD technique has strengths and limitations in relation to the nature of the system and the fault(s); a combination of various techniques may often be used to achieve an effective and accurate detection for RAC systems (Estrada-Flores et al. 2006).

1.1.2 Application of FDDs in RAC

The applications of FDDs can be seen in a wide range of industry, including critical systems such as power plant (Gross et al. 1997; Tan and Lim 2004), aircraft (Marcos et al. 2005; Lu et al. 2015) and emergency department (Harrou et al. 2015) which generally involve advanced sensors and instrumentations, as compared to those used in non-critical systems such as RAC systems.

FDDs for RAC systems are mainly employed to help reduce energy wastage due to faulty operation, food spoilage due to faulty components, human discomfort due to faulty controls, damage or excessive wear and tear of equipment due to unfavourable operating conditions, etc. (Viser et al. 1999; Grace et al. 2005; Rueda et

al. 2005). Compared to critical systems encountered in, say, the nuclear power generation and aviation industry, the budgets available for incorporating FDDs in RAC systems are much smaller, as faults in the latter are generally more tolerable and are less likely to cause fatalities or catastrophic failures. Therefore, it is essential that FDDs developed for the latter should use as few sensors and as simple measurements as possible to detect the faults, therefore keeping the cost down as well as making it simple to implement (Venkatasubramanian et al. 2003).

Over the years, many FDD methods had been developed for RAC systems, although they are mainly oriented towards water chillers (Jia and Reddy 2003; Cui and Wang 2005; Reddy 2007a) and air-conditioning systems (Viser et al. 1999; Kelso and Wright 2005) for buildings; applications of FDDs in other systems such as supermarket refrigerated display cabinets (Assawamartbunlue 2000) and heat pumps (Kim et al. 2010) have also been looked at in recent years.

It appears that all the current FDD techniques are developed for single phase secondary refrigerants, such as air or water, and no research had been done on the development of FDD for two-phase binary ice systems. Although binary ice has its unique characteristics, binary ice systems still share many similar features, including certain faults, with conventional single phase liquid chillers. Therefore, some insights into chiller faults and the detection methods will help to gain a better understanding of the FDD development of binary ice systems.

Generally faults can be classified into two main groups: hard faults and soft faults. A hard fault means that some physical components fail to function. These include components failure, such as a broken belt or a stuck valve, electrical faults, such as control box failure or burnt motor, and so on. On the other hand, soft faults refer to degradation of the system/component performance such as refrigerant leakage and heat exchanger fouling (Comstock et al. 2002b). A hard fault is relatively easy to detect with simple measurements or observations but soft faults may not have sufficient impact on system behaviours until certain severity levels are reached. Thus most of the researches related to fault detection for RAC have been focussing on soft faults.

Various surveys on common faults in RAC equipment were carried out by previous researchers (Stouppe and Lau 1989; Breuker and Braun 1998a; Comstock et al. 2002b), for both hard and soft faults. For example, Comstock et al. (2002b) examined the service records of five domestic chiller manufacturers. Among all the chiller faults, the most frequently occurred faults were in the control box (about 33% of all faults), followed by refrigerant leakage (19%). Other less frequently occurring faults were liquid line faults (5%) and condenser fouling (4% average). Their reviews so far indicate almost all the FDD methods are developed based on certain pre-defined faults that are considered important in terms of their influence on system efficiency and operation.

FDD techniques had been studied/developed by various researchers, for water chiller (Reddy 2007a) and for glycol systems (Rueda et al. 2005). Generally, those methods are based on the measurements of flow temperature, pressure, flowrate, etc. A more detailed review of those works will be given in Chapter 2. Though PCS systems share many common faults with other indirect systems (e.g. refrigerant leakage, heat transfer fluid flow restriction), some faults are only unique to them (e.g. incorrect solution concentration and malfunction of the ice generator). A representative number of faults will be studied in this project and attention will be paid particularly to those that are unique to binary ice systems.

1.2 Binary ice and binary ice systems

1.2.1 Phase change slurries (PCSs)

For single phase fluids, such as glycol solution, ethanol solution, water and brine, the energy absorbed, as sensible heat, increases the temperature of the fluid. Though many of them have reasonably large values of specific heat capacity, their temperature increases are still large when absorbing the thermal load, making the component/system design relatively more complicated (Sharma et al. 2009). On the contrary, PCSs can store and release large amount of latent heat during phase changes and correspondingly they require smaller mass flow rates, less pumping power, smaller chillers and pipe sizes, as well as smaller thermal storage units (if any) for a given cooling capacity. They also experience much smaller temperature changes across the heat exchangers when performing a cooling function.

Many materials or mixtures can be potentially used as PCSs for refrigeration applications. The freezing point is an important parameter to consider when selecting a suitable PCS for a particular application, which depends on the type and concentration of the material; it should match with the desired operational temperature range (Sharma et al. 2009). Other selection criteria include the chemical stability and low cost (Zalba et al. 2003; Sharma et al. 2009).

1.2.2 Binary ice properties and production

A water-ice binary solution is among some of the first used PCSs. It is cheap, easy to obtain, safe and also with a very large latent heat. For sub-zero temperature applications, a freezing point depressant (or additive) has to be added, glycol, ethyl, ethanol and NaCl being some of the popular ones. By selecting an appropriate type of additive/solute and using a suitable concentration, an aqueous solution-ice mixture, also known as binary ice, can be generated when its temperature is reduced to below the freezing point.

A number of ice generation methods have been developed. They can be broadly divided into the following groups: mechanical-scraper type (Kauffeld et al. 1999; Stamatiou et al. 2005), vacuum type (Paul 1996), direct contact type (Byrd and Mulligan 1986; Fukusako et al. 1999), fluidized-bed ice generator (Klaren and Van Der Meer 1991), ice generators using sub-cooled water with different types of nucleation initialization (Mito et al. 2000) and ice slurry generators with specialized ice nucleating and ice repelling surfaces (Zwieg 2002). Among them, mechanical-scrapers are the most commonly applied type in industry because the heat transfer rate from the solution to the primary refrigerant can be greatly increased by agitation, leading to energy and space savings (Kauffeld et al. 1999).

Scrape surface ice generator (SSIG) is one of the most popular mechanical-scraper type ice generators. The SSIG is essentially a co-axial concentric heat exchanger with the primary refrigerant flow in the annular space providing cooling to the solution flowing in the inner cylinder. A very thin layer of ice forms on the inner surface of the cylinder when the local solution temperature drops below its freezing point, and is then removed by the rotating scrapers. During this process, both the solution and ice concentrations increase, and the flow temperature decreases gradually along the SSIG towards the exit; the actual decrease, typically between 2 to

3 ℃, depends on various parameters such as the length of the SSIG and initial solution concentration.

To describe the states of binary ice, three independent variables are needed, namely solution and ice temperature (usually assumed to be the same (Kauffeld et al. 2005)), carrier fluid concentration and ice concentration. When the binary ice is generated in a solution with a known initial concentration, only two of the variables are needed.

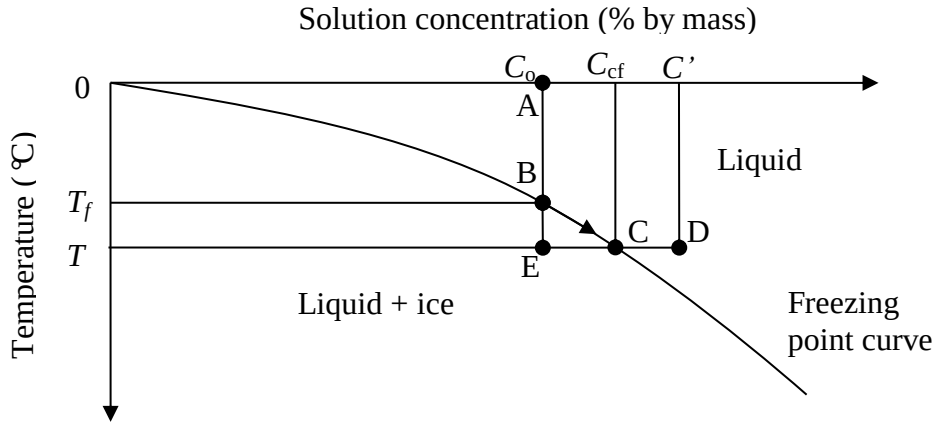

Figure 1.2 Phase diagram of a binary ice mixture

Figure 1.2 shows part of a typical phase change diagram of a hypo-eutectic solution (Ge and Wang 2009) at different temperatures (Y-axis) and solution concentrations (by mass[2], X-axis). The freezing point curve (assumed under standard atmospheric pressure) gives the freezing temperature at a certain solution concentration, which decreases when the solution concentration increases. Above the freezing point curve, the solution is a single-phase liquid, whereas below the curve, a mixture of ice particles suspended in solution can be formed.

Take a solution with an initial concentration, C_o, at temperature 0 ℃ (point A) as an example. When being cooled, solution remains as liquid until its temperature drops (assuming it is being cooled by an external medium) to its freezing point T_f (point B). At this point, part of the water begins to freeze. If the solution is cooled further down to a lower temperature T and the water is taken out during this freezing process, the solution concentration increases, moving from point B towards point C

[2] Concentration by mass = mass of solute/total solution mass

(with the corresponding solution concentration changing from C_o to C_{cf}) along the freezing point curve. At the same time, more and more ice is produced, and at point C, the corresponding ice concentration (C_{ice}) can be calculated by:

$$C_{ice} = 1 - \frac{C_o}{C_{cf}} \qquad 1.1$$

where C_{cf} is the concentration of the carrier fluid at point C.

An important property of binary ice related to the pumping power is the viscosity which increases with the solution concentration and ice concentration (Kumano et al. 2010a). Comparing a binary ice mixture (Point E in Figure 1.2) to a solution with a concentration of C_{cf} (Point C), both at the same temperature, the viscosity is larger at point E when there are ice particles in the mixture. However if the initial solution concentration is increased to C' (Point D), its viscosity at the same temperature will be significantly higher than that of Point C, leading to potentially a lower viscosity at Point E than at Point D.

Due to the presence of ice particles in the carrier fluid, the rheological behaviour of ice slurries is much more complex than a single phase fluid (Egolf and Kauffeld 2005). When the ice concentration is low, ice slurry flow behaves like Newtonian fluid; for suspensions containing a large amount of ice particles, non-Newtonian behaviours resulted (Darbouret et al. 2005). It has been observed that the transition of Newtonian fluid to non-Newtonian fluid happens at ice concentrations by mass between 6% and 15% (Ayel et al. 2003) which are lower than that commonly encountered in SSIGs (typically around 20% in practical applications) where binary ice are often treated as non-Newtonian.

One of the non-Newtonian models that can be applied to describe the behaviour of binary ice is Bingham flow (Frei and Egolf 2000). Figure 1.3 tells the difference between a Newtonian fluid and a Bingham fluid. Bingham fluid (Bingham 1917) behaves like rigid body when shear stress is lower than the yield stress τ_0. Once the shear stress overcomes the yield stress, the suspensions become viscous fluid, which is pumpable.

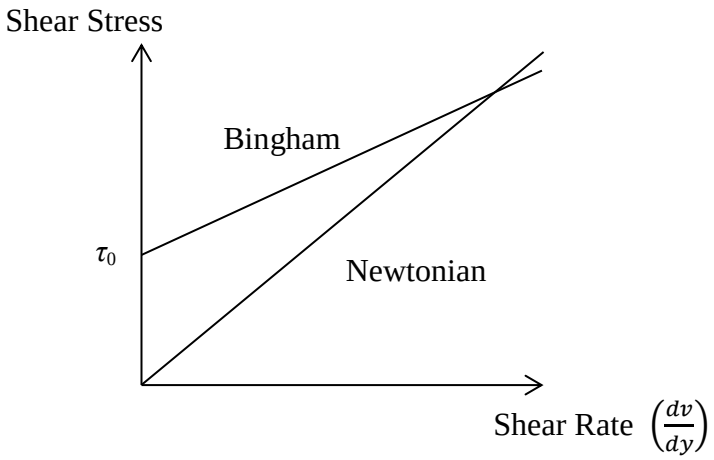

Figure 1.3 Rheogram for Newtonian and Bingham fluid

The relationship between the shear stress τ_B and shear rate $\frac{dv}{dy}$ for Bingham fluid is:

$$\tau_B = \tau_0 + \mu_B \frac{dv}{dy} \qquad 1.2$$

while the same relationship for Newtonian flow is

$$\tau_N = \mu_N \frac{dv}{dy} \qquad 1.3$$

where μ_B and μ_N, shown as the gradients of the lines in Figure 1.3 are the dynamic viscosities for Bingham fluid and Newtonian fluid respectively. The pumping power to enable the Bingham fluid to start moving from quiescent state should be large enough to overcome τ_0. The ice particles build some kind of internal structure when no stress is applied (Kauffeld et al. 2005). Once the yield stress is exceeded, the structure collapses, and the fluid begins to move.

From the figure, it can be deduced that when the flowrate in a given pipe increases, the shear rate and the corresponding shear stress both increase. When the flowrates are small, the required shear stress for a Bingham fluid is always larger than that for a Newtonian fluid. However, for the case shown in Figure 1.3, the viscosity of the Bingham fluid is smaller as indicated by the gradients. When the flow rate increases, the required pumping power for the Bingham fluid will eventually be smaller than that of the Newtonian fluid, thus saving pumping power at higher flow rates.

Therefore, there are two main reasons that using binary ice as secondary refrigerant will reduce pumping power consumption. First, for a given cooling capacity, the required flowrate of binary ice is much smaller than a pure liquid due to the involvement of latent heat when the ice particles melt. Second, for a binary ice mixture, its viscosity could be potentially smaller than the single phase solution of a higher concentration at the same temperature.

The relevant thermal-physical properties of binary ice such as viscosity, specific heat, specific enthalpy, density and thermal conductivity can be determined by combining the properties of the carrier fluid and ice at a given temperature once the ice concentration has been determined. The equations and calculation details can be found in *Handbook on Ice Slurries* (Kauffeld et al. 2005) and will be included in Appendix A and B.

1.2.3 Binary ice systems and their operations

The application of binary ice started from early 1990s (Paul 1992; Snoek 1993) and nowadays, they are widely employed. One of the most important application domains is the comfort cooling for large buildings (Wang and Kusumoto 2001). Using binary ice as the secondary refrigerant instead of chilled water can decrease the air distribution temperature and significantly reduce the air flowrate needed for a certain cooling capacity, meaning smaller equipment and less fan power for air distribution will be required.

Japan has the most binary ice air conditioning systems installed in the world, for over 400 buildings; while Europe has approximately 150 systems in 2009 (Rivet 2009). Examples include the Capcom Building (Bellas and Tassou 2005) which saved 4% of overall building running cost due to the reduced fan power and Herbis building in Osaka (Wang and Kusumoto 2001), where about 1/3 of the peak system load was reduced by using thermal storage involving binary ice.

Food preservation and processing is another large application area for binary ice. Ice slurry can be used as direct contact cooling agent for fast cooling of food such as fish (Wang et al. 1999), or as indirect coolant in heat exchangers during food processing for industries such as dairy production (Gladis 1997) and breweries (Kauffeld et al. 2010). It can also be used in large kitchens (Campos et al. 2005) and

supermarket display cabinets (Lueders 1999; Davies and Lowes 2002). Other possible applications include mine cooling (Kidd 1995), medical cooling (Brooker et al. 1997; Becker et al. 2000; Laven et al. 2007), firefighting (Lowes 2002), etc.

There are different strategies for the implimentation of a binary ice cooling system. Figure 1.4 displays a typical layout of a binary ice system for central air conditioning for buidings. Ice is generated by a vapour compression refrigeration. The ice and its carrier solution are then stored in a fully agitated tank before being pumped to the terminal units. Depending on the cooling demand, the fluid can return with/without ice to the tank. Under some circumstances, the storage tanks are not agitated. The concentrated ice at the top can be used for immersed cooling for food processing or medical use, while the pure liquid at the bottom can be pumped to the cooler for general comfort cooling (Guilpart et al. 2005).

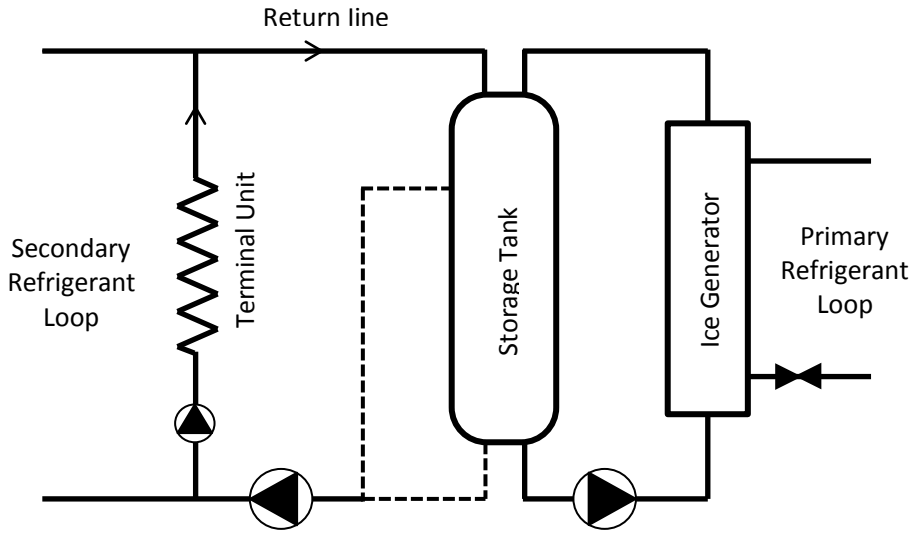

Figure 1.4 General binary ice system diagrams

In summary, the properties of binary ice and the operation characteristics of binary ice cooling systems are quite different from those of the conventional secondary refrigeration systems. The existing FDDs developed for the latter are not expected as being capable of handling the faults in binary ice systems. Therefore in this report, a new method is proposed.

1.3 Outline of thesis

Chapter 1 brings out the general concepts of FDD and binary ice systems. The unique features of binary ice systems have been introduced. It is necessary to develop a new FDD approach for binary ice systems as no existing method is applicable.

The literature review (Chapter 2) looks into the development of FDD for conventional liquid chillers as they share some common features with binary ice systems. Observations have been made and based on which the methodology of this study is proposed.

The FDD method is designed based on a particular binary ice test rig available in the laboratory. In Chapter 3, the experimental setup of this test rig is described. A prebuilt ice generator is coupled with a tank equipped with immersion heaters which simulates the cooling load. This test rig is monitored by various sensors to provide normal/faulty data for the studies.

For a model based FDD, a simulation model of the system is needed to provide fault free benchmark for the fault detections. As reviewed in Chapter 2, a single type of model may not be able to serve the FDD purpose well. Therefore in this study, a hybrid model, which consists of a dynamic analytical mode for the ice generator and a dynamic ANN model for the rest of the system, is applied. Chapter 4 looks at the process of ice forming in detail and the development of the associated mathematical formulations of the analytical model.

For the ANN model, its basic concept and the configuration method is presented in Chapter 5. The analytical model and the ANN model are calibrated and trained respectively, and validated with the data collected from the test rig. The coupled hybrid model and its validation is also covered in Chapter 5.

Based on the hybrid model, Chapter 6 focuses on the development of the actual FDD approach. The influences of the selected faults on various measured/derived parameters are investigated. The parameters for the detection and the diagnosis are selected respectively based on the above influence. To handle the dynamic feature of the system, a unique method called CUSUM test has been used to

speed up the detection and reduce false alarm. In addition, the diagnosis of some double faults is also addressed.

The results and discussions are presented in Chapter 7, where the results of the FDD approach are evaluated. Last, the whole project is concluded in Chapter 8.

2. Literature review

As pointed out previously, binary ice systems are similar to single phase liquid chillers in many ways. Therefore, the development of a FDD approach for a binary ice system can start from gaining a better understanding and analysing the existing FDD methods for single phase systems. In this chapter, previous researches related to FDD of RAC systems, in particular the vapour compression liquid chillers, are reviewed. The first part of the review focuses on the methods to obtain fault-free prediction data for fault detection in RAC applications. The development of analytical, black box and grey box models are examined here. The second part surveys the work on applying the modelling results together with the real system measurements for FDDs, including the selection of parameters and thresholds, and the development of diagnosis approaches. This is followed by a look into the evaluation of the FDDs performance by previous researchers, in terms of detection/diagnosis accuracy, speed, false alarm rate, etc. The motivation and objective of this project, and the overall research plan/methodology are then provided, based on the observations made from the previous work.

2.1 Vapour compression liquid chiller models

The implementation of FDDs is based on the comparisons of fault-free data and the measured data. In general, there are two ways to obtain fault free data: via historical data log or via model predictions (Chiang et al. 2001). Historical records are usually taken under specific working conditions at the specific time and therefore it may be difficult to apply them for general FDD purpose, as the data base can be too small to cover all the possible situations when faults are encountered. On the other hand, the development of a prediction model requires much less data points, and the models can produce simulated results over a wide range of conditions; this makes prediction models a preferred option to produce faults free data (Katipamula and Brambley 2005).

To develop a suitable model for a FDD, there are some general considerations.

- Accuracy

A reliable prediction model should be an accurate reflection of the actual system. The accuracy of the model has a great influence on the reliability of the FDD, in terms of detection accuracy, rate and speed (Reddy 2006). If a model has small predictions errors, the thresholds for fault detection(s) can be reduced, and for FDD applications, this would enable an earlier detection of a fault and reduce the false alarm rate (Sreedharan and Haves 2001).

- Data requirement

Prediction models often require data for validation, training or/and calibration, depending on the types of the model (Katipamula and Brambley 2005). Two main issues need to be addressed: 1) the number and type of the model input parameters and 2) the amount of data points required. The monitoring of the system parameters requires specific instrumentation and costs money; some parameters may not be acquired easily due to system constrains, such as acquiring the internal wall temperature of a ready built heat exchanger. Thus it is desirable to build a model which would require fewer input parameters that should also be cheap/easy to measure, in order to improve applicability and to save the cost of FDD. As for the second issue, generally speaking, making available a large amount of data points for model training and calibration would increase the accuracy of a model. However, data recording is both time consuming and expensive. A model should be developed in a way that it requires a smaller amount of data points while maintaining an acceptable level of accuracy.

- Physical relevance of the modelling parameters

Particularly for analytical/mathematical models, the parameters involved must have physical meanings and they should be, as far as practically possible, directly related to key operating characteristics or/and certain types of fault, making their detection relatively straight forward.

As mentioned in Section 1.1.1, three types of models have been developed for FDDs, namely analytical model, black box model and grey box model. Some previous studies are surveyed below.

2.1.1 Analytical model

To build an analytical model for a refrigeration system, a deep understanding of the associated physical principles that govern the system behaviour and operational characteristics is needed. The models are usually built from component level before system integration (Koury et al. 2001). For transient analytical models, the key to describe the dynamic behaviour of chillers is to capture the transient characteristics of the heat exchangers (evaporator and condenser), because they hold most of the refrigerant charges of the system. The expansion valve and the compressor can be treated as steady state all the time as their condition changes are much faster compared with the heat exchangers.

For instance, sub-models of evaporator and condenser usually consist of a set of time-space partial differential equations representing heat, mass and momentum balances within the heat exchangers, which can be solved to determine local heat transfer, temperature and pressure at any specific time (Katipamula and Brambley 2005). For compressors and expansion devices, as their thermal inertia are quite small (Bendapudi et al. 2002b), quasi-steady state assumptions are often applied. The component models are then coupled together with the thermodynamic states of refrigerant and mass continuity. The enthalpies, mass flowrates and properties of refrigerant at the outlet of one component become the inlet to the next coupled component.

Detailed mathematical models are difficult to construct and require relatively huge computational time; to reduce the complexity of the modelling and simulation, assumptions are often made. Common assumptions from literatures include using the idealised refrigeration cycle, constant refrigerant charge level (McIntosh et al. 2000), 1-D refrigerant flow in heat exchangers (Nyers and Stoyan 1994; He et al. 1997), etc. Assumptions vary with modelling approaches and they may affect the accuracy of the model and hence the reliability of the FDDs. Many of the assumptions may also be valid for the binary ice system involved in this study. By analysing the application and viability of the common assumptions for various RAC systems, it may help identifying the appropriate ones for the current study.

Many analytical models have been built but they are mainly developed for system or component designs, not many of them have been used for FDDs. Some

examples of mathematical models for general vapour compression system simulation are given below. Attention will be paid to the type of system, the selection of modelling parameters and the model's potential of being employed for FDD purpose.

Browne and Bansal (2002) built a detailed dynamic model for a packaged liquid chiller. For individual system components, correlations of heat and mass transfers were developed. System geometrical parameters, such as size of the heat exchangers, total mass of chilled and cooling water, total amount of refrigerant and the assumed/estimated distribution within individual system components were needed as modelling parameters. The required input variables included chilled water and cooling water temperatures and mass flowrates, wall temperatures of condenser and evaporator, ambient temperature, as well as the estimated building load and the set point temperatures of the evaporator water outlet and condenser water inlet. Empirical regression had been used for the compressor sub-model, to improve the overall model accuracy. The simulation could be applied to calculate the cooling capacity, compressor input work and refrigerant temperatures of condenser and evaporator. The model provided good results for the transient period during system start-up. When the system was operating under steady state, the modelling accuracy was 90%; the errors were due to the omission of the control system in the model, though physically it was incorporated in the system. The model may not be suitable for general FDD applications as the distribution of the refrigerant cannot be easily measured in practical situations, as well as the wall surface temperatures of the heat exchangers.

He et al. (1997) developed a model for describing the dynamics of vapour compression cycles. In particular, the dynamics associated with the evaporator and the condensers were modelled based on a moving-interface approach in which the position of the two-phase/single-phase interface inside a one-dimensional heat exchanger could be properly predicted. Two sets of lumped parameters were applied in this model for the two-phase and the single phase zones separately. However, it is believed the lumped parameter models would not be suitable for binary ice system in which the properties of the binary ice change significantly inside the heat exchanger even under a small temperature variation.

In modelling a variable speed chiller system, Koury et al. (2001) developed a transient distributed model for the condenser and the evaporator, in which the heat

exchanger was divided into small elements. Conservation equations and local heat transfer coefficients were applied for individual elements. A steady state assumption was employed for calculating the refrigerant mass flowrate through the compressor and the expansion valve. The model could predict system behaviour during start-up, compressor speed and TEV valve flow area variations. The use of finite element method helped increase the reliability of the model. Moreover, the ability of predicting system behaviours during dynamic change made it possible for dynamic fault detections.

In general, it is difficult to apply and adapt a particular model to other chillers as each has a unique set of heat transfer coefficients depending on the type of heat exchanger employed and flow conditions encountered. However, with the help of calibration variables and/or experimental data, it is possible to modify a detailed physical model, developed for a system, and adapt it for another similar system. McIntosh et al. (2000) modified a detailed model from Braun (1988), which was originally developed for a 5500-ton centrifugal chiller, to be applied to a laboratory 2000-ton centrifugal chiller. This calibration method could in fact be also used to improve modelling accuracies of a given system.

Bendapudi et al. (2002a) developed an analytical model of a centrifugal chiller which they claimed to be potentially suitable for FDD purpose. Unlike all the dynamic models they have reviewed and presented in an earlier report (Bendapudi et al. 2002b), which were not able to predict accurately the dynamic behaviours of centrifugal liquid chillers, this model considered refrigerant re-distribution between components as part of the dynamic features. The influences of the control feedback were also included in the modelling. The model was capable of predicting the compressor start-up and load changes.

Although some previous efforts had been made to applying analytical models to FDDs, full analytical models are still considered not common for FDD applications. The correlations, e.g. He et al. (1997), relating the relevant parameters are difficult to develop and computationally intensive to solve even after simplifying assumptions have been made. Browne and Bansal (2002) showed that the poor accuracy encountered in some of the pure analytical models could be improved by empirical calibrations. In addition, some common essential input parameters such as internal

heat exchanger wall temperature and the refrigerant distribution in individual components are difficult to determine in real applications.

2.1.2 Black box model

Black box model, as the name suggests, does not show the internal physical relationships between its input and output parameters. The model links the inputs to the outputs by developing its own set of mathematical correlations. There are two main kinds of black box model: Artificial neural networks (ANN) (Kubat 1999) and regression models (Sen and Srivastava 1990).

- **ANN model**

Artificial neural networks, which simulate the biological neural structures in human brain (Bar-Yam 2003), have the ability of machine learning and pattern recognition (Bishop 2006). An ANN model consists of interactive artificial neurons, which are considered as computational units. The neurons are grouped into an input layer, an output layer and hidden layer(s). Figure 2.1 shows a simple example of an ANN with only one hidden layer. This network has m inputs (x_1, x_2...x_m), k hidden neurons (f_1, f_2…f_k) and a single output (y).

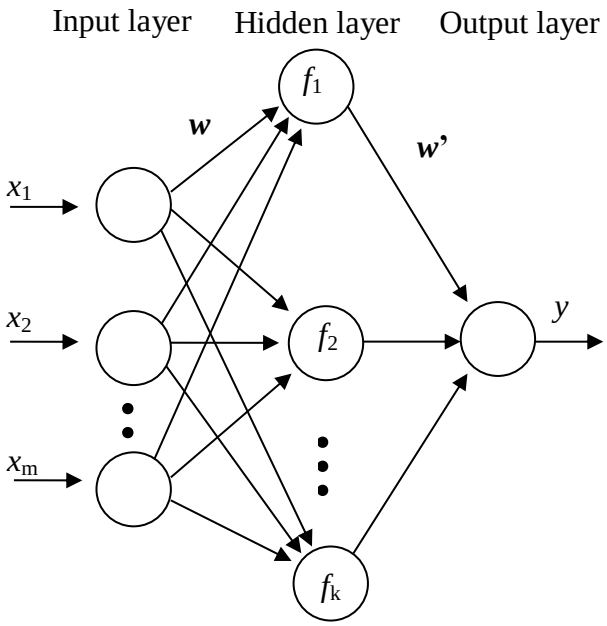

Figure 2.1 A typical structure of an ANN model

Each individual neuron in the input and output layer represents a parameter of the model, and each neuron of the hidden layer contains an activation function. The arrows between the input and the hidden layer are referred to as a $m \times k$ weight matrix $\boldsymbol{w}$, while the arrows between the hidden and output layer form a $k \times 1$ weight matrix $\boldsymbol{w'}$. The input values are multiplied by the weight matrix first and then added together before passing to the activation function in the hidden neurons. For instant, the input (l_j) to the j^{th} (j = 1 to k) activation function can be calculated by

$$l_j = \sum_{i=1}^{m} w_{i,j} x_i + b_j \qquad 2.1$$

where $w_{i,j}$ is the weight (usually a number between 0 and 1) and b_j is the bias (taken as between -1 and +1). The outputs of the activation functions are then weighted and summed again to generate the final model output(s), which can be expressed by,

$$y = \sum_{j=1}^{k} w'_j f_j \left(l_j\right) \qquad 2.2$$

The number and type of activation function are chosen by the users (Swider 2003), depending on the amount of training data available and the desired accuracy. In practice, the same activation function is selected for all the hidden neurons in an ANN network. Step function, Gaussian function and sigmoid function are three typical activation functions (Halm-Owoo and Suen 2002). ANN training is to match the calculated model outputs with measured training data pattern by adjusting the weight and bias matrixes to keep the errors between the calculated and measured data to a minimal level (Yegnanarayana 2009). One of the most common training techniques is the back propagation algorithm (Hu et al. 2007).

Among various ANN types, multilayer perceptron (MLP) and radial basis function (RBF) are most often applied for chiller fault detection modelling (Swider et al. 2001; Rueda et al. 2005; Navarro-Esbrí et al. 2007). For MLP, the activation functions are usually chosen as a *tanh* function (which is a kind of sigmoid function (Ertunc and Hosoz 2006)) and the network shown in Figure 2.1 is a typical MLP. RBFs commonly use Gaussian distribution (Albrecht et al. 2000) as an activation function, and instead of using the weight matrix $\boldsymbol{w}$ and bias $\boldsymbol{b}$ as shown in Equations 2.1 and 2.2 for MLP, the centre $\boldsymbol{\mu}$ and the standard deviation $\boldsymbol{\sigma}$ are adjusted to match the network output with the training data.

MLP and RBF can both provide highly accurate predictions, while the accuracy of MLP is even higher (Swider 2003). However, it was reported that when compared to MLP, RBF is less computationally intensive and needs less training time (Swider et al. 2001).

Some examples of application of ANN models for chillers are presented below. An ANN model using the RBF network was reported by Swider et al. (2001). Model inputs were chosen from parameters which could be easily measured or derived, including cooling capacity, evaporator chilled water outlet and condenser cooling water inlet temperatures. The model was implemented by Matlab and tested with data from a single screw chiller and from a twin-circuited chiller under steady state conditions. Two steps were involved in the network training, 1) optimise the centre of the Gaussian functions and this was carried out by using *K*-means algorithm (MacQueen 1967) and 2) adjust the standard deviations of the Gaussian functions to be the same as the distance between the Gaussian functions, which is a common practice. The accuracy of the predicted chilled water inlet and cooling water outlet temperatures were within 0.5%. For COP and electrical power consumption of the compressor, prediction accuracies were within 5%. The author concluded that a RBF network can be applied to provide accurate predictions for vapour compression liquid chillers.

Navarro-Esbrí et al. (2007) developed a RBF model for a variable-speed vapour compression glycol chiller. The key features of this model were its low data requirement for training and it had also been validated outside the range of the training data. In order to obtain a good accuracy using limited numbers of input variables and training data, the number of neurons needed to be increased gradually until the pre-set training goal was achieved. It took the return water/glycol temperature to the evaporator, the condensing water inlet temperature, the evaporator refrigerant outlet temperature and the compressor rotation speed as inputs to predict the cooling capacity, compressor power consumption and chilled fluid outlet temperature. Eight steady state tests were undertaken with various cooling loads and condensing conditions; 6 of them were applied for model training and validation and the other 2 were for testing the ability of the model. The model was validated with data from both inside the training data range and outside the range. The validations

showed that the prediction accuracies for both ranges were very good, although the former was slightly better.

Rueda et al. (2005) built a set of ten MLP ANN models to detect refrigerant leakage based on ten system output parameters which were the secondary fluid outlet temperatures for both condenser and evaporator, the refrigerant temperatures at both inlet and outlet of condenser and the evaporator and compressor suction and discharge pressures. It took two secondary fluid flow inlet temperatures as inputs, one from the condenser and another from the evaporator. A *tanh* activation function and conjugate training (Barnard and Cole 1989) were employed. The model provided high coefficient of variance of around 0.99.

The black box model has shown certain advantages, when compared to analytical approach, especially in modelling complicated systems. Ertunc and Hosoz (2006) developed a MLP ANN model of a refrigeration system. Their work was complicated by the fact that an evaporative condenser was used in the system. Compared with air- or water-cooled condenser, its operation related to both dry bulb and wet bulb temperatures, which made it relatively harder to be modelled physically. The input parameters were cooling load, air mass flowrate to the condenser, and the air dry and wet bulb temperature at the condenser inlet. Output parameters included condenser heat rejection rate, refrigerant mass flowrate, compressor power, compressor motor electric power and COP. Weights of the neurons were adjusted by a back propagation algorithm (Bryson and Ho 1975). This model had a good prediction performance with errors of around 2% ~ 4%.

Static ANN networks can also be adapted to simulate dynamic system behaviours based on the same network structures (e.g. MLP or RBF) (Yoon and Lee 2010). The inputs and outputs of a dynamic ANN are time series data. The value of an output at a particular moment is usually determined by the inputs at the previous moment(s) as well as the previous value(s) of the output itself. These inputs can be taken at one (known as one step delay) or more previous time steps (Chetouani 2008). The detailed structure of dynamic ANNs employed in this project will be described in Chapter 5.

Many dynamic ANNs of refrigeration systems have been built by previous researchers. One was developed by Bechtler et al. (2001) using a RBF network to simulate the start-up and transient fluctuations of chiller based on three outputs (i.e. compressor power consumption, COP and chilled water inlet temperature) and three inputs (i.e. cooling water inlet temperature, chilled water outlet temperature and evaporator capacity). It was found that when sudden change occurred to the system, the model generally provided a much smoother prediction than the actual variation creating larger errors. This was thought to be caused by the lack of training data and the use of a large sampling interval (30s). Only previous values of one time step were used.

Yoon and Lee (2010) designed a dynamic RBF network with a one-step delay to predict the refrigerant temperatures at five different positions within the primary circuit. As the temperature of refrigerant at a particular position was influenced by what happened upstream of the flow, in order to predict the temperature at this location, the previous value of an upstream position was also used as an network input together with the previous values of the inputs and output of the current position. However, the selection of the time step must be careful and precise to ensure the upstream influence was captured. The authors also compared their network with two MLP networks trained by different methods, and concluded that the RBF had the best accuracy, though other paper (Swider 2003) pointed out that MLP structures had better accuracies when training time was not an issue.

Hu et al. (2007) developed a dynamic ANN model for an air handling unit based on an MLP network. The inputs included the mass flow rates of both chilled water and the supply air, as well as the inlet temperatures of the chilled water and the air flow. The outputs were the outlet temperatures of the chilled water and the supply air. Having been trained by 410 data patterns, the errors for more than 90% of the model predictions were smaller than 5%. It could be used as a prediction model for FDD purposes.

- **Regression model**

A regression model is another kind of black box model and it has a general form as:

$$\mathbf{t} = \beta^T \cdot \mathbf{X} + \boldsymbol{\varepsilon} \qquad 2.3$$

where vector **t** is the model output parameter matrix, **X** represents the experimental independent variables, $\boldsymbol{\beta}^T$ represents a transpose matrix of the fitted coefficients, which has no physical meaning, and **ε** is the remained error. The process of regression is to find a suitable parameter matrix $\boldsymbol{\beta}$ that best matches the input vector **X** into output vector **t**. Fitting can be done by minimizing the sum of least squares error (LSQ) (Björck 1996), the negative log likelihood (LLH) (Platt 1999) or ordinary least square (OLS) method (Björck 1996).

Linear regression is one of the simplest regression methods. A bi-linear regression model was presented by Stylianou (1997), using the evaporator and condenser water inlet temperatures as the independent variables. The regression equation was:

$$y = \beta_0 + \beta_1 T_{\mathrm{e,in}} + \beta_2 T_{\mathrm{c,in}} + \varepsilon \qquad 2.4$$

where y was the dependent output variable of the model (e.g. COP), β_0, β_1 and β_2 were regression coefficients and ε was the error that needed to be minimized by adjusting the regression coefficients.

After training, this model could provide predictions with frictions of variance (Everitt and Skrondal 2002) higher than 99%. This linear regression model, which was very easy to develop and only required relatively a small amount of training data, had advantages when the target system was relatively simple. However, when a more complicated system, such as twin-circuited chillers were evolved, the accuracies of prediction dropped significantly (Swider 2003).

A non-linear polynomial regression method was applied to predict the performance indexes in Cui and Wang's work (2005). All the indexes were considered functions of cooling load Q, chilled water supply temperature $T_{\mathrm{e,in}}$ and condenser water entering temperature $T_{\mathrm{c,in}}$. The regression model took the following form:

$$y = \beta_0 + \beta_1 T_{\mathrm{e,in}} + \beta_2 T_{\mathrm{c,in}} + \beta_3 Q + \beta_4 T_{\mathrm{e,in}} T_{\mathrm{c,in}} +$$

$$\beta_5 T_{\mathrm{e,in}} Q + \beta_6 T_{\mathrm{c,in}} Q + \beta_7 Q^2 + \varepsilon \qquad 2.5$$

The output variable *y* could be the performance indexes: *COP*, $LMTD_{\mathrm{e}}$, $LMTD_{\mathrm{c}}$, motor efficiency, isentropic efficiency and refrigerant mass flowrate. Eight regression coefficients were employed. The model was validated with steady state fault free field data by OLS method. The coefficients of determination (Steel and Torrie 1960) for all model outputs were higher than 90%.

Regression models can be applied for transient simulations as well. Similar to the dynamic ANN models, dynamic regression models also involve a delay line using the current and previous value(s) of both the input and output as the model input to predict the future value(s) of the output.

Riemer et al. (2002) proposed an auto regressive moving average (ARMA) model. For an auto-correlated time series $\boldsymbol{x}$, the value at a certain time step could be determined by using the previous values of the same time series, as demonstrated below.

$$x_t = \alpha_1 x_{t-1} + \alpha_2 x_{t-2} + \cdots + \alpha_p x_{t-p} + z_t + \beta_1 z_{t-1} + \beta_2 z_{t-2} + \cdots$$

$$+\beta_q z_{t-q} \qquad 2.6$$

where $z_t = x_t - x_{t-1}$ was the difference term of *x* between time steps; $\alpha_1,\ \alpha_2 \ldots \alpha_p$ and $\beta_1,\ \beta_2 \ldots \beta_q$ were the regression coefficients; *p* and *q* were chosen by the user, based on the nature of the time series $\boldsymbol{x}$. This model could be applied to predict chilled water flowrate, chilled water supply temperature and the evaporating temperature.

In general, black box models, including ANN and regression models, show great advantages when modelling complex nonlinear systems compared to analytical models that are based on first principle. Both ANN and regression models are capable of handling dynamic system simulations and of producing relatively good accuracies when large amount of measured training data are needed, which could be regarded as a disadvantage.

2.1.3 Grey box model

To minimise the drawbacks of analytical models and black box models, grey-box models are developed. There are various ways of formulating a grey-box model, e.g. a serial approach or a parallel approach (Estrada-Flores et al. 2006). A serial approach means an output of the black box model can be used as an input to the white box model (or vice versa). On the other hand, for the parallel approach, the same input data are sent to both the black and white box models at the same time. The model outputs were first calculated by the white box model, while the black box model compared the analytical results with the real fault free measurements and generated a correction signal to improve the overall accuracy.

The serial approach is often applied in the modelling of refrigeration systems (Estrada-Flores et al. 2006). When building up a component level physical model for a system, a black box sub-model can be applied for the complex components such as the compressor (Browne and Bansal 2002). Other examples of serial approach grey-box models for FDD applications include the thermodynamic models Gordon and Ng (2000), Lee (2004), Ng (2008), and the characteristic models of Jia and Reddy (2003).

The thermodynamic grey-box model of Gordon and Ng (2000), developed for centrifugal and reciprocating chillers, was based on the First and Second Laws of Thermodynamics, describing the energy and entropy balances of the chillers, as given below:

$$\frac{T_{\mathrm{e,in}}}{T_{\mathrm{c,in}}}\left(1+\frac{1}{COP}\right)-1=\frac{T_{\mathrm{e,in}}}{Q_{\mathrm{e}}}\Delta S_{\mathrm{t}}+Q_{\mathrm{leak}}\frac{T_{\mathrm{c,in}}-T_{\mathrm{e,in}}}{T_{\mathrm{c,in}}\times Q_{\mathrm{e}}}+\frac{R\times Q_{\mathrm{e}}}{T_{\mathrm{c,in}}}\left(1+\frac{1}{COP}\right) \qquad 2.7$$

where the internal entropy generation rate in the chiller due to internal irreversibility (ΔS_{T}, kW/K), the equivalent heat loss from the chiller (Q_{leak}, kW) and the thermal resistance of the heat exchangers (R, K/kW) were the regression coefficients all of which had physical meanings, and they were obtained using a regression model. All the other parameters in the equation could be obtained from measurement. The training of this model was to use a set of the above measured parameters under fault free condition to determine ΔS_{T}, Q_{leak} and R by multiple linear regressions. The model could then be used to predict system COP. In this case, ΔS_{T}, Q_{leak} and R were the model parameters of a first principle model that cannot be measured directly. The

model was first transformed into a regression function to obtain the above three coefficients. Then they could be applied as constant inputs to Equation 2.7 to calculate the model output.

One advantage of this kind of grey-box model is that as the regression coefficients of the grey-box models are physically meaningful and it is possible to carry out fault detection and diagnosis by examining their variations during faulty conditions. Saththasivam and Ng (2008) applied the above model for faults detection. Instead of relying upon the model output COP for FDD, they claimed that the values of ΔS_T and R could be used to indicate the health of the chillers. ΔS_T could be linked to the operation of the compressor and the expansion valve (e.g. an increased ΔS_T may suggest excessive oil in the compressor), whereas the thermal resistance R was related to heat transfer rates in the evaporator and condenser (e.g. an increased R could indicate reduced cooling water flow or condenser fouling). For a given chiller system, those coefficients were considered as constants under normal operating conditions.

Equivalent heat loss Q_{leak} was less likely to be influenced by operation conditions when compared with the other two, hence less useful as a FDD detection parameter. During the fault detection process, 12 fault free data sets from a 90-ton centrifugal chiller were applied to determine ΔS_T and R by the regression method. Input parameters based on measured values included: cooling load, secondary fluid inlet temperatures for the condenser and evaporator and COP, and model outputs were ΔS_T and R, and they were compared with the constant values for FDD.

Another example of a serial hybrid model was the characteristic model developed by Jia and Reddy (2003). It combined refrigeration cycle analysis with regression correlations. Simplified lumped physical models were developed first to calculate the characteristic parameters of the components, that describe the performance of the components and were linked to certain types of faults (e.g. motor efficiency and polytrophic efficiency for the compressor, overall heat conductance (i.e. UA values) of the evaporator and condenser, the product of the fluid friction coefficient (a function of refrigerant velocity) and the cross-sectional area of the orifice for the expansion valve, and COP for the overall system performance).

When using the models for FDDs, the above characteristic parameters were first calculated by using a set of fault free measured data under different working conditions, and then they were fitted into regression functions taking cooling water inlet, chilled water inlet and chilled water outlet temperatures as inputs. The fitted regression functions were then used as baseline models for fault detection. This method was considered as an inversed serial grey-box model because the using of white box model is prior to the regression model.

The three main types of refrigeration system models each have their strengths and limitations. Comparisons of different models, mainly based on the accuracy, data requirement and computational requirement, had been done by various researches (Peitsman and Bakker 1996; Sreedharan and Haves 2001; Swider 2003). Swider (2003) compared four regression models, including a grey box model, and two ANN models when applying them to a single-circuit centrifugal chiller and a twin-circuit twin-screw chiller. The four regression methods included linear regression, bi-quadratic (Yik and Lam 1998) regression, multivariable regression and the Gordon and Ng's (2000) thermodynamic grey box model; the two ANN models were a RBF model from Swider et al. (2001) and a MLP model using *tanh* activation function. All, except the bi-quadratic model, used the same three input variables: cooling capacity, condenser water and evaporator water inlet temperatures; the bi-quadratic model only needed the first two, and they all were trained with the same set of data. The output of all the models was COP.

In terms of modelling accuracy, all the above models provided accurate predictions for the centrifugal chiller, but the Gordon and Ng's thermodynamic model had the advantage of requiring less training data due to its physical meaningful equations. However, for the more complicated twin-screw twin-circuit chiller, only the two ANN models could produce acceptable predictions, the four regression models could only provide accurate predictions when they were improved by setting up separate models for each circuit, hence reducing the system complexity in modelling sense. Generally speaking, when there were enough training data, the ANN models gave the highest accuracy, followed by the three regression models, and the thermodynamic model was the least accurate. The results also showed that although MLP gave slightly better prediction results than RBF, they required longer training

time. The thermodynamic model showed its advantage when the training data were highly limited.

In conclusion, the selection of a prediction model for FDD should consider the complexity of the target system and the selected faults, the availability of the measurements and the accuracy of the prediction.

2.2 FDD approaches

The fault detection and diagnosis can be separated as two steps (Cui and Wang 2005) or be integrated as one single step (Bailey and Kreider 2003; Rueda et al. 2005). In this review, the common approaches for detection and diagnosis will be presented separately.

2.2.1 Fault detection

Most FDDs are performed by comparing model predictions with real data. The development of fault detection approach involves selecting suitable detection parameters, determining the status (static or dynamic) of the system and calculating the appropriate thresholds.

- Selection of fault detection parameter

A large number of parameters, including measured and derived, are available to describe system behaviours. Under faulty conditions, some of these parameters need to be identified as they are more sensitive to the fault(s) and thus will produce relatively larger residuals while others will not be affected much. Table 2.1 lists the measurements used in some FDD studies; temperature, pressure, flowrate and electrical power were the main data group. Temperature measurements include the refrigerant temperatures around the system circuit, and the condenser/evaporator secondary fluid temperatures, usually taken at the inlet and outlet of the heat exchangers. Refrigerant pressures are normally measured at inlet and outlet of major components. Flowrate measurements are required for condenser and evaporator HTFs and sometimes the refrigerant flowrate is acquired as well. Electrical power consumption of compressor is often regarded as an important measurement (Comstock et al. 2002a). In some FDD development, oil pressure and temperatures were also used (Rueda et al. 2005).

Table 2.1 Measurements and derived parameters used for previous FDD development

	Castro (2002)	Ertunc and Hosoz (2006)	Lee (2004)	Navarro-Esbrí et al. (2007)	Peitsman and Bakker (1996)	Reddy (2007a)	Rueda et al. (2005)	Stylianou (1997)
T_{com}	✓	✓	✓	✓	✓	✓	✓	✓
$T^r_{e,in}$	✓	✓		✓	✓		✓	✓
$T^r_{e,out}$	✓	✓		✓	✓	✓	✓	✓
$T_{TXV,in}$	✓	✓		✓	✓			✓
$T^r_{c,out}$	✓	✓		✓	✓	✓	✓	✓
$T_{c,in}$	✓		✓	✓	✓	✓	✓	✓
$T_{c,out}$	✓		✓	✓	✓	✓	✓	✓
$T_{e,in}$	✓	✓	✓	✓	✓	✓	✓	✓
$T_{e,out}$	✓	✓	✓	✓	✓	✓	✓	✓
m_r	✓			✓	✓			
$m_{c,sec}$		✓	✓	✓	✓	✓	✓	✓
$m_{e,sec}$		✓	✓	✓		✓	✓	✓
p_c		✓		✓		✓		✓
p_e		✓		✓	✓	✓		
p_{dis}			✓	✓	✓		✓	✓
p_{suc}			✓	✓	✓		✓	✓
$p_{TXV,in}$				✓	✓		✓	
$p_{TXV,out}$				✓	✓		✓	
W		✓	✓	✓	✓	✓		
Q_e		✓				✓		
Q_c						✓		
N				✓				
TO							✓	
PO							✓	

It can be seen some researchers considered relatively more parameters than the others, though not all their parameters were eventually used for FDD. The selection of FDD parameters depended on the numbers and the types of faults involved and their sensitivity towards the chosen faults and the cost of implementing the measurements, which resulted in some parameters being common to almost all the works. The refrigerant discharge temperature and secondary flow temperatures/flowrates were

measured/used in nearly every test, as they are both easy to obtain and are sensitive to many kinds of faults. In general, temperature and pressure can be measured with inexpensive sensors, while flow meters and power meters are relatively more expensive. To achieve a cost effective and reliable FDD method, the measurement points and sensor types need to be carefully selected to ensure that accurate detection can be obtained with minimum number of sensors.

- Dynamic VS steady state

It is generally acknowledged that chillers operate for most of the times under unsteady conditions (Yoon and Lee 2010). Any changes of operation conditions, e.g. start-up, load fluctuations, feedback controls, climatic change, etc. can result in transient operations, where system parameters keep varying, making it difficult to detect the faults. On the other hand, most of the existing FDD methods aim at fault detection under steady state and they are applicable in transient systems provided certain quasi-steady criteria/conditions are satisfied.

The criteria of steady state detection vary with individual systems, with a variety of techniques available from published literature. The simplest method is to assume that steady state condition is reached after a specified period of time following a change in operation. However, this period is hard to specify accurately and it varies with equipment type, cooling load, ambient temperature, etc. A more reliable steady state detection algorithm is to check, based on sensor measurements, whether the operating system is meeting certain steady state criteria.

Rueda et al. (2005) developed a two-part steady state detector in which both parts need to be satisfied. The first part was to detect whether this system was on or off by measuring the pressure ratio. In the second part, the present and the previous values of the parameter that had the slowest response to condition variation were compared, which was identified as the compressor discharge temperature in their case. If the temperature change was less than 1 K in 10 minutes, the operation was considered as steady.

Castro (2002) developed another steady state detector based on the calculation of the exponentially weighted moving average. For each measurement, more than 7 points were taken for calculating a moving average. If the ratio of the standard

derivation of the 7 measurements to the moving average was smaller than a certain specified tolerance, a steady state condition was declared.

There are also some dynamic FDDs aiming at detecting faults without the need of a steady state detector and they will be reviewed later.

- **Threshold selection**

Fault detections are carried out by comparing residuals between fault free data and actual measurements with pre-determined fault free thresholds. Residuals normally increase with the severity levels of the fault and they exist even under faulty-free conditions due to natural data variations as well as the modelling and measurement errors/uncertainties. Thresholds are set up benchmarks for residuals to distinguish faulty and normal operations. The setting of threshold is a trade-off between detection sensitivity and false alarm rate (Reddy 2007a).

FDD methods with small thresholds can detect a fault at an earlier stage, but the residuals should be big enough to accommodate the modelling error and measurement uncertainties to avoid false alarm.

Using fixed thresholds is the most common practice in FDDs. It can be applied for both static (Salsbury and Diamond 2001; Rueda et al. 2005) and dynamic (Chen and Lan 2009) FDDs. The values of the thresholds are usually determined by errors of modelling and measurements. Mean standard errors (Everitt and Skrondal 2002) have been applied to regulate the thresholds (Ng 2008). When using 1-mean standard error as a threshold, the false alarm rate was about 32%, but when using a 2-mean standard error, the false alarm rate dropped to 5%. T-value thresholds (Reddy 2007a) have also been used to reduce false alarm rate. It was essentially a trial-and-improve process. The threshold was tested with fault free data and if the false alarm rate was higher than anticipated, a larger threshold would then be chosen.

However, the errors/uncertainties vary with operational conditions. One fixed value is not ideal for detecting faults under various conditions. Therefore some adaptable threshold estimation methods have been developed (Cui and Wang 2005; Navarro-Esbr íet al. 2006; Reddy 2007a) for FDD development for chillers.

Cui and Wang (2005) included an online threshold estimation scheme that could adapt thresholds according to the measurement error and modelling error. The thresholds were functions of cooling load, condenser flow inlet and evaporator water flow outlet temperatures. It was stated that smaller thresholds should be selected under larger cooling load and when encountering lower condenser flow inlet temperature because the parameters were more sensitive to faults under those conditions. This matched with the results from Comstock et al. (2002a), i.e. the sensitivity of a measured parameter to a fault (defined as the ratio of the measured residual under a certain fault level to the maximum experimental uncertainty of the parameter) increases with cooling load and decreases with condenser flow inlet temperature.

Navarro-Esbr íet al. (2006) designed an algorithm to determine thresholds for dynamic fault detections. The threshold at a certain time was calculated using the quadratic error between the measurement and prediction as well as the standard deviation of the modelling error at the previous time step. This method was able to reduce false alarm rate when the cooling load was changed.

Under dynamic operations, the residual may go beyond the threshold for a very short period of time due to fluctuation or measurement error even when no fault is presented in the system. In this case, a rule is needed to define an actual 'exceeding of the threshold' condition to avoid false alarm. A CUSUM (cumulative sum) (Hinkley 1971; Basseville 1986) test can be applied to monitor the changes of a time series. The test aims to detect small changes of the mean of the data sequence. It assumes that under fault free condition, the residual sequence is normal distributed with a mean value of zero, while the presents of a fault will change its mean (Basseville and Nikiforov 1993). By using this method, the random isolated residual points that go beyond the threshold but do not change the mean of the time series; thus it won't be identified as a fault and hence the chance of false alarm is reduced.

The adaptable threshold methods are able to reduce the false alarms caused by a sudden change of the working condition in a system, while the CUSUM test can significantly reduce the false alarms caused by random measurement errors or fluctuations. In general, the adaptable threshold methods require a full understanding of a specified system and involve complicated mathematic formulations. The author

considers CUSUM test a better approach as it has a standard procedure that can be simply adjusted for different systems. In addition, comparing with the dynamic threshold method the calculation process of CUSUM test is much simpler.

2.2.2 Fault diagnosis

Having detected an abnormal operation condition, the fault itself needs to be identified. Compared with fault detection, fault diagnosis is more difficult. In this section, the influence of various faults on different parameters will be reviewed. The methods to develop fault diagnosis algorithms are also discussed.

Variations in normal operation conditions due to fluctuations of load or ambient temperature may influence system outputs which are similar to those created by certain faults (Navarro-Esbr íet al. 2006). In addition, control feedback may try to correct the faulty outputs or multi-faults may cancel out the influence of each other; all these make diagnosis harder to perform (Wang and Cui 2005).

Fault diagnosis requires a full understanding of how faults influence individual system outputs. Comstock et al. (2002a) carried out a comprehensive review on the responses of chiller parameters to some common faults. They analysed the deviations of some key parameters under different chiller loads with different fault types and severity levels. As expected, all the deviations increased with rising fault severities. It also revealed that the system parameters were more sensitive to faults when the chiller loads were large. Some parameters were particularly sensitive to certain types of fault because those faults could only influence part of the system. They introduced a concept of fault sensitivity for certain measurements, using a ratio of the residual at the largest fault level to the maximum measurement uncertainty. The larger the ratio, the more sensitive the measured parameter towards certain faults would be. For example, in their study, considering the condenser flow restriction, the flow temperature difference between inlet and outlet was the best indicator for the presence of the fault.

Table 2.2 shows how various faults influence the operating characteristics of the evaporator, including evaporating temperature and pressure T_e and p_e, secondary fluid flow temperature difference ΔT_e, discharge and suction superheat temperature $T_{sh,dis}$ *and* T_{sh}, evaporator approach temperature difference T_{ea}, over all heat

conductivity UA_e and the log-mean temperature difference $LMTD_e$. In the table, ↑ represents an increase of a parameter when a fault is encountered, ↓ for a decrease and - means it remains unchanged. It is noticeable that for flow restriction in evaporator, contradictory observations were reported, due to the differences in the equipment types and working conditions. Relevant parameters for the condenser are shown in Table 2.3.

Table 2.4 shows the trends for the compressor as well as for the whole system. Isentropic efficiency η_{isen}, compressor discharge temperature T_{com} and electrical work input (W) to the compressor are the common indicators for the compressor. System COP, chiller efficiency $\eta_{chiller}$ and refrigerant mass flowrate, m_r, are often used for monitoring the performance for the entire system. The information in these tables was collated from a number of published papers (Rossi and Braun 1997; McIntosh et al. 2000; Castro 2002; Comstock et al. 2002a; Cui and Wang 2005; Reddy 2007a; Saththasivam and Ng 2008).

Table 2.2 Variations of measurements in evaporator

	Evaporator							
Faults	T_e	T_{sh}	ΔT_e	T_{ea}	UA_e	$LMTD_e$	p_e	$T_{sh,dis}$
Refrigerant leak	↓	↑	↓	-	-	-	-	-
Refrigerant overcharge	↑	-	-	-	-	-	↓	↑
Liquid line restriction	↓	↑	↓	-	-	-	-	-
Condenser fouling	↑	↓	↑	-	-	-	-	-
Evaporator fouling	↓	↓	↓	↑	↓	-	-	-
Condenser flow restriction	-	↓	-	-	-	-	↑	-
Evaporator flow restriction	-	-	↑	↑(↓)	↓	↑	↑	↓(↑)
Non-condensables	-	-	-	-	-	-	-	-

T_{ea}: evaporator approach temperature difference (= $T_{e,\,in}$ - T_e)

Table 2.3 Variations of measurements in condenser

	Condenser						
Faults	T_c	T_{sc}	ΔT_c	T_{ca}	UA_c	$LMTD_c$	p_c
Refrigerant leak	↓	↓	↓	↓	↑	-	↓
Refrigerant overcharge	-	↑	↑	↑	↓	-	↑
Liquid line restriction	↓	↑	↓	-	-	-	-
Condenser fouling	↑	↓	↓	-	↓	↑	↑
Evaporator fouling	↓	↓	↑	-	-	-	-
Condenser flow restriction	↑	↑	↑	↑	↓		↑
Evaporator flow restriction	↓	-	-	-	-	-	-
Non-condensables	-	↑	↑	↑	↓	↑	-

T_{ca}: condenser approach temperature difference (= T_c - $T_{c,out}$)

Table 2.4 Variations of measurements in compressor and at system level

	Compressor			System		
Faults	η_{isen}	T_{com}	W	COP	$\eta_{chiller}$	m_r
Refrigerant leak	-	↑	↓	↓	↓	↓
Refrigerant overcharge	-	-	↑	-	↑	
Liquid line restriction	-	↑	-	-	-	↑
Condenser fouling	-	↑	-	↓	↑	-
Evaporator fouling	-	↓	-	↓	-	-
Condenser flow restriction	-	↑	↑	↓	↑	-
Evaporator flow restriction	-	↑	↑	↓	↑	-
Non-condensables	↑	-	-	↓	-	-

$\eta_{chiller:}$ chiller efficiency (= cooling capacity/total electrical work input)

It can be seen from Table 2.2 to Table 2.4 that some faults have a larger impact on certain components than the others, e.g. evaporator performance is not too sensitive to non-condensable gas which is mainly trapped in the condenser. In addition, some faults are known to produce similar fault signatures at component levels, e.g. liquid line restriction and refrigerant leakage will have the same influences on the evaporator behaviour. To isolate the source of the faults, parameters need to be carefully examined and selected so that each individual fault can be represented by a unique pattern of variations of the parameters.

Rule based methods are also commonly used for fault diagnosis. A set of fault diagnosis rules is developed according to the changes of selected parameters under various faulty conditions. The residuals between measured and predicted parameters are used as inputs to the method and conclusion are drawn after searching through the whole rule space (Katipamula and Brambley 2005).

Cui and Wang (2005) developed a rule based diagnosis method using performance indexes. They claimed, when compared to direct sensor measurements, performance indexes were able to provide a more complete description of the system health. Six performance indexes were used, including LMTD of the condenser and evaporator, mass flowrate of refrigerant, compressor isentropic efficiency, motor efficiency and coefficient of performance. A fault diagnosis classifier based on the impact of certain faults on individual indexes was applied to distinguish certain pre-defined faults. However, their approach had only achieved a successful diagnosis rate of 16% for the reduced evaporator flow. The corresponding rates for refrigerant

leakage, condenser fouling, non-condensable and excess oil were 25%, 27%, 54% and 95% respectively.

A rule based system was also employed by Castro for a two-stage chiller (Castro 2002). The faults considered included condenser/evaporator fouling, liquid line restriction, refrigerant under- and over-charge. To develop an appropriate fault classification rules, for individual specified faults, residuals of 12 parameters were calculated. For each fault, two parameters with the largest normalized residuals were picked out for fault diagnosis. If the use of two parameters were not able to identify a fault, the parameter with the next largest residual should also be included, until a fault could be diagnosed. This method could diagnose most of the faults with good accuracy, except for liquid line restriction which had around 75% mis-diagnosis at a 30% restriction level. They suggested one possible reason for the low diagnosis accuracy could be due vapour flashing in the pipe creating similar symptoms as liquid line restriction. Their rules of selecting parameters could be modified and applied to the development of other fault diagnosis methods.

Reddy (2007a) applied Characteristic Features (CFs) for fault diagnosis. Examples of the CF employed included the *UA* value of the condenser and the condenser water temperature difference. He observed that some CFs had a linear relationship with chiller load. Under faulty conditions (e.g. reduced condenser water flow and refrigerant leakage), the y-intercept and/or the gradient would change.

When the fault detection rules are simple, they can be implemented manually; otherwise, certain pattern recognition programme would be needed. ANN fault classifier, whose output is the identified fault type, is a widely applied pattern recognition method. There are two common kinds of ANN fault classifier: (i) the residuals of the selected fault diagnosis parameters are transferred to simple pattern of -1, 0 and 1, representing the direction of variation of the parameters. The simplified patterns are used as input to the ANN classifier (e.g. Cho et al. (2005)), and (ii) the residuals are taken directly as inputs to train an ANN to generate the type of the fault as its output.

In general, rule based diagnosis methods exhibit low accuracies in detection of faults with low severity levels. To improve accuracy, Stylianou (1997) developed a

fault classifier based on a statistical pattern recognition algorithm (SPRA). Residuals of discharge temperature, sub-cooled temperature, evaporator temperature, suction line temperature, condenser and evaporator flow outlet temperatures, discharge and suction pressures were calculated. The statistical properties of the residuals, including the mean, minimum value, maximum value, standard derivation, skewness and kurtosis (Groeneveld and Meeden 1984), were the inputs to the fault classification algorithm. The algorithm calculated the chance of a certain residual belonging to each type of faults, and the residual with largest possibility helps to pinpoint the fault.

Most of the fault diagnosis methods are aiming at single fault. However, the co-occurrence of two or more faults is possible in many real systems. Cho et al. (2005) summarized that the interference between two faults could be grouped into three categories: 1) the magnitude of residuals of the single faults were similar with the double fault's combined residuals, 2) the combined residuals were the sum of both of the single fault and 3) the two individual faults influence different system parameters. When the ANN classifier taking simplified residual patterns develop for single fault was applied when multiple fault exist, it might not be able to tell the difference whether a single or a multiple fault existed as they may had the same input to the system. To solve this problem, they proposed a residual ratio method. This method compared the residual of two selected parameters and used the range of the ratios to differentiate between a single fault and a double fault when they had the same fault pattern.

In addition to the above reviewed quantitative model-based FDDs, qualitative model can also be used for FDD. Instead of using numerical inputs and outputs, qualitative parameters are used instead (e.g. temperature can be described as 'hot' or 'cold'). Expert systems (Kaldorf and Gruber 2002; Soyguder and Alli 2009) and decision trees (Katipamula et al. 2003) both fall into this category. The qualitative model based FDDs are usually very specific to a particular system and they are highly dependent on the knowledge of the developer. They are not widely applied in commercial systems (Katipamula and Brambley 2005); therefore in this study, qualitative model based FDD is not considered.

2.3 Evaluation of FDD performance

A good FDD technique should be able to provide fast and reliable results with minimum costs. In general, the following aspects are needed to be considered when evaluating a FDD.

1. High detection accuracy

An accurate method has a better chance to detect and diagnose a fault successfully. It can find out a fault and its location when the fault occurs.

2. High detection speed

A fast detection method will detect a fault at a very early stage, before it causes more energy wastage and damages to the system.

3. Low false alarm rate

False alarm rate needs to be balance with detection speed. A smaller threshold can increase sensitivity while also increase the false alarm rate.

4. Cost effective

Unlike other critical systems, the budgets for FDDs of RAC systems are usually very limited. The initial installation costs as well as the running and maintenance cost should be kept low.

5. Easy to use

The method should be easy to implement, provide straight forward result and solutions for the targeted faults.

Reddy (2007b) proposed a FDD evaluation method. Two indexes were used to rank the fault detection capability and the combined capability of fault detection and diagnosis separately. The fault detection index was calculated based on the false negative rate, the opportunity of occurrence and the energy penalty for each type of the fault. On the other hand, regarding the second index, referred as the diagnosis evaluation index, they considered the rates of four diagnosis results, namely correct and unique, correct but non-unique, incorrect and unable to diagnosis, combining

them each with a weight factor which is related to the time and cost taken to diagnose, evaluate and repair the fault. The two indexes were numbers between 0 and 1, while a larger number indicates the FDD being evaluated generates a better result. This method could be applied to compare the performance of different FDDs. The false alarm rate was not involved in the index calculation, as they were fixed to the same number by adjusting the thresholds.

2.4 Summary of observations

Based on the literature review, some observations on the development of FDD techniques for RAC systems can be made:

- Large numbers of faults have been reported but only a few selected ones have been researched extensively for FDD development and most studies have been focussing on faults that would lead to performance degradations, examples include: refrigerant leakage or over-charge, cooling water or HTF flow restriction and heat exchanger fouling.
- For model based approaches, there are two main types of FDD models, namely analytical (white box) model and data-driven (black box) model, each with their relative advantages and weaknesses. A popular approach is in fact to combine the two, forming a hybrid (grey box) model which aims at eliminating some of the limitations of the previous two model types. There are two ways to form a hybrid model: serial approach and parallel approach. They can be combined in some cases.
- Within each model types, different techniques of FDD can be employed depending on a large number of factors, such as the accuracy or the data required.
- Many analytical models have been developed, for mainly analysing system behaviour under varying operation conditions, and they are able to predict both steady and transient behaviour. However they are not specifically developed for FDD purposes and they may not be applicable or adaptable for FDD purposes.
- Most models require experimental data for calibration (white box models), training (black and grey box models) and/or validation (all models).
- Large numbers of measured parameters are usually involved in FDD development and application; some can be used directly in diagnosis rules (e.g.

condenser/evaporator HTF inlet/outlet temperatures, condensing and evaporating temperatures/pressures, HTF flowrates in condenser/evaporator, compressor power consumption) but others are used indirectly for deriving performance index or CF, such as *COP*, *UA* and *LMTD* for fault classification.

- When a RAC system incorporates a control system, it is usually more difficult for the FDD to diagnose the faults as the controls may try to correct or compensate the faults by adjusting certain parameters.
- Most existing FDD techniques can only detect faults under steady state conditions and therefore a steady state detector (an algorithm) is needed. Some methods have been observed to be able to detect and diagnose faults under transient conditions.
- The selection of inputs and outputs to the model is depending on the FDD method. An input can even become an output for the same model when using different FDD methods.
- Some faults exert more influence on certain parameters than others; the sensitivities of individual parameters vary with the types of fault as well as the system types.
- If more than one fault occurs in a system, they may interact with each other resulting in more difficult diagnosis. The detection of double fault is similar to that of a single fault, but the diagnosis method usually differs. Residual ratio method is one of the approaches that can diagnose double fault. No work related to triple or more co-occurrence fault had been observed.

2.5 Research objectives and originality

From the above, it can be seen that existing FDDs may not be suitable for binary ice systems and it appears that a new FDD approach needs to be developed, especially looking at some faults that are unique to binary ice systems. Therefore, the objectives of this research are as follow:

1. To fully understand the operation (both steady and dynamic) and control characteristics of a binary ice system as well as the scraped surface ice generator, under both faulty and fault-free conditions.

2. To build a dynamic hybrid model to predict the behaviour of binary ice system by coupling an analytical model of the ice generator and a system level ANN model.
3. To develop a FDD approach that can be employed to detect several pre-defined faults in a binary ice system. The approach should be capable of detecting the faults without a steady state detector, i.e. under transient conditions, and of identifying some pre-defined double faults.

Attention is paid to establish how the types/numbers of the faults and the systems types influence the choice and the number of the parameters to be measured or derived. Parameters that have been identified include condenser cooling water inlet and outlet temperatures and flowrate, pressures and temperatures of the primary refrigerant at inlet and outlet of individual main components, temperatures of binary ice at the inlet and outlet of the SSIG (for deducing the solution and ice concentrations), power consumption of the compressor and binary ice flow velocity. The final selections of parameters applied in the FDD technique will be decided based on the analysis of the experimental data.

2.5.1 Selection of faults

The main research aim is to develop a simple, effective and accurate FDD method to detect and diagnose several pre-defined faults in an on-off controlled binary ice system. The faults cover both conventional chiller faults and specific faults for binary ice systems. It is worth noting that although refrigerant over-/under- charge is recognised as one of the most common faults in refrigeration systems, it has already been extensively studied by various researchers (Grace et al. 2005; Assawamartbunlue and Brandemuehl 2006; Navarro-Esbr íet al. 2006). Therefore it is not included in this project. As far as the author is aware, no FDD specifically developed for binary ice systems has been constructed. Detailed experimental data is collected from a dedicated test facility and this will enable a full understanding of the operating characteristics of a binary system be obtained, under both fault-free and faulty conditions.

This project will be based on a laboratory binary ice system (further details given in Chapter 3) using an ethanol-water solution as the heat transfer fluid. The primary circuit consists of a vapour compression refrigeration system with a 3kW

(power rating) semi-hermetic reciprocating compressor, a water-cooled shell-and-tube condenser, an evaporator (providing around 2.5kW of cooling capacity at T_e of around -30 ℃) and a thermostatic expansion valve (TXV). The secondary circuit consists of a scraped surface ice generator, a circulating pump and a storage tank equipped with immersion heaters, in steps of 2, 3 and 4kW, etc. to simulate the load. The capacity regulation is effected by using an on-off thermostat control for the compressor with a temperature sensor monitoring the outlet temperature of the binary ice from the ice generator.

The faults chosen in this study include both some common chiller faults as well as faults that are unique to binary ice systems, as listed below.

- Condensing water flow reduction
- Binary ice flow reduction
- Incorrect solution concentration (increase and decrease)
- Ice generator broken blade
- Ice generator blade motor failure

2.5.2 Methodologies

A pre-used binary ice test rig was re-commissioned to incorporate all the necessary instrumentation and to provide all the necessary data. A measurement matrix was implemented in order to acquire a full set of operation data at various loads and temperature set-points for the binary ice flow temperature and condenser inlet water temperatures. The pre-selected faults were introduced artificially to the system. The sensitivities of various parameters with respect to any adjustments or changes were thoroughly assessed.

For model based FDD techniques, the measured data from the test rig were compared with fault free model predictions. Then the residuals between the two were used as input to the detection and diagnosis rules to check whether a fault exists and identify the fault. As a result, there were two main tasks in FDD construction: 1) to develop a model providing fault free data and 2) to identify the rules for diagnosis.

To help analyse the behaviour of the ice generator, a mathematical model based on heat and mass balances was constructed. It was used to establish the

relationships between ice production rate, the flow temperature, the initial solution concentration and temperature, evaporating temperature, etc. Some of the data obtained from the experiment was used to validate the model.

Different to the above analytical model for the ice generator, the model used for the primary circuit of the system was an ANN model. Its structure (the number of the hidden layers and the type of the activation function for ANN) were determined first. Next, the input/output parameters were selected based on the nature of the system and chosen faults. The input parameters were controllable by the user, such as the flowrates and inlet temperatures of the condenser water and binary ice, and initial solution concentration of binary ice, while the outputs were chosen from the parameters that were determined by the inputs, i.e. binary ice outlet temperature and ice concentration, evaporating and condensing temperature, power consumptions of compressor and system COP. Fault free data obtained from the test rig were divided into two groups: part of the data was applied for model training, with the help of *Matlab* to calculate the modelling coefficients, and others was used for model validation.

The analytical model and the ANN model were then coupled together to form a hybrid model to provide fault free benchmark for the FDD application, It was necessary to use the hybrid model instead of a pure analytical or a pure ANN model because the development of an accurate analytical model for the entire binary ice system would be very difficult and a pure ANN model was not able to predict some parameters such as the ice concentration and cooling load. The model coupling was carried out by sending some of the ANN outputs, such as T_e, to the analytical model as inputs. The two models also share some measured parameters as inputs, making the overall model both serial and parallel in nature - a unique feature of the proposed model.

The main task for developing fault diagnosis method was to establish the suitable thresholds of the residuals for the selected output parameters that can indicate the existence of a fault. The thresholds should be neither too small (to reduce false alarm) nor too large (to detect a fault at an early stage).

Fault diagnosis was carried out by analysing the combinations of the parameter variations (increase or decrease) during faulty conditions. Diagnosis rules were formed by a set of unique patterns of parameter variations that could represent each of the pre-selected fault. Ideally the rules should include as few parameters as possible. To set up the rules, different faults were introduced to the test rig and the faulty data were compared with fault free data. A full list of the residuals of all the output parameters was built up. By carefully selecting the parameters, a unique pattern for each fault was found.

The performances of the FDD approach was evaluated at different fault severity levels. The relationships between threshold and detection and diagnosis accuracy were examined.

3. Experimental setup

3.1 Introduction

A scraped surface binary ice system, originally built by the company called SRC as a pilot test rig to investigate the feasibility of binary ice application in supermarket refrigeration, was given to the RAC Research Group for this research project. It was re-commissioned and reconfigured to provide the necessary test data for the development of the FDD model.

In addition to allowing the author to appreciate and understand more thoroughly the operating behaviour of a scraped surface binary ice system, the test rig was to serve two main purposes: (1) to obtain fault-free data for training, calibrating and validating both the analytical SSIG model and the grey-box system model and (2) to obtain data for various experimentally simulated pre-specified faults for the development of FDD algorithm as presented in Chapter 6.

The test rig, as shown in Figure 3.1, consisted of two circuits, the primary refrigerant circuit and the secondary binary ice circuit, which were coupled to each other by the binary ice generator. A detailed description of the two circuits and the associated components of the test rig are given in the next section.

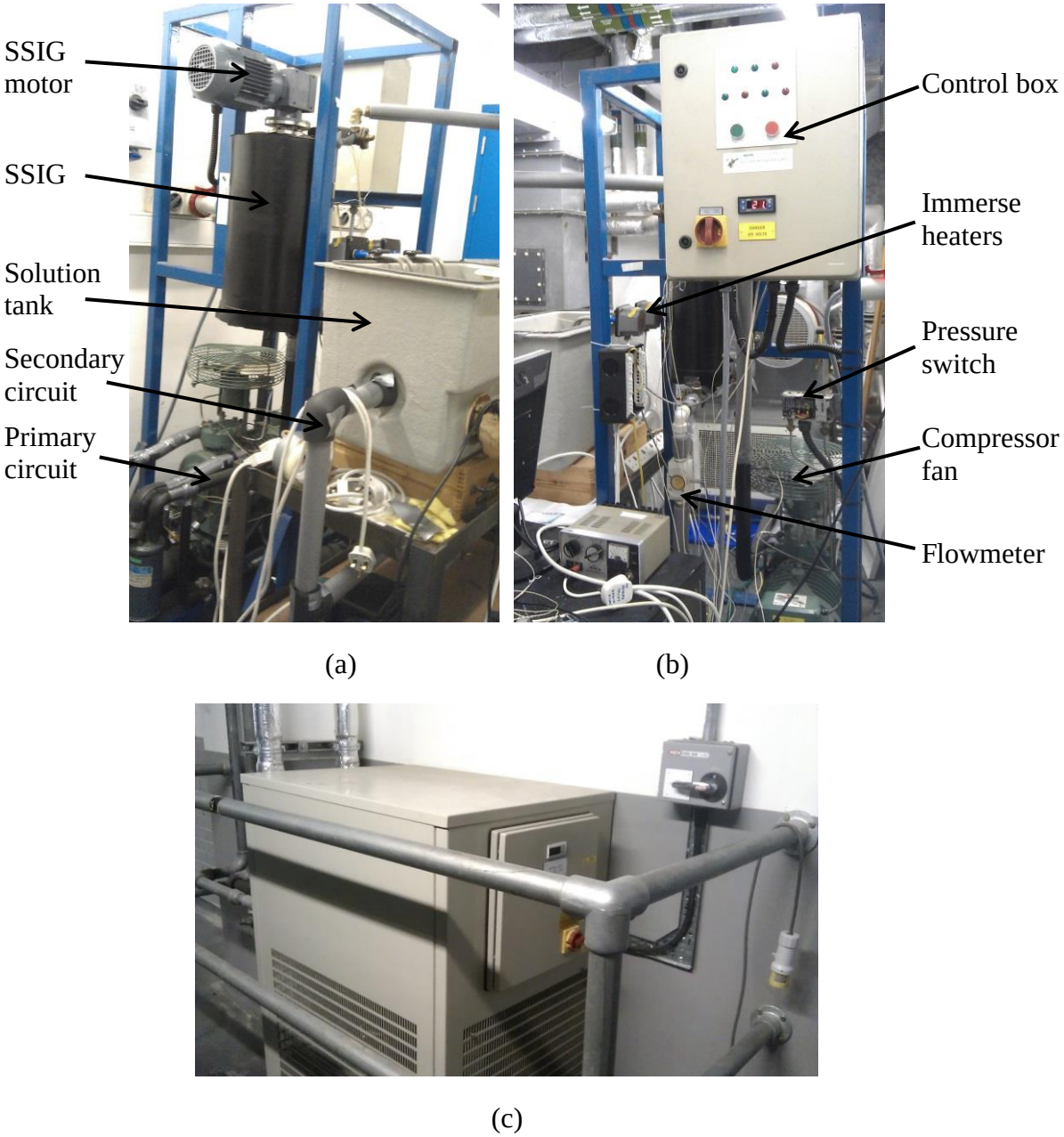

Figure 3.1 Test rig, (a) and (b): primary and secondary circuit, (c): chiller unit for the condenser cooling water.

3.2 Experimental Setup

3.2.1 Primary circuit

The primary circuit is shown schematically in Figure 3.2. The specifications for some of the main components and descriptions of various safety and operational controls are given below.

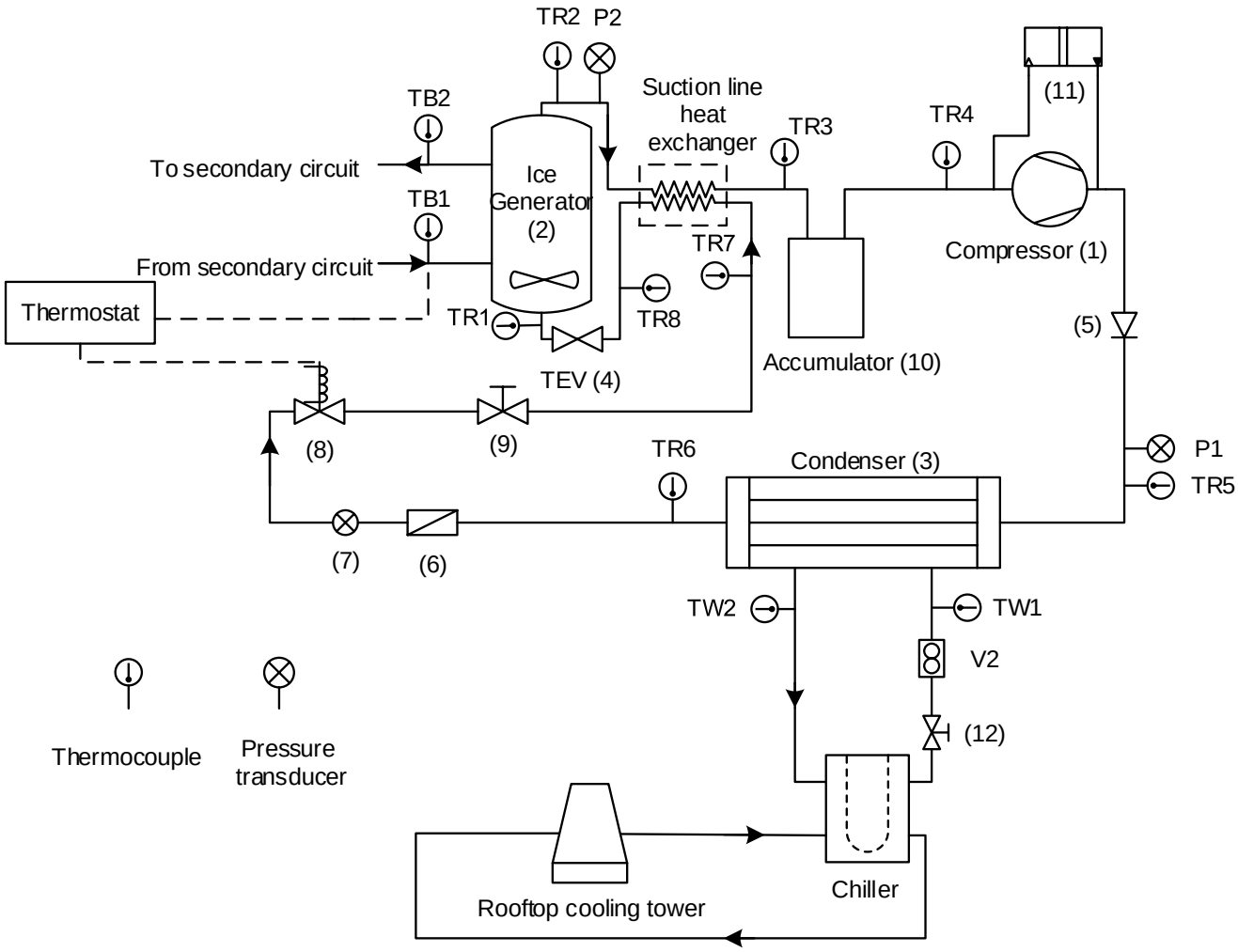

Figure 3.2 Schematic diagram of the primary circuit

Compressor (1)

The compressor (Bitzer 2DL-2.2) was a 3-phase, fan-cooled, semi-hermetic reciprocating compressor (displacement rate: 13.3m^3/h, nominal speed of 1450 rpm at 50Hz) with an estimated cooling duty of 3 kW at evaporating temperature of -20 ℃, condensing temperature of 30 ℃ and a discharge temperature of around 45 ℃ when run with R507. The cooling fan was mounted above the cylinder head.

The compressor was protected by a built-in current overload protector, as well as a HP/LP pressure switch (11, Danfoss KP 17) which was connected to the discharge and the suction lines of the compressor; when a certain pre-set current or pressure values were exceeded, the compressor motor would shut down. The

compressor was also equipped with a crankcase heater. The crankcase heater was automatically switched on when the system was stopped to prevent the refrigerant from dissolving into the oil (or foaming).

Ice generator/evaporator (2)

A FLO-ICE Generator DWT 3/4TR from Integral Technology was installed for ice production. Details of the dimensions were given in Chapter 4. Ice particles were scraped off by a two-blade scraper rotating at a speed of 168 rpm. The scrapers were driven by a 3 phase motor (SEW EURODRIVE WAF20) mounted at the top of the ice generator driving the scraper via a reduction gearbox. Based on an initial solution concentration of 15%, a binary ice outlet temperature of -7 ℃ with a temperature drop of 2 ℃ across the ice generator (assuming ice particles present at both inlet and outlet of the ice generator) and a binary ice flowrate of 0.1 kg/s, the rated capacity is about 2.5 kW.

Condenser (3)

The condenser was a Bizter (K122H) shell-and-tube water-cooled condenser with a nominal duty of 5.8 kW (based on 0.14 l/s water, 3-pass, with 10K temperature increase). The refrigerant vapour entered the shell side of the condenser which received cooling water from a process water chiller (FLOWCOOL SCW 10/S, Figure 3.1c), which in turn rejected its heat via a rooftop cooling tower. A temperature controller (CAREL μC^2) was employed to provide control of the flow temperature set point and the on/off differential for the process chiller (Appendix C).

Expansion valve (4)

A Danfoss TES 2 expansion valve with a rated capacity of 4.9 kW at an evaporating temperature of -20 ℃ was used; the valve was also equipped with an external equalizer. The expansion valve modulated the refrigerant flow rate, hence the capacity, by approximately maintaining a specified degree of superheat at the evaporator outlet. The sensing bulb was attached to the refrigerant outlet of the ice generator and the superheat was normally set to around 3 ℃.

Pipe line and liquid/vapour heat exchanger

1/4'' (for liquid line), 5/8'' and 7/8'' (for vapour line) copper tubes were used in the primary circuit. The suction line and the liquid line were installed side by side and a thermal conductive paste was applied to enhance thermal contact between them, thus to facilitating the heat transfer from the relatively warm liquid exiting the condenser to the relatively cold vapour exiting the evaporator. Wherever appropriate, insulations were applied to minimise heat gains/ losses from/to the ambient.

Refrigerant

The system was originally designed for using R22. Due to supply issues of HCFC, it was decided to replace R22 with R507 which was a popular retrofit refrigerant for R22. R507 (also known as R507A) was an azeotropic mixture of HFC-125 and HFC-143a (50% wt./50% wt.) which was suitable for medium to low temperature applications. A Bizter software was used to verify there were only little changes in capacity and refrigerant mass flow rate when switching from R22 to R507 for the compressor. Accordingly, the old oil was flushed out and replaced, so was the filter drier too. The thermodynamic properties of R507 can be dound in Appendix D

Other auxiliary components of primary circuit are listed in Table 3.1.

Table 3.1 Auxiliary components for the primary circuit

Component	Type	Description
Oil	Emkarate RL 32H	~ 2.3 L
Non-return valve (5)	Danfoss NRV	Preventing back flow
Filter dryer (6)	Danfoss DML 052	Removing dirt and moisture from refrigerant
Sight glass/Moisture indicator (7)	Danfoss SGI 6	Indicating moisture level in system Giving a visual indication of the flow circulation. Assisting detection of flash gas and refrigerant charging
Solenoid valve (8)	Danfoss BML	Stopping refrigerant flow according to control signal
Suction line accumulator (10)	AC&R Components S-7061	Preventing liquid refrigerant going into the compressor

Control of the primary circuit

The primary circuit was controlled by a control box designed with over load protections for both the compressor and the ice generator motor. When the system was switched on, the scraper of the ice generator would start first, in order to avoid blade damage. The compressor, along with its cooling fan, would start about a minute after the scraper.

The binary ice temperature at the outlet of the SSIG was monitored and controlled by a PTCS 1.5M -50/140 Silicon thermocouple and a thermostat (Elliwell, Appendix E), in association with a liquid line solenoid valve (8), which was used to implement an on/off control of the compressor for regulating the system capacity. When the temperature dropped below a pre-set value (with a band width of 2K), the thermostat would trigger a cut out of the refrigerant flow by closing the solenoid valve. As a result, the evaporating pressure would drop and the compressor would be cut off by the LP switch. As the temperature of binary ice rose above the upper band limit, the thermostat would signal the opening of the solenoid valve so that the refrigerant was allowed to enter the evaporator causing its pressure to rise, signalling the compressor to start again when the evaporating pressure reached approximately 3 bar. One shortcoming of this type of capacity control was that the number of starts/stop per hour for the compressor was limited; this could also result in a large flow temperature variation of the secondary flow, especially when the cooling capacity was small. Thus a too small band width setting was not recommended.

3.2.2 Secondary circuit

The secondary circuit, Figure 3.3, was for thermally simulating the consumption of binary ice by providing an artificial heat load using various immersion heaters (15) installed in a solution tank (14). It had a centrifugal pump to circulate the binary ice through the tank and a hand valve (16) to adjust the flowrate of binary ice.

Pump (13)

A Wilo TOP-S 30/7 centrifugal pump, capable of operating at temperatures as low as -20 ℃, was used. A bypass connection with a ball valve (17) was incorporated

to ensure steady operation of the pump under small flowrates. A drain tap was installed at the pump discharge line for maintenance purpose.

Solution tank (14) and heaters (15)

A 68 litre fibreglass insulated tank from Drayton Tank was equipped with five immersion heaters (15) (two 1 kW, two 2 kW and one 3 kW) to provide the thermal loads to the refrigeration circuit. The heaters could be turned on and off separately to provide step variations of the load. One of the 2kW heaters was controlled separately by a PID temperature controller to provide fine tuning of the temperature. A shutdown valve (18) was installed to isolate the tank from the pump if necessary. The tank was also equipped with a mechanical stirrer driven by a low speed electrical drill to promote even temperature distribution within the bulk of the solution.

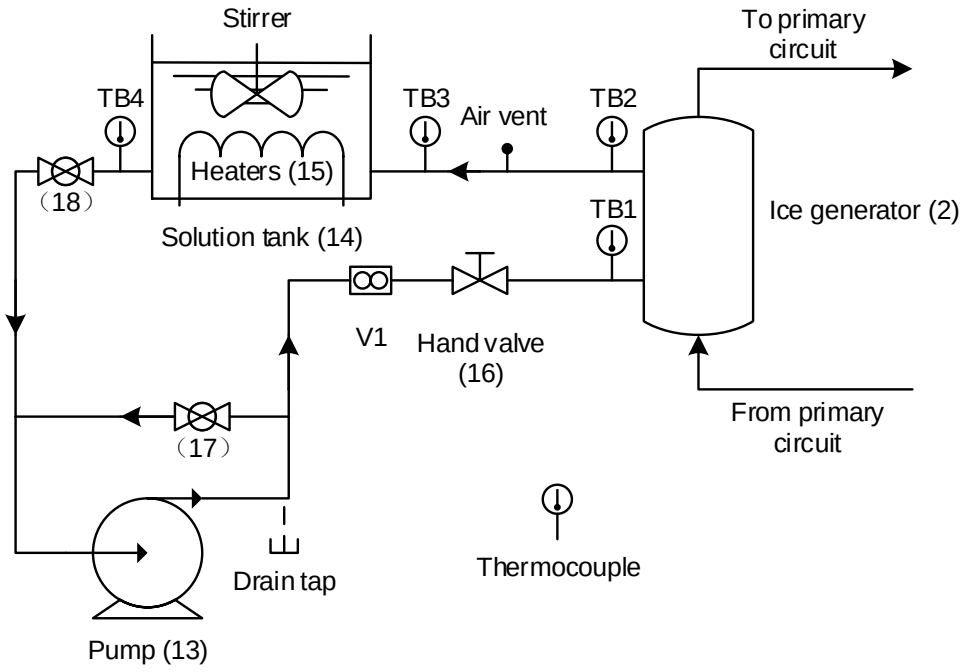

Figure 3.3 Schematic diagram of the secondary circuit

Secondary solution

The fluid used to generate binary ice was aqueous ethanol solution. The initial design ethanol concentration was 15% by weight.

Pipeline

20mm PVC pipes were installed throughout the secondary circuit, all of which were insulated.

3.3 Instrumentation

3.3.1 Sensors

The test rig was equipped with various sensors to monitor the system behaviours and a data logging system to record the data. The measured parameters included temperature, flowrate, pressure and power consumption.

- **Thermocouple**

Temperatures of refrigerant, secondary fluid and the cooling water at different locations of the circuits were all measured by type T thermocouples (copper-constantan, welded tip, glass fibre insulated). The sensitivity and uncertainty/accuracy of type T thermocouples are approximately $43\,\mu V/^{\circ}C$ and $\pm 0.5\,^{\circ}C$ respectively. For the refrigerant temperature measurements, the thermocouple were attached on the outer surface of the copper refrigerant tube and insulated from the surrounding environment. Thermocouples used to measure the secondary fluid and cooling water temperatures were dipped into the liquid directly (with the exceptions of the thermocouples at the entrance and exit of the ice generator TB1 and TB2, which were attached on the outer surface of the tube). All the thermocouples were calibrated and when tested for the same temperatures none of them deviated more than 0.5 ℃ from the others. Any two thermocouples that exhibit the closest readings with each other were paired together to measure temperatures at the inlet and outlet of the same component.

- **Pressure transducers**

Two Cole-Parmer Ashcroft G2 Pressure Transducers with a range of 0-500 psig (0 to 34.5 bar) and a corresponding analogue output of 4 to 20 mA were installed. The high-pressure side transducer P1 was installed at the refrigerant inlet of the condenser while the low-pressure side transducer P2 was installed at the evaporator outlet, monitoring respectively the evaporating and condensing pressures. The pressure transducers provided an accuracy of ±1% full scale which was considered adequate for this type of work.

❖ **Power meter**

The compressor power consumption measurement was carried out with a Multitek M100-WA2 power transducer which took the line current of one phase and the line voltage for all three phases. It was configured to measure three-phase three-wire balanced load power up to 5 kW and the maximum working current it can take was 7 A. The output is 0 - 20 mA current, corresponding to 0 - 5 kW. The wiring diagram is presented in Appendix F.

❖ **Flowmeter**

Two flowmeters were used in the tests. An Omega FPR302 Low-Flow Meter with a measuring range between 0.38 - 37.9 litre/min was employed to determine the flowrate of the binary ice in the secondary circuit (V1 in Figure 3.3). This turbine type flowmeter measured the volume of the flow passing through it by a turbine wheel which turned with a fix number of rotations for a given volume of fluid flow. The meter generated a current pulse for each rotation. A ratemeter (Omega DPF75-A) was used to read the pulse rate (number of pulses/min) and convert it into flowrate using a *K*-factor (expressed as the number of pulses per litre) given by the manufacturer. This flowmeter's accuracy was ± 1% of full scale. A detailed operation procedure of the flowmeter and the ratemeter can be found in Appendix G.

Essentially, the flowrate (litre/min) could be calculated as below,

$$\text{Flowrate} = \frac{Pulse\ rate}{K} \qquad 3.1$$

where *K* was a unique factor for each flowmeter. For the one employed in the tests, *K* was 164.8 pulse/litre as stated by the manufacturer.

A calibration of the Omega FPR302 flowmeter was carried out to verify the accuracy of the *K* value for the range of flow rates likely to be encountered in the tests. This was done by first comparing the actual flow rates, determined by measuring known volumes water through the flowmeter over specified periods of time, with the nominal flowrates based on the pulse rates and the manufacturer's stated *K*-factor. It can be seen in Figure 3.4 that although all the measurements fell within the ± 1% FS range, some of the data at low flow rates were outside the ± 20% error band, resulting in larger relative errors at low flowrates if the same *K*-factor was applied for the entire range.

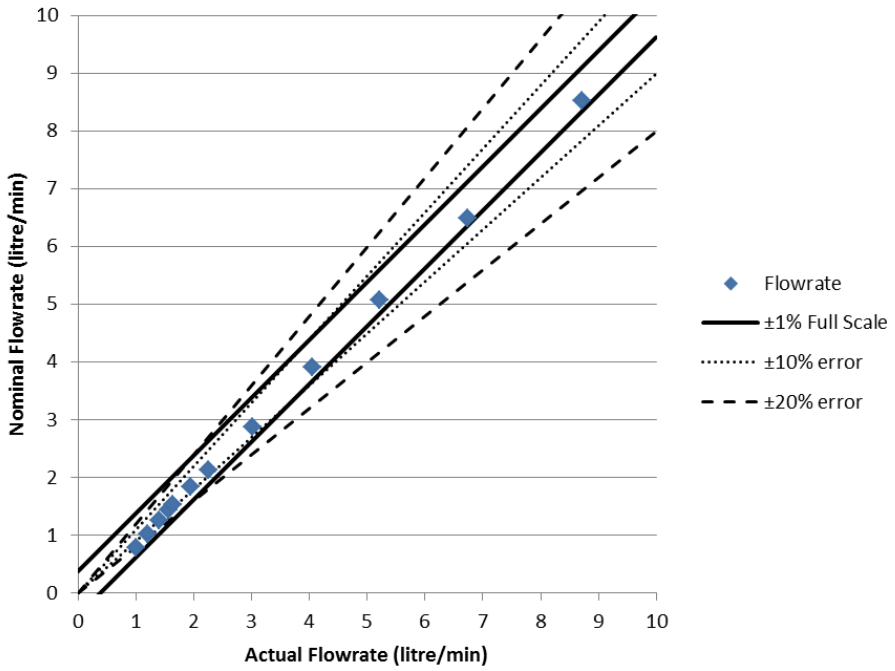

Figure 3.4 Omega FPR302 flowmeter calibration

Therefore, to increase the measurement accuracy, the *K*-factor was calibrated for different ranges as shown below.

$$K_{\text{actual}} = \frac{Flowrate_{\text{nonimal}} \times K_{\text{nominal}}}{Flowrate_{\text{actual}}} \qquad 3.2$$

Variation of actual *K*-factors with the flow rates are shown in Figure 3.5. When the flow rate was less than 4 litre/min, there were significant deviations between the actual *K*-factor and the manufacturer's value. A correction was implemented through the data logging software using the following equation obtained by data fitting.

$$K_{\text{calibrated}} = \frac{164.8u}{0.1836+u} \qquad 3.3$$

where u is the nominal volume flowrate (litre/min) from the meter. The $K_{calibrated}$ was then used in Equation 3.1 to determine the actual flowrate.

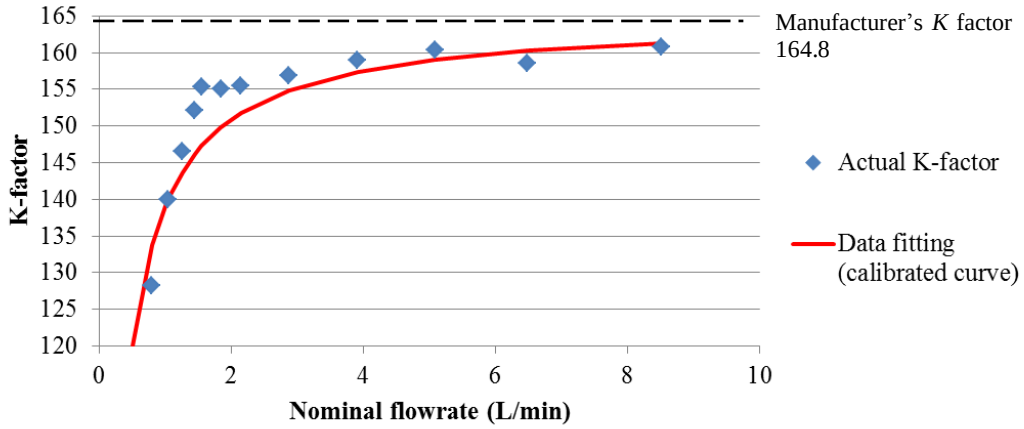

Figure 3.5 Variations of actual *K*-factor with flow rate

Table 3.2 presents the results of the flowmeter calibration. Each data point represents an average value of several repeated measurements. It can be seen that the calibrated readings provided significantly improved accuracies at the low flow rate within the 3L/min range.

Table 3.2 Flowmeter calibration results

Actual flowrate (L/min)	Flowmetre reading without calibration, i.e. using the manufacturer's *K* value (L/min)	Discrepancy (%)	Flowmetre reading with calibration, i.e. based on calibrated *K* values (L/min)	Discrepancy (%)
1.11	0.95	14.64	1.13	1.93
1.16	1.02	11.87	1.20	4.00
1.17	1.03	11.52	1.22	4.22
1.84	1.72	6.05	1.91	3.95
1.91	1.76	7.24	1.96	2.35
2.76	2.63	4.68	2.81	1.98
3.09	2.94	4.85	3.12	1.09

The cooling water flowrate was measured by an Omega FV102 Vortex Shedding Flowmeter (V2). It could handle flowrate between 4.5 and 45.4 litre/min with an accuracy of ± 5% full scale and provided a 4 mA (corresponding to zero litre/min) to 20 mA (at 45.4 litre/min) output signal to the data acquisition system. This flowmeter was checked against the previously calibrated flowmeter Omega

FPR302. A good accuracy of about ±6% was noted within the designed cooling water flowrate range, which was considered adequate for this study.

❖ **Solution concentration**

The concentration of the ethanol solution may change overtime due to evaporation, condensation, etc. and therefore it was required to check regularly to ensure it is within the specified concentration tolerance of ± 0.5% of the initial concentration. This was done by using a set of hydrometers which can measure specific gravity between 0.65 and 1.10, and with a resolution of 0.0005. Figure 3.6 shows the density (or specific gravity) of the solution and its temperature for a range of concentrations (Melinder 1997); tables and equations are also available to provide the solution density as a function of temperature and concentration.

Specific gravity was measured on a regular basis according to the following procedures. A 3kW heater and the solution pump were turn on (to ensure through mixing), but the refrigeration unit remained switched off. The heater was then turned off when the solution temperature reached around 22 ℃. The solution was allowed to cool down gradually, with the pump still running, and a measurement of the specific gravity of the solution in the storage tank was taken manually when the temperature dropped to 20 ℃, and the measurement was checked against the published data. The solution level in the tank was also noted each time. If necessary, water or ethanol would be added.

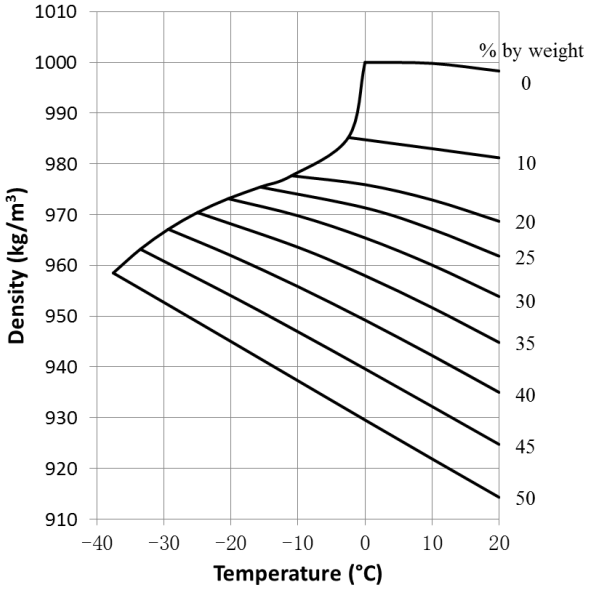

Figure 3.6 Relationships between the ethanol density and its concentration and temperature (Melinder 1997)

In summary, Table 3.3 presents all the sensor types, their locations in the test rig as well as their measurement uncertainties.

Table 3.3 Sensor measurement points and measurement uncertainties

Temperature	**Uncertainty**	**Pressure**	**Uncertainty**
TR1: Ice generator refrigerant inlet	± 0.5 ˚C	P1: Compressor discharge pressure	±1% full scale
TR2: Ice generator refrigerant outlet	± 0.5 ˚C	P2: Ice generator refrigerant outlet	±1% full scale
TR3: Accumulator inlet	± 0.5 ˚C		
TR4: Compressor inlet	± 0.5 ˚C	**Flowrate**	
TR5: Compressor discharge	± 0.5 ˚C	V1: Binary ice	± 5%
TR6: Condenser refrigerant outlet	± 0.5 ˚C	V2: Condenser cooling water	± 6%
TR7: Condenser outlet before suction line heat exchanger	± 0.5 ˚C		
TR8: TEV inlet	± 0.5 ˚C	**Power meter**	
TW1: Condenser water inlet	± 0.5 ˚C	W: Compressor	± 10%
TW2: Condenser water outlet	± 0.5 ˚C		
TB1: Ice generator binary ice inlet	± 0.5 ˚C		
TB2: Ice generator binary ice outlet	± 0.5 ˚C		
TB3: Tank inlet	± 0.5 ˚C		
TB4: Tank outlet	± 0.5 ˚C		

3.3.2 Data acquisition

The outputs of all the sensors were fed into a PC via a data logger (Datascan Module 7320 and 7020) and a PS232 link (Figure 3.7). Module 7320 was a measurement processor and 7020 was its expansion module. Each module had 16 input channels and 3 poles for each channel. The data logger accepted DC voltage, thermocouples or current as inputs. Each individual channel, with a maximum allowable sampling rate of 1*Hz*, was connected with a sensor and was configured according to the type of the signal from the sensor using a data acquisition software package *Dalite*, storing the data in the txt format on the computer.

Figure 3.7 The data logging system

Two types of output signal were involved in the test, namely thermocouple and 4-20mA current. The connection methods for both types are shown below.

- Thermocouple

The data logger was capable of taking the voltages generated by the thermocouples and converted them into temperatures according to the type of the thermocouple. Thermocouples were connected to the data logger using 2 core compensating cables, as shown in Figure 3.8.

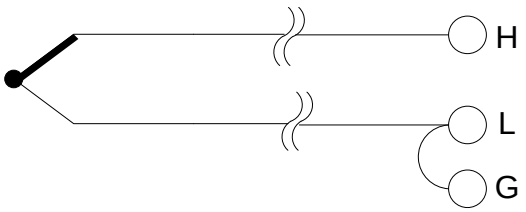

Figure 3.8 Thermocouple wiring diagram using 2 core compensating cable

- 4-20 mA current output

Sensor with 4-20mA current output could provide a fixed current representing its reading at a specific moment when a closed circuit was formed by connecting a resistor across its output terminals. A voltage was generated across the resister, which was picked up by the data logger and converted into current according to the resistor value. The pressure transducers, flowmeters and the power meter all belonged to this

type. 62 **Ω** resisters were used in all the connections as specified by the data logger. Figure 3.9 shows the wiring diagram.

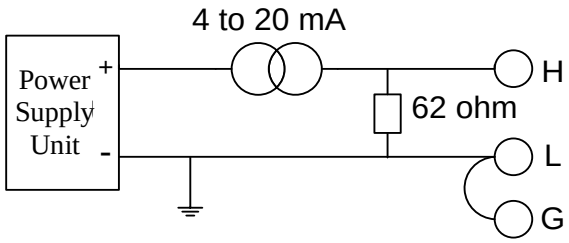

Figure 3.9 sensors with 4-20mA outputs wiring diagram

3.4 Experimental procedures and results

In this section, the operation procedure of the test rig was described. Some test results were also presented here, in order to confirm that the system was functioning as expected and to illustrate the operation characteristic of the binary ice system. Both standard pressure and vacuum testing had been carried out before the refrigerant was charged into the primary circuit to ensure that no leakage existed. The system was first charged with nitrogen to a pressure of 30 bars and kept for 48 hours. The pressure held well, the variations were purely due to the daily changes in the ambient temperature. Then the primary circuit was evacuated down to 250 micron to remove the moistures and kept for overnight. After the test rig had passed both tests, about 2.7 kg of R507 was charged into the system through the suction line service valve until there was no visible bubble in the liquid line sight glass when the system was running.

Figure 3.10 to Figure 3.13 illustrate a set of data recorded during a 3-hour test during which the binary ice flow rate was adjusted. A 10-second sampling interval and a 15% wt ethanol solution were used in this test. The components were started from off cycle according to the following sequence:

1) Time step 10 (i.e. 100 seconds from start), binary ice tank stirrer starts
2) Time step 17, the secondary circuit pump starts
3) Time step 28, process chiller and cooling water pump start
4) Time step 40, ice generator scraper motor starts
5) Time step 46, compressor and fan switched on

6) Followed by the heater (2kW) being switched on when the solution's temperature got closer to the freezing point.

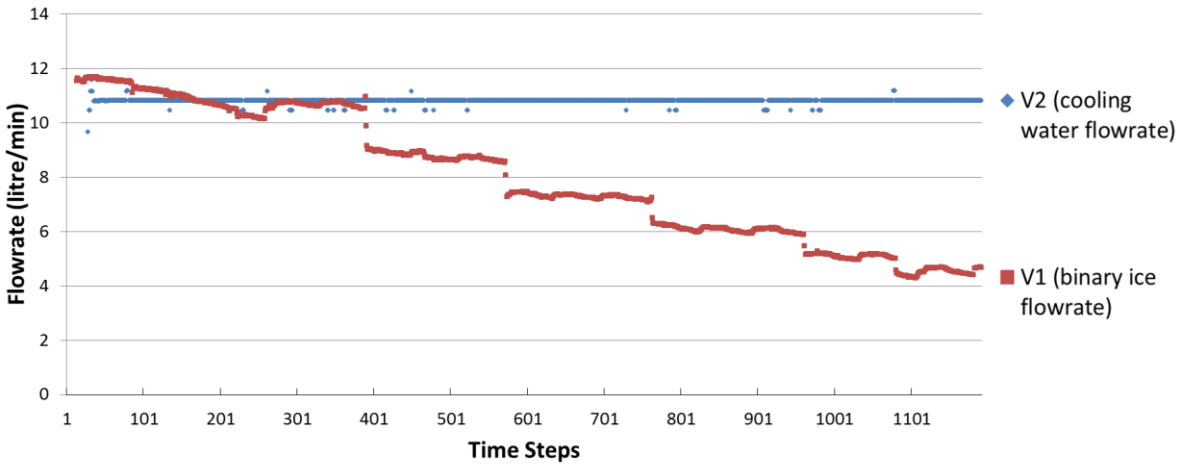

Figure 3.10 Binary ice and cooling water flow variations

Figure 3.10 shows both the flowrate of the binary ice (V1) and of the cooling water (V2). Initially, binary ice flowrate was set at 11.6 litre/min, then it was manually adjusted to 9.0, 7.5, 6.3 and 5.2 litre/min at time step 393, 574, 764 and 962 respectively. Each time when the flow rate was adjusted, it took about 10 minutes (~ 1 cycle) to acquire a stable cycle pattern. The system was allowed to run for two further cycles (~20 minutes) before the flowrate was changed again. In total, data for 15 cycles were captured. The cooling water flowrate was kept constant at 10.8 litre/min during the whole 3-hour test, though some occasional minor fluctuations were noted.

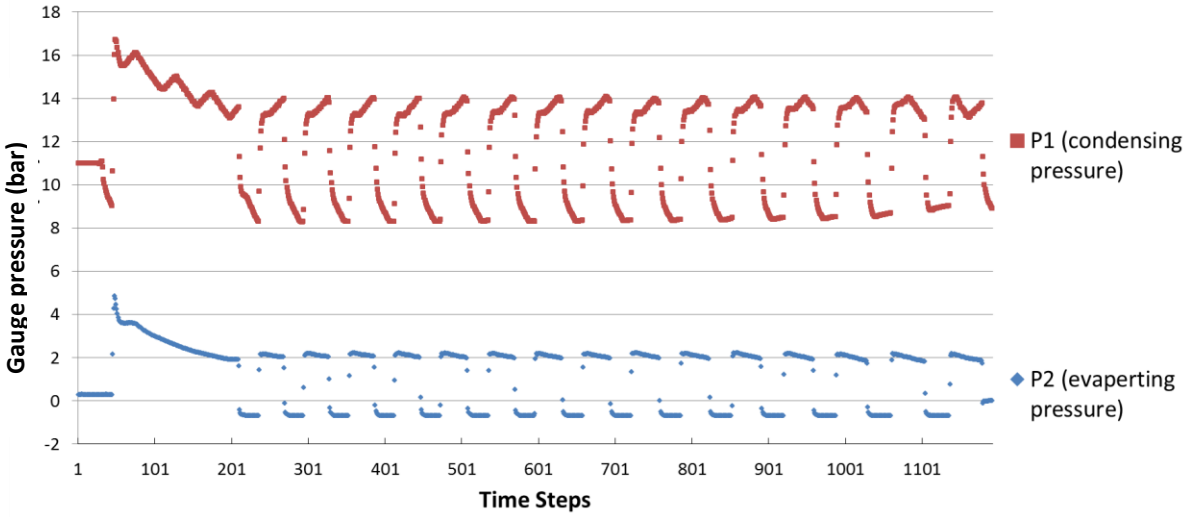

Figure 3.11 Condensing and evaporating pressures

Figure 3.11 shows the variations of the condensing (P1) and evaporating (P2) pressures when the binary ice flow rate was reduced. The initial decrease of the condensing pressure at around 28th time step was caused by the starting of the process chiller. When the compressor started at around 46th time step, both pressures increased rapidly. At the 210th time step, the compressor was turned off as the binary ice temperature reached its set point; then both pressures dropped. The cyclic variations of the pressures followed the compressor on/off cycle. The decreased binary ice flowrate resulted in a slightly lower evaporating pressure during the on cycle while the pressure remained the same during the off cycle. The average condensing pressure during on-cycle did not vary much; this was attributed to the fact that the heaters input was kept constant during the tests, so were the temperature and the flow rate of the cooling water. The noted changes in the profile shape with both the on and off period were believed to be caused by the cyclic variation in the cooling water temperature (also see Figure 3.12).

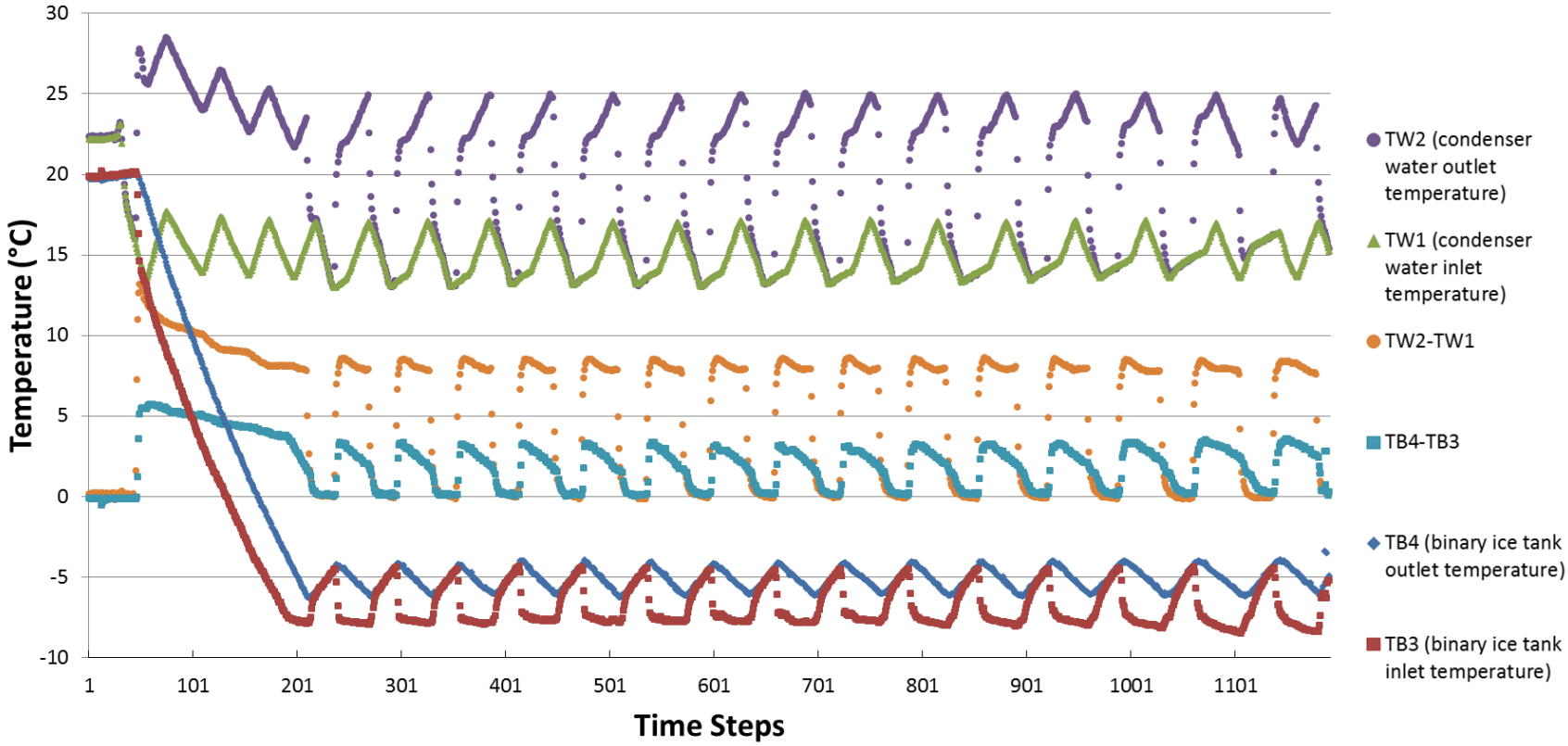

Figure 3.12 Temperatures of cooling water and binary ice

The tank inlet (TB3) and outlet (TB4) temperatures of the binary ice, and the condenser cooling water inlet (TW1) and outlet (TW2) temperatures are shown in Figure 3.12 which also plots the corresponding differences between the in- and outlet temperatures, i.e. (TB4-TB3) and (TW2-TW1) respectively. Initially, both the binary ice temperatures and their difference decreased steadily until the outlet temperature (TB4) reached its set point and the compressor was cut off at around 210^{th} time step. After that, cooling water temperature differences (TW2-TW1) decreased almost linearly with time within individual compressor on-cycles, and naturally had very small values when the compressor was off.

A decrease in binary ice flowrate appeared to increase the binary ice temperature difference (TB4-TB3) slightly and resulted in small temperature differences even during compressor off cycle which were not present previously. The change of binary ice flowrate had negligible influences on the (TW2-TW1) values throughout the 15 cycles. It was worth noting that the last three cycles of TW1 and TW2 showed different profiles compared with others. This is because the on-off timings of the compressor and the process chiller varied with respect to each other. The unique change of profile must not be interpreted as a fault.

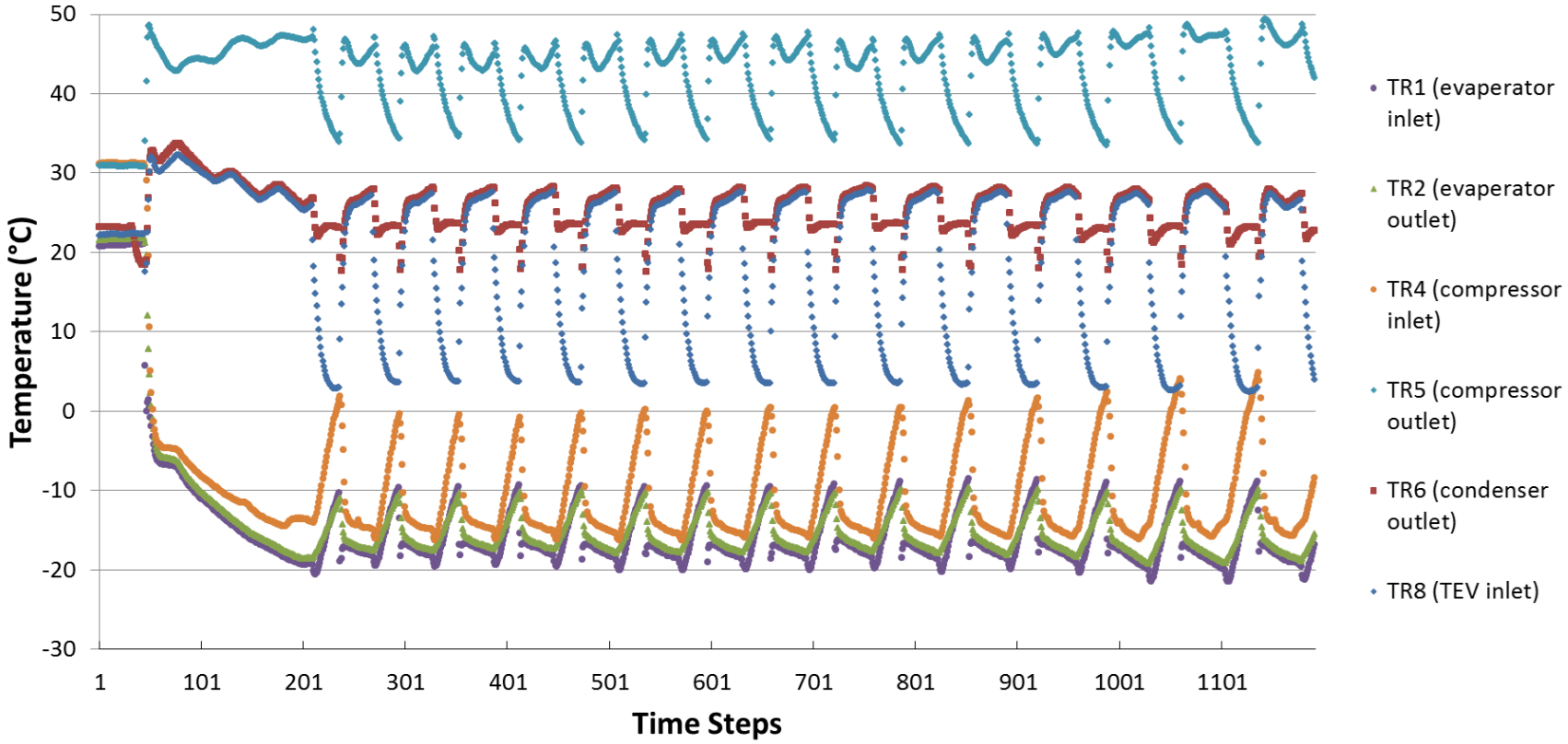

Figure 3.13 Refrigerant temperatures at different locations of the primary circuit

Figure 3.13 displays the variations of refrigerant temperature at various locations of the primary circuit. As expected, the outlet temperature (TR2, superheated vapour) of the evaporator was slightly higher than the inlet saturation temperature (TR1), representing typically 2 to 3 ℃ superheat. Both temperatures increased rapidly during the compressor off-cycle periods, but there was an initial small decrease in TR1 following the shutdown of the solenoid valve, causing the saturation pressure in the evaporator to drop before the compressor stopped completely. When the compressor was back on again, both temperatures decreased, though once again TR1 momentary dropped (for ~20 seconds) sharply, before their differences returned to around 2~3 ℃. Both TR1 and TR2 were observed to decrease due to the temperature drop of the binary ice when its flow rate was decreased.

Qualitatively, the profile of the refrigerant temperature at the compressor inlet (TR4) was very similar to TR1 and TR2, but with higher values due to the heat gained in the suction line heat exchanger. Due to the drop in TR2, the discharge temperature (TR5) also increased during the compressor on-periods when the binary ice flow rate was decreased.

During on-cycle periods, the temperature at the inlet to the expansion valve (TR8) is lower than TR6 at the condenser outlet; this was due to the heat released to the suction line vapour. When the compressor stopped, the drop in TR8 was significantly larger than that of TR6, as the former's location was closer to the evaporator which had a much lower temperature, but the latter was kept high by the condenser cooling water. When the compressor restarted, the profiles of these two temperatures were qualitatively similar to that of TW2 and the binary ice flowrate appeared to have little influences on the maximum and minimum of these two temperatures.

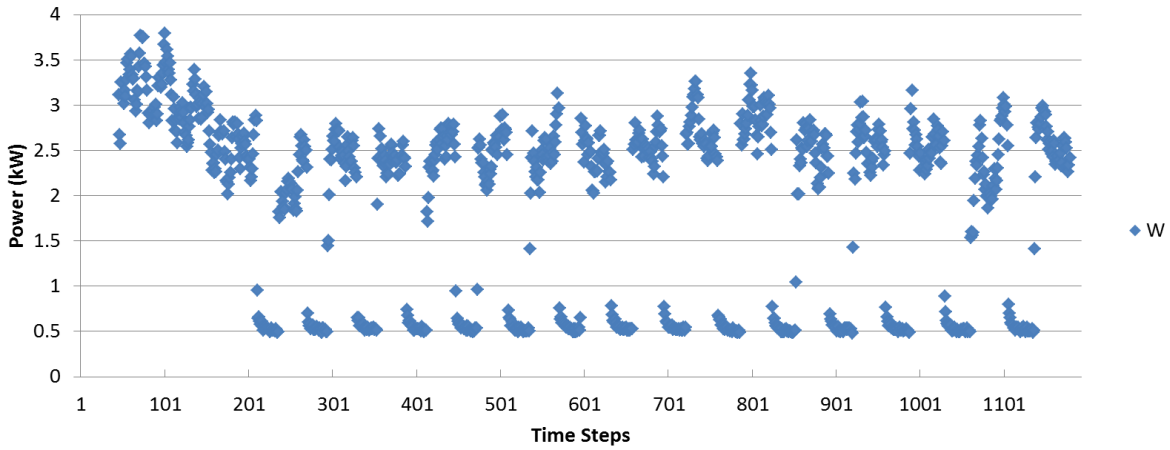

Figure 3.14 Compressor power consumption

The power consumption of the compressor is shown in Figure 3.14. During the initial system start-up stage, the compressor remained on for a longer duration (up to around 210 time steps) trying to pull down the solution from the relatively high room temperature; the corresponding power consumption for this stage was higher compared with the cyclic variations of the power consumption during the rest of the on-off cycles. During the on cycles, the typical average power consumption was about 2.5 kW regardless the decrease of the binary ice flowrate, while the consumption maintained at a relatively constant value of 0.5kW during off cycles under the stand-by mode. A typical cycle will have a compressor on-off time ratio of 6:4, and the ratio will increase slightly when the binary ice flowrate decreased.

A quick energy balance was carried out for a typical cycle to assess whether overall the measurements were accurate and reliable, and the results showed that a very satisfactory match was obtained taking into account of some heat and energy loss such as compressor heat lost to and the heat gained by the solution from the environment. Calculations show that for 370 seconds over an on-cycle period, the average power consumption of the compressor was 2.5kW. The cooling capacity of the ice generator calculated based on the properties and temperature difference of the binary ice was 3.6 kW. The condenser capacity calculated based on the cooling water flowrate and temperature difference was about 5.8 kW. It can be seen that the energy picked up from the cooling duty plus the work input from the compressor matched with the energy released to the cooling water, to within 5%. When considering the secondary circuit, the heater used to simulate the load was 2kW and was kept on all

the time for both on (370 seconds) and off cycle (240 seconds), providing a heat input of 1220 kJ in total. The 3.6 kW ice generator operated for 370 seconds during the on cycle, therefore the heat absorbed from the binary ice is 1332 kJ. The two matched within 10% of each other; the difference heat could be due to the heat picked up from the environment.

3.5 Fault simulations

The following system parameters were varied to provide data under both fault free and experimentally simulated faulty working conditions. The design (fault free) operation conditions were:

Cooling water flowrate: 10.6 litre/min

Initial binary ice solution concentration: 15% by weight

Binary ice flowrate: 9 litre/min at -7 ℃

As the study mainly was aiming at single fault detection, for each set of test, only one fault would be generated.

- Cooling water flow restriction

Cooling water flow restriction was simulated by throttling the valve (12) at the condenser water inlet. The fault was generated at 3 severity levels: 9.6, 8.1 and 7.0 litre/min.

- Binary ice flow restriction

The binary ice flowrate was controlled by the hand valve (16). Again, 3 levels of fault were introduced by reducing the flowrate to 7.5, 6.3 and 5.2 litre/min.

- Incorrect solution concentration

Ethanol solution concentrations of 10%, 12.5%, 17.5% and 20% were employed as faulty concentrations. Tests started with a small concentration and then certain amount of pure ethanol was added gradually. The total amount of the volume was kept the same by taking the extra solution out after the desired concentration was obtained.

♦ Broken SSIG scraper

A broken blade in the ice generator was simulated by switching off-on the scraper motor for a specific time profile. The validity and limitations of this idea will be discussed in Chapter 6.

♦ Ice generator motor failure

The ice generator motor failure was a hard fault. It could be simulated by simply switching off the motor resulting in no binary ice being produced. The secondary fluid leaving the ice generator would contain no ice and with a higher solution concentration than its original value. Further discussion will be covered in Chapter 6.

Table 3.4 Parameter variations during faulty conditions in conventional chillers and the current binary ice system

Fault	Chiller		Binary ice system	
Cooling water flow restriction	increase	P_e, T_c, TCA, P_c, T_{com}, W	increase	T_c, TCA, P_c, T_{com}, W
	decrease	T_c, T_{sc}, UA_c, COP, T_{sh}	decrease	T_c, T_{sc}, UA_c, COP
Secondary fluid flow restriction	increase	T_e, $LMTD_e$, T_{com}, W, ΔT_{sec}	increase	$LMTD_e$, T_{com}
	decrease	UA_e, T_c, COP	decrease	UA_e, COP, T_e

Table 3.4 compares the influence of the first two main faults on conventional chillers as noted from the literature with those observed from the current binary ice system. Some key differences and similarities were noted. For examples, for the first fault, most of the system parameters were noted to vary with similar patterns between the two system types, except P_e and T_{sh} were found not to vary by any noticeable extent in the binary ice system. On the other hand, for the second fault, the two systems shared variations in 5 common parameters, namely $LMTD_e$, T_{com}, UA_e, T_e and COP when the secondary flow rate was reduced, though some had different directions of changes. In addition, it appeared that the compressor power consumption W was not sensitive to the second fault in the binary ice system but increased in the chillers

fault. Furthermore, another unique difference was that ΔT_{sec} was not involved in the current binary ice system as temperature change of the binary fluid was found to be insensitive to faults; in contrary, ΔT_{sec} was often used as an indicator for chiller faults.

- Double faults

  Three sets of double faults are also covered, including:

  1. Binary ice flow reduction + solution concentration increase (BR+SCI)
  2. Cooling water flow reduction + solution concentration increase (CR+SCI)
  3. Binary ice flow reduction + broken blade (BR+BB)

The double faults were simulated by adding two single faults together, both at their highest severity level. For example, a BR+SCI fault was created by reducing the binary ice flowrate to 5.2 l/min, while increasing the concentration of the original ethanol solution to 20%.

4. Modelling of scraped surface ice generator

In this chapter, the construction of a mathematical model of the binary ice generator is presented. The model represents a component level sub-model of the scraped surface ice generator, which was used for analysing the effects of various operation conditions on the ice generation process. More importantly, the model was also used to obtain some of the parameters which were not directly measurable but could potentially be used for FDD; examples included internal wall surface temperature and ice concentration.

The SSIG model was a quasi-steady state distributed model. It was capable of predicting various key parameters, such as binary ice outlet temperature, the outlet ice concentration and the cooling capacity of the ice generator. The model was validated and calibrated, in terms of heat transfer coefficient, using experimental data.

4.1 The development of an analytical model of the SSIG

4.1.1 Scraped surface ice generator

Figure 4.1 shows the schematic configuration of a binary ice generation system, which is essentially a vapour compression refrigeration system with its evaporator functioning as an ice generator.

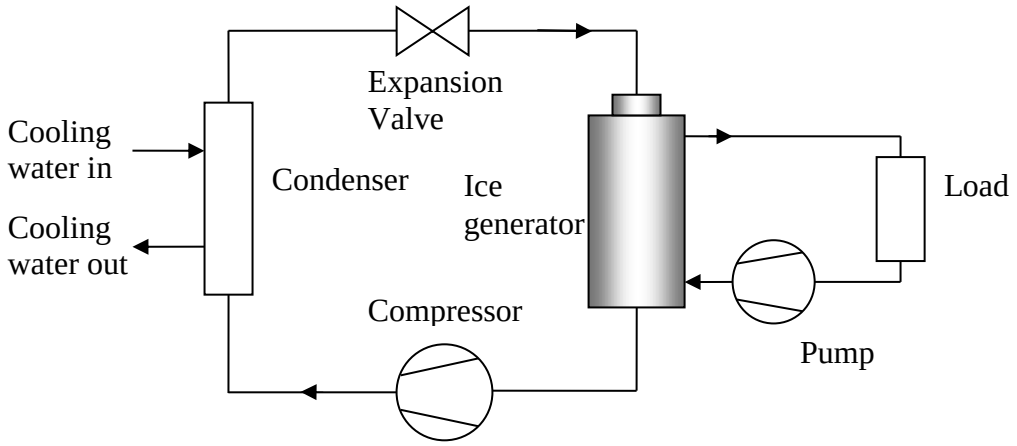

Figure 4.1 Schematic arrangement of a binary ice system

Figure 4.2 presents the internal details of the ice generator which is of a mechanical scraped surface type (Stamatiou et al. 2005).The SSIG contains two concentric cylinders, with scraper blades attached to a centrally rotating shaft which is driven by an electric motor. The numbers of blades vary with design (in this case, two blades are mounted) and the blades are spring loaded to maintain sufficient scrapping contact with the inner surface of the inner cylinder. The whole heat exchanger is insulated to prevent heat gain from the surroundings. The primary refrigerant flows in the annular gap between the two cylinders; it evaporates and absorbs heat from the secondary fluid that flows in the inner cylinder. Ice particles form as the evaporating temperature of primary refrigerant is sufficiently below the freezing point of the secondary fluid (Schwartzberg and Liu 1990).

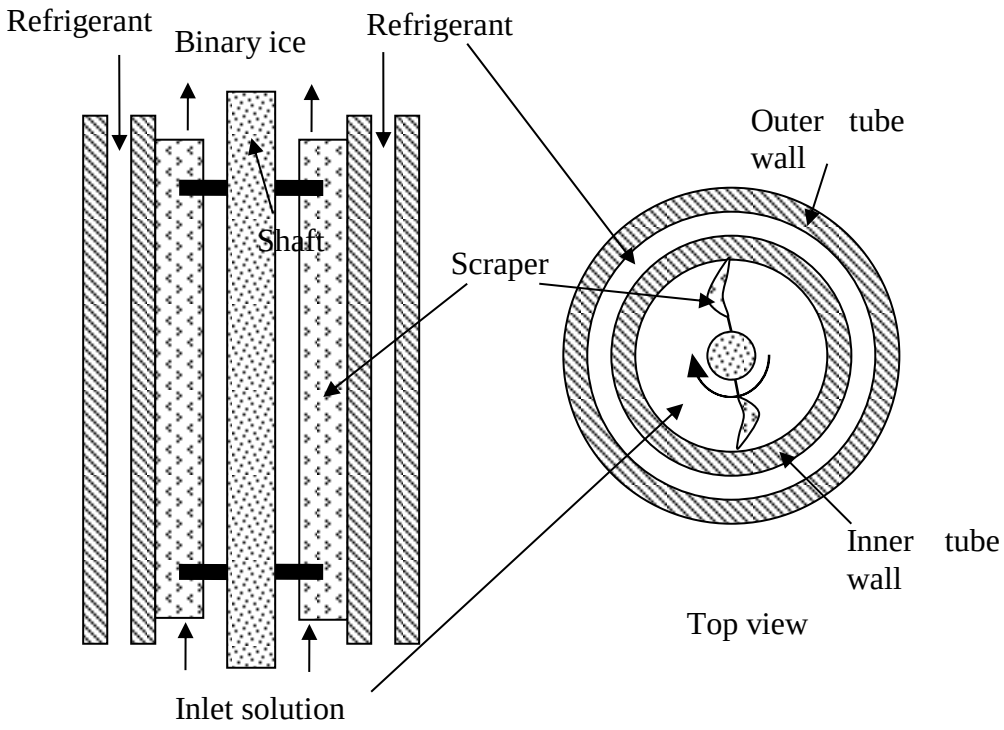

Figure 4.2 Structure of a scraped surface heat exchanger

Contrary to a conventional single-phase secondary system, at outlet of the ice generator, the secondary fluid is an ice-liquid mixture and its thermo-physical properties are functions of solution concentration, ice concentration as well as the

flow temperature (Kauffeld et al. 2005); all these parameters will have to be incorporated in the present model.

The performance of the ice generator is usually characterized by its ice production rate which needs to be controlled and matched with the load characteristics. Too much ice built up on the surface between two scraping actions would increase the required scraping power (Qin et al. 2006), also potentially cause damage to the scrapers and freeze-up/blockage in the heat exchanger. On the other hand, a low ice production rate reflects poor system efficiency, resulting in possible single phase operation and unable to benefit from the latent heat of ice. The mean diameter of the ice particles is generally approximated to be the thickness of the ice layer when it is scraped off from the surface, and this is determined by the growth rate of the ice layer and the rotating speed of the scraper. Binary ice with smaller particle sizes, having a larger surface area to volume ratio, usually provides a better heat transfer characteristics (Kauffeld et al. 2005).

The ice production rate can be determined by the following parameters: evaporating temperature of the refrigerant, mass flow rate and properties of the secondary fluid, scraping speed, number of the blades, fluid inlet temperature. As previously reviewed, faults such as refrigerant leakage and over-charge will influence evaporating temperature/pressure; flow restriction will decrease the mass flowrate of binary ice; mechanical damage of the scraper motor or the blade leads to incomplete or slow ice removal from heat exchanger surface, creating a similar effect to heat exchanger fouling. For a given SSIG, all of the above faults will affect heat transfer as well as ice production rates, influencing the properties/conditions (temperature, carrier fluid solution concentration and ice concentration) of the binary mixture at the heat exchanger outlet. These properties can be either directly measured or deduced from other measurements.

The SSIG model takes initial solution concentration, evaporation temperature, inlet solution temperature, solution mass flowrate and scraper rotating speed (rev/s) as input parameters. The dimensions of SSIG and the refrigerant side heat transfer coefficient h_o, a function of refrigerant *Re* and properties, etc., are also needed as input modelling parameters. The model outputs include: outlet flow temperature, ice concentration or ice production rate, cooling capacity and COP.

4.1.2 Modelling approach and formulation

The modelling of SSIGs had been carried out by previous researchers. Examples include heat transfer models of SSIG for making ice creams (Bongers 2006) and for freezing aqueous solutions (Qin et al. 2006). The above two models were both designed to simulate a fixed amount of fluid being cooled and frozen inside the heat exchanger with no flow, thus they are not entirely applicable for the current study. The model being built here is based on a transient freezing model for forced flow inside a convectively cooled tube (Seeniraj and Hari 2008). The original model used water as secondary fluid and no scraper was involved. Therefore two major modifications were carried out: (i) replace the water by ethanol solution and (ii) incorporate the rotating scraper blades.

Figure 4.3 illustrates the ice generation process inside a SSIG, with the corresponding physical and operation parameters given in Table 4.1. *r* and *z* represent respectively the radial and axial coordinate, with *z* = 0 defined as the inlet of the ice generator and *z* is positive upward.

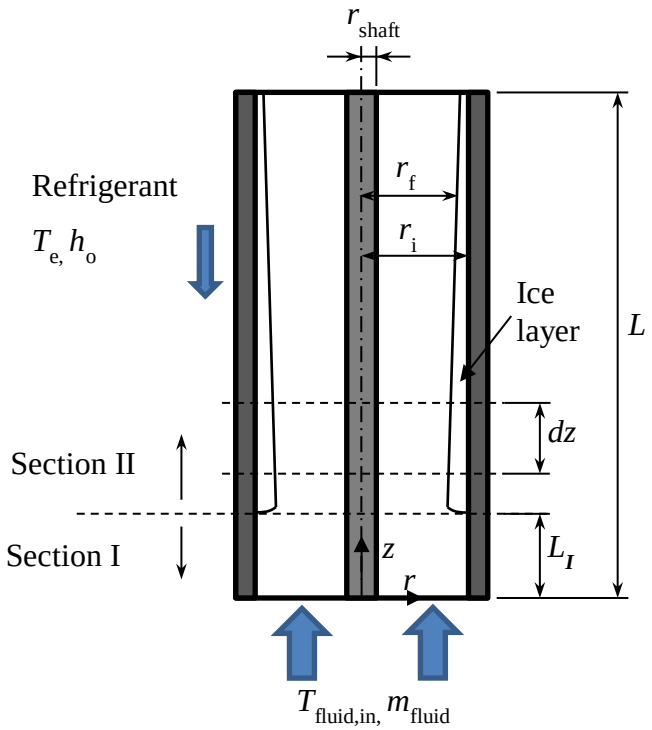

Figure 4.3 Ice layer on the inner surface of SSIG (blades not shown)

Table 4.1 Physical and operation parameters of the SSIG

r_i	Inside radius of inner cylinder [m]	C_o	initial solution concentration [kg/kg]
r_{shaft}	Radius of the rotating shaft [m]	$T_{fluid,in}$	Inlet solution temperature [°C]
r_f	Radial distance of the ice front [m]	m_{fluid}	Mass flowrate of the solution [kg/s]
r_o	Outside radius of inner cylinder [m]	L	Total length of the heat exchanger [m]

To simplify the simulation, assumptions were made but some of them could be removed if necessary. On the primary refrigerant side, evaporating temperature T_e (which was sufficiently lower than the local solution freezing point) and the convective heat transfer coefficient h_o were both assumed to be constant along the entire length of the SSIG. The adoption of assuming a constant h_o along the heat exchanger length was noted in many other researchers (Admiraal and Bullard 1993; Dehghan et al. 2015) to simplify the calculations. In addition, the constant h_o was also used in all simulations. This was considered justified/valid for the following reasons. First the test ranges were relative small and thus h_o was not expected to vary much. Second, the simulations were verified by comparing the calculated binary ice temperatures with the measured ones, and a good agreement was observed. The thermal resistance of the wall was initially assumed negligible (Lakhdar et al. 2005). Due to the agitating action of the scraper blades, no temperature gradient in radial direction in bulk fluid was assumed; in other words, the ice particles scraped off from the surface and carrier fluid were mixed instantaneously to form a homogeneous mixture. The temperature of the suspended ice particles was assumed to acquire approximately the same as the bulk flow temperature at the same axial coordinate, with no heat conduction in axial direction in the ice layer (Seeniraj and Hari 2008). The fluid boundary layer was assumed to be renewed immediately with bulk fluid after the scrapping action (Rao and Hartel 2006).

In the model, the flow region could be divided into two sections along the axial direction. Solution with an initial concentration of C_o and temperature $T_{fluid,in}$ entered from the bottom end of the cylinder. In the first section, sensible heat was absorbed by the evaporating refrigerant on the other side of the cylinder. The solution temperature gradually decreased, along the positive z direction, approaching the freezing point of the solution and signifying the end of Section I in which no ice was being produced. The length of Section I was determined by the difference between the

fluid inlet temperature and its freezing point, the flowrate, the refrigerant temperature and the overall heat transfer coefficient.

When the flow temperature gradually dropped to its freezing point, ice crystals started building up on the inner surface, signifying the start of Section II. Due to the agitation of the rotating blades, the bulk flow temperature at this stage could be assumed as the local freezing temperature (Qin et al. 2003). As water was taken out, solution concentration of the flow increases and the solution freezing point decreased along the positive *z* direction. As T_e was assumed to be constant at this stage, the difference between T_e and the local freezing point of the fluid decreased along *z* direction, causing it harder to form ice and thus the ice thickness decreased as well. The ice layer grew rapidly from zero to its maximum value at the beginning of Section II. This increase was difficult to be model accurately; therefore it was assumed to be a step jump. If the ice generator were long enough, it was possible that the ice layer thickness eventually reduces to zero and an ice free section III would form near the end of the ice generator.

- **Heat transfer without phase change (Section I)**

As the thermal resistance of the cylinder wall is neglected, there is no temperature gradient across the wall. Taking a small section of the cylinder (*dz*) as a control volume, the heat removed from the flow to the wall (second term of Equation 4.1) balances the energy absorbed by the refrigerant (3rd term).

$$dQ = h_o A_o (T_e - T_{wall}) = h_I A_i (T_{wall} - \bar{T}_{fluid}) \quad 4.1$$

where

$$h_I = \frac{Nu_I k_l}{2(r_i - r_{shaft})} \quad 4.2$$

and h_o and h_I are the convective heat transfer coefficients of the refrigerant and the solution respectively, A_o and A_i are the outer and inner heat transfer areas of the cylindrical section, T_{wall} is the wall temperature, $\bar{T}_{fluid}$ is the average bulk flow temperature in the control volume, k_l is bulk thermal conductivity of solution, Nu_I is the Nusselt number for Section I. According to (Stamatiou et al. 2005), the Nusselt number of a laminar or transition flow inside the heat exchanger without phase change can be expressed as:

$$Nu_{\mathrm{I}} = \frac{2}{\sqrt{\pi}}\left(\frac{2Nr_{\mathrm{i}}\rho_{\mathrm{l}}C_{\mathrm{p,l}}B}{k_{\mathrm{l}}}\right)^{0.5} \quad 4.3$$

where N is the rotational speed of the scrapers (rev/s), ρ_{l} is the density and $C_{\mathrm{p,l}}$ is the specific heat capacity of the fluid, and B is the number of blades per 360 degrees. As expected, the higher the rotational speed or the larger the blade number, the higher would be the heat transfer coefficient.

Initially, the value of heat transfer coefficient h_{o}, is chosen as 3000 W/(m^{2}K) according to previous researches for similar conditions (Greco and Vanoli 2005) for R507. It is then calibrated according to the measured data.

Based on energy conservation, heat transfer rate dQ can also be equated to the heat loss of secondary flow, Equation 4.4.

$$dQ = C_{\mathrm{p,l}}m_{\mathrm{fluid}}\Delta T_{\mathrm{fluid}} \quad 4.4$$

where m_{fluid} is the mass flowrate of the solution and $\Delta T_{\mathrm{fluid}}$ is the temperature change of the solution across the control volume in the z direction.

If the outlet fluid temperature of a control volume drops below the freezing point, this control volume will be assumed as the last element of Section I. The total heat transfer rate from the solution to the refrigerant in Section I can be obtained by summing up the heat transfer rate of individual control volumes.

$$Q_{\mathrm{total}} = \sum dQ \quad 4.5$$

- **Heat transfer with phase change (Section II)**

In Section II, ice builds up on the cylinder surface. The heat absorbed by refrigerant represents partly the latent heat released due to solidification and partly the enthalpy drop of the solution across the control volume. The energy paths are shown in Figure 4.4a. Under quasi-steady state, the temperatures of the solution entering and exiting the control volume dz can be considered constant. With no scrapping action taking place, at any time t, the thickness of ice layer is $r_{\mathrm{ice}} = (r_{\mathrm{i}} - r_{\mathrm{f}})$ and it will increase by $(\partial r_{\mathrm{f}})$ over a period of Δt. The corresponding temperature profile between the fluids, the cylinder wall and the ice layer is shown in Figure 4.4b.

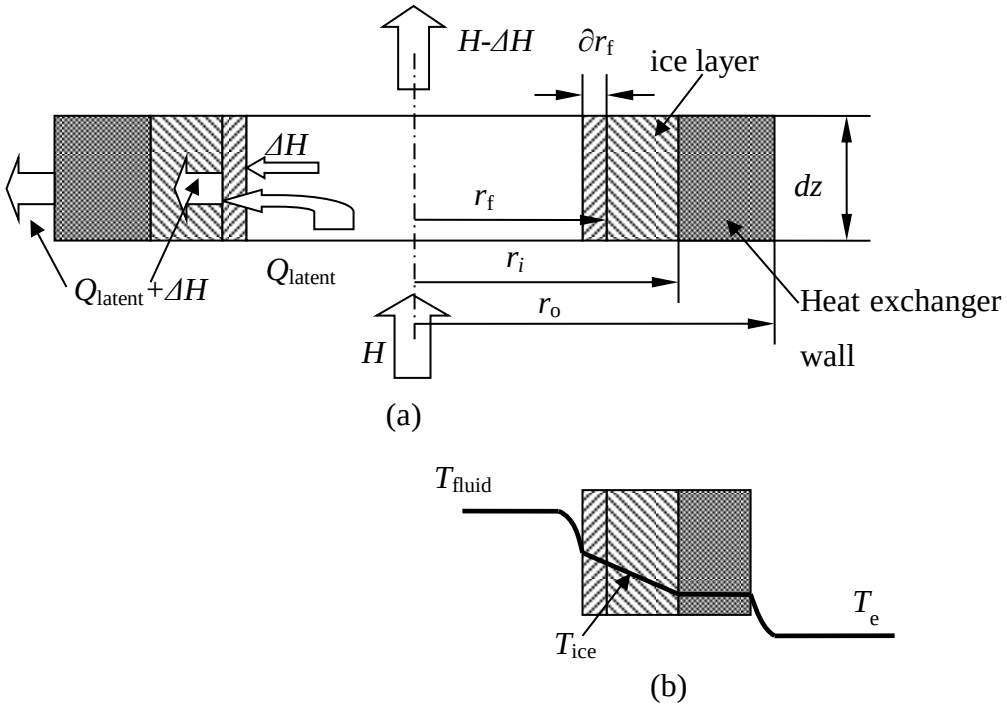

Figure 4.4 Ice layer building up on the inner surface of a SSIG, (a) heat transfer within a control volume and (b) temperature profile at the cross section

The evaporating temperature stays relatively constant at T_e outside the heat exchanger wall, and increases at the boundary layer near the wall. As the wall is assumed to have no thermal resistance, temperature remains the same inside it. The temperature was assumed to have a linear profile inside the ice layer (Seeniraj and Hari 2008), when the influence of the temperature to the thermal resistance of the ice is ignored. There is a sharp temperature increase in the boundary layer of the fluid near the inside surface of the ice layer, until temperature reaches the freezing point of the fluid, which is also regarded as the local fluid temperature.

Across the control volume in the z direction, the enthalpy drop (ΔH) of the bulk fluid (i.e. the sensible heat component), represented by the middle term of Equation 4.6, is equal to the convective heat from the bulk flow to the ice layer (i.e. the last term of the equation).

$$\Delta H = m_{\text{fluid}} C_{p,\text{l}} \frac{\partial T_{\text{fluid}}}{\partial z} dz = -h_{\text{II}} A_{\text{i}} \left(T_{\text{fluid}} - T_{\text{ice}}|_{r=r_{\text{f}}} \right) \qquad 4.6$$

where $T_{\text{ice}}|_{r=rf}$ is the temperature of ice at the solid/fluid interface, h_{II} is the localised heat transfer coefficient of binary mixture in Section II, T_{fluid} is the bulk temperature

of the fluid, which is assumed to be equal to the local freezing temperature of flow at Section II.

At the ice/solution interface ($r = r_f$), the heat conduction through the ice layer, left hand side of Equation 4.7, is equal to the total amount of convective heat from the solution to ice layer (ΔH), i.e. the first term on the right, and the latent heat released by ice formation (Q_{latent}), represented by the second term on the right.

$$-k_{ice}\left(\frac{\partial T_{ice}}{\partial r}\right)_{r=r_f} A_f = h_{II} A_f \left(T_{fluid} - T_{ice}|_{r=r_f}\right) - \frac{\partial r_f}{\partial t}\rho_{ice} L_{ice} A_f \qquad 4.7$$

where

$$h_{II} = \frac{Nu_{II} k_{fluid}}{2(r_i - r_{shaft})} \qquad 4.8$$

and A_f is the surface area of ice layer when $r = r_f$, k_{ice} is the thermal conductivity of ice, k_{fluid} is the thermal conductivity of binary ice, ρ_{ice} is the density and L_{ice} is the specific latent heat of the ice. Under quasi steady state, T_{fluid} is a function of axial coordinate *z*.

Equation 4.9 indicates that at the boundary between the two sections, the temperature of the fluid is at its freezing point.

$$T_{fluid}(z = L_I) = T_f(C_o) \qquad 4.9$$

where L_I, is the length of Section I. For a given solute, the freezing temperature, T_f, is a function of solution concentration, and its calculation procedure is given in the Appendix A.

The radial distance of the freezing ice front r_f is a function of time *t*, axial coordinate *z*, as well as the angular position within the cylinder with respect to the blade position; the distance between r_f and r_i represents the local ice thickness. Figure 4.5 shows the profile of the ice layer when the cylinder wall is unwrapped to approximate a flat surface for an element in Section II. *B* is the number of the blades per 360 degrees and $\frac{2\pi}{B}$ is the angular distance (in radians) between two blades. After each scraping at a given angular position, ice gradually accumulates on the surface, until being scraped off by the next blade.

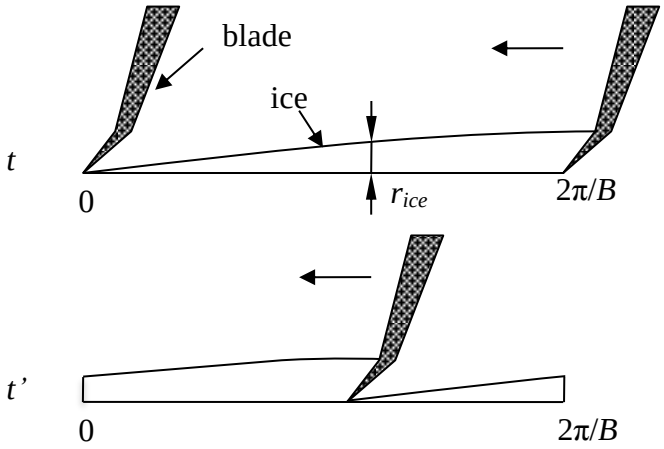

Figure 4.5 Ice layer profile on the unwrapped SSIG surface

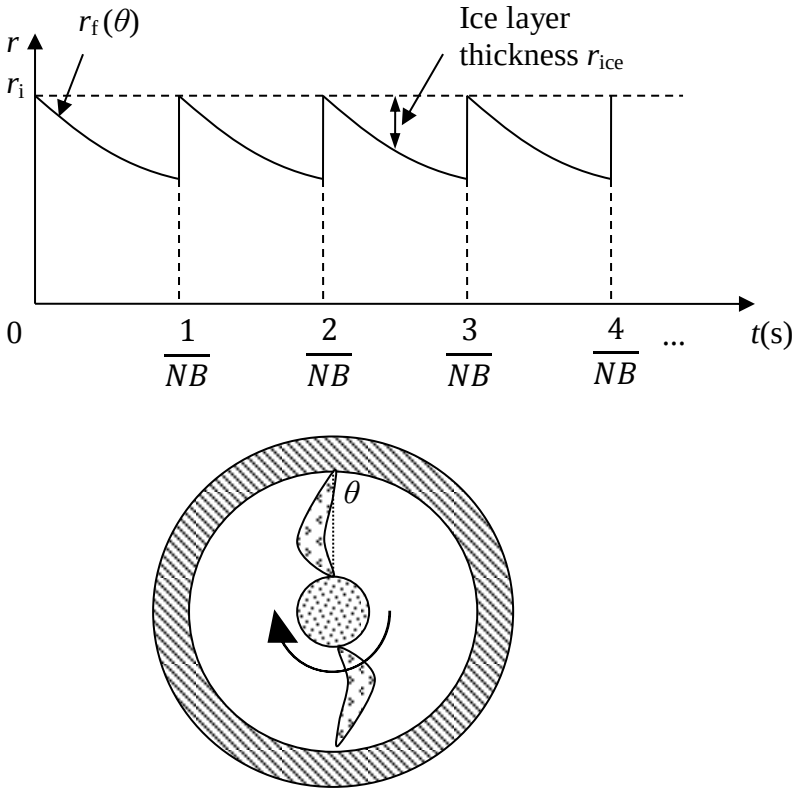

Figure 4.6 r_f as a function of time at a given axial position

Figure 4.6 illustrates schematically the periodical variation of ice front position r_f with time (solid line in Figure 4.6) at a fixed angular position, say θ; $\frac{1}{NB}$ represents the time interval between two scrapings and the sequential scrapping off of

ice at this location occurs at time $t = \frac{n}{NB}$ where n = 1, 2, 3, etc. When the rotational speed or the number of blade increases, the time interval between two scraping actions will decrease as well as the maximum ice thickness (r_i -r_f) or ice particle sizes, but the ice concentration will increase as illustrated in later predictions.

Lakhdar et al. (2005) developed an empirical correlation for calculating the Nusselt number for ethanol-water solution in a SSIG with phase change, and it can be applied for Section II. The conditions of use are compatible to current SSIG configuration and operation.

$$Nu_{\mathrm{II}} = 4.47 {Re_{\mathrm{a}}}^{0.27} {Re_{\mathrm{r}}}^{0.38} {C_{\mathrm{o}}}^{0.8} \tag{4.10}$$

where Re_a is axial Reynolds number and Re_r is rotational Reynolds number, defined as:

$$Re_{\mathrm{a}} = \frac{2\rho_{\mathrm{bi}} u (r_{\mathrm{f}} - r_{\mathrm{shaft}})}{\mu_{\mathrm{bi}}} \tag{4.11}$$

$$Re_{\mathrm{r}} = \frac{4\rho_{\mathrm{bi}} N {r_{\mathrm{f}}}^2}{\mu_{\mathrm{bi}}} \tag{4.12}$$

where u is the axial bulk velocity of solution, ρ_{bi} is the density and μ_{bi} is the dynamic viscosity of the binary ice. The calculation procedures for various properties of binary ice mixture, including thermal conductivity, density and dynamic viscosity can be found in the Appendix A and B, and they are all based on the local solution temperature and concentration.

All the released latent and sensible heat from the control volume is absorbed by refrigerant, i.e. the right hand term of the equation 4.13, on the other side of the cylinder, assuming the steel cylinder has not thermal resistance.

$$k_{\mathrm{ice}} \frac{\partial T_{\mathrm{ice}}}{\partial r}\bigg|_{r=r_{\mathrm{i}}} A_{\mathrm{i}} = h_{\mathrm{o}} [T_{\mathrm{ice}}(t, z, r_{\mathrm{i}}) - T_{\mathrm{e}}] A_{\mathrm{o}} \tag{4.13}$$

The heat conduction in the ice layer at a given z location can be expressed by quasi- steady state 1-D heat conduction equation for a cylinder.

$$\frac{1}{r}\frac{\partial}{\partial r}\left(r \frac{\partial T_{\mathrm{ice}}}{\partial r}\right) = 0 \tag{4.14}$$

4.1.3 Numerical solutions

Calculations involved in Section I are mainly for determining the position of the boundary between Sections I and II. All the fluid properties in Section I can be assumed constant as their variations with temperature are quite minimal. Equations 4.1 and 4.4 are applied to determine the outlet flow temperature of each successive control element, which is then compared with the freezing point temperature at initial concentration C_o. Sections II starts when the flow temperature drops below this freezing point. The length of Section I is

$$L_I = a \times dz \tag{4.15}$$

where a is the number of control volume in Section I to achieve the freezing condition; typically dz is set at 5mm. It is possible to have L_I reached the full length of the ice generator; this represents the condition that no ice is being produced and the ice generator is essentially functioning as a chiller, i.e. no ice in and no ice out.

For section II, fluid bulk temperature T_{fluid} (z) and radial distance of the freezing front r_f (t,z) can be determined by solving equations 4.6, 4.7, 4.13 and 4.14 simultaneously.

The differential equation 4.14 has a general solution in the form of:

$$T_{ice} = C_1 \ln r + C_2 \tag{4.16}$$

Combining it with Equation 4.13, C_1 and C_2 can be obtained

$$C_1 = \frac{h_o\left(T_e - T_{ice}|_{r=r_f}\right)}{h_o \ln(r_i/r_f) + k_{ice}/r_i}$$

and

$$C_2 = T_{ice}|_{r=r_f} - \frac{\ln r_f h_o\left(T_e - T_{ice}|_{r=r_f}\right)}{h_o \ln(r_i/r_f) + k_{ice}/r_i} \tag{4.17}$$

Then equation 4.16 becomes

$$\frac{\partial T_{ice}}{\partial r} = \frac{h_o\left(T_e - T_{ice}|_{r=r_f}\right)}{(h_o \ln(r_i/r_f) + k_{ice}/r_i) r} \tag{4.18}$$

Substituting Equation 4.18 into Equation 4.13 yields

$$\frac{-k_{\mathrm{ice}}h_{\mathrm{o}}\left(T_{\mathrm{e}}-T_{\mathrm{ice}}|_{r=r_{\mathrm{f}}}\right)}{(h_{\mathrm{o}}\ln(r_{\mathrm{i}}/r_{\mathrm{f}})+k_{\mathrm{ice}}/r_{\mathrm{i}})r_{\mathrm{f}}}=h_{\mathrm{i}}\left(T_{\mathrm{fluid}}-T_{\mathrm{ice}}|_{r=r_{\mathrm{f}}}\right)-\frac{\partial r_{\mathrm{f}}}{\partial t}\rho_{\mathrm{ice}}L_{\mathrm{ice}} \qquad 4.19$$

The differential equations, Equations 4.6 and 4.19, are solved to get two unknowns, namely the T_{fluid} and r_{f} in Section II by using the predictor-corrector Euler method (Butcher and Wiley 2008). For each control volume *dz*, the inlet temperature, solution and ice concentration of binary mixture at any time are known from the outputs of the previous control volume; (the inlet ice concentration of the first control volume in Section II is taken as zero). By using a guessed temperature at the solid/liquid interface ($T_{\mathrm{ice}}|_{r=r\mathrm{f}}$), T_{fluid} and r_{f} can be found according to equations 4.6 and 4.19. A new interface temperature $T_{\mathrm{ice}}|_{r=r\mathrm{f}}$ can then be calculated and compared with the guessed value. If the difference between them is within a pre-set tolerance, the calculations can be considered completed, then the calculation proceeds to the next control volume; if not, the new interface temperature should be used instead of the guessed value until the calculation converges.

When the dynamic response of a system is much faster than the change of its operation conditions, it can be assumed that the system is operating under quasi-steady state. The assumption had been successfully applied in many transient heat transfer models including both liquid chillers (Browne and Bansal 2000; Wang et al. 2000) and binary ice system (Knodel et al. 2000). In this study, the system is also assumed to operate under quasi-steady state for the purpose of modelling and simulation.

To simulate transient operations, the input time variables, including the measured inlet fluid and evaporating temperatures, were discretised into time steps first. The SSIG model predicted a new set of outputs, such as the outlet of the fluid temperature, for each time step under the specified inlet variables. Then the procedure was repeated for the next time step. The final outputs of the model captured both the temporal and spatial variations of the variables, describing the status of the fluid inside the SSIG. Essentially, a quasi-steady state SSIG model was composed by a series of steady state predictions.

Figure 4.7 shows the flow chart of the simulation process at any given instant.

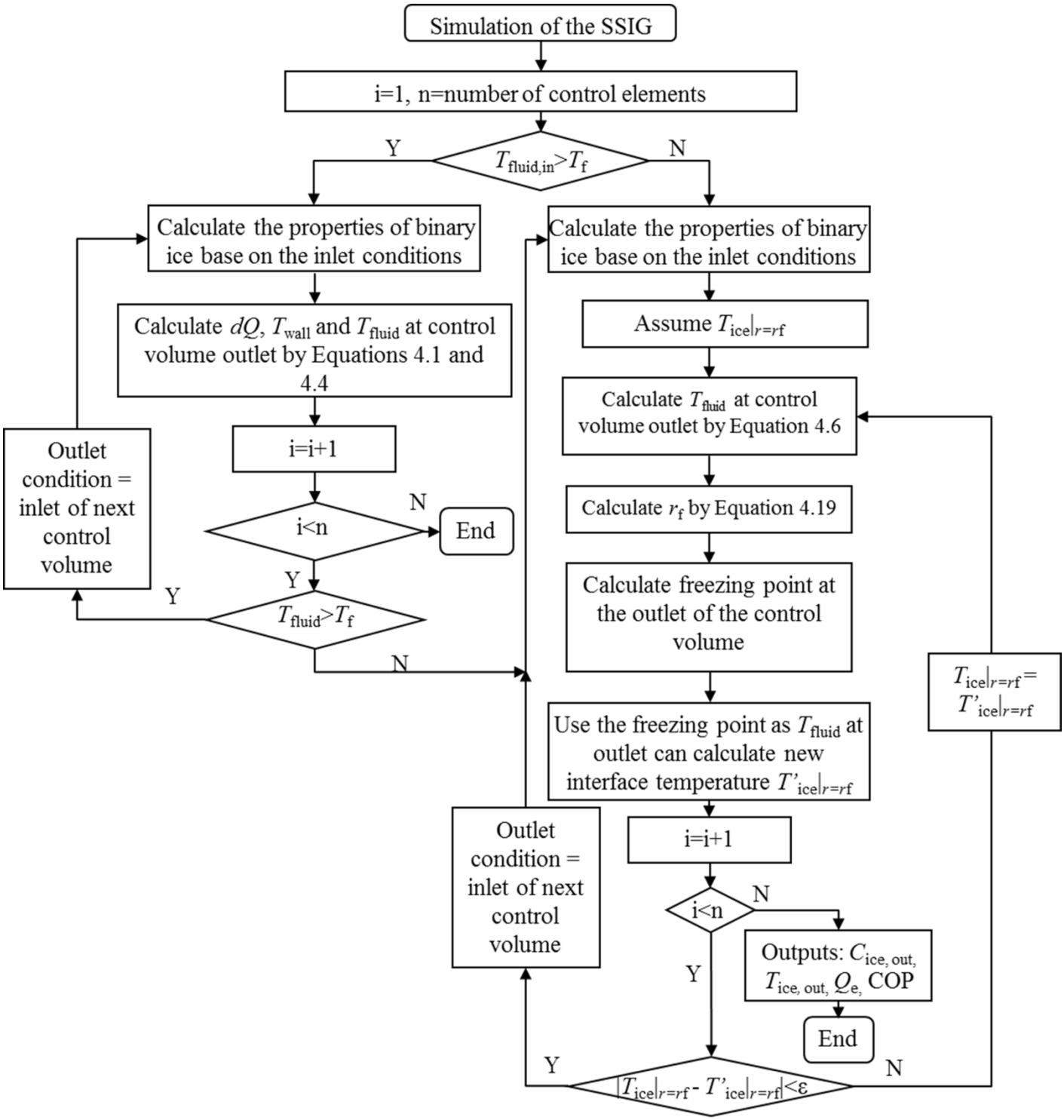

Figure 4.7 Flow chart of modelling process at a given time step

In addition, as an on/off control was used in the system, the model incorporated a detector taking the power consumption of the compressor as an input to detect whether the compressor was running. The simulation process of the SSIG was kept unchanged when the compressor is off-cycle, but the heat transfer coefficient of the refrigerant was artificially set to a very low value, as the refrigerant flow had been cut off.

4.2 Model validation and results

The fluid used to generate ice is ethanol-water solution. The dimensions of the SSIG were estimated based on the laboratory unit:

Table 4.2 Dimensions of the SSIG

r_i	Inside radius of inner cylinder [m]	0.10
r_o	Outside radius of inner cylinder [m]	0.11
r_{shaft}	Radius of the rotating shaft [m]	0.02
L	Total length of the heat exchanger [m]	0.46
B	Number of blade per 360 °	2
N	Scraper rotation speed [rpm]	168

4.2.1 The validation of the model

The verification of the code was done by testing the code against some set scenarios as well as some manual calculations to ensure the algorithm and the calculation steps were correctly implemented to produce the expected results. As for validations, the simulation results were compared with the experimental data obtained from the test rig described in Chapter 3. These were based on the data from several complete on/off cycles under different conditions, though only one set of representative data was presented here. The initial ethanol mass concentration was 15%. The inlet binary ice temperature and the refrigerant evaporating temperature were measured and used as the model inputs. The flow rate of binary ice was set at 9 litres/min and remained constant during the test. The set point of the binary ice temperature at the inlet of the SSIG was -5 ℃ with a differential of +2 ℃. All the data was taken with a 10 second interval (i.e. each time step corresponds to 10 seconds).

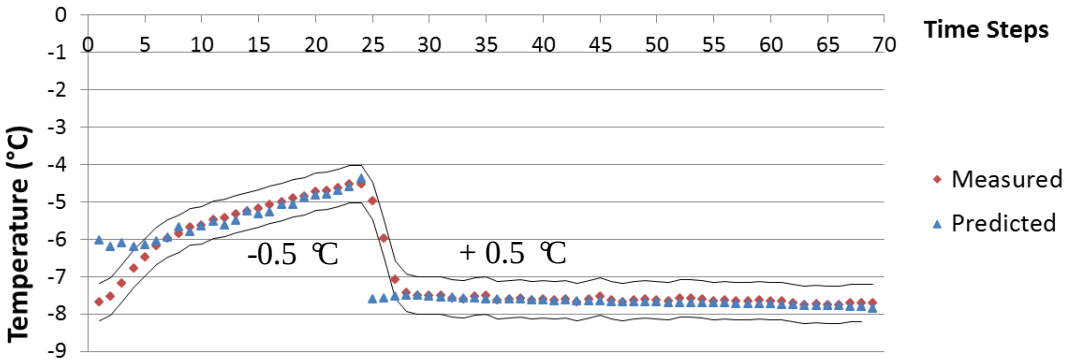

Figure 4.8 Comparison of measured and calculated binary outlet temperature

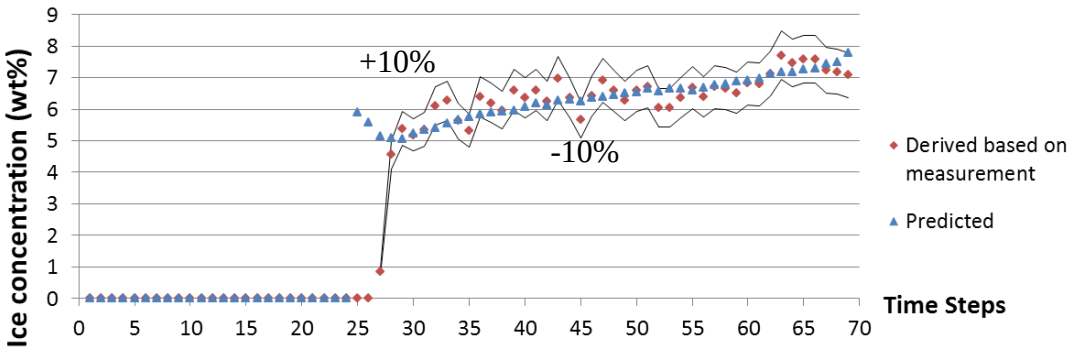

Figure 4.9 Comparison of derived and calculated ice concentration at the SSIG outlet

Figure 4.8 and Figure 4.9 show validation results of binary ice temperature and ice concentration (the ice concentration was derived from measured binary ice temperature based on the initial solution concentration) at the SSIG outlet. Within the first 24 time steps, the compressor was cycled off by the thermostat and thus no ice was produced. During this period, the binary ice outlet temperature increased gradually. At around the 25th time step, the compressor was turned on. The temperature dropped rapidly while the ice concentration (calculated based on predicted and measured temperatures) rose to a value of about 7%.

More than 90% of the temperature and ice concentration predictions fell respectively within the ±0.5 ℃ and ±10% band of the measured or derived values. The derived ice concentrations (based on measurement) in the first 25 time steps were zero as all the measured solution temperatures were found to be above the freezing point during this period so no ice was formed. Potentially, there could be some

measurement errors leading to a positive concentrations, but it was not possible to have negative concentration. Therefore, no error band was included for this part of the data. Large discrepancies mainly occurred when sudden changes of the system operation happened (i.e. during compressor off/on switching). It can be seen from Figure 4.8 that the model under-predicted the binary ice outlet temperature when the compressor was not running, while the prediction became much more accurate during the compressor running (within ±0.2 ℃ error band). The coefficient of determination (R^2) for the binary ice outlet temperature prediction 0.85. In Figure 4.9, much larger discrepancies between the derived and predicted values were observed during the compressor on-cycle suggesting that even small error in the temperature prediction could result in large difference in the ice concentration. When the compressor was not running, as long as the predicted binary ice temperature was above the freezing point, the ice concentration would stay at zero. The R^2 for the ice concentration prediction is 0.90.

4.2.2 Simulated behaviour of the SSIG

Having validated the model, it can be used to simulate and understand the general behaviours of the SSIG. Another main advantage of having an analytical model is its ability of calculating some immeasurable parameters such as the ice particle size and the axial variation of the fluid temperature within the SSIG. In this section, the validated model is used to generate data to demonstrate some operating characteristics of the binary ice system.

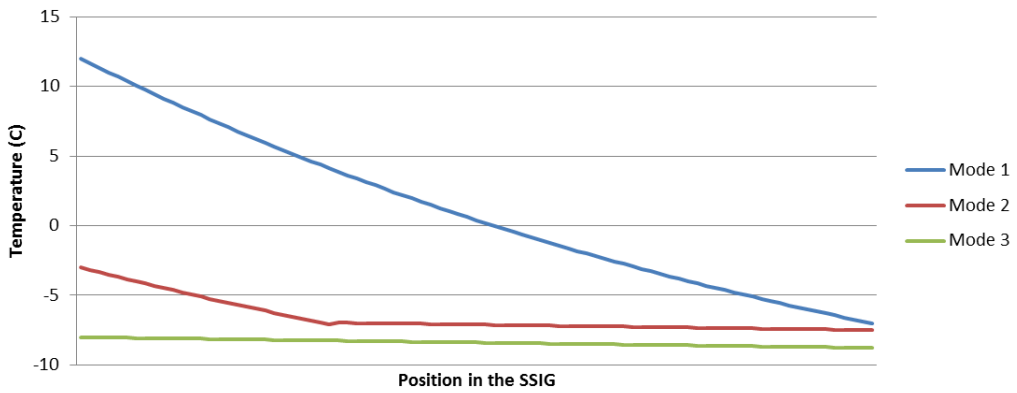

Figure 4.10 Variations of binary ice temperature along the SSIG for the three modes of operation

Figure 4.10 shows the simulated axial temperature profiles of the fluid along the SSIG under different loads when the compressor is running; the left hand side represents the inlet to the SSIG. In general, 3 different modes can be expected.

Mode 1: No ice is produce in the SSIG. The SSIG inlet liquid temperature is high enough that the liquid cannot be cooled down to its freezing point in the ice generator. Therefore the SSIG essentially operates as an ordinary liquid chiller with a significant difference between inlet and outlet temperatures.

Mode 2: Initial part of the scraped heat exchanger acts as a liquid chiller bringing the fluid temperature down towards its freezing point, while the rest produces ice. The profile can be divided into two sections as discussed previously. The temperature gradient of the first section is much larger than the second section and the boundary between the two sections moves with the load conditions.

Mode 3: Ice is generated along the entire length of the SSIG. In this case, the fluid going into the ice generator already contains some ice in it. The temperature of the fluid drops slightly along the SSIG.

Among the three operation modes, mode 2, particularly with a small length of Section I, is the most desirable one. In Mode 1, no ice can be produced, suggesting the cooling capacity is too small when compared to the required load. It should be avoided through proper design and sizing of the equipment. Binary ice systems normally incorporate with control mechanisms (Guilpart et al. 2005) to ensure the appropriate amount of ice is generated to avoid ice blockage. When the load is too low (Mode 3), the system will be cycled-off by the control monitoring the inlet temperature. Therefore, in practice, Mode 2 is the most likely to occur.

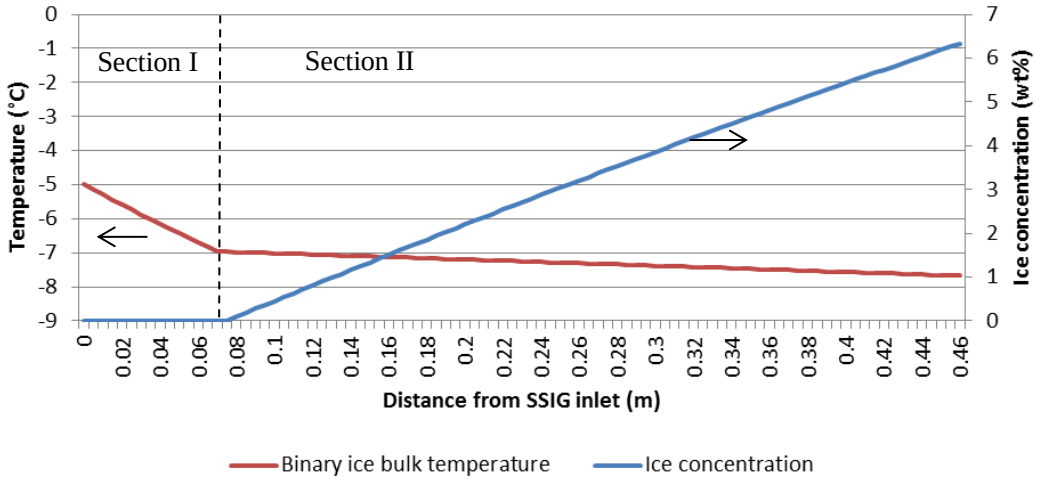

(a)

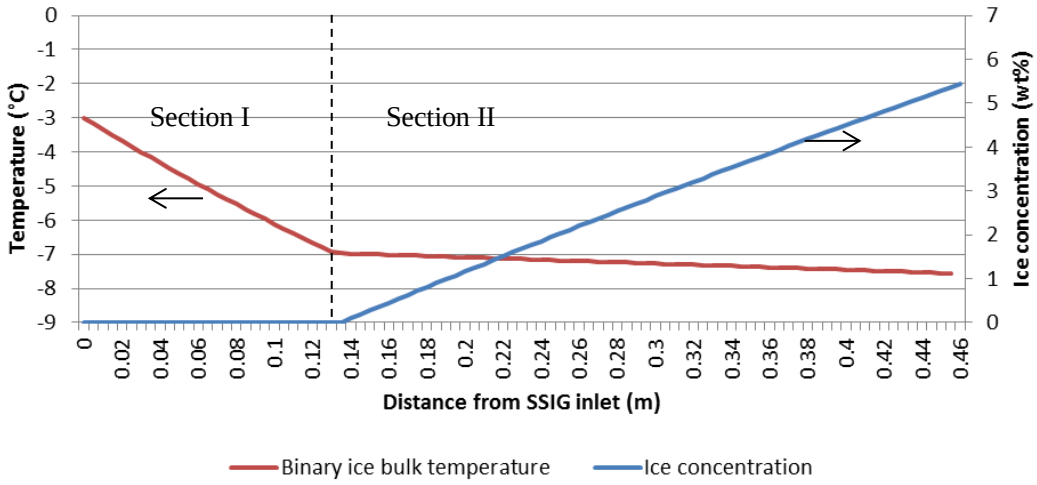

(b)

Figure 4.11 Local fluid temperature and ice concentration along the SSIG

Figure 4.11 illustrates the binary ice temperature and ice concentration profiles along the SSIG under Mode 2 with a fixed evaporating temperature. It can be seen that there are two distinct gradients of temperature profile along the length of the SSIG, with relatively much larger temperature drop in Section I; in fact, over 70% of the overall temperature drop takes place in the first 20% of the length in Figure 4.11a. As expected, Section II experiences a much smaller temperature drop (no more than 1 ℃), due to involvement of the latent heat. The ice concentration increases steadily in a slightly non-linear manner to ~6.3%.

As the load changes, both the gradients and the lengths of the two sections will change accordingly. Figure 4.11b demonstrates the binary ice temperature and ice

concentration with a higher inlet temperature but with all other working conditions remained unchanged. Section I becomes longer when the difference between the inlet temperature and the freezing point is larger. At the outlet of the ice generator, the ice concentration (~5.4%) is smaller thus less ice is produced when compared to Figure 4.11a. Unless the length of the SSIG exceeds an estimated length of 2.3m based on the design working conditions of the test rig, it is rather unlikely that Section III will occur.

Figure 4.12 shows the maximum thickness of the ice layer between two scraping actions along the SSIG, which is thicker at the initial part of Section II, suggesting the predicted ice particle sizes are between 6 to 8 μm. The reason is that when water is taken out from the solution, solution concentration goes up and the freezing point of the remained liquid decreases, and this leads to a smaller difference between the solution freezing point and the wall surface temperature, assuming the evaporating temperature remains constant; the generated ice layer becomes thinner. A limitation of the model is that it can only predict a sudden jump of ice thickness between section I and II; however as in reality, the thickness increases from zero thickness over a short distance.

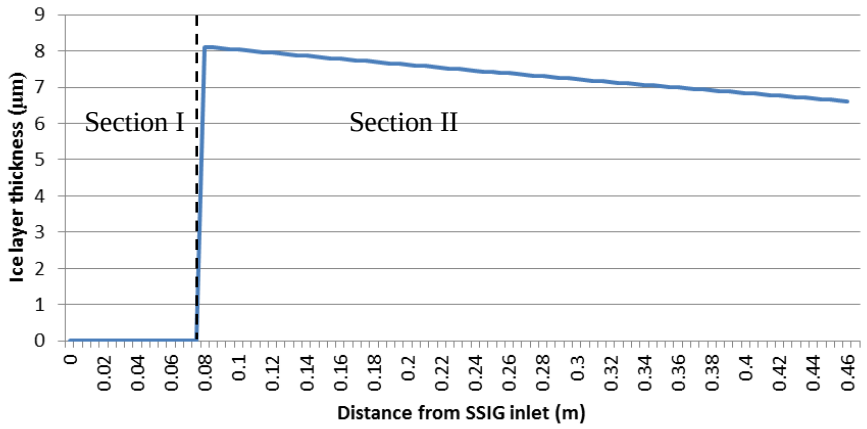

Figure 4.12 Maximum ice layer thickness between two scrapings along the SSIG

To make full use of the SSIG, the length of Section I should be kept as short as possible during operation. The length is determined by the many parameters such as the fluid inlet temperature, the flowrate, the solution freezing point and the evaporation temperature. In practice, if the same solution concentration is used, then the freezing point is a fixed value. The evaporation temperature cannot be controlled

directly. Therefore only the influences of the first two parameters are addressed here. The length of Section I against the inlet fluid temperature $T_{fluid,in}$ under three different flowrates is shown in Figure 4.13 Apparently, when the inlet temperature is higher (i.e. a higher load), more heat needs to be taken out from the solution in order get to the freezing point. This leads to a longer section without producing ice. A larger flowrate also increases the length of section I.

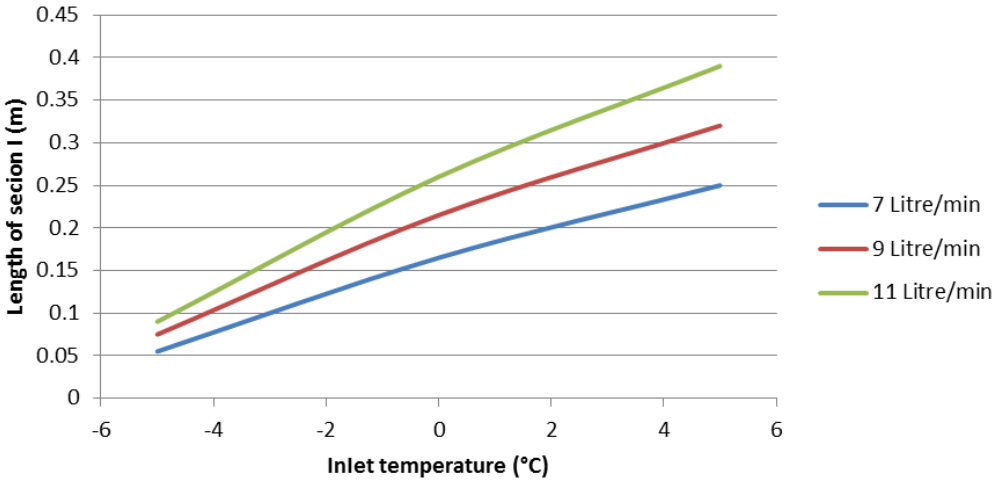

Figure 4.13 Variation of the length of Section I against the inlet fluid temperature $T_{fluid,in}$ under three different flowrates

The following figures (Figure 4.14 - Figure 4.16) present the variations of some of the model outputs due to changes in working conditions that could be caused by occurrence of a fault. Y-coordinate on the right is the temperature of binary ice at the SSIG outlet and the left hand is the cooling capacity of the SSIG, for a range of evaporating temperatures, flowrates and initial solution concentrations, while the inlet temperature is kept constant at -5 ℃. Depending on the combination of various parameters, individual data points can fall into one of the three possible operation modes described earlier.

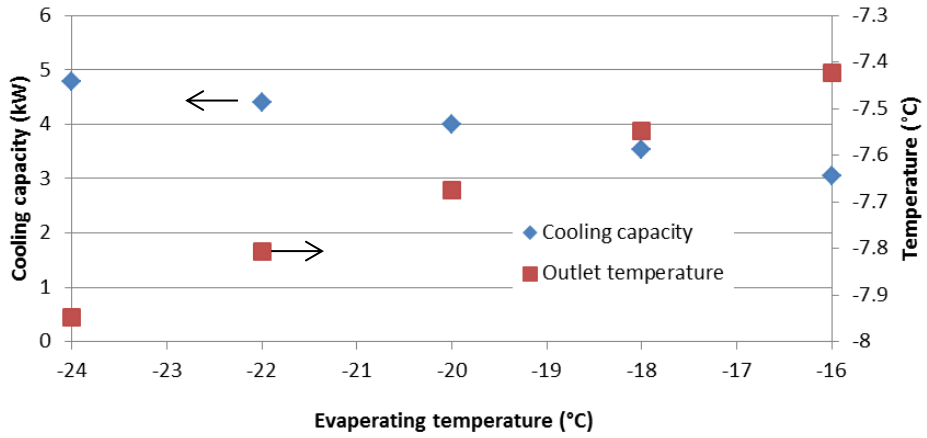

Figure 4.14 Binary ice temperature and cooling capacity at ice generator outlet against evaporating temperature (design T_e = -20 ℃, flowrate fixed at 9L/min, initial solution concentration at 15% by mass)

The effects of evaporating temperature are shown in Figure 4.14. A lower evaporating temperature increases the temperature difference between the binary ice and the refrigerant under the same initial solution concentration and the inlet temperature, resulting in a lower flow temperature at the outlet and a higher cooling capacity. It is worth noting that, in a system, one would normally expect the cooling capacity increases with increasing T_e, as the refrigerant mass flow rate increases due to higher suction vapour densities at higher T_e. However, the presented results are for the SSIG alone in which the refrigerant mass flow rate is assumed constant. Therefore the capacity decreases as the T_e increases. Faults such as binary ice flow reduction and cooling water flow reduction would change the evaporating temperature.

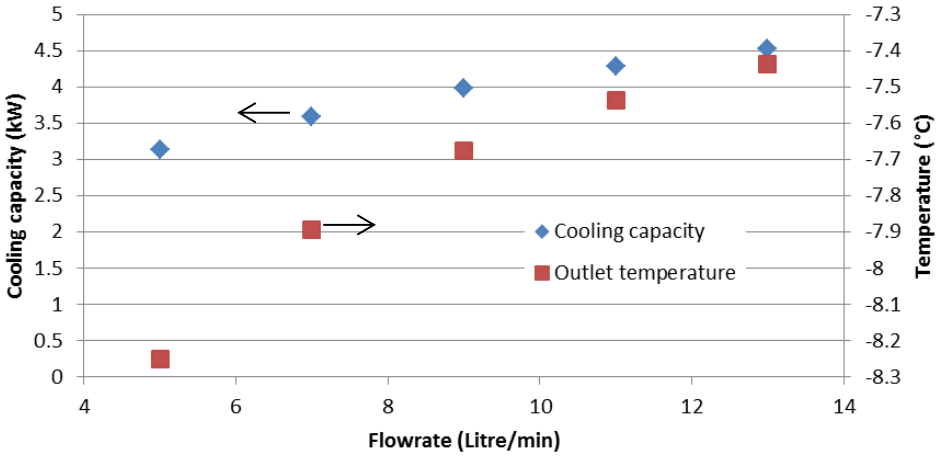

Figure 4.15 Variations of outlet flow temperature and cooling capacity with flowrate (design flowrate = 9 Litre/min, design T_e = -20 ℃, initial solution concentration at 15% by mass)

Flowrate could decrease due to flow restriction, which is a common fault in secondary system. Figure 4.15 indicates that a lower solution flowrate would lead to a lower outlet flow temperature. Though this results in a higher ice concentration, the cooling capacity reduces due to the reduced flow rate.

The output parameters will deviate from the expected values when an incorrect solution concentration is assumed in the model, which can be interpreted as a fault. Figure 4.16 shows that both cooling capacity and outlet temperature drop when the initial solution concentration is increased. A fluid with a higher solution concentration has a lower freezing point. Although the fluids enter the heat exchanger at the same temperature, the temperatures at the end of Section I (or at the beginning of Section II) are at the freezing points corresponding to individual initial concentrations. For a fluid with a lower freezing point (i.e. with a higher initial solution concentration), its temperature difference with the refrigerant is smaller (as observed from the measurements), resulting in a lower cooling capacity. In addition, a higher initial solution concentration also leads to a decrease in the length of Section II. As the cooling capacity is much higher in Section II than in Section I due to the involvement of latent, a shorter Section II will reduce the overall cooling capacity too.

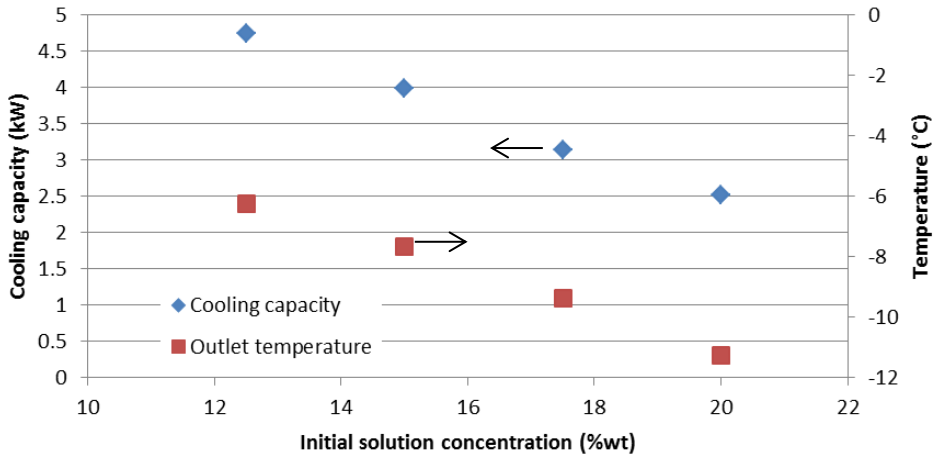

Figure 4.16 Outlet binary ice temperature and cooling capacity against initial solution concentration (weight of ethanol/total solution weight) (design flowrate = 9 Litre/min, design T_e = -20 ℃, design solution concentration at 15% by mass)

5. Development of the overall hybrid model

This chapter presents the establishment of the overall system level model for the entire binary ice system. The ANN modelling of the primary circuit are described in the following two sub-sections; Section 5.1 introduces the basic concept and the modelling tools for the chosen ANN model, followed by the presentation of the training procedures in Section 5.2. Section 5.3 describes the hybrid coupling of the physical model of the scrape surface ice generator in the secondary circuit with the ANN model of the primary circuit. The results of the overall model are then discussed in relation to why a hybrid coupling approach to create the overall system model is needed as well as the associated advantages.

5.1 Establishment of the ANN model

Refrigeration systems are known to be non-linear and of dynamic nature (Haves and Khalsa 2000); binary ice systems are of no exceptions. It is very difficult to set up physical meaningful equations to represent accurately the correlations among all the inter-dependant parameters involved in the system components, in particular the compressor. According to Rasmussen and Jakobsen (2000), the development of a pure analytical compressor model could be impossible. Many existing first principle compressor models (He et al. 1997; Koury et al. 2001) are mainly for design and general control purpose instead of operation monitoring which usually requires much higher accuracy as in fault diagnosis. Therefore it is not practical to develop a pure analytical model for the primary circuit for FDD purpose. As an alternative to the analytical model, black box method based on ANN was employed in this study to simulate the system parameters/indexes of the primary circuit. The model was constructed within the *Matlab* environment using its neural network toolbox (The MathWorks 2010).

To construct an ANN model, the following steps need to be followed:

1. Data collection
2. Create the ANN network
3. Configure the network

4. Train the network including initialization of the weights and biases
5. Validate the network

The data is collected via experiment measurements, which has been discussed in Chapter 3. For Step 2, whether a steady state or a dynamic ANN model should be used will be decided within which further choices are available (e.g. MLP and RBF under steady state, NARX and Auto-Regressive Moving Average under the dynamic category). In addition, the type of the activation function should be chosen; possibilities include Gaussian function, sigmoid function, etc. In this step, various parameters should be examined for their use as input or output parameters, depending on the data availability and the purpose of the simulation. In general, the control variables (e.g. condenser cooling water flowrate) are chosen as inputs and the parameters that are sensitive to faults chosen as outputs for FDD purpose. However, the combinations must be assessed carefully in relation to specific system types and study objectives. The next step is to set up the structure of network, including the number of hidden layers, the number of the neutrons in the hidden layer and the number of the delay steps; the last parameter is needed for dynamic modelling which will be explained later.

Steps 4 and 5 are automatically performed by *Matlab*, though certain default settings can be changed by the users, to achieve for instance a better training time or accuracy. During network training (Step 4), the experimental data are fed into the network to help it adjust the weights in order to match the model output data to the desired values (i.e. the measured outputs). The outcome of the training is validated in Step 5. The network can be trained repeatedly until a user specified accuracy is achieved, and the fully trained model can then be employed to simulate the operation of the system.

5.1.1 Model structure

This section provides more details of Step 2 as how various decisions are made. Chapter 2 reviewed some of the ANN models used by previous researchers for chillers. Two types of ANN model architectures are popular and commonly applied, namely RBF and MLP. The pros and cons of the two types have been discussed also in Chapter 2. On their own, these two architectures are only for static/steady state predictions. However, for the test rig employed in this project, an on/off thermostat

was used to control the compressor capacity, which made it impossible to acquire a real steady state. Therefore a static model based on the averaged value of the data could not fully characterise the system behaviour.

To establish a reliable dynamic model, the Nonlinear Auto-Regressive model with eXogenous input (NARX) (Billings 2013) is widely used to reproduce the process dynamics under various operating conditions because of its high accuracy (Ingrassia and Morlini 2007).

NARX dynamic neural networks have an input vector that contains both lagged input and output values of the dynamic system. The model can be used to predict the current value of a time series data using the past value of the driving (exogenous) time series, as well as the past value of same series that being predicted (Chetouani 2008). It can be defined by the following function *f*:

$$y(t) = f\left(y(t-1), y(t-2), \dots, y\left(t-n_y\right), u(t-1), u(t-2), \dots, u(t-n_u)\right) \quad 5.1$$

where the current value of the dependent output *y*(t) is regressed on previous n_y values of the output *y* and previous n_u values of the independent (exogenous) driving input *u*. In some cases, multiple independent driving data sets can be involved. For example, to predict the binary ice outlet temperature (*y*) of the SSIG, the driving input(s) *u* could be chosen from the binary ice inlet temperature, its flowrate, the evaporating temperature, etc. The NARX model can provide good predictions, because it uses the additional information contained in the previous values of *y*.

The NARX model can be implemented by using a feed-forward neural network (i.e. MLP network) to approximate the function *f*. The term 'feed-forward' means that the connections between nodes only allows signals to be sent in one direction to the next layer of nodes and not back to the previous layer, as illustrated in Chapter 2.

The MLP neural network itself is a static system. When combined with an input structure known as the Tapped-delay-line (TDL), the dynamic characteristics can be incorporated into the system; the overall architecture is referred previously as

NARX. Figure 5.1 shows that the input time series $\boldsymbol{u}$ passes through a TDL with n_u delays. At a certain time t, the output of the TDL is $u(t\text{-}1)$, $u(t\text{-}2)\ldots u(t\text{-}n_u)$.

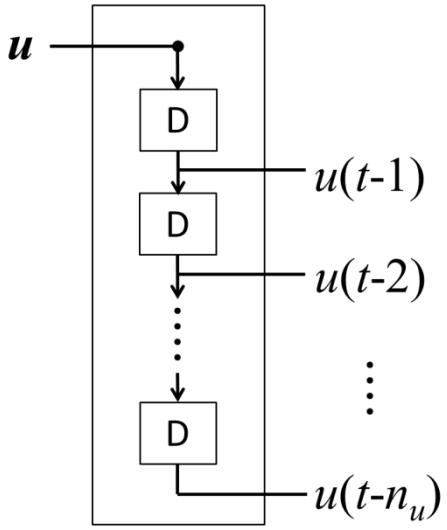

Figure 5.1 Tapped delay line

There are two ways to implement a NARX dynamic network, either as a parallel architecture or a series-parallel architecture as shown in Figure 5.2. The parallel architecture is a recurrent dynamic network where the predicted output of the network is fed back to the input layer, while the series-parallel architecture uses the true measured past output from the system to form part of the input vector of the network instead of feeding back the predicted value.

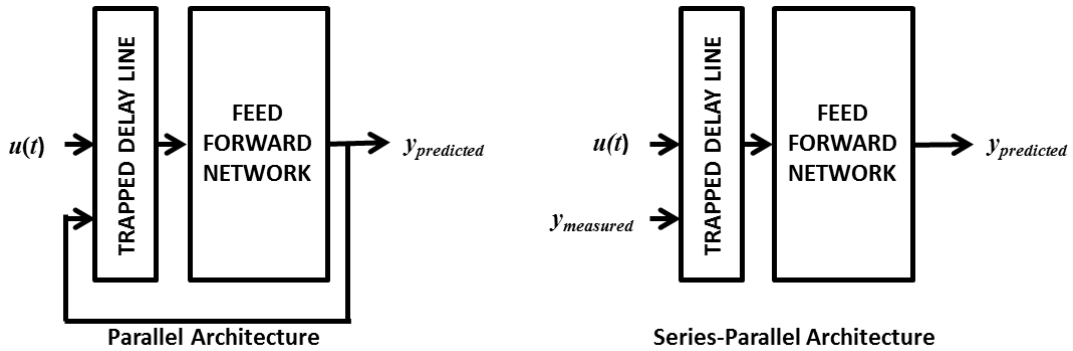

Figure 5.2 Dynamic network structures

For the current study, the series-parallel architecture is chosen because the measured outputs of the system are available. It also has a major benefit over the parallel architecture, i.e. the measured outputs $y(t)$ which are expected to be more accurate than the predicted output in the parallel architecture are available to be fed

into the TDL, resulting in a more accurate final prediction of $y(t)$. Thus the parallel architecture should only be considered when the measured output is not available.

Having determined the basic structure of the network, as part of Step 2, the input and output parameters are chosen carefully. The aim of FDD was to use fewer sensor measurements to detect as many faults as possible. Therefore, a model developed for FDD purpose should use parameters that are easy to obtain from direct measurements and/or from simple calculations and it should keep the number of inputs as small as practically possible. Based on the observations of the measurements in Chapter 3, the parameters describe the condition of the condenser cooling water (i.e. inlet temperature and flow rate) and the secondary circuit operation (i.e. the temperature and the carrier fluid solution concentration of the binary ice at the outlet of the ice generator and the corresponding flow rate) are taken as the inputs to the NARX model.

Theoretically, any parameters can be used as model output due to the fact that black box models discard any physical relationships among the parameters. In this study, the independent variables that can be controlled directly are considered as inputs as described above, while the dependent variables which are sensitive to selected faults are to be taken as outputs, namely the condenser cooling water temperature difference (ΔT_w) which was chosen because it can be influenced by fault such as the cooling water flow reduction. Also as observed in Chapter 3, other outputs parameters that are seen to reflect both normal system behaviours and mal-function operations include the evaporating temperature, compressor power, discharge temperature, condensing temperature, etc. The values of the above parameters need to be measured and used in the training of the ANN model. They may not be monitored for FDD in the later stage.

5.1.2 The application of *Matlab* Neural Network Toolbox

The construction of the NARX model was implemented with Matlab Neural Network Toolbox. The Toolbox offers a number of tools that make it possible to configure (Step 3), train (Step 4) and validate (Step 5) the neural networks. Graphical User Interface (GUI) and the command-line functions are two main tools for the above tasks.

The GUI provides a point-and-click control of the neural network toolbox, allowing the users to setup the network structure with little knowledge of programming language. With the help of GUI, the users can load the input/output data, divide them into three groups respectively for training, validation and testing, and change the proportions of the latter two, choose the number of neurons in the hidden layer and number of delays in the TDL (i.e. the n_u and n_y). The default setting for the training data proportion is set at 70%. GUI also allows users to visualize the training results showing the network response (i.e. the network output) and error (discrepancy between the output and the measured output). Furthermore, the GUI can automatically generate MATLAB scripts (command lines) that allow the tasks to be modified and improved if desired.

In addition, the command lines can be written manually using the command-line function, which gives user more flexibility in terms of choosing certain network parameters/functions such as the transfer function, training function, performance function etc. To make the best use of these two tools, GUI is normally used first to set up the network and automatically generate the scripts as a template, and then the command-line function is used to manually modify the scripts to obtain the desired network. For the current study, mainly GUI was used.

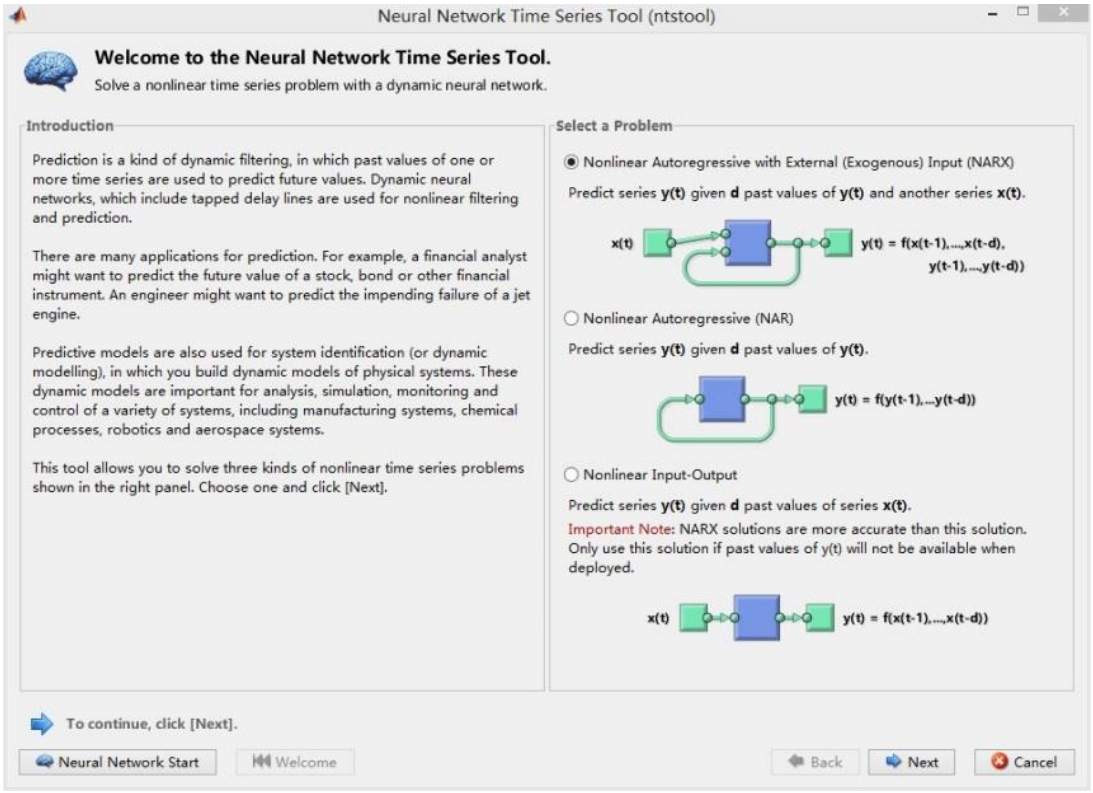

(a)

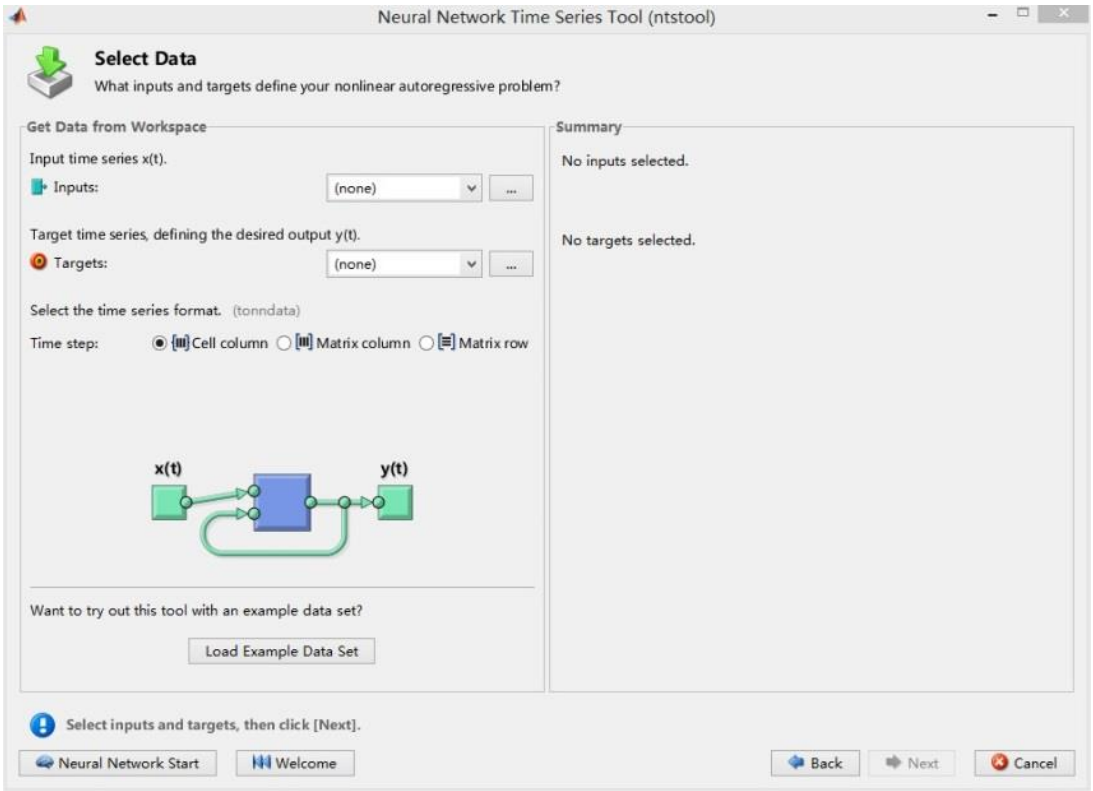

(b)

Figure 5.3 Matlab Neural Network Toolbox GUI
(a) select the network structure, (b) select the input and output data

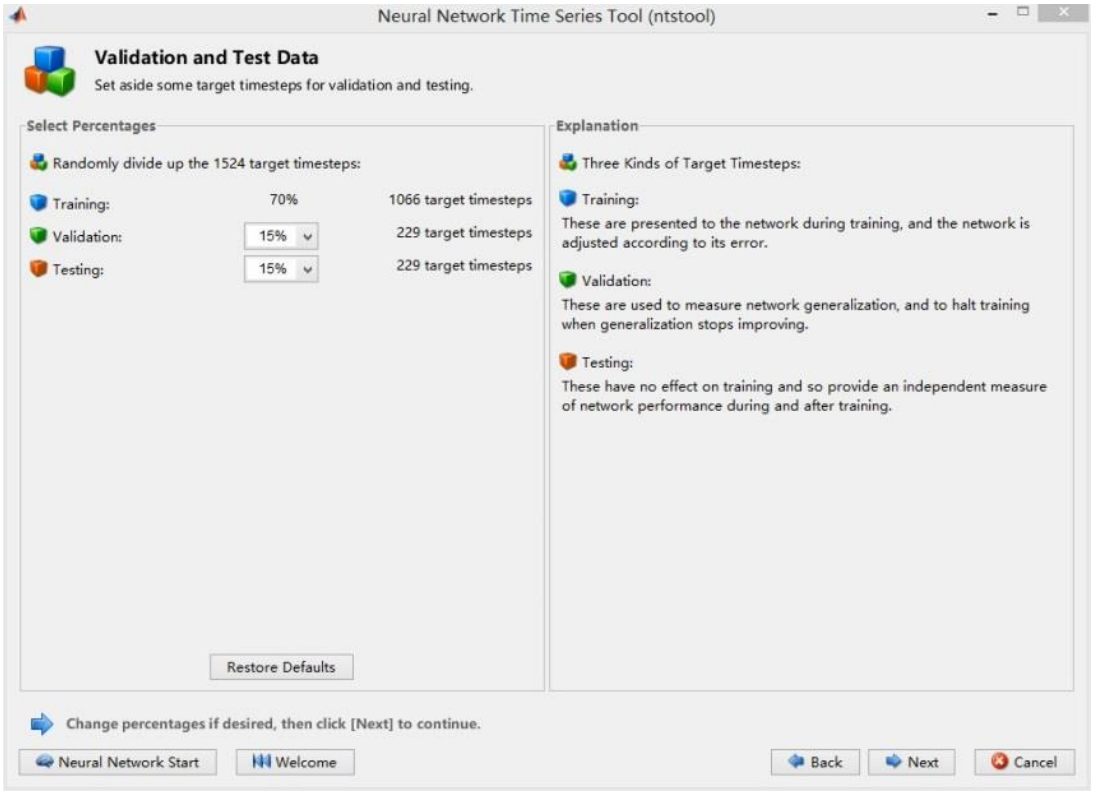

(c)

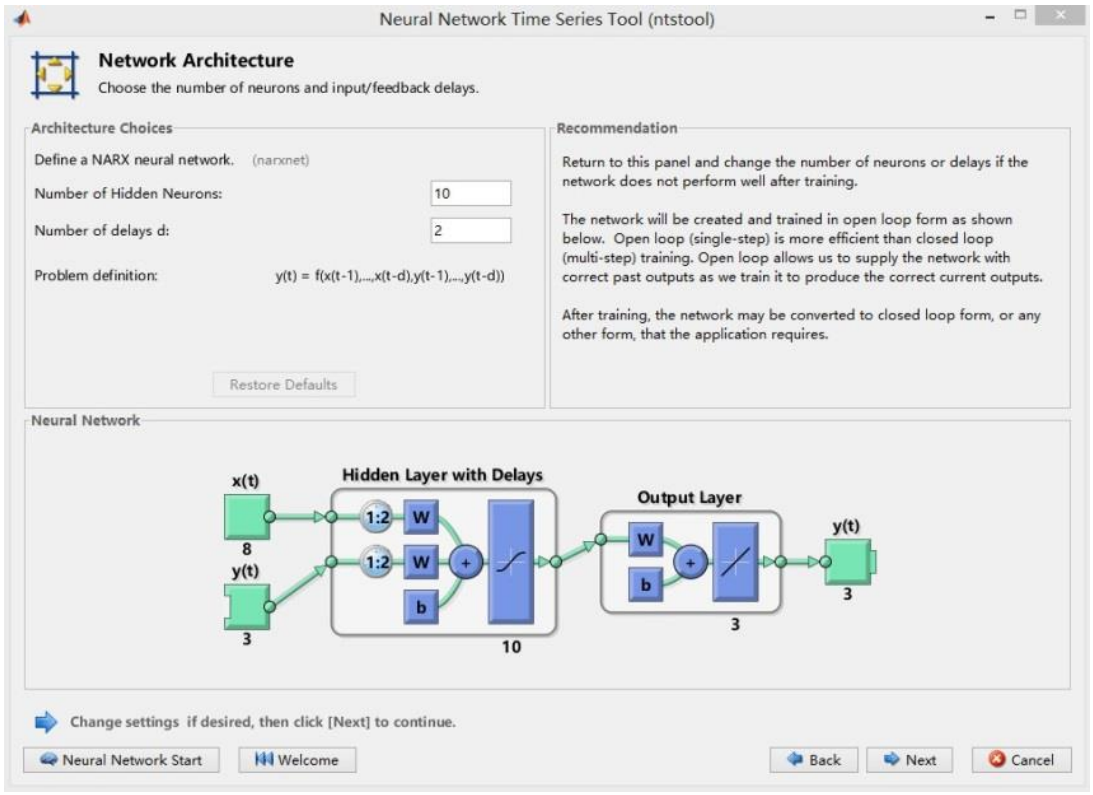

(d)

Figure 5.3 Matlab Neural Network Toolbox GUI (continued)
(c) choose percentage for the validation and testing data and (d) choose the number of neurons and delays.

Figure 5.3 a-d demonstrate the procedures of creating a NARX model using the *Matlab* GUI. The first step is to choose the desired network structure, three structures are available and NARX, as explained previously, is chosen for this study, Figure 5.3(a). The time series of the measured and calculated data of various parameters, originally stored in Excel files in a matrix format (time-step × number of variables), need to be imported to the *MatLab*. As shown in Figure 5.3(b), they can be specified and uploaded as either inputs or target outputs. The user also needs to instruct the GUI whether the time-step is represented by the row or the column of the matrix by selecting the time series format. Among all the data, 70% (by default) of them will be used for model training, the split of the rest of 30% between validation and testing can be varied as shown in Figure 5.3(c). *Matlab* will randomly divide the data into the above three groups each time this process is repeated as requested by the user. The number of neurons in the hidden layer and the number of delay for both $y(t)$ and $u(t)$ in the TDL can then be specified by the user, Figure 5.3(d). The default settings of Matlab for above two parameters are 10 neurons and 2 delays respectively.

A brief description on their setting is given below:

- Number of hidden neurons

The determination of the optimal number of the hidden neurons requires a trail-and-error approach. The users can change the number and select the one that creates the best performance, i.e. with a minimum difference between the model output and the measured output. Adding additional neurons to the hidden layer will generally increase accuracy but also increase the training time, thus a trade-off is needed. Preliminarily observations suggested that the Matlab default setting of 10 hidden neurons provided good accuracy for the binary ice system under investigation. Increasing the number did not increase the accuracy significantly.

- The number of delays

The number of delays is determined by the operating characteristics of the system regarding the time response of the outputs to the variation of the inputs. For binary ice systems, or in general refrigeration systems, the change of the dependent parameters, such evaporating temperature, with respect to the

variations of control parameters, such as cooling water flow rate is slow. Therefore a larger sampling time Δt can be used, and accordingly only a small delay number is needed, as suggested by (Yoon and Lee 2010). Once again, preliminary observations indicated that 2 delays were sufficient to give good accuracy when compared to 3 or 4 delays.

In addition, *MatLab* allows users to choose the transfer function between the input and output layers. The default transfer functions, Tan-sigmoid function in the hidden layer of a dynamic network, and the Linear transfer function in the output layer, are used; as commented by Cybenko (1989) this combination can be used to approximate any functional forms.

5.2 Model training and validation

Having set up the network architecture, the relevant data can be fed into the network for training purpose. This section first explains the data processing and training algorithm of the ANN. The control variables which are selected as inputs and some of the possible outputs are listed. The results of the NARX model were compared with the measured values.

5.2.1 Data pre-processing

Measured data are in different value range. When being used as network input, large value will saturate sigmoid transfer function, resulting in a very slow training progress (Glorot and Bengio 2010). Pre-processing essentially normalise the both input and target output data to within [-1, 1] so to avoid saturation of the transfer function (Chetouani 2008) thus improving the training efficiency of the network. Post processing then transforms the normalised output back to the original data range after model training stage to enable user carry out result comparison.

The data pre-processing is completed by *MatLab* function mapminmax. The normalised value can be calculated as:

$$u_{\mathrm{nor}}(i) = \frac{2\times[u(i)-u_{\max}]}{u_{\max}-u_{\min}} - 1 \qquad 5.2$$

where $u(i)$ is the i^{th} element of the original input/target time series, $u_{\mathrm{nor}}(i)$ is its normalised value, $u_{\max}$ is the maximum value of the time series and $u_{\min}$ is the

minima value. Both the pre- and post-processing are automatically completed by *Matlab* toolbox.

5.2.2 Back-propagation training algorithm

The network training is the procedure of adjusting the weights and bias in order to obtain good simulation accuracy. A performance function can be applied to assess the network accuracy and the Mean square error (mse) is used in this study, defined as:

$$\text{mse} = \frac{1}{N}\sum_{i=1}^{N}\big(y(i) - a(i)\big)^2 \qquad 5.3$$

where $y(i)$ is the training target, $a(i)$ is the network predicted output and *N* is the number of time steps in target/output time series. Network training aims at minimising the mse. The back-propagation training algorithm (Werbos 1974) is one of the most commonly used training and learning mathematical procedure that automatically adjusts the weights and biases of the network. Being a back-propagation algorithm, the trainlm (Levenberg-Marquardt) algorithm (LMA) (Rumelhart et al. 1986) is provided as the default training function in *Matlab*. It is a very fast method, suitable for small networks with less than thousands of weights, hence used for this study.

Back-propagation training is an iterative procedure. The training is carried out in steps as follows:

1. Initialized the weights. Some random numbers between [-1, 1] are automatically generated by *MatLab* toolbox to start with.

2. The weighted input data are forward propagated through the network to the output layer to obtain the network outputs.

3. The outputs are back propagated to the hidden layer to calculate the gradient of the weights.

4. A new weight matrix can be generated by moving the original weights to the opposite direction of the gradient.

5. Use the new weight matrix to replace the original one. Go back to step 2 and repeat the process.

To stop the loop, certain criteria must be fulfilled: i) the value of the performance function is smaller than the pre-set goal, ii) the gradient of the weight is smaller than a certain number or iii) the performance function fails to decrease in a certain number of iterations. If one of the above criteria is achieved, the training is stopped and the appropriate weights which can minimize the network error are considered found.

5.2.3 Data management

Generally speaking, the system parameters can be divided into two groups: the control variable and the internal state (dependent) variables. Control variables are the independent parameters that can be changed by the user directly and are used as inputs to the neural network. Table 5.1 provides a list of the variables and the ranges used in the experiments.

Table 5.1 List of control variables in the binary ice experiments

Control Variable	Physical Meaning	Unit	Range
u_{ice}	Binary ice volume flow rate	L/min	3.5 ~ 11.0 (5 settings)
u_w	Cooling water volume flow rate	L/min	7.1 ~ 10.8 (4 settings)
C_o	Original ethanol solution concentration	%wt	10 ~ 20 (5 settings)
$T_{w,in}$	Cooling water inlet temperature	℃	13.4 ~ 18
$T_{ice,\ in}$	Binary ice inlet temperature	℃	-4 ~ -8

On the other hand, internal state variables which are dependent on the control variables can be used as indicators to the system working conditions, representing the outputs of the model. They are either directly measured parameters or derived performance indexes. Some of the state variables are showed in Table 5.2 and a full list will be presented and their relevance for FDD will be examined in Chapter 6.

Table 5.2 List of internal state variables as the model outputs

State variable	Physical meaning	Unit	Formulation
T_{dis}	Compressor discharge temperature	℃	Measured
T_e	Evaporating temperature	℃	Measured
W	Electrical power consumption of the compressor	kW	Measured
ΔT_w	Cooling water temperature difference	℃	$T_{w,out}$ - $T_{w,in}$
Q_c	Condenser capacity	kW	$u_w \rho_w c_p \Delta T_w$
$T_{c,\ out}$	condenser refrigerant outlet temperature	℃	Measured

The experimental data used in the network training were collected from the test rig described in Chapter 3. All data were recorded with a 10 second interval. Altogether about 100 patterns of fault free data were collected, involving 5 input parameters and one output for each pattern; each network is designed to handle only one output at a time. Typically, each pattern represents 3 on-off cycles of compressor lasting about 30 minutes. Out of these 100 patterns, around 75 of them were sent into the neural network toolbox for training, testing and validation, and the rest were randomly reserved and applied for manual assessment of the model accuracy as presented in Section 5.2.4. Majority of the 100 patterns were for "no ice-in but ice-out" mode of operation, as previously described in Chapter 3. Any manual start-up and shut down data were not used in the model training.

5.2.4 **Results comparison**

This section presents selective data from the primary circuit when applying different cooling water and binary ice flow rate, keeping the temperature set points for the cooling water and binary ice, as well as the load constant. The influences of the variations of the several control parameters on the selected system outputs are described. The recorded data are also compared with the NARX model predictions to demonstrate the prediction accuracy.

During the tests, the original ethanol solution concentration remained unchanged at 15%wt The temperature of the cooling water was controlled by an external cooling unit that was not included in the NARX model, and was set at 15 ℃ with a +2 ℃ differential, giving a corresponding actual inlet cooling water temperature variation between 13.8 and 17.5 ℃ in a cyclic manner. The compressor was controlled by a thermostat detecting the temperature of binary ice at the ice generator inlet, which was set at -7 ℃ with a +2 ℃ differential, corresponding to a temperature variation between -7.6 and -5 ℃.

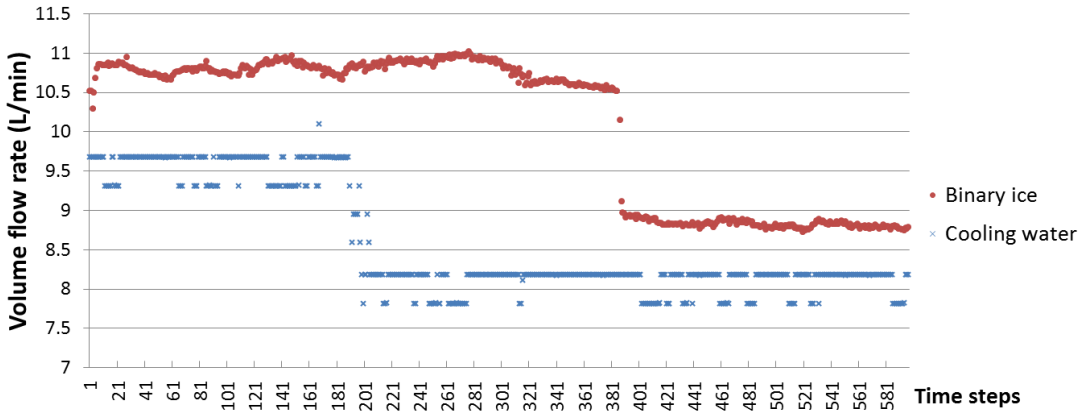

(a)

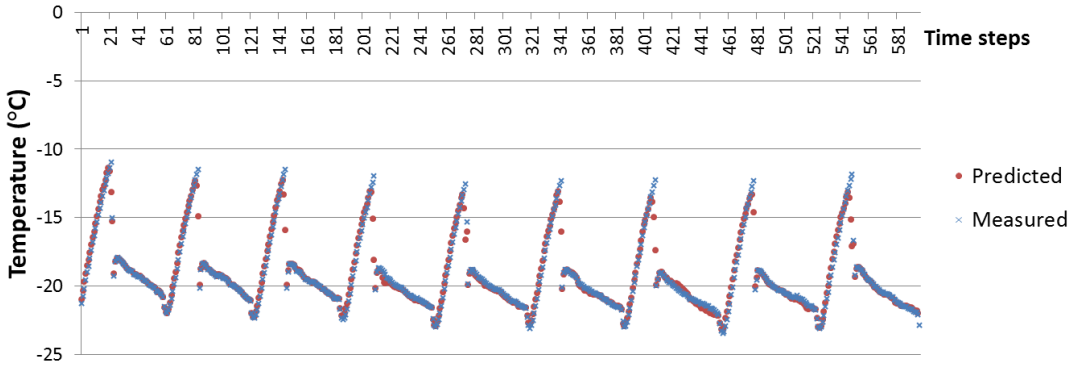

(b)

Figure 5.4 Comparison of NARX model prediction with measurements
(a) variations of cooling water and binary ice flow rates, (b) comparison of predicted and measured evaporating temperature

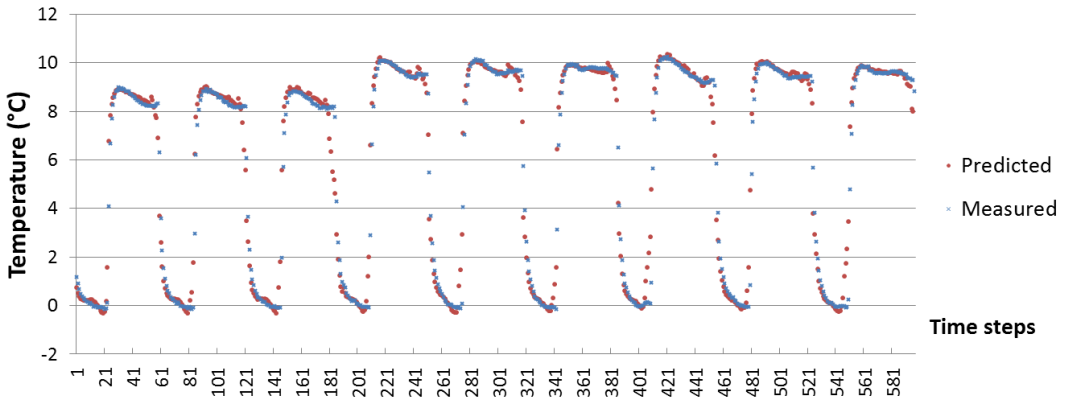

(c)

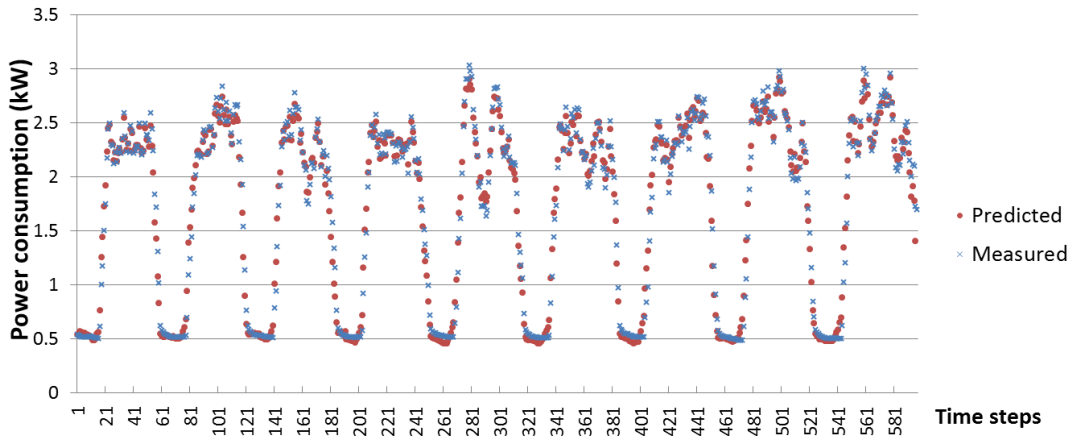

(d)

Figure 5.4 Comparison of NARX model prediction with measurements (continued)
(c) comparison of predicted and measured cooling water temperature difference and (d) comparison of predicted and measured compressor power consumption

Figure 5.4a shows three patterns (each lasted about 200 time steps, representing about three compressor on-off cycles) of the cooling water and the binary ice flow rates which were adjusted. The initial part of the data representing the system start-up period was not included. The time step 1 represents the moment when the compressor was switched off by the thermostat. The flow rates were kept steady at the beginning for around 200 time steps (10s per step), and the cooling water flow rate was reduced for the next 200 time steps, followed by a reduction of the binary ice flow rate for the last pattern.

Figure 5.4b, 5.4c and 5.4d compare the predicted parameters with the experimental data and good prediction accuracies were obtained in general. Figure 5.4b shows the prediction of evaporating temperature T_e. Regarding the accuracy of model prediction, the coefficients of determination (R^2) is 0.95. Errors mainly occur

at the compressor restart point. The cooling water temperature difference ΔT_w are shown in Figure 5.4c. The predictions of ΔT_w had the best accuracy among the three parameters showed here, R^2 is 0.99. In Figure 5.4d compressor power W consumption is displayed, showing a residual power rating of about 0.5 kW. The predicted W has a R^2 value of 0.98.

Overall it can be shown that the ANN NARX for the primary circuit is capable of predicting the transient data well with very good accuracy, except when the moments when the compressor was cycled on or off.

5.3 Hybrid model coupling

As discussed in Chapter 2, both analytical models and black box models have their limitations. The above black box model for the primary circuit is easy to setup and can provide good simulation results. However, it can only predict the parameters that are available from measurements or relatively simple calculations. Due to the unavailability of certain measuring equipment in the current project, some parameters that are important for FDD were not measured (e.g. refrigerant mass flow rate), and due to the unique characteristic of binary ice system, some parameters cannot be directly calculated through the measured data (e.g. ice concentration, carrier fluid concentration and ice generator cooling capacity).

In practice it is also unlikely that a refrigeration system will have flow meter to measure the refrigerant flow rate or will have a calibrated conductivity meter to monitor the solution concentration in real time. These parameters are all related to binary ice system performance/operation and can be potentially used as FDD parameters. Therefore, a pure black box model to include both the primary and the secondary circuits may not have sufficient numbers of output for FDD purpose, thus a hybrid model coupling a black box model with an analytical model is proposed in this study.

Generally, when coupling two models together, it involves identifying the following:

1. The models to be coupled
2. The coupling interface
3. The relevant control and dependent variables (i.e. the inputs and outputs parameters respectively)

For the current project, the two models involved are an analytical SSIG model and a NARX model for the primary refrigerant circuit of the system. The coupling interface is taken as the physical interface where the primary and secondary refrigerant circuits are linked, i.e. the entries to the ice generator for both the primary refrigerant (T_e) and the binary ice ($T_{ice,in}$).

There are two ways to couple the two models. The first was by sharing their inputs. The parameters describing binary ice status, which are the original solution concentration C_o, the inlet temperature $T_{ice,in}$ and the volume flow rate u_{ice}, are fed into both models as inputs, because they are linked to the operation of both primary and secondary circuit directly.

The second way is to loop an output from one model to become an input of the other. During the development of the SSIG model, an assumed evaporating temperature was employed as a model input. However, T_e is a function of the load for a given system, and therefore it is an output parameter of the primary circuit. As a result, the two models are coupled by using the T_e from the ANN of the primary circuit as an input to the mathematical model of the SSIG.

Occasionally, the calculation of certain parameter requires outputs from both of the models. For example, to calculate system COP, the evaporator capacity and the compressor power consumption are needed. So W is also sent to the analytical model as a coupling parameter. The coupled model is shown in Figure 5.5.

The main benefits of adopting the loop approach are: 1. The model is now capable of predicting some un-measurable variables, such as COP which could be an index for FDD. 2. The robustness and performance of the resulting FDD technique can be improved, as some of the SSIG model inputs are taken from the ANN model instead of from the sensors, such as T_e and W. This is because in order to obtain the

fault free predictions for FDD, the inputs to the SSIG model need to be fault free as well. When a fault occurs, if the SSIG model takes the measured faulty T_e and W as inputs, its outputs cannot be regarded as fault-free, thus they are not capable of being applied as benchmarks for fault detection. Instead, the T_e and W predicted by the ANN model are fault-free even under faulty conditions. When they are fed into the SSIG model, fault-free predictions can be made.

Therefore, combining the analytical SSIG model with the NARX black box model is expected to give a better accuracy when compared to a full analytical model.

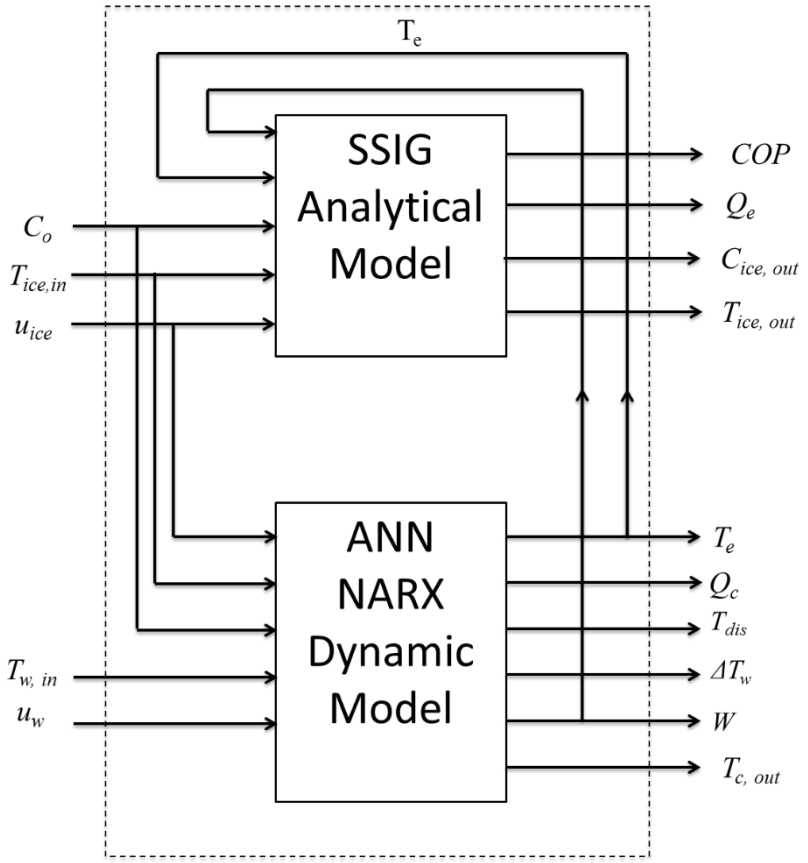

Figure 5.5 The coupling of SSIG and ANN model

5.4 Results and discussion

The output data of the hybrid model could be divided into two groups, one was directly from the ANN model (e.g. T_e, Q_c, T_{dis}, etc.) and the other group was from the analytical model (e.g. $T_{ice,out}$ and $C_{ice,out}$). The validations of the former were discussed in Section 5.2.4 and this section only discussed the validation of the second group.

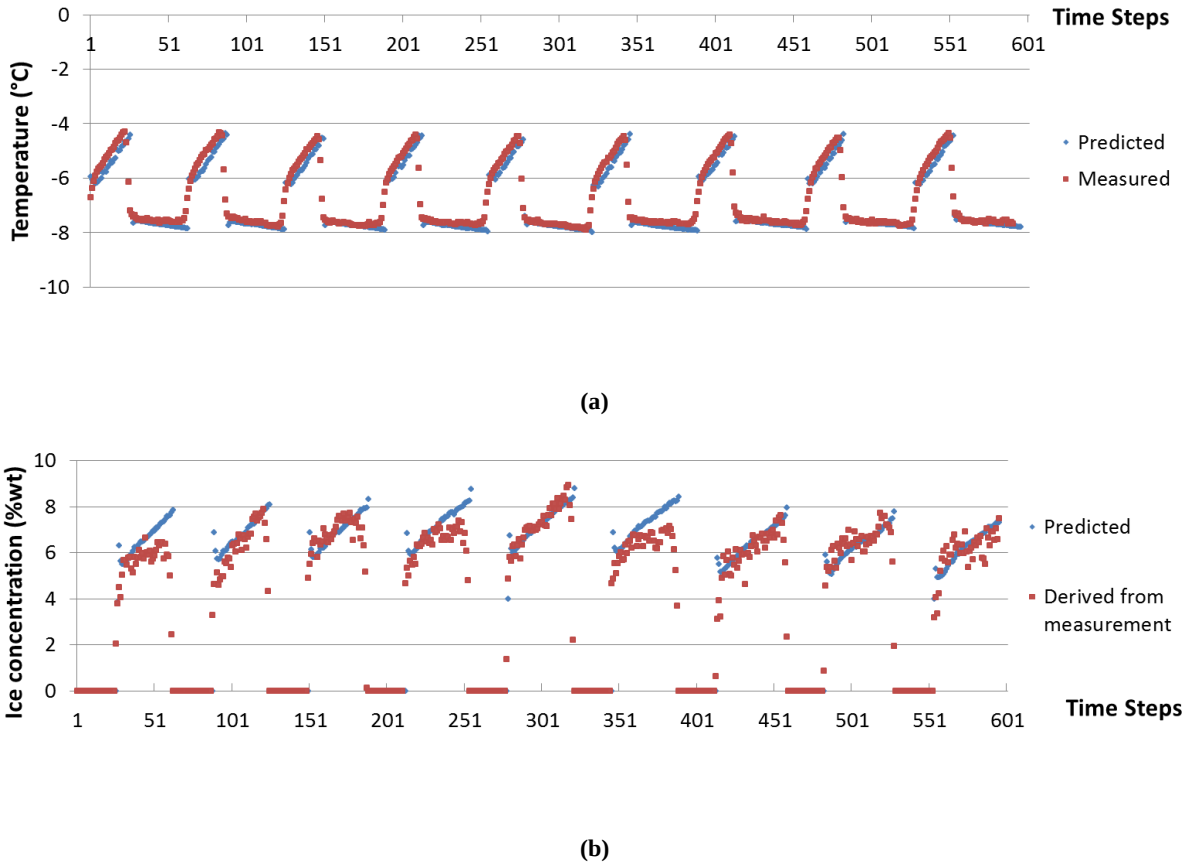

Figure 5.6 Hybrid model prediction validation, (a) comparison of predicted and measured binary ice outlet temperature, (b) comparison of predicted and derived (from measurement) outlet ice concentration

Figure 5.6 presents sample results of the hybrid model. The data was taken from the same tests described in Section 5.2.4. The predicted evaporating temperature showed in Figure 5.4b was used as input to the analytical mode. Figure 5.6a displays both predicted and measured temperatures of binary ice at the outlet of the ice generator, Figure 5.6b presents the corresponding ice concentrations. When the compressor was off, cooling capacity was very close to zero, therefore no ice was produced. The binary ice outlet temperature increased significantly until it reached the high setting of the thermostat and triggered on the compressor. Then the binary ice

temperature dropped below its freezing point instantly. During the cooling process, the ice concentration raised steadily, while the temperature decreased in a small range along with the cooling capacity.

The coefficients of determination of the hybrid model outputs for the binary ice outlet temperature and ice concentration were 0.82 and 0.83 respectively, which were lower compared to the corresponding R^2 of the analytical model (0.85 and 0.90 respectively). However, when both models were validated using data taken from a reduced cooling water flow tests, the R^2 values for the analytical model dropped to 0.78 and 0.75 (reasons as explained in Section 5.3), whereas the R2 values stayed the same for the hybrid model. Therefore, it would appear reasonable and logical to use the hybrid model to generate fault free predictions.

6. Faults detection and diagnosis

This chapter will first analysis the influence of the selected faults on various parameters of the binary ice system. This is followed by a discussion on how the parameters, including several derived ones such as the cooling capacity of the SSIG, are identified to allow comparisons between predicted and measured/derived values, for the purpose of generating residuals. The sensitivity of the parameters to different faults will be examined.

Next, appropriate thresholds of the residuals to distinguish a faulty condition from a normal one are determined. A control chart algorithm, i.e. CUSUM test (Page 1954; Hinkley 1971; Basseville 1986; Schein and House 2003), is applied here for the dynamic fault detection. A rule based algorithm is then set up for the fault diagnosis. The latter aims at reducing the number of sensors needed to a practical minimum while being able to diagnose faults in an efficient way.

Most existing FDD methods only focused on single fault detections. However multiple faults could take place at the same time, and this makes FDD more challenging. Some studies on multiple faults are to be included in this research to highlight some of the technical challenges such as establishing whether more than one fault exists. In addition to single fault analysis, three sets of double faults were considered: a set which consists of two randomly chosen faults, a set in which two faults appear to have opposite effects on certain parameters and a final set in which the faults will have similar impacts on certain system parameters.

6.1 Faults and their influences on the binary ice system behaviour

In order to detect a fault, the impacts of the fault on the system behaviour/performance must be examined systematically and carefully. Prior to attempting a fault detection, there must be a clear definition of the ‘fault-free’ condition. Table 6.1 lists selected faults and the settings of the relevant control variables used in the tests. When the system is running with the nominal design values, the system is defined as fault-free, while all other combinations of values represent

some kind of faults, except that both the load and the cooling water temperature were fixed in the study.

The levels of the faults are differentiated by the degrees of deviation of the actual values from the nominal ones; a larger deviation suggests a more severe fault (i.e. a higher fault level, e.g. Level 3 for cooling water flowrate reduction). Three levels of faults had been introduced for cooling water and binary ice flowrate reduction, while two levels of faults had been simulated for either the solution concentration increase or decrease. As for the scraper fault, both the scenarios of a completely broken blade (i.e. only one blade left for providing the scraping action) and the scraper motor failure were considered in this study.

Table 6.1 Values of the control variables under both fault-free and various levels of faulty conditions

Fault	Control variable	Nominal Value (normal operation)	Severity Level		
			1	**2**	**3**
Cooling water flowrate reduction	Cooling water flowrate V2	10.8 l/m	9.6 l/m	8.1 l/m	7.0 l/m
Binary ice flowrate reduction	Binary ice flowrate V1	9 l/m	7.5 l/m	6.3 l/m	5.2 l/m
Solution concentration increase	Initial solution concentration C_o	15% wt.	17.5% wt.	20% wt.	-
Solution concentration decrease	Initial solution concentration C_o	15% wt.	12.5% wt.	10% wt.	-
A broken SSIG scraper	Experimentally simulated by switching on/off the scraper motor at a fixed time intervals	motor always on	Only one completely broken blade is considered and was simulated by 20/20 seconds on/off cycles.		
Scraper motor failure	Stop the motor	Motor on	Motor off		

Figure 6.1 demonstrates the mechanism of residual generation. The nominal values of the control variables in Table 6.1 are used as default parameters and conditions of the hybrid model. The corresponding outputs represent the fault-free predictions; the validations have already been shown in Chapter 5. They will then be compared with either the direct measured parameters or the parameters derived from the sensor measurements.

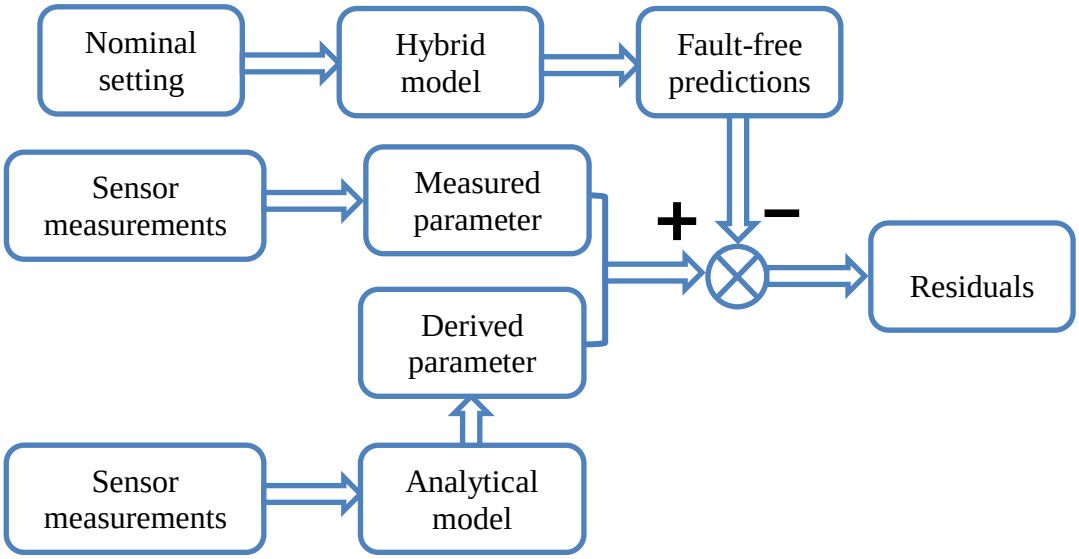

Figure 6.1 The generation of residuals

Table 6.2 listed some of the derived parameters which have been commonly applied by other researches in chiller FDDs. It is worth noting that only the ones that can be determined by simple calculations are listed in the table. Other parameters such as the solution concentration and ice concentration at the outlet of the SSIG need to be obtained using the analytical model. Other direct measured parameters have already been listed in Chapter 4. The table also includes the estimated errors/uncertainties of the derived parameters, as calculated by the error propagation equation (Clifford 1973). Taking a derived parameter $N = f(a, b, c, \ldots)$ for example, where $a, b, c, \ldots$ are independent measurements, its absolute error $|\Delta N|$ can be expressed in Eq. 6.1, as

$$|\Delta N| = \left|\frac{\partial f}{\partial a}\right| \Delta a + \left|\frac{\partial f}{\partial b}\right| \Delta b + \left|\frac{\partial f}{\partial c}\right| \Delta c + \cdots \qquad 6.1$$

where Δa, Δb and Δc are the absolute errors of the measurements a, b and c respectively. These errors are needed for the calculation of the sensitivity factor in Equation 6.2.

Table 6.2 Errors of derived parameters

Parameter	Equation	Estimated Error
Degree of superheat (℃), ΔT_{sh}	TR2 - Saturation temperature	± 2.5 ˚C
Binary ice temperature difference (℃), ΔT_{ice}	TB1-TB2	± 1 ˚C
Degree of sub-cooling (℃), ΔT_{sc}	Saturation temperature - TR6	± 2.5 ˚C
Degree of discharge super heat (℃), $\Delta T_{sh,dis}$	TR5 - Saturation temperature	± 2.5 ˚C
Condenser cooling water temperature difference (℃), ΔT_{water}	TW2-TW1	± 1 ˚C
Condenser capacity (kW), Q_c	V2$\rho_w Cp_w$(TW2-TW1)	± 0.9 kW

Table 6.3 Observed dynamic variations of evaporator and condenser parameters under faulty conditions with the corresponding sensitivity factor in brackets

	Parameter \ Fault		Binary ice reduction (Level 3)	Cooling water reduction (Level 3)	Solution concentration increase (@20% wt)	Solution concentration decrease (@12.5% wt)	A broken scraper (motor off time 50%)	Scraper motor failure
Evaporator	T_e [℃]	On	↓(-1.2)	↓↓(-4.9)	↓↓(-5.3)	-	↓↓(-4.3)	↓↓(-8.3)
		Off	-	↓↓(-5.6)	↓↓(-5.1)	-	↓↓(-3.0)	
	ΔT_{sh} [℃]	On	-	↓↓(-0.3)	-	-	↓(-0.2)	↑↑(0.3)
		Off	-	↓(-0.8)	↓(-0.8)	↓(-1.2)	-	
	p_e [bar]	On	↓(-0.2)	↓↓(-0.8)	↓(-0.7)	-	↓(-0.7)	↓↓(-1.5)
		Off	↓(-0.06)	-	-	-	-	
	Q_e [kW]	On	↓↓(0.3)	-	↓(0.6)		↓↓↓(0.4)	↓↓(0.2)
		Off	-	-	↓		-	
Condenser	$\Delta T_{sh,dis}$ [℃]	On	↑↑(0.8)	↑↑↑(2.4)	↑↑(0.7)	↑↑(3.6)	↓↓(-1.1)	↓↓↓(-4.6)
		Off	-	↑(0.9)	-	↑↑(1.9)	-	
	$T_{c,out}$ [℃]	On	↑(0.4)	↑↑(5.7)	↓(-1)	↓(-0.4)	↓(-1.0)	↓↓(-5.3)
		Off	↓(-1.6)	↑(2.9)	↓(-3.3)	↓(-2.2)	↓(-1.4)	
	ΔT_{sc} [℃]	On	-	↑↑(0.3)	-	-	↓↓(-0.2)	↓↓↓(-1.3)
		Off	-	-	↑↑(0.07)	↑(0.3)	-	
	ΔT_{water} [℃]	On	-	↑↑(2.6)	↓(-1.0)	↓(-1.2)	↓(-0.5)	↓↓(-2.5)
		Off	-	↑↑↑(0.7)	-	↓(-0.1)	-	
	p_c [bar]	On	-	↑(4.9)	↓(-0.4)	↓(-0.2)	↓(-1.4)	↓↓(-6.9)
		Off	-	↑(1.3)	↑(0.4)	↓(-0.4)		
	Q_c [kW]	On	-	↓(-0.4)	↓(-0.2)	↑(0.02)	↓(-0.3)	↓↓↓(-1.0)
		Off	↓↓(-0.05)	↑↑(0.1)	-	-		

Table 6.4 Observed changes in the average values of compressor & system and ice generator parameters under faulty conditions with corresponding sensitivity factor in brackets

	Parameter \ Fault		Binary ice reduction (Level 3)	Cooling water reduction (Level 3)	Solution concentration increase (@20% wt)	Solution concentration decrease (@12.5% wt)	A broken scraper (motor off time 50%)	Scraper motor failure
Compressor & system	T_{dis}[℃]	On	↑↑(0.8)	↑↑(19.0)	↑(2.6)	↑↑(17.7)	↓(-7.8)	↓↓(-34.9)
		Off	-	↑(7.5)	-	↑(8.6)	↓(-1.6)	
	W [kW]	On	-	↓(-5.7)	↓(-9.8)	↓(-15.6)	↓↓(-33.2)	↓↓(-45.8)
		Off	-	-	-	-	-	
	COP	On	↓(0.3)	↓(0.2)	↓(0.5)	↓(0.8)	↓↓(1.3)	↓↓(1.6)
		Off	↓(0.1)	↓(0.2)	↓(0.2)	-	-	-
	Duration* (s)	On	↑	↑↑	↑	↑	↑↑	N/A
		Off	↑	-	-	-	-	-
		Total	↑	↑	↑	↑	↑↑	-
Ice generator	$T_{ice,out}$[℃]	On	↓(-0.5)	-	↓↓(-3.6)	↑↑(2.4)	↑(1.2）	↑↑↑(7.7)
		Off	↓(-1.0)	-	↓(-0.8)	↑(0.3)	-	-
	$T_{ice,in}$[℃]	On	-	-	-	-	-	↑↑(3.6)
		Off	-	-	-	-	-	-
	ΔT_{ice}[℃]	On	↑↑(0.4)	-	↑↑↑(1.75)	↓↓(-1.3)	↓↓(-0.4)	↓↓↓(-2.0)
		Off	↑↑↑(0.4)	↑(0.08)	↑↑↑(0.4)	↓↓(-0.2)	-	-
	C_{out}[%wt]	On	↑(0.4)	-	↑↑05.8)	↓↓0-3.3)	↓(-0.8)	↓(-0.8)
		Off	-	-	↑↑f6.9)	↓↓9-3.1)	-	
	$C_{ice,\ out}$ [%wt]	On	↑↑(0.2)	-	↓↓(0.6)	↑↑(0.3)	↓↓↓(-0.3)	↓↓↓(-0.3)
		Off	-	-	-	-	-	-

**Same durations are observed for all the parameters listed in Tables 6.3 and 6.4.*

In Table 6.3 and Table 6.4 the changes in the average values during both the compressor on- and off-cycle durations, as well as the sensitivity factors (in brackets) of certain derived and measured parameters under the five specified faulty conditions are presented. The parameters are separated into 4 groups, relating to the evaporator, condenser, compressor & system level and the binary ice generator respectively. The relative impacts on the parameters are illustrated qualitatively by the direction and the number of the arrows, whilst a "-" represents no noticeable changes; essentially the larger the numbers of arrows, the greater the percentage changes of the parameters caused by the faults.

In general, parameters with large percentage changes are chosen to be employed for fault detection. However, for certain parameters that have small absolute values, a small change in their value would lead to a large percentage variation. These small changes in certain occasions could be even smaller than the measurement uncertainties/errors, making the detections of the associated faults difficult should they be chosen as a possible detection parameter. Particularly in the current research,

the value of the binary ice temperature difference (ΔT_{ice}) is small (typically ~2 ℃). A residual (~ 0.4 ℃) caused by a small fault could lead to a large percentage change (i.e. 3 arrows). With a measurement uncertainty of ± 1 ℃ for ΔT_{ice}, this suggests that the residual of ΔT_{ice} is not significant enough to indicate a fault, and more importantly percentage changes may not be an appropriate indication whether a parameter is suitable or not to be used for FDD.

Instead of using the percentage changes, the sensitivity factor *S* (Comstock et al. 2002a) is considered a more appropriate indication; it is essentially a signal-to-noise ratio, as expressed:

$$S = \frac{Residual\ of\ a\ parameter\ at\ the\ highest\ fault\ level}{Maximum\ uncertainty/error\ of\ the\ parameter} \qquad 6.2$$

The corresponding sensitivity factors are also presented in Tables 6.3 and 6.4. The uncertainties needed in the calculations were taken from Table 3.3 in Chapter 3 and Table 6.2. A large sensitivity factor means that the given parameter is more sensitive to the occurrence of the fault; therefore, it is more likely to be selected to detect the fault.

The influences of the above listed parameters to individual selected faults are examined below.

- **The binary ice flowrate reduction**

The temperature difference of the secondary fluid is one of the most common parameters used in detecting a secondary flow reduction according to published literatures. However, in the current study, the change of binary ice temperature difference (ΔT_{ice}), i.e. the residual, is very small (0.4 ℃, even for the severity Level 3). Combining with the uncertainty in the temperature measurement, the resulted small sensitivity factor of 0.4 suggests indeed that it is not suitable for fault detection. Contrary to the conventional chiller behaviour, most of the parameters do not seem to have significant variations (sensitivity factor mainly ranging from -0.5 to +0.5) under the reduced binary ice flowrate, with only three exceptions observed to have a relativity large sensitive factors during the compressor on cycle; these are the evaporating temperature (-1.2), the discharge super heat (0.8) and the discharge temperature (0.8).

- **Cooling water flow reduction**

A reduction in cooling water flow rate is known to have larger influences on the parameters on the condenser side rather than on the evaporator side, regardless whether it is a binary ice system or a chiller, suggesting similar FDD approaches could be adopted. The experimental observations showed a good agreement with other researchers in terms of response behaviour. It is noted that the cooling capacity stays constant when the cooling water flowrate drops. This is because the condenser is oversized; it is adequate to remove the heat absorbed by the evaporator even under a reduced flowrate. Most of the condenser parameters are sensitive to the change of cooling water flowrate, with sensitivity factors ranging from -5.7 to 19, suggesting it has a large impact on the discharge temperature (T_{dis}) and the power consumption of the compressor (W).

- **Initial solution concentration increase or decrease**

The change of initial solution concentration has influences on many parameters of both the primary and the secondary side of the system, as shown in Tables 6.3 and 6.4, respectively. In general, one would expect the influence on certain parameters due to concentration increase is the opposite of that caused by a concentration reduction, as reflected by the parameters associated with the ice generator in Table 6.4. However, from a closer examination of Tables 6.3 and 6.4, some of the parameters have the same directional changes at certain concentrations both below and above the nominal concentration at 15% wt. For instant, the T_{dis} was found to increase when the solution concentration is raised from 15% to 20% as well as when the concentration is reduced from 15% to 12.5%. This could be explained by the fact that when the solution concentration is increased up to a particular level, no ice can be produced, assuming the set point remained unchanged; the SSIG essentially behaves like a chiller. This obviously affects how certain parameters vary.

In addition, if the solution concentration drops too much, then for a given temperature set point, the compressor will never cycle off and ice will be continuously produced. Eventually, there will be an ice-in and ice-out mode of the SSIG operation and the ice concentration will continue to increase and the flow to drop, leading eventually to a flow stoppage. This is encountered when the solution concentration is dropped to 12.5%wt. To avoid the flow stoppage, the measurements were made by

resetting the set point from -5 ℃ to -3 ℃, and this could result in some of the variation patterns noted.

Furthermore, based on the sensitivity factor, it was also observed a parameter suitable for detecting a concentration decrease may not be suitable to detecting an increase, depending on the magnitudes of the concentration changes, e.g. $\Delta T_{sh,dis}$.

- **Broken scraper and motor failure**

The SSIG used in this study has two spring loaded blades 180 ° apart. There are several possible cases regarding blade breakage/operation. 1) One blade is either partially or totally broken, leaving part of the surface scraped with half of the scraping frequency by the other blade. This is likely to occur at the outlet end of the SSIG as the blades are subject to more mechanical wear and tear. 2) There could be problems with the spring loading/setting which causes the blades to loss physical contacts with the inner surface of the SSIG resulting in a permanent thin layer of ice between the scraping blades and the surface. Binary ice can still be produced if the gap between the blades and the inner surface is small. However, in an extreme condition, the gap may become too large for the ice thickness to fill depending on the T_e, resulting in no scraping action at all and the binary ice production ceases. 3) Both blades are completely broken with no scraping action at all. This is expected to have, to a large extent, a similar consequence as having a very large gap in the second case. 4) Scraper motor failure in which the blades are not rotating; this is also expected to produce similar results as Case 3, though in this case, the agitation caused by any rotating elements within the SSIG would be completely absent.

Essentially all the above cases can be divided into two situations: one still has binary ice production capability and the one without. As previously mentioned, only two scenarios involving (i) a completely broken blade (i.e. only one blade left for providing the scraping action) and (ii) the scraper motor failure are considered in this study; the former represents a fault with binary ice production and the latter without.

In the present setup, it is practically difficult to take out any blades from the SSIG, and thus an approach was “invented” to experimentally simulate scenario (i), i.e. a completely broken blade, by switching the SSIG motor according to certain on/off schedules, e.g. a complete breakage of one blade could be achieved by

switching periodically half of the motor time off. The feasibility of this idea or the validity of this logic could be assessed by first obtaining some analytical results reflecting the above scenario, and comparing with measured results. Some representative analytical results are presented in Figure 6.2 and Figure 6.3.

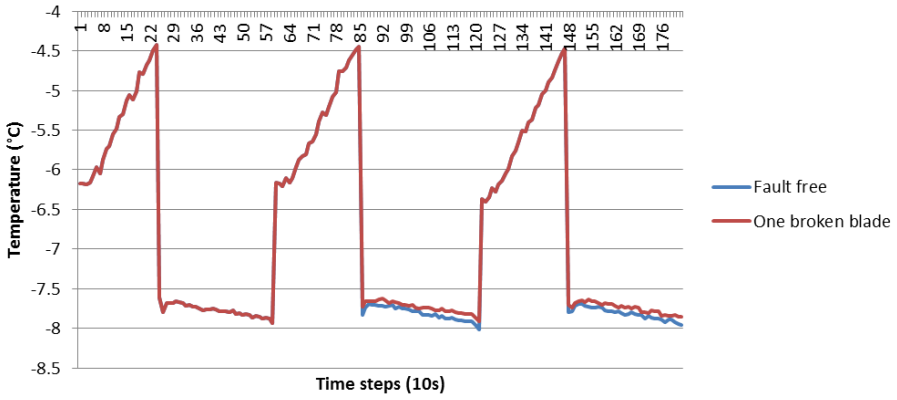

Figure 6.2 Simulated binary ice outlet temperature under fault free and one broken blade conditions

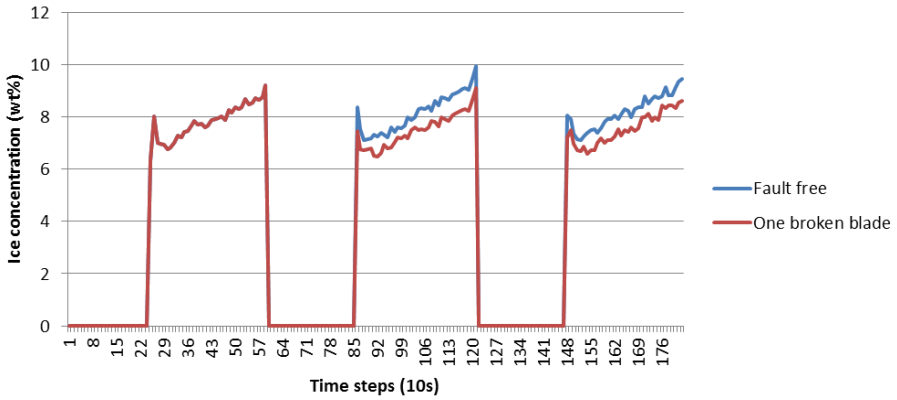

Figure 6.3 Simulated binary ice outlet ice concentration under fault free and one broken blade conditions

The mathematical simulation of scenario (i) was performed under some initial assumptions. First, both the evaporating temperature and the compressor cycle duration remained unchanged, not influenced by the faults. In reality, the T_e is expected to be lower than the fault-free value due to the increased thermal resistance, and the cycle duration is expected to increase due to reduced system capacity. However, it is possible to refine/improve the simulation at a later stage by using the measured values of T_e and cycle duration. Second, no partial blade breakage is encountered. In Figure 6.2 and Figure 6.3, the simulated outlet temperature and ice concentration of the binary ice mixture over 3 cycles are presented for fault free and

faulty operations. The faults were introduced at the start of the second cycle. The same fault free measured parameters (i.e. evaporation temperature, initial solution concentration and binary ice flowrate) are used as inputs for the simulation.

It can be seen that at the beginning of the second cycle when the compressor is off (~time step 57 to 85), the fault has no influence on the outlet conditions of the binary ice. When the compressor is re-started at time step of around 86, the fault results in a higher temperature and a lower ice concentration respectively, relative to the fault free condition. This is due to a thicker ice layer cumulating on the SSIG inner surface, thus increasing the overall thermal resistance. The temperature differences between faulty and fault free conditions are rather small (~ 0.2 ℃).

For the comparison, four tests were carried out with different off/on schedules of the blade motor including 10s/30s, 20/20, 10s/10s, and 30/30. The intervals are chosen as a compromise between not too long to protect the blade and not too short to protect the blade motor. The results of Test 1 and 2 are presented in Figure 6.4, as they both have the same total motor off/on cycle duration of 40 seconds.

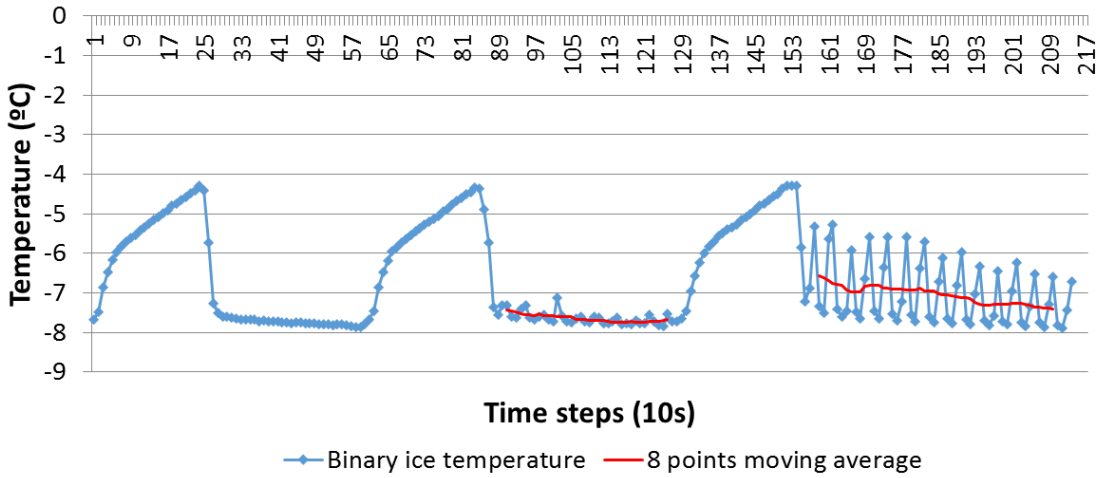

(a)

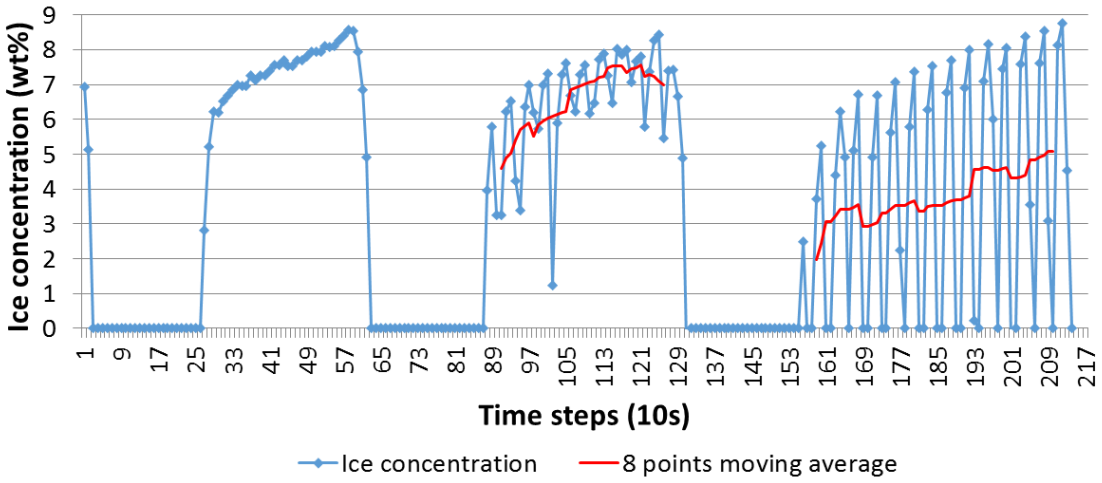

(b)

Figure 6.4 Measured output of the faulty blade Tests 1 and 3. (a) binary ice temperature at the SSIG outlet, (b)ice concentration at the SSIG outlet.

In Figure 6.4, three compressor cycles are shown. The first cycle is fault free, with the blade motor rotating all the times. The second cycle is for Test 1 (i.e. 10s on/30s off) and the third cycle is for Test 3 (i.e. 10s on/10s off). The periodic off/on switching of the blade motor resulted in the oscillations of the binary ice outlet temperature as well as the ice concentration. When the blade is stopped, no scraping was taken place, the ice accumulated on the surface increased the thermal resistance. In addition, the lack of agitation reduced the heat transfer coefficient significantly, hence an increase in the outlet temperature of the binary ice due to reduced cooling and a decrease in the ice concentration. As the blade stopped for a longer duration in

test 3, the outlet temperature of binary ice is higher than in test 1, and as expected the magnitudes of oscillations of the two parameters are much bigger too.

The measured (oscillating) results cannot be directly compared with the results in Figure 6.2 and Figure 6.3, nor can they be used directly for fault detection, as they are generated in a unique experimentally simulated condition. Therefore, an 8-point average is used to obtain the "modified" measured results as the orange lines shown in Figure 6.4a and Figure 6.4b; it is clear they share a very similar trends with the previous mathematical simulations (Figure 6.2 and Figure 6.3) for a broken blade, i.e. the average binary ice outlet temperatures are higher and the corresponding ice concentration is lower than the fault free values. Therefore, one could argue that the motor on/off switching method can be interpreted as an alternative way to experimentally create a broken blade scenario, but it is necessary to establish an appropriate off/on schedule as well as a suitable total duration.

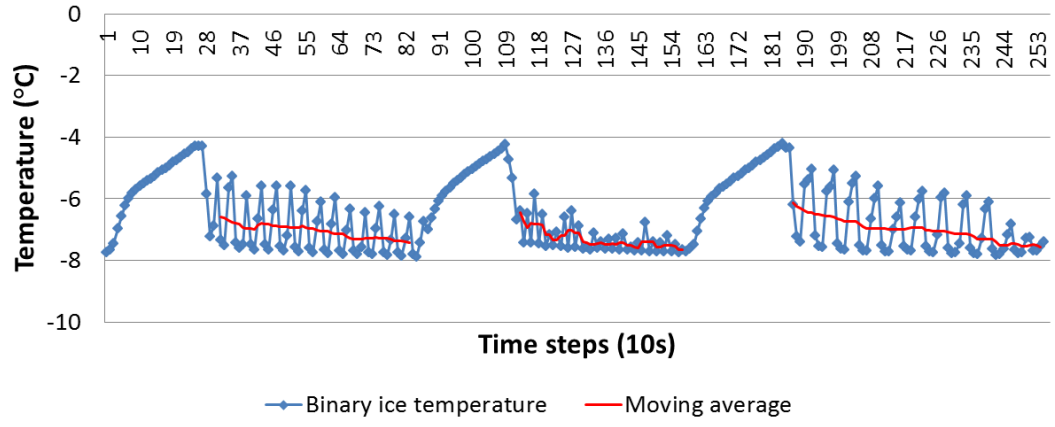

(a)

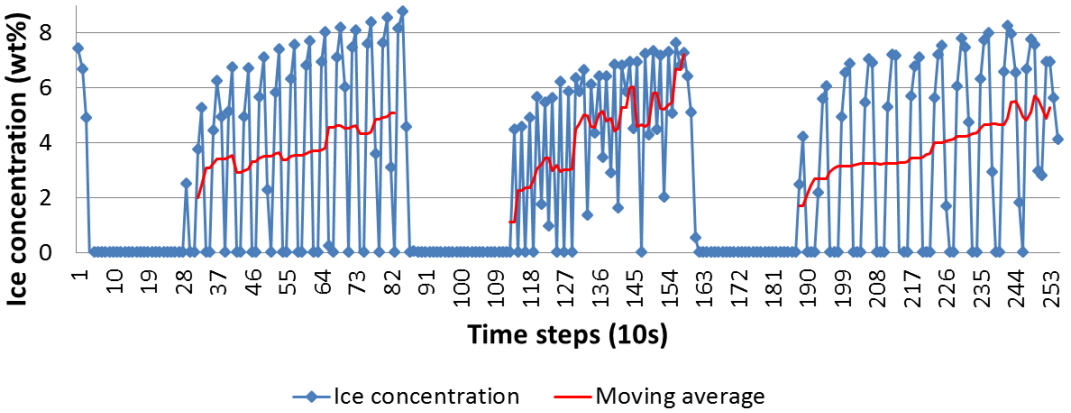

(b)

Figure 6.5 Measured output of the faulty blade Test 3, 4 and 2 a) binary ice temperature at the SSIG outlet, b)ice concentration at the SSIG outlet

Figure 6.5 demonstrates the SSIG outlet binary ice temperature and the ice concentration for again three compressor cycles (time step 1~73, 74~160 and 161~253). The SSIG blade motor off/on schedules (Test 3: 10s/10s; Test 4: 30s/30s; Test 2: 20s/20s respectively) are all having the same 50% off/on proportion but with different total cycle durations from 20s to 60s. It can be seen that the compressor stays on for a longer time when the motor off/on switching is less frequent (i.e. Test 4), and at the same time, the binary ice temperature rose and its ice concentration dropped when compared to a more frequent off/on schedule (i.e. Test 3), as a result of the increased thermal resistance. As expected, the magnitudes of the oscillations also became larger when the motor overall cycle duration is increased. In general, it is

observed that while keeping the same off/on proportion, an increase in total motor off/on duration has a very similar effect as increasing the off duration proportion while keeping the total cycle duration unchanged.

When choosing the appropriate blade motor off/on schedule, all the modified test results are compared with the mathematical simulations in Figure 6.2 and Figure 6.3. The simulations shows that the increase in the binary ice temperature when the one of the blades is broken is rather small, which should also be reflected closely by the modified measured results. Among all the tests, the 10s/10s and 10s/30s motor schedules appear to be suitable in terms of the magnitudes of changes. However, as the motor switching was carried out manually, it is practically difficult to have accurate switching timing when involving short switching intervals such as 10s, causing irregular oscillation pattern as seen in the first cycle in Figure 6.5 and also leading to rather unstable moving point averaging. As a result, the 20s/20s schedule was chosen as a compromise between having a close match with simulated results and avoiding irregular oscillations. When analysing the measured data in Figure 6.5, 2- to 12-point moving averages have been trialled and the best fitted curves are chosen for individual off/on schedules. Therefore, in this study, a broken blade fault is to be experimentally simulated by switching the blade motor with an off/on schedule of 20s/20s coupled with an 8-point moving averaging.

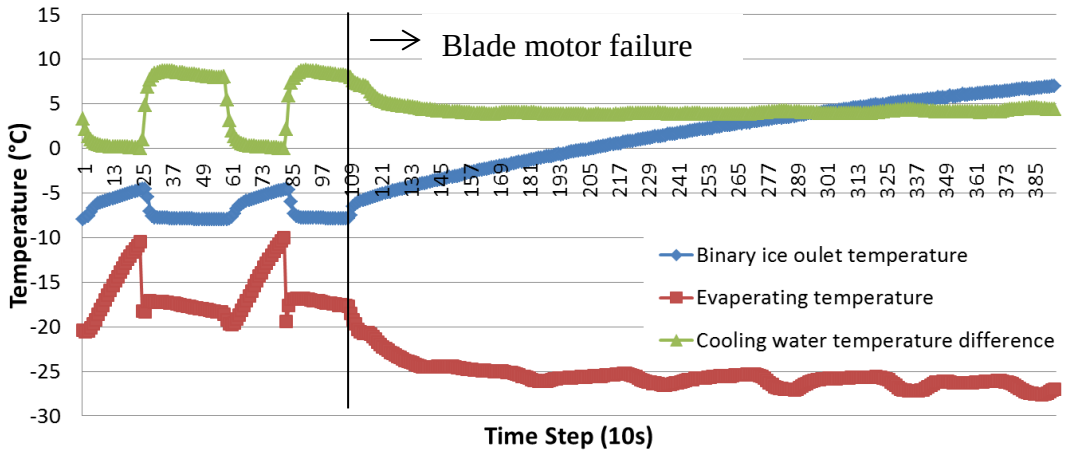

Figure 6.6 Variation of some of the parameters in the binary ice system after a SSIG blade motor failure

For the blade motor failure (scenario ii), the hard fault can be experimentally simulated by switching off the scraper motor thus stopping all scraping actions. (Note: the motor must not be switched back on until all the ice has melted to avoid blade damage!). During the test, the system was allowed to run for at least a complete compressor cycle under fault-free condition before a scraper motor failure occurred (by turning off the blade motor) in order to generate a set of fault free measurements for comparison purpose. Figure 6.6 demonstrates the change of the binary ice outlet temperature, evaporating temperature and the cooling water temperature difference, before and after the motor failure which took place at time step 108, i.e. near the middle of the second compressor on-cycle.

When the ice thickness gradually built up after the blades had been stopped, the cooling capacity of the system momentarily dropped below the 2 kW heater load inside the tank. Therefore the outlet solution temperature of the SSIG kept increasing, though the rate of its increase is decreasing, and the compressor stayed on all the times as it was not capable of bringing down the solution temperature in the tank to the set point. The temperature difference between the evaporator and the solution gradually increased to restore the thermal equilibrium between the load and capacity. Therefore, the binary ice outlet temperature would eventually be stabilised at a higher temperature (around 10 ℃) and the ice thickness inside the SSIG would stop increasing.

It appears that several parameters could be used to detect this fault. The evaporating temperature decreased to below its normal operating temperature of around -20 ℃ to -27 ℃. The cooling water temperature difference also dropped by about 5 ℃, as less heat was rejected by the condenser under the reduced cooling capacity. The variations of some other parameters under this fault are also included in Table 6.3 and 6.4; as observed, many of them are very sensitive to this fault, so it would be detected relatively easily.

It is clear from Table 6.3 and 6.4 that how individual faults influence the system parameters differently. For binary ice flow reduction, the most sensitive parameters are the discharge temperature and the evaporating temperature. For reduced cooling water flow, its temperature difference between the condenser inlet

and out let, as well as the capacity of the condenser, are the most influenced. As a result, it is possible to find a unique pattern for each kind of fault.

6.2 Development of the fault detection approach

In order to detect a fault, three main tasks are involved, as presented in the following sub-sections. First is to find out the suitable parameter(s) that can be applied as the fault indicators. This step is closely related to the influences of the faults on various system parameters discussed in the previous section and will be described in Section 6.2.1. Second is to monitor the residuals of the chosen parameters; a monitoring method called CUSUM test (Page 1954) is used for the dynamic FDD of the binary ice system in this study, as presented in Sections 6.2.2 and 6.2.3. The final task (Section 6.2.4) is to determine the appropriate threshold that triggers the fault alarm; a demonstration on the application of CUSUM test is also given.

6.2.1 Selection of fault detection parameters

The selection of the parameters used for fault detection was based on Table 6.3 and Table 6.4. In an ideal situation, one would like to identify a single parameter that is sensitive to all of the selected faults, thus reducing the complexity of the fault detection process. In order to reduce the detection time, this parameter should also be sensitive to the fault regardless whether the compressor is running or not. In reality, one would try to employ as few as practically possible the number of parameters needed.

Among all the parameters listed in Table 6.3 and Table 6.4, the evaporating temperature T_e is noted to be sensitive to all the specified faults, during the compressor on-cycle. Additionally, the condenser cooling water temperature difference ΔT_{water} was selected, due to the fact that most of the faults, except binary ice flow reduction, were found to have an influence on it even during the compressor off-cycle. Unlike some of the previous works where the temperature difference of the secondary fluid was applied as fault indicator (Rueda et al. 2005; Ertunc and Hosoz 2006), the binary ice temperature difference in this study would not be suitable as reflected by its low values of sensitivity factor for most of the faults. Therefore it is not suitable to be selected as a fault detection parameter.

Having identified the two parameters for fault detection (T_e and ΔT_{water}), the detection relies on the monitoring of their residuals as a function of time. Several different kinds of methods for detecting changes have been developed by previous researches, e.g. generalized likelihood ratio (Willsky and Jones 1976), statistical process control (Oakland 2008), filtered derivatives detectors (Basseville and Benveniste 1983), etc. Basseville and Benveniste (1983) compared some of the techniques and concluded that the CUSUM test is one of the best for dealing with noise/disturbance in the signal for the following reasons.

1. Optimality of minimizing the delay for detection for a fixed false alarm rate
2. Robustness to disturbance and noise, especially when the noise to signal ratio increases
3. More efficient in tracking changes in the relevant parameters.

Other researchers including Box and Ramirez (1992) and Basseville and Nikiforov (1993) had further improved the CUSUM test in terms of robustness and fault detection speed. Chetouani (2008) had successfully demonstrated its application in real-time process monitoring of a dynamic FDD system. Therefore, in this study CUSUM test is applied.

6.2.2 CUSUM test

CUmulated SUM (CUSUM) test is a statistical quality control method applied in sequential analysis (Chetouani 2008). It aims to detect the changes in the mean of a time series prediction $y(t)$, as in the case of dynamic system modelling. In fault detection, it is often used as a part of the real time detection tool to track the changes of the residuals (Schein and House 2003). The reasons that the CUSUM test was involved in addition to directly employing the residuals are 1) to reduce false alarm rate and 2) to enlarge the deviations between the measured and the predicted values by accumulating their differences.

The residual between the measured and predicted parameters should be in theory very small under fault free conditions. However, any noises, disturbances, measurement and modelling errors may increase the residuals even under fault free conditions and this would cause a false alarm depending on the threshold setting. CUSUM test serves to reduce the frequency of the false alarm.

In a fault detection scheme, the residual r(t) between the measured and the predicted parameters is defined as:

$$r(\mathrm{t}) = y(\mathrm{t}) - \hat{y}(\mathrm{t}) \tag{6.3}$$

where y(t) is the measured parameter and $\hat{y}(\mathrm{t})$ is the fault free prediction, r(t), y(t) and $\hat{y}(\mathrm{t})$ are all time series. Meanwhile, the residual r(t) can also be expressed as

$$r(\mathrm{t}) = \mu(\mathrm{t}) + \varepsilon(\mathrm{t}) \tag{6.4}$$

where $\varepsilon(\mathrm{t})$ is the Gaussian noise with variances of $\sigma^2$and $\mu(\mathrm{t})$ is the mean value defined by

$$\mu(\mathrm{t}) = \begin{cases} \mu_0 & \text{if t} \leq \tau - 1 \\ \mu_1 & \text{if t} \geq \tau \end{cases} \tag{6.5}$$

A fault occurred in the system at the τ^{th} time step. μ_0 is the mean value of the residual before the fault and μ_1 is the mean value after the fault. It is assumed that only the mean values of the residuals are changed due to the fault and the fault has little influence on the noise levels. In practice, μ_0 is usually known from fault free residual data analysis.

The method aims at detecting a possible jump of $\pm$ ½δ on either side of the mean value μ_0, where δ is a pre-specified threshold, namely an increase to (μ_0+δ/2) or a decrease to (μ_0-δ/2), and two separate conditions for triggering the alarm can be applied:

For an increase in the mean value of the residual,

$$\begin{cases} U_0 = 0 \\ U_n = \sum_{t=1}^{n} \left(y(\mathrm{t}) - (\mu_0 + \frac{\delta}{2}) \right) \\ m_n = \min(U_t)\ (1 \leq \mathrm{t} \leq n) \\ \text{Alarm when } U_n - m_n > \lambda \end{cases} \tag{6.6}$$

and for a decrease in the mean value of the residual,

$$\begin{cases} T_0 = 0 \\ T_n = \sum_{t=1}^{n} \left(y(\mathrm{t}) - (\mu_0 - \frac{\delta}{2}) \right) \\ M_n = \max(T_t) \ (1 \leq \mathrm{t} \leq n) \\ \text{Alarm when } \ M_n - T_n > \lambda \end{cases} \qquad 6.7$$

where U_n and T_n are the cumulative sums for the increase or decrease of the mean value and λ is the statistical threshold. The selection of δ is usually related to the standard deviation of the data set under fault free condition and λ can be chosen based on the desired detection speed and the false alarm rate (Chetouani 2008).

In order to understand the applications of CUSUM test and the interpretation of the results from the current dynamic on-off cycles, some artificially predicted and measured parameters are generated so that the exact characteristics of the residual patterns can be studied and understood.

Six different cases are examined representing various combinations of fault free and faulty conditions; each case, all having the same step function, consists of 6 cycles of a predicted parameter, say temperature values, i.e. 15 data points at 5 ℃ and 10 data points at 0 ℃, to represent the on-off nature of the binary ice system, as shown in Figure 6.7. The individual patterns of the measured values are described as follow and it is believed that they cover all the likely combinations of possible scenarios of residual variations. The corresponding average values of the residuals of each case are shown in Table 6.5.

Table 6.5 Average value of the residuals

Cycle number	Cycle 1		Cycle 2		Cycle 3		Cycle 4		Cycle 5		Cycle 6	
	On	**Off**	**On**	**Off**	**On**	**Off**	**On**	**Off**	**On**	**Off**	**On**	**Off**
Case 1	-0.02	0.02	-0.01	0.09	0.00	0.00	-0.07	0.02	0.03	-0.03	0.06	0.05
Case 2	0.01	-0.02	0.71	0.68	0.73	0.71	0.70	0.71	0.66	0.69	0.70	0.72
Case 3	0.00	0.03	-0.72	-0.73	-0.68	-0.70	-0.71	-0.67	-1.02	-1.03	-0.98	-1.00
Case 4	-0.02	-0.01	0.56	0.01	0.62	0.01	0.73	-0.03	0.98	0.01	0.97	0.03
Case 5	0.03	0.00	0.58	-0.62	1.02	-0.99	1.04	-0.99	0.61	-0.63	0.01	0.03
Case 6	0.02	-0.02	0.13	0.23	0.39	0.61	0.74	0.87	1.11	1.21	1.31	1.54

Case 1: The measured values are artificially generated such that the residuals are small. The average values of the residuals for individual on-off sections are very close to zero, typically representing fault free conditions. Two random data points were deliberately set to have a larger residual.

Case 2: The first cycle remains as fault free as in Case 1. Faulty conditions are introduced from cycle 2, with similar positive residuals for all the on- and off-sections for the rest of the 5 cycles.

Case 3: Negative residuals are introduced for cycle 2 to cycle 6, with a larger magnitude for the last two cycles, equivalent to the fault getting more severe.

Case 4: The measured values are "generated" in such a way that they mimic the situation when the fault only impact on the parameter during the compressor on-period, as observed in the study. The residuals are increasing during on-cycle as the fault becomes more severe, with an average of around 0.6 for cycles 2 and 3, around 0.7 for cycle 4, and around 1.0 for the last two cycles, whereas the residuals always remain small during off cycle periods.

Case 5: The on-cycles are set to have positive residuals whilst the off-cycles are set to have negative ones with the same magnitude. The magnitude of residual is increased from around 0.6 in Cycle 2 to around 1 in Cycles 3 and 4, then drops back to around 0.6 in Cycle 5, and assuming the fault disappears in the last cycle. This may be useful in detecting temporary faults.

Case 6: The residuals increase gradually and progressively for both the on- and off- periods

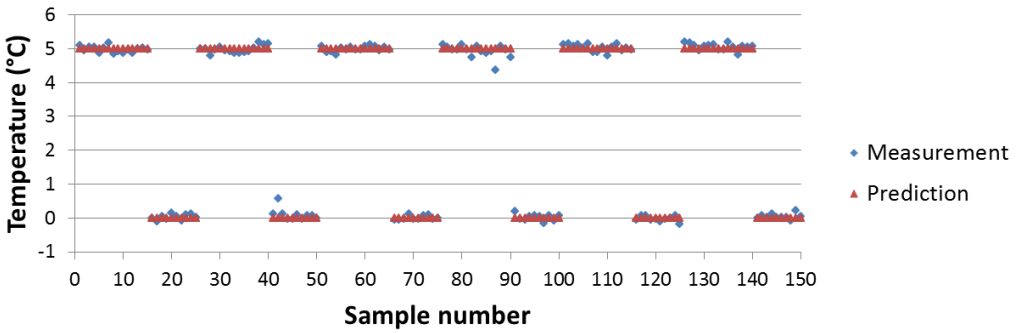

(a) Case 1

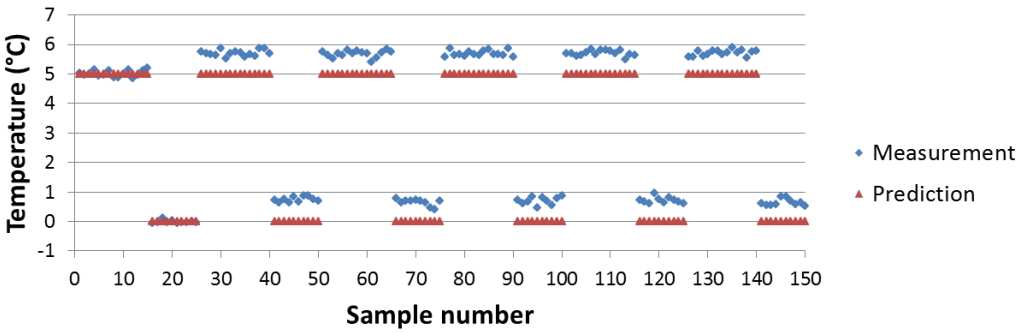

(b) Case 2

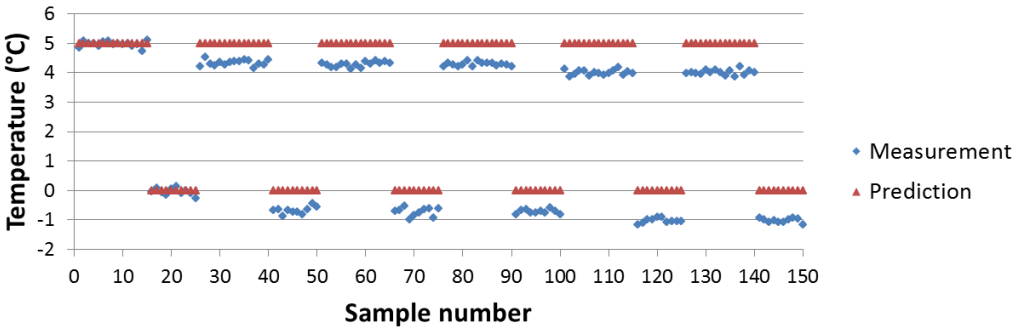

(c) Case 3

Figure 6.7 Fictitious generated model prediction and measured data under various fault-free and faulty patterns.

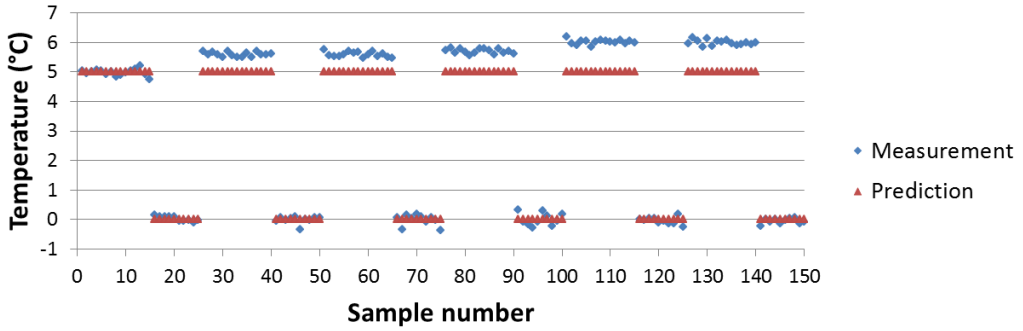

(d) Case 4

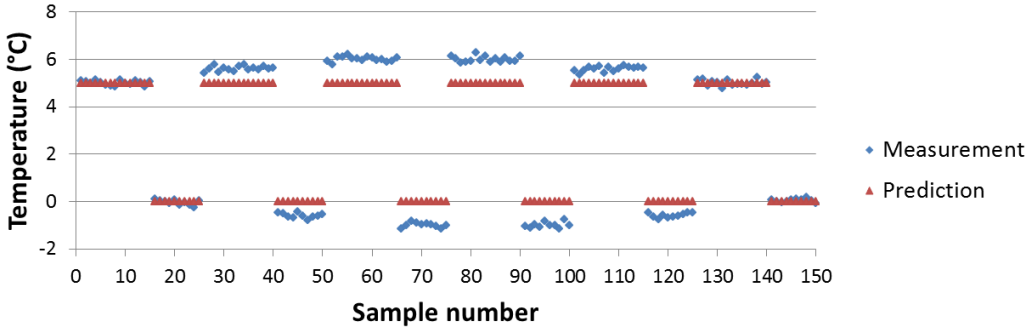

(e) Case 5

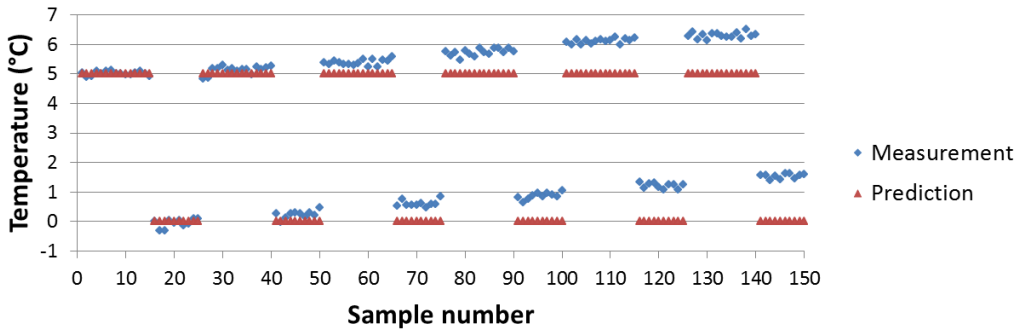

(f) Case 6

Figure 6.7 Fictitious generated model prediction and measured data under various fault-free and faulty patterns (continued).

CUSUM tests are performed on the residuals data of the above cases. Average value of the fault free residuals (μ_0) should be close to zero. In the current analysis, μ_0 is chosen to be 0. For the CUSUM, $\delta/2$ is set at 0.5. For each of the 6 Cases, two tests (U_n-m_n, T_n-M_n) corresponding respectively to increasing (positive residuals) and

decreasing (negative residuals) directions are carried out simultaneously. All the CuSum results are shown in Figure 6.8.

In Case 1, two data points are deliberately set to fall outside the $\delta/2$ of ±0.5 (i.e. data point 42 and 87 in Figure 6.7a). Two spikes have been detected as shown in Figure 6.8a in the corresponding positions. These would appear as isolated incidences, such as one off signal interference, and since majority of the residuals are close to zero and the CUSUM test results were not accumulating, they should not be identified as a fault, as expected for Case 1.

As the residuals in Case 2 stay at a positive constant value of around 0.7 in the last 5 cycles for both on and off periods, the CUSUM output (U_n-m_n) in the increase direction rises steadily, implying the likelihood of a fault. As expected the output for the decrease direction remains at zero since no negative residuals are present. In Case 3, as the residuals are having negative values, T_n-M_n increases gradually, also implying the likelihood of a fault as similar to Case 2. An increase in the severities of the fault in cycle 5 and 6 is introduced and hence a faster accumulating effect (or a steeper gradient) is noted.

In Case 4, since only the on-cycle periods are set to have positive residuals and the off-cycle periods are set to have close to zero residual, naturally T_n-M_n will have only zero output. From the start of Cycle 2 (sample number 26), U_n-m_n starts to increase due to positive residuals but starts to drop during off cycle period when very small residuals are encountered; eventually U_n-m_n drops back to zero again. This suggests that the fault can only be detected during on cycles. This pattern repeats for the 3rd cycle as they have the same residuals behaviour. As the fault severity increases, a higher peak value of U_n-m_n is noticed in the 4th cycle (sample number 76), resulting in a longer time needed for it to drop back to zero value, when compared to the two previous cycles. The last two cycles are set to have the same residual (~1) which are larger than that of the previous 3 cycles, representing an even more severe fault. U_n-m_n are found to reach such a high value in the 5th cycle that it is not able to return to zero during off-cycle period and hence U_n-m_n increases further during the last cycle, making the fault more detectable.

In Case 5, the 2nd on-cycle has the same rising trend of U_n-m_n values as in the 2nd on-cycle of Case 4, but as it has a negative residual for the off-cycle, it has a faster drop of the U_n-m_n back to zero value. When the residuals are increased to 1 in the 3rd cycle, the U_n-m_n values achieve the same peak value as that of the 5th cycle in Case 4 as they both have the same residuals. However, once again due to the negative residuals during the off cycle part of the 3rd cycle in Case 5, the U_n-m_n values are able drop back to zero without further accumulating. This is different from the situation of the last two cycles in Case 4 where the U_n-m_n values accumulate to a higher peak. Essentially, that makes fault detection easier in Case 4 when there are no negative residuals to cancel out the accumulating effect. In other words, once the U_n-m_n values drop back to zero, they will not be able to assist the detection of the subsequent faults. The pattern of T_n-M_n is similar to U_n-m_n, only the maximum values for individual peaks are smaller, as only fewer data points are included in the off-cycle.

In Case 6, positive residuals appear during both on-cycle and off-cycle periods, and their values increase steadily from the beginning of the 2nd cycle. The CUSUM test however, only manages to show an increase in U_n-m_n at sample number 66, i.e. nearly at the middle of the 3rd cycle. The delayed detection is due to the setting of $\delta/2$, suggesting the setting of an appropriate $\delta/2$ is crucial for early detection.

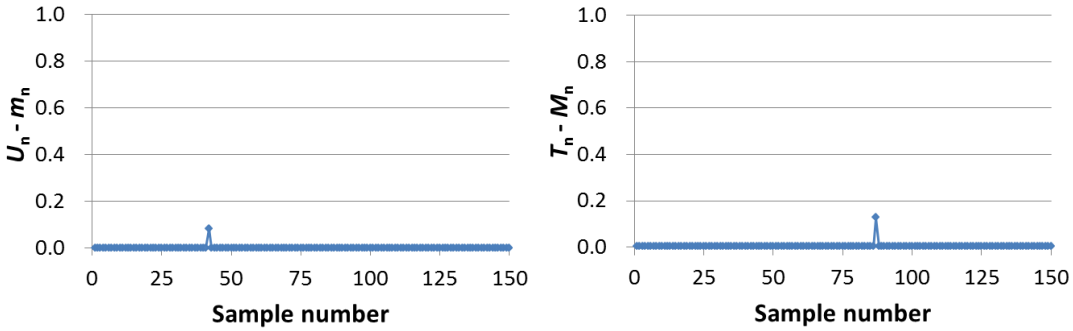

(a) Case 1

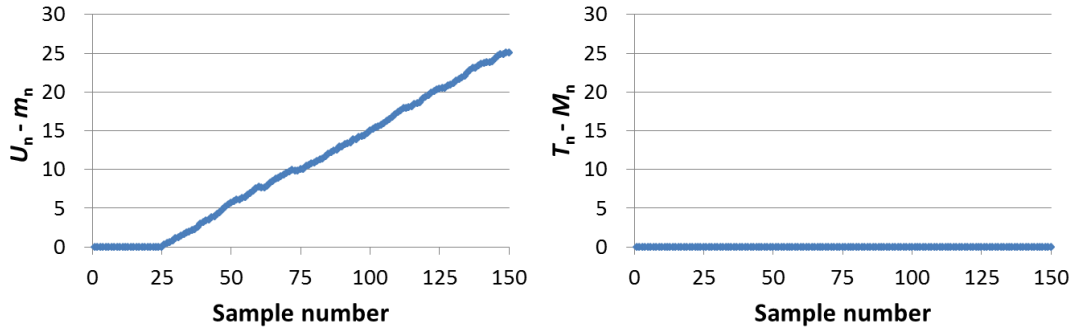

(b) Case 2

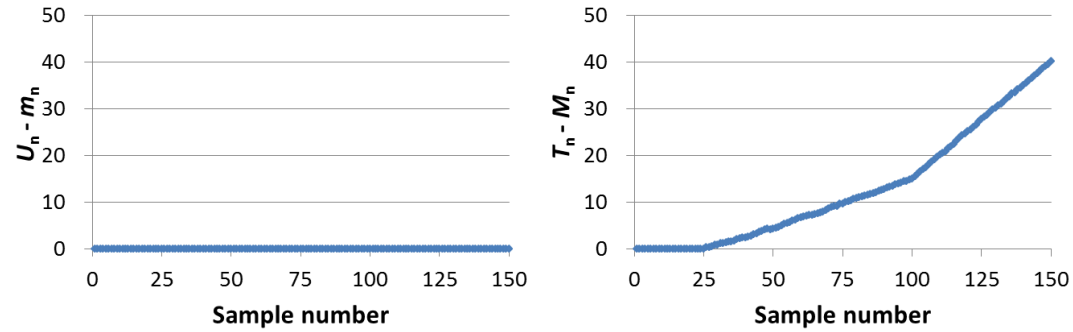

(c) Case 3

Figure 6.8 CUSUM test results for the artificially generated data.

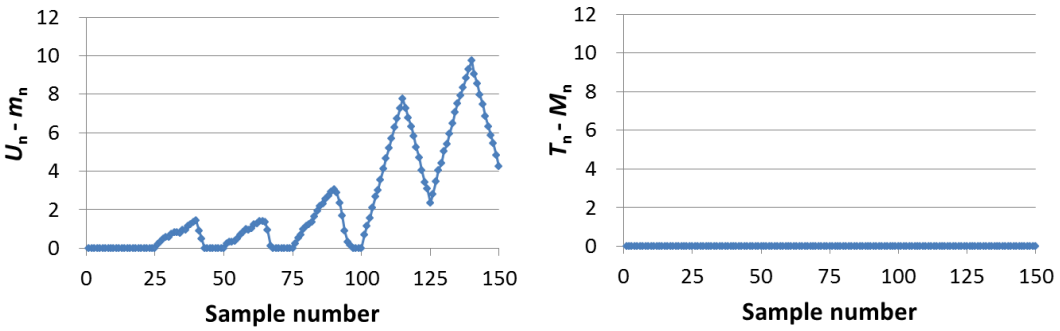

(d) Case 4

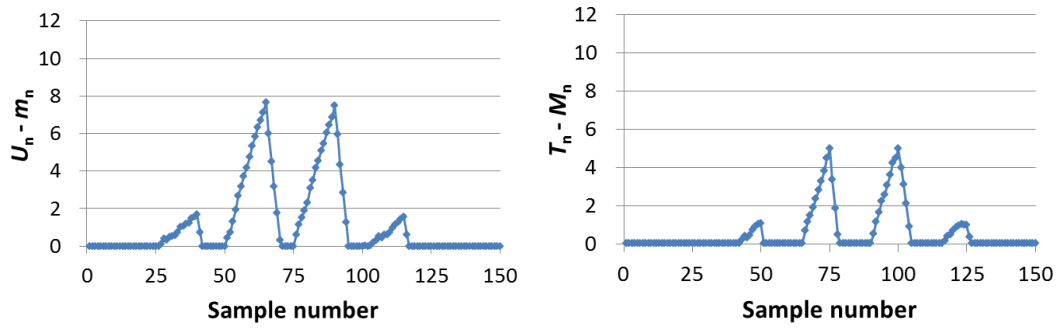

(e) Case 5

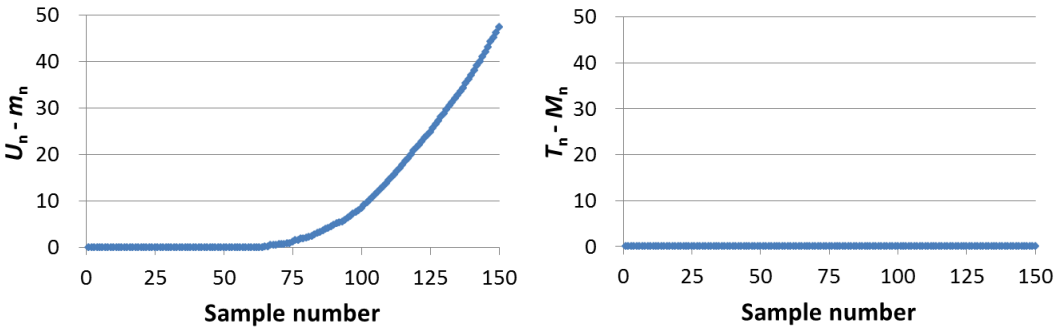

(f) Case 6

Figure 6.8 CUSUM test results for the artificially generated data (continued).

In general, when the data points exceed the pre-set limit of $\delta/2$, a positive output of the CUSUM test in the corresponding direction would result. If the subsequent data points are still beyond this limit, the CUSUM outputs will accumulate from the previous ones. On the other hand, when the subsequent data points are within the limit or exceeding the limit in the opposite direction, the corresponding CUSUM output would reduce.

The detection of a fault depends on the selection of the two thresholds; $\pm\delta/2$ determines when U_n-m_n or T_n-M_n will produce positive outputs and λ decides when to report the present of a fault. Figure 6.9 demonstrates the detection of a fault with different setting of these two thresholds.

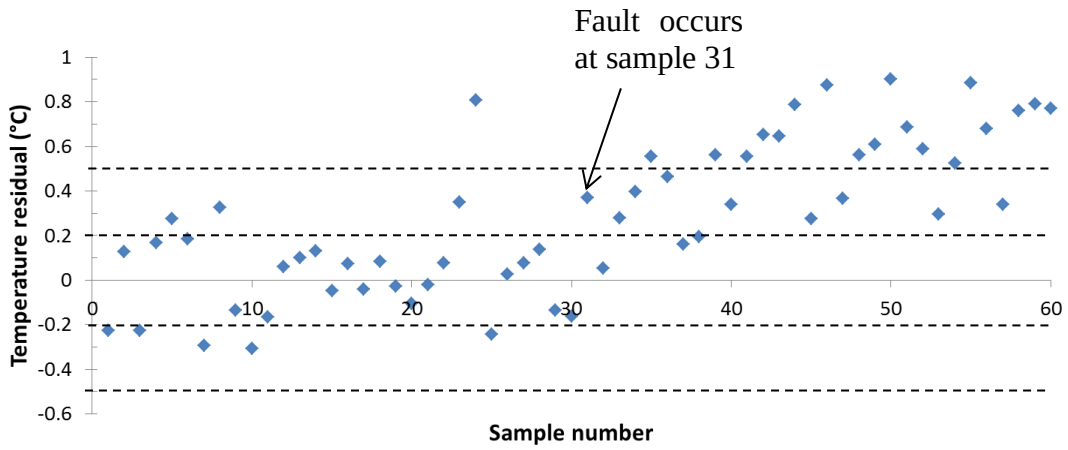

(a)

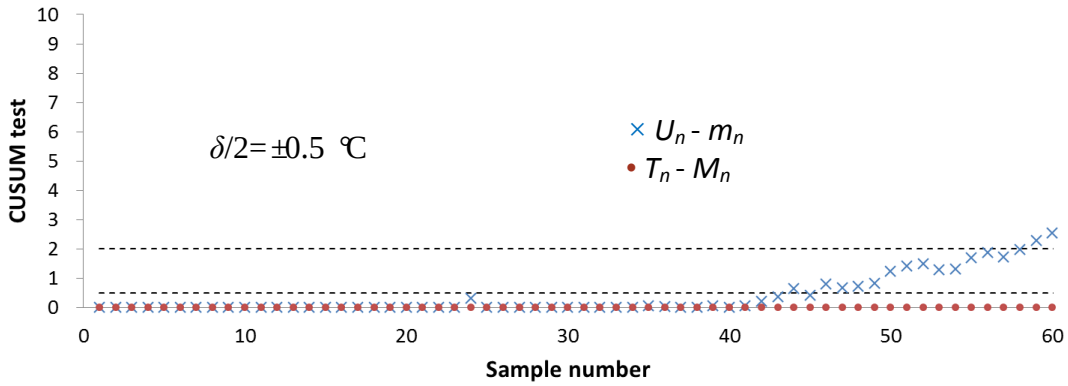

(b)

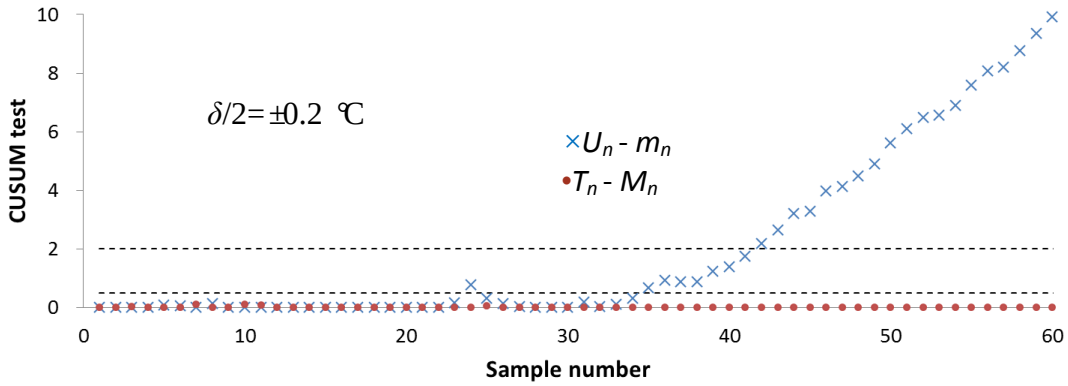

(c)

Figure 6.9 Selection of the thresholds, (a) residual data set, (b) CUSUM test results when *δ/2* is 0.5 ℃, (c) CUSUM test results when *δ/2* is 0.2 ℃.

Some artificially generated temperature residuals are shown in Figure 6.9a, together with two pair of $\pm\delta/2$ lines ($\pm$0.2 °C and $\pm$0.5 °C). The first 30 residual data points have an average value of around zero, hence regarded as a fault free period, with a standard deviation of 0.2. A linear function is artificially generated to create some faulty data from 31st data point and to gradually increase the residual values, reflecting increasing level of severity. The corresponding CUSUM test results for $\delta/2$ = $\pm$0.5 °C and $\pm$0.2 °C are plotted respectively in Figure 6.9b and 6.9c which also show the two selected λ, i.e. λ = 0.5 and 2.0.

When $\delta/2$ is chosen to be $\pm$0.5 °C, only one point in the fault-free zone is outside the boundaries so U_n-m_n only have one positive response (data point 24th). In response to the fault function, the U_n-m_n begins to rise steadily from data point 40. When $\delta/2$ is reduced $\pm$0.2 °C, the steady increase of U_n-m_n starts earlier at data point 35. As expected, since the fault function is increasing in the positive direction, the T_n-M_n values for both tests stay close to zero throughout. It is clear that the CUSUM test responds to a fault earlier when a smaller $\delta/2$ is chosen.

The second consideration is to choose an appropriate threshold for raising an alarm λ. Again, two settings (λ = 0.5 and 2) were tested. In Figure 6.9b, $\delta/2$ = $\pm$0.5, all the CUSUM outputs, including the 24th data point, stay within λ = 0.5 in the fault free period, i.e. no false alarm is detected. U_n-m_n first exceeds the threshold of λ = 0.5 at data point 44th and exceeds the large threshold setting of λ = 2 with a further delay at data point 59th. In Figure 6.9c, $\delta/2$ = $\pm$0.2, U_n-m_n at data point 24th is now larger than the λ = 0.5, which resulted in a false alarm if this λ value is chosen and the fault is first detected at data point 35th. If λ is set at a higher value of 2.0, the detection is achieved at a later time (data point 42nd) but with no false alarm. In general, the detection speed is noted to increase when a smaller λ is used for a given $\delta/2$.

When comparing the above four combinations of the threshold settings, a small λ with a small $\delta/2$ have a larger chance of creating false alarm, while a large λ with a large $\delta/2$ delays the detection significantly. In this illustration, both a large λ with a small $\delta/2$ or a small λ with a large $\delta/2$ managed to avoid a false alarm and to trigger the alarm correctly at about the same time (at 42nd and 44th data point respectively). However, the former is considered to be a better option in the author's

opinion, because it has a better tolerance of the random noise signals going beyond the $\pm\delta/2$ boundary in the fault free period. In Figure 6.5b, U_n-m_n at data point 24th is too close to λ = 0.5 when $\delta/2$ is 0.5 ℃, but the corresponding U_n-m_n has a larger margin from λ = 2 when $\delta/2$ is 0.2 ℃ (Figure 6.5c). Therefore, it is better to choose a small $\delta/2$ value (one standard deviation of the fault free residual data has been suggested) with a large λ.

The detection process is shown in Figure 6.10. Both of the parameters selected, as discussed in Section 6.2.1, for fault detection need to go through the CUSUM test separately. If the either of the test triggers the alarm, then a fault is present.

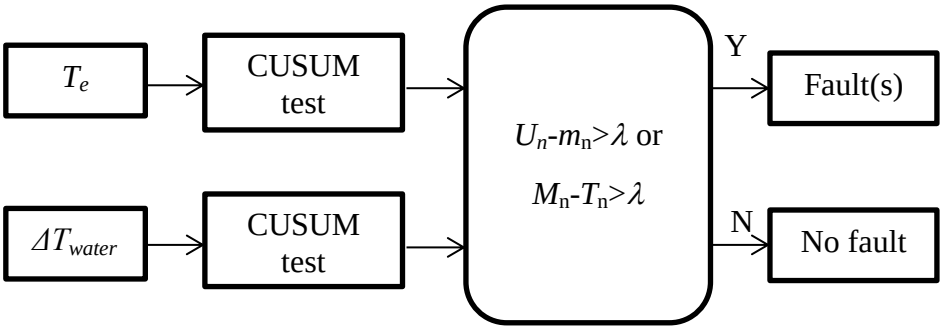

Figure 6.10 Fault detection procedure

6.2.3 Residual pre-processing

This section illustrates how to prepare the residual data for the CUSUM test. In relation to the fault of cooling water flowrate reduction, Figure 6.11 shows the residuals of the cooling water temperature difference across the condenser, i.e. the differences between the predicted values and the measured values of the temperature differences. The first three compressor cycles (from time step 1 to around 189) were under fault free condition; while the fault of cooling water flowrate reduction was introduced at the 190 time step. It is evident that the residuals increase within the on-cycle period under this fault, and during the last part of this on-cycle period it is also clear that the residuals increased at a slower rate relative to those under the first three fault free cycles. It is worth to point out that the residuals became much larger at

the compressor starting-up and shutting-down moments even under fault free conditions, reflecting poor accuracies of the prediction model for these periods.

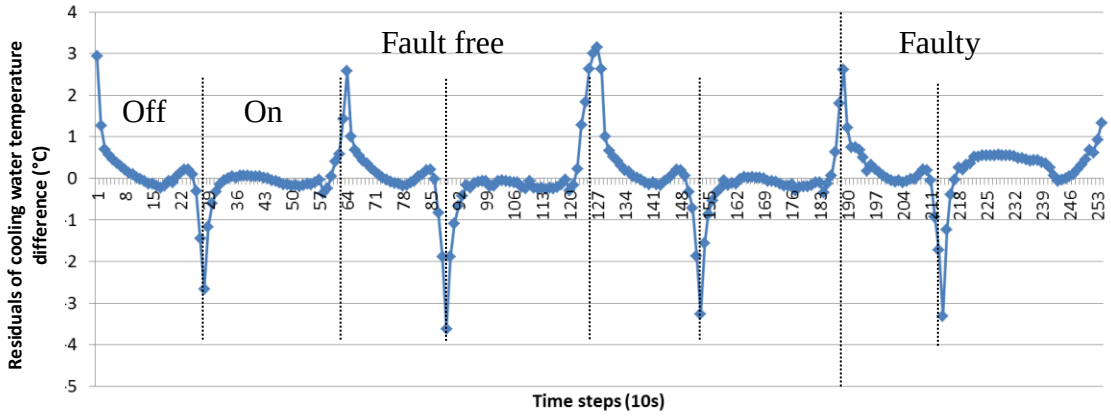

Figure 6.11 The residuals of the cooling water temperature difference

The residuals caused by the modelling errors during the compressor on/off moments are much larger than the residuals resulting from the actual fault. Pre-processing of the residuals is therefore needed to avoid false alarm during these moments, assuming the fault can be detected during other parts of the cycle operation. Figure 6.12 illustrates the CUSUM test results following equations 6.6 and 6.7 based on the original residuals of cooling water temperature difference (detailed CUSUM test procedures are presented in next section). Both U_n - m_n and M_n - T_n have increasing outputs in the first three fault free cycles. The bumps in Figure 6.12a for U_n - m_n occurred when the compressor is being turned off while in figure 6.12b for M_n - T_n they occurred when the compressor is restarted. A larger and wider bump means the local residuals are larger based on earlier observations of the 6 fictitious cases. In the faulty zone, the U_n - m_n values due to the fault during the on-cycle period is much smaller, making it impossible to detect the fault without creating any false alarm.

(a)

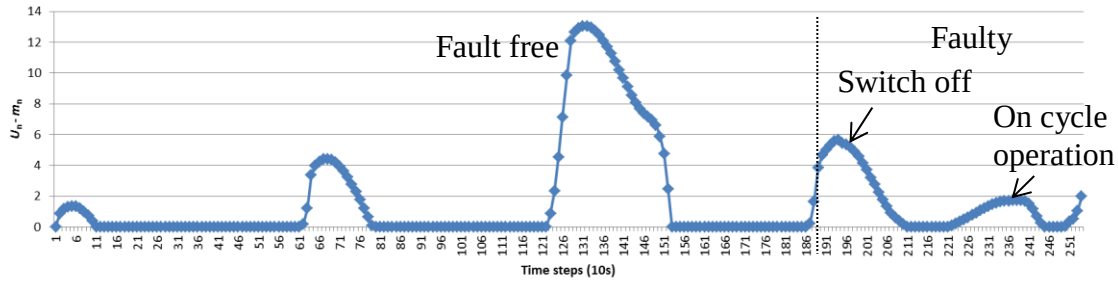

(b)

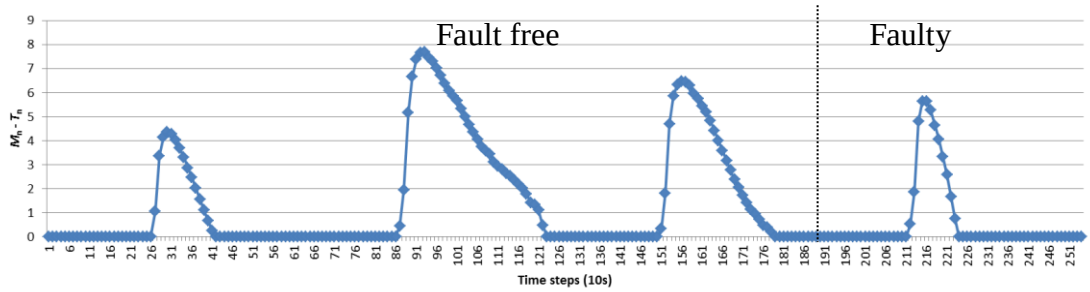

Figure 6.12 CUSUM test results of the original residuals of ΔT_{water}, (a) increase in the mean residual and (b) decrease in the mean residual

(a) 3-point resetting

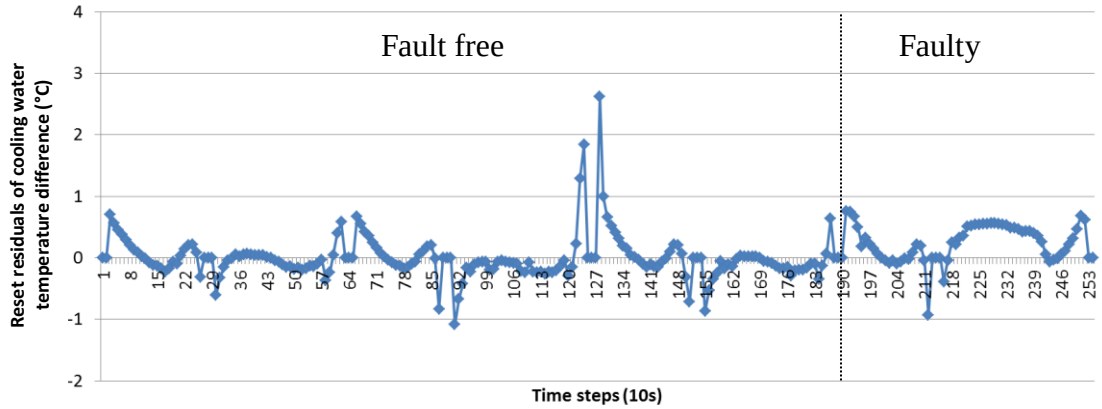

(b) 5-point resetting

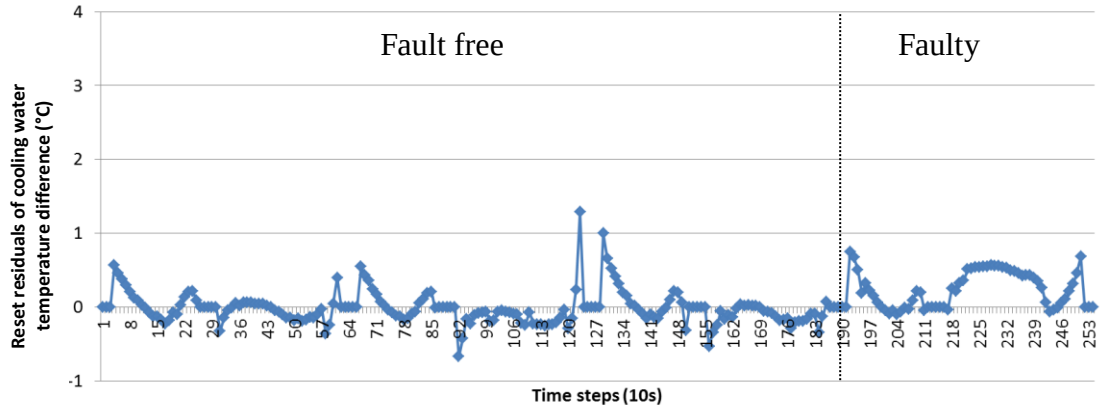

(c) 7-point resetting

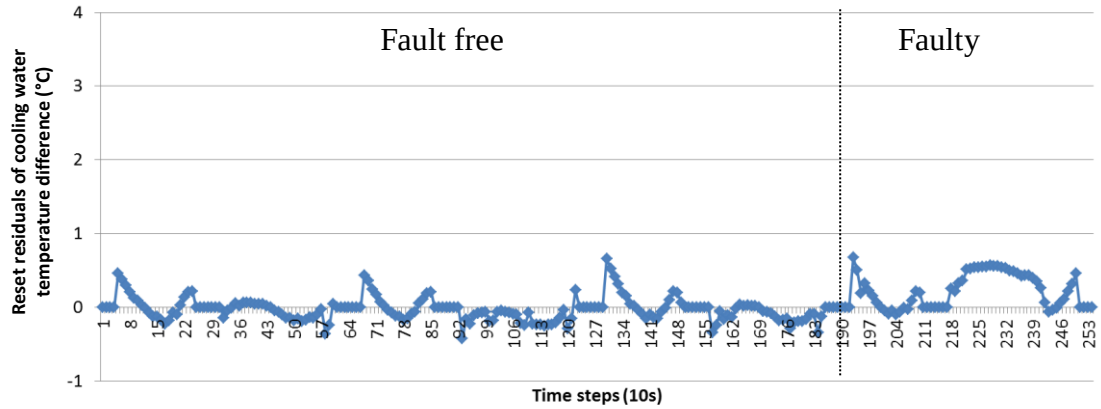

Figure 6.13 Reset residuals of the cooling water temperature difference ΔT_{water}

In order to avoid the prediction errors being interpreted as a fault, a software detector is created to detect the compressor on-off or off-on switching moment as signalled by the compressor power meter. A certain number of data points with large residuals near the switching moments were then set to zero. With the current sampling interval of 10 seconds, three tests were carried out, namely 3, 5 and 7 residual data points centred at the switching moment were respectively set to zero. The results are shown in Figure 6.13. It appeared that a 5 point-resetting is sufficient to reduce the maximum residual to less than 1 °C which is comparable to the faulty residual levels in the faulty zone, and there were no noticeable differences between 5-point and 7-point resetting. Therefore the 5-point mode was chosen to reduce the influences from the modelling error. When more than one parameter is involved in fault detection, this resetting strategy needs to be applied to individual parameters separately, each may require a different number of resetting points, depending on the modelling accuracy of the parameter.

The proposed data chopping method is essentially the same as ignoring the associated alarm within these switching periods, hoping the fault could be picked up later, but it would delay the detection as seen later in Figure 6.14a that the genuine peak representing the fault would be ignored near the switching periods.

6.2.4 Fault detection procedures

Having "pre-processed" the residual data set to reduce the influences of the modelling error, the fault detection can be now implemented via the CUSUM test; 3 steps need to be followed.

1. Calculate the mean values μ_0 of the residuals and this should have a value of around zero during the fault free period.

2. Detecting a change in the mean values μ_0 based on the selection of $\delta/2$.

3. Determining as soon as possible the time when a fault occurs based on the threshold, λ.

The mean value μ_0 of the fault free residuals of ΔT_{water}, excluding the reset-to-zero data points, shown in Figure 6.13b is calculated to be 0.01 ℃ and the corresponding standard deviation is 0.8 ℃ (before the residual resetting), over 3

complete cycles. The outputs at various stages of the CUSUM test calculations from Equations 6.1 and 6.2 are given in Table 6.6, which illustrates how the equations are implemented. Due to space limitation, only three blocks of data of a time series measurements of 4 complete cycles were presented. The first and second blocks are both for fault free conditions, and a fault was introduced in the 3rd block of residual data.

Table 6.6 CUSUM test spreadsheet calculations

Time step	$\Delta T_{water}(t)$ [℃] residual	Increase in mean				Decrease in mean			
		$y(t)-(\mu_0+\delta/2)$	U_n	m_n	$U_n - m_n$	$y(t)-(\mu_0-\delta/2)$	T_n	M_n	$M_n - T_n$
1	0.00	-0.41	-0.41	-0.41	0.00	0.39	0.39	0.39	0.00
2	0.00	-0.41	-0.82	-0.82	0.00	0.39	0.78	0.78	0.00
3	0.00	-0.41	-1.23	-1.23	0.00	0.39	1.17	1.17	0.00
4	0.00	-0.41	-1.64	-1.64	0.00	0.39	1.56	1.56	0.00
5	0.00	-0.41	-2.05	-2.05	0.00	0.39	1.95	1.95	0.00
6	0.38	-0.03	-2.08	-2.08	0.00	0.37	2.72	2.72	0.00
7	0.30	-0.11	-2.20	-2.20	0.00	0.29	3.40	3.40	0.00
8	0.20	-0.21	-2.40	-2.40	0.00	0.19	4.00	4.00	0.00
9	0.13	-0.28	-2.69	-2.69	0.00	0.12	4.51	4.51	0.00
10	0.09	-0.32	-3.01	-3.01	0.00	0.08	4.99	4.99	0.00
11	0.02	-0.39	-3.39	-3.39	0.00	0.01	5.41	5.41	0.00
⋮									
148	-0.01	-0.42	-62.64	-62.64	0.00	0.38	55.76	55.76	0.00
149	-0.83	-1.24	-63.88	-63.88	0.00	-0.44	55.32	55.76	0.44
150	0.00	-0.41	-64.29	-64.29	0.00	0.39	55.71	55.76	0.05
151	0.00	-0.41	-64.70	-64.70	0.00	0.39	56.10	56.10	0.00
152	0.00	-0.41	-65.11	-65.11	0.00	0.39	56.49	56.49	0.00
153	0.00	-0.41	-65.52	-65.52	0.00	0.39	56.88	56.88	0.00
154	0.00	-0.41	-65.93	-65.93	0.00	0.39	57.27	57.27	0.00
155	-0.42	-0.83	-66.77	-66.77	0.00	-0.03	57.23	57.27	0.03
⋮									
190	1.22	0.81	-83.99	-84.81	0.81	1.21	68.01	68.01	0.00
191	0.75	0.34	-83.65	-84.81	1.16	0.74	69.15	69.15	0.00
192	0.75	0.34	-83.32	-84.81	1.49	0.74	70.28	70.28	0.00
193	0.67	0.26	-83.05	-84.81	1.76	0.66	71.35	71.35	0.00
194	0.50	0.09	-82.96	-84.81	1.85	0.49	72.24	72.24	0.00
195	0.18	-0.23	-83.19	-84.81	1.62	0.17	72.81	72.81	0.00
⋮									

The first block presents the fault free residuals from the beginning of the data set when the compressor was switched off, noting that the first 5 residual points were set at zero. It is common to set the δ in equation 6.1 as the same value as one standard deviation (Chetouani 2008), i.e. $\delta/2$ was thus set to be ±0.4 ℃ and as all the data points in the first block are within this range, therefore the CUSUM test results (U_n-m_n) and (T_n-M_n) are all zero.

For the second block, as before, the residuals for 5 data points were set to zero during the switching moment. However, it is evident that relatively large prediction errors (or residuals) were still encountered before (time step 149) and after (time step 155) the switching moment that were not reset to zero; both exceed a half δ of 0.4 ℃. These residuals lead to a positive value of T_n-M_n in the CUSUM test at the corresponding time steps, suggesting that a positive CUSUM output may not always imply a fault (i.e. a false alarm).

The last block in Table 6.6 presents some of the residuals from time step 190 after a fault of flow reduction has been introduced. A series of positive (U_n-m_n) values suggests that the mean values of the residuals are increasing from the original value of 0.01 ℃. Meanwhile, (T_n-M_n) remains at zero as it can only have a value when the residual is negative. Essentially, whenever a series of positive values of (U_n-m_n) or (T_n-M_n) occur, potentially a fault could be present.

The CUSUM test results (U_n-m_n) and (T_n-M_n) for the entire four cycles are shown in Figure 6.14a and Figure 6.14b respectively. Since only 5 residual data points were set to zero during the on-off/off-on switching moments, it is possible to have some data points in the vicinity of these periods to exceed ±½δ due to modelling errors resulting in some small positive test results (small spikes).

When the fault of the cooling water flowrate reduction occurred at time step 190 in the 4th cycle, the residuals of the ΔT_{water} increased (as seen the faulty cycle in Figure 6.13b). The CUSUM test output in the faulty zone of Figure 6.14a increased sharply for a short period when compressor shut down and went back to zero (even after the 5-point resetting, followed by a larger peak for a longer period of time when the compressor was re-started at time step 221. The short section between the two peaks suggested that the cooling water restriction had a very little influence on ΔT_{water} when the compressor was not running.

(a)

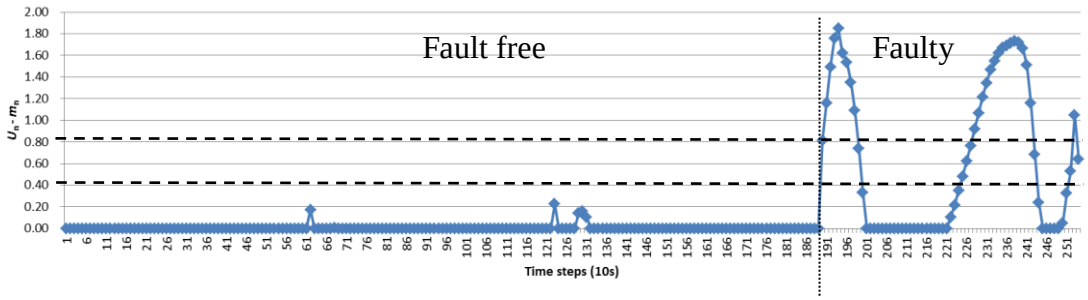

(b)

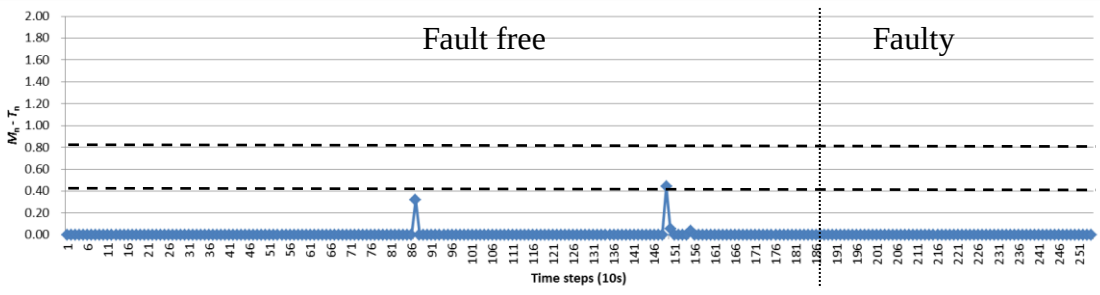

Figure 6.14 CUSUM test results of the ΔT_{water} residuals after 5-point resetting, (a)U_n-m_n and (b) M_n-T_n

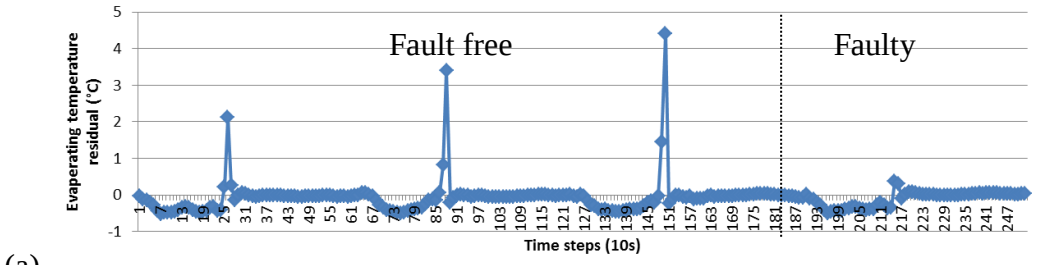

(a)

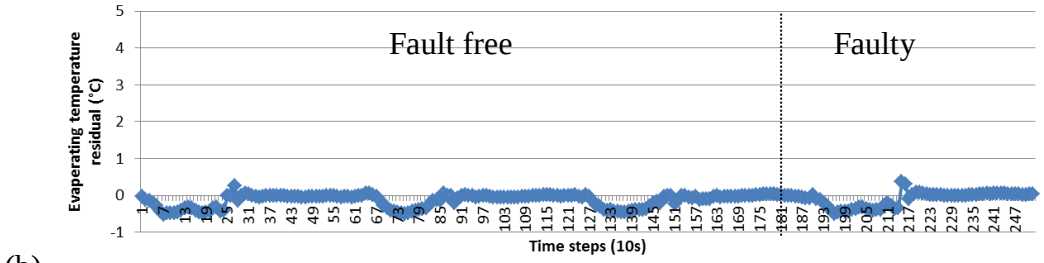

(b)

Figure 6.15 (a) The residuals of the evaporating temperature T_e, (b) The residuals of the T_e after 5 data points being reset

Figure 6.15a shows the residuals of the evaporating temperature for the same four cycles. It was noticed the evaporating temperature also experienced larger prediction errors at the compressor on-off moments though the prediction accuracy of T_e was much better during off-on moments; as a result, as shown in Figure 6.15b, two data points were needed to be set to zero during switching-off moment but none were set to zero during switching-on moment. It could also be seen that the model prediction errors during the compressor off periods were larger than that of the on periods.

From Table 6.3 (Section 6.1), it can be seen that the evaporating temperature was not too sensitive to the cooling water flow reduction, which can also be noted from Figure 6.13b when comparing the fault-free with the faulty cycles, both having the similar patterns of T_e residuals, thus suggesting that T_e is not a suitable parameter for detecting this fault.

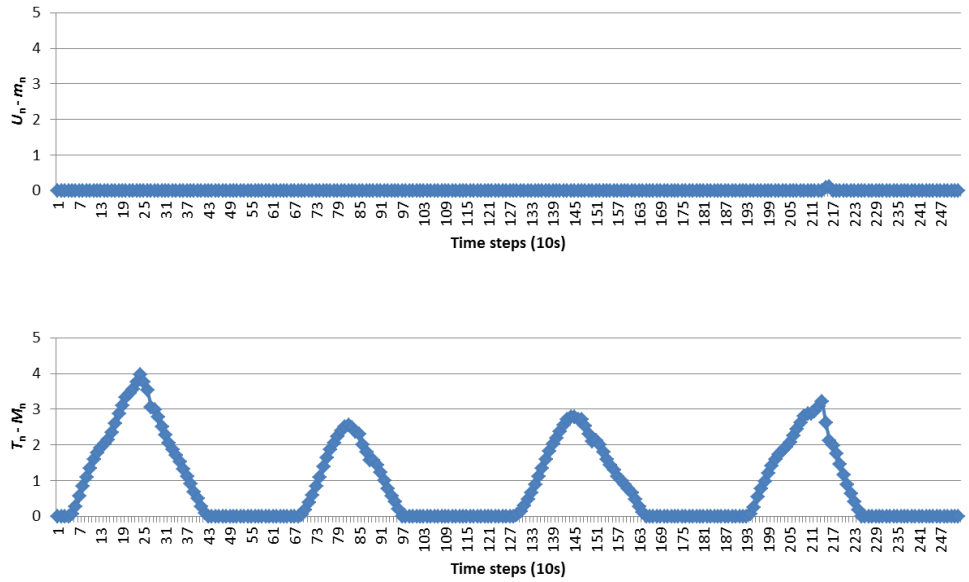

Figure 6.16 CUSUM test results for evaporating temperature residual

For the same fault, the CUSUM test procedures were performed for the evaporating temperature of all the 4 cycles. The results are presented in Figure 6.16. U_n - m_n remains at zero throughout as there are no large positive residuals and T_n - M_n has large peaks each time corresponding to negative residuals during off-cycle periods. The sizes of the peaks in both fault free and faulty zone are very similar, making it difficult to select a suitable threshold that can detect the fault without causing a false alarm, implying that the off-cycle residuals are not suitable to be used as a fault indicator and the evaporating temperature is not an appropriate choice to detect a cooling water flow restriction fault.

The final step in fault detection is to determine a suitable fault-free threshold λ that can detect fault at a low severity level without causing too many false alarms. As mentioned previously, it is better to choose a small $\delta/2$ at one standard deviation of the fault free residual and adjust the value of λ accordingly. An easier way is to set the threshold according to the CUSUM test results. In Figure 6.14, two thresholds, λ = 0.4 and 0.8, are tested. The λ = 0.4 threshold is able to tolerate the small jumps in Figure 6.14a and at the same time detect the fault at the 191 time step. In Figure 6.14b, using the same λ = 0.4, a false alarm is triggered at 149 time step. However, if the threshold is set to 0.8, the possibility of the false alarm is eliminated. The drawback is that the fault is detected 10s later than with the smaller threshold. In this case, because the

delay in detection is rather small, it is more important to avoid the false alarm. Thus λ could be selected as 0.8.

The CuSum tests and the similar analysis had been carried out for all the other specified faults. Table 6.7 shows the results of the threshold selection. The standard deviation after the residual resetting of the fault free residuals is used as δ for both ΔT_{water} and T_e. λ was selected manually to achieve the quickest detection speed while avoiding any false alarm for individual faults. Therefore, 4.0 was chosen respectively for ΔT_{water} and T_e, i.e. the largest among all the possible λ for individual faults.

In practice, at any instant only one of the two mentioned parameters is needed to raise an alarm for each type of fault. ΔT_{water} was not sensitive to the binary ice flow reduction fault and the broken scraper fault, therefore the two faults can only be flagged by T_{e}. Similarly, the solution concentration decrease fault could only be flagged by ΔT_{water}. For the rest three faults, as the sensitivity factors of T_{e} were all larger than those of ΔT_{water}, the alarms were triggered by the former in most cases.

Table 6.7 The selection of threshold for various faults

Faults	ΔT_{water}		T_{e}	
	δ [℃]	λ	δ [℃]	λ
Binary ice flow reduction	0.01	4.0	0.07	4.0
Cooling water flow reduction	0.01	3.8	0.07	4.0
Initial solution concentration increase	0.01	3.8	0.07	3.7
Initial solution concentration decrease	0.01	4.0	0.07	4.0
Broken scraper	0.01	4.0	0.07	3.8
Scraper motor failure	0.01	4.0	0.07	4.0

6.3 The development of the fault diagnosis approach

The procedures described in the previous section are capable of reporting the existence of a fault. However, to determine the type and cause of the fault, a fault diagnosis/classification is needed. The rule-based fault classification process involves the use of the various variation patterns associated with a particular fault(s). Various classifiers have been used previously, ranging from the use of diagnosis tables to artificial neural network (ANN) classifiers (Wang et al. 1998; House et al. 1999). For

this study, an ANN based pattern recognition strategy is used for automatic fault classification (Cho et al. 2005). The development of the fault classifier will be introduced first, followed by a demonstration of fault diagnosis example (a cooling water flow reduction fault). Double fault diagnosis will also be addressed here.

6.3.1 Fault classifier

The fault diagnosis is carried out essentially by identifying the unique patterns of variation of various parameters under certain faulty conditions. To enhance the reliability of the fault diagnosis, a common practice is to use the fault sensitive factors in Table 6.3 and 6.4. Depending on the sign and the magnitude of the numerical values of the sensitivity factors, they are replaced by either -1, 0 or 1, representing respectively a decrease (i.e. sensitivity factor < -1), normal (i.e. little ± changes or no changes) or an increase (i.e. sensitivity factor > 1) in the value of the selected parameters. However, there is one exception for which the -1 and 1 boundaries of the sensitivity factors are revised to ±0.5 for the parameters when a binary ice flow reduction fault is encountered, as explained previously.

Table 6.8 Fault diagnosis patterns

Diagnosis Parameters / Output Faults		$T_{c,\,out}$	ΔT_{water}	T_{dis}	$T_{ice,out}$
1	Binary ice reduction	0	0	1	-1
2	Cooling water reduction	1	1	1	0
3	Solution concentration increase	-1	-1	1	-1
4	Solution concentration decrease	0	-1	1	1
5	A broken scraper	-1	0	-1	1
6	Scraper motor failure	-1	-1	-1	1
7	Unable to determine	-	-	-	-

The number of the parameters should be kept as few as possible, in order to keep the FDD method simple and cost effective. Therefore, if a parameter has the

similar response under different faults, it is not useful for the diagnosis purpose, and if several parameters have the same pattern of variation for the same faults, only the one with the largest fault sensitive factor is employed. Having analysed all the variation patterns of the chosen parameters in Tables 6.3 and 6.4, the final selected parameters are listed in Table 6.8 together with the individual and unique fault recognition patterns. If two faults share the same pattern, it implies that extra parameter(s) is needed.

An ANN classifier is employed to help the automatic recognition of the patterns for the associated faults. The inputs to the ANN are unique -1, 0 and 1 code combinations of the selected parameters and the output is the fault(s). The hidden layer contains a single neuron and a linear transfer function. The network is trained with the data in Table 6.8. The output of the ANN classifier contains 7 Codes (1, 2 …7): 6 for each of the single faults and 1 for the situation when it is unable to diagnose the fault. If an input pattern matches with any of the fault pattern in Table 6.8, the ANN output will indicate the fault type. Otherwise, Code 7 will be reported; this could be due to modelling or measurement inaccuracies, poor design of the diagnosis method, or the existence of unspecified faults.

6.3.2 The diagnosis of a cooling water reduction fault

In Section 6.2.4, a cooling water reduction fault was used as a demonstration for the fault detection method; the same fault is used to illustrate the development of the diagnosis procedure. For a specified threshold, the presence of a fault is flagged up when the CUSUM test result is larger than the threshold for one of the two fault detection parameters, i.e. ΔT_{water} and T_{e}, as discussed in Section 6.2.1, followed by the activation of the fault diagnosis classifier.

The first step for the fault diagnosis is to compare the measured/derived values of the fault diagnosis parameters listed in Table 6.8 to the model predictions, generating the corresponding time-series of the residuals which are tested again by the CUSUM tests. For each of the parameters listed, an appropriate threshold has been chosen, as discussed previously. A value of -1 or 1 is assigned when the CUSUM test result is lower or higher than the lower and upper limits of λ. If the result stays within the limits, a zero value is assigned. The next step is to compare the unique pattern of -1, 0 and 1 for the 4 chosen parameters with those presented in the table to identify the

individual fault. Since the pattern is of dynamic nature, the fault can be diagnosed at any time after it has been detected, potentially making this FDD approach applicable for real-time applications.

6.3.3 Double fault diagnosis

During the operation of the binary ice system, it may be possible that more than one fault could develop at any given time. The fault diagnosis method in Section 6.3.1 was mainly developed to cope with a single fault, thus it is not expected to diagnose a double fault. From the literature review presented in Chapter 2, it was noted that very little previous work on chillers FDD looked into double fault. In this section, a diagnosis strategy was developed to differentiate the occurrence of a single and a double fault scenario. The work is unique in a sense that the diagnosis is implemented using dynamic data, and the double faults being selected could have opposite fault signatures making both detection and diagnosis difficult. In this study, however it is also assumed that triple fault scenarios are excluded.

As previously mentioned, three sets of double faults are investigated. If two faults have similar influence to the system behaviours, the residuals of some of the parameters are expected to add up, usually making them easier to be detected, though their diagnosis become more challenging when it is needed to differentiate it from a single fault. When two simultaneous faults affect the parameters in the opposite manners, they may cancel the some of the effects of each other, leading to harder detection as well as diagnosis. In the third set, the two faults are affecting different system parameters, thus creating a new fault signature. This could potentially be mis-diagnosed as another single fault.

Based on the above, the system behaviours in Table 6.8 were examined and accordingly, three pairs of faults are respectively selected.

1. Binary ice flow reduction + solution concentration increase (BR+SCI)
2. Cooling water flow reduction + solution concentration increase (CR+SCI)
3. Binary ice flow reduction + broken blade (BR+BB)

Following the similar procedures described in Section 6.1, experimental fault simulations were carried out according to the selected double faults. To avoid complications, the single faults involved were all kept at their maximum severity level,

though the logics in developing the strategy remains unchanged regardless of the severity levels. Observations on system behaviours under double faults were made and the associated residuals are transformed into fault pattern, as presented in Table 6.9, which enables unique double faults to be diagnosed. It should also be noted that no additional parameters were found to be necessary when these three double faults are involved.

Table 6.9 Fault patterns for both single and double faults

Fault \ Parameter		$T_{c,\,out}$	ΔT_{water}	T_{dis}	$T_{ice,\,out}$
1	Binary ice flow reduction (BR)	0	0	1	-1
2	Cooling water flow reduction (CR)	1	1	1	0
3	Solution concentration increase (SCI)	-1	-1	1	-1
4	Solution concentration decrease (SCD)	0	-1	1	1
5	A broken scraper (BS)	-1	0	-1	1
6	Scraper motor failure	-1	-1	-1	1
7	Unable to determine	-	-	-	-
8	BR+SCI	-1	-1	1	-1
9	CR+SCI	1	1	1	-1
10	BR+BS	-1	0	1	1

It is noticed from Table 6.9 that both CR+SCI and BR+BS created their distinct pattern different to all the other faults. They can be diagnosed using the previously mentioned ANN fault classifier (Section 6.3.2) trained with additional fault patterns. However, BR+SCI has the same pattern as SCI fault, necessitating additional considerations. One initial thought is to use extra parameters other than those shown in Table 6.9. However, having analysed the variations of all the available parameters in Tables 6.3 and 6.4, none of them can be used to create a different pattern for either the single (SCI) or the double fault (BR+SCI), due to the close similarity of their fault influences.

To resolve this, the method proposed by Cho et al. (2005) was used. They developed a residual ratio method for the diagnosis of a single and a double fault, in an air handling unit, which have the same fault pattern; in their study, no extra parameters were required when compared to those used for the single faults. The main

principle is to use the magnitudes of the ratios between certain existing parameters to differentiate between a single and a double fault which have the same fault pattern. Their method is adapted and adopted for the current application.

From Table 6.9, it can be seen that BR and SCI have the same influences on a group of two parameters (T_{dis} and $T_{ice,out}$) but different influences on the other group of two parameters ($T_{c,\,out}$ and ΔT_{water}). Assuming a SCI fault exists first and a BR fault follows, the residuals of those in the first group are expected to become larger but those in the latter group will not change much. Therefore it is possible to diagnose a fault by analysing the ratio between two parameters, one from each group. The parameter with the highest sensitivity factor in each group should be chosen and accordingly, in this study ΔT_{water} and T_{dis} are selected. The residual ratios (RR) for the single fault SCI and the double fault BR+SCI can respectively be calculated, using the average of the compressor on-cycle data, as:

$$\mathrm{RR_{SCI}} = \frac{\left|\Delta T_{\mathrm{water,normal}} - \Delta T_{\mathrm{water,faulty}}\right|_{\mathrm{SCI}}}{\left|T_{\mathrm{dis,normal}} - T_{\mathrm{dis,faulty}}\right|_{\mathrm{SCI}}} = 1.4 \qquad 6.8$$

and

$$\mathrm{RR_{BR+SCI}} = \frac{\left|\Delta \mathrm{T_{water,normal}} - \Delta \mathrm{T_{water,faulty}}\right|_{\mathrm{BR+SCI}}}{\left|\mathrm{T_{dis,normal}} - \mathrm{T_{dis,faulty}}\right|_{\mathrm{BR+SCI}}} = 0.8 \qquad 6.9$$

It is clear that based on the difference of RR magnitude (in absolute term), it can be distinguished whether a single or a double fault occurs, knowing a double fault will reduce the value of the ratio, due to the fact that the change in T_{dis} will be added up and hence a smaller RR. Having analysed different combinations of severity levels, it can be concluded that if a residual ratio of larger than 1 represents a single SCI fault, otherwise a double BR+SCI fault occurs. Though the use of only two parameters is sufficient to diagnose a BR+SCI fault, further ratios based on other combinations of parameters could be used if necessary.

In conclusion, to diagnose a possible double fault, the ANN classifier that has been trained by the fault patterns in Table 6.9, will be applied first. The classifier has 8 output types excluding Code 7, 5 for single faults (Code 2 to Code 6), 2 for double faults (Code 9 and Code 10) and 1 for SCI or SCI+BR (Code 1 same as Code 8). If

the last one is encountered, a residual ratio calculator is activated, and the final step of the diagnosis will be carried out by comparing the residual ratios.

7. Results and discussion

This chapter starts with a summary review of the overall implementation of the designed FDD. The performance of the fault detection and diagnosis are evaluated and presented. The evaluation of the FDD results is carried out by analysing the detection speed and accuracy, the false alarm rate and diagnosis accuracy, under various severity levels. How the performance is affected by the number and the selection of the parameters involved as well as the setting of the thresholds are also examined and discussed.

7.1 Implementation of the FDD

The flow chart of the overall FDD implementation procedure is presented in Figure 7.1, which consists of two main steps: a fault detection step and a fault diagnosis step. The binary ice system and its hybrid model are running in parallel, and the real time measurements are being input to the hybrid model from which the chosen time dependent outputs are generated. As previously discussed, this stage only involves the residuals of the cooling water temperature difference and the evaporating temperature that are fed into the CUSUM test. Once either of the two test results exceeds the pre-selected threshold, a fault is detected and declared. In the second step, a set of chosen measured/calculated fault diagnosis parameters are compared to their fault free model predictions. Once again the residuals of these parameters need to go through the CUSUM test, and the test results are used to generate the fault diagnosis patterns, as previously shown in Tables 6.8 and 6.9. The patterns are sent to the ANN fault classifier (or the double fault classifier when a double fault is involved), which based on the fault pattern, automatically generates the type of fault as its output. At this point, either a fault is diagnosed or it is not possible to identify the fault.

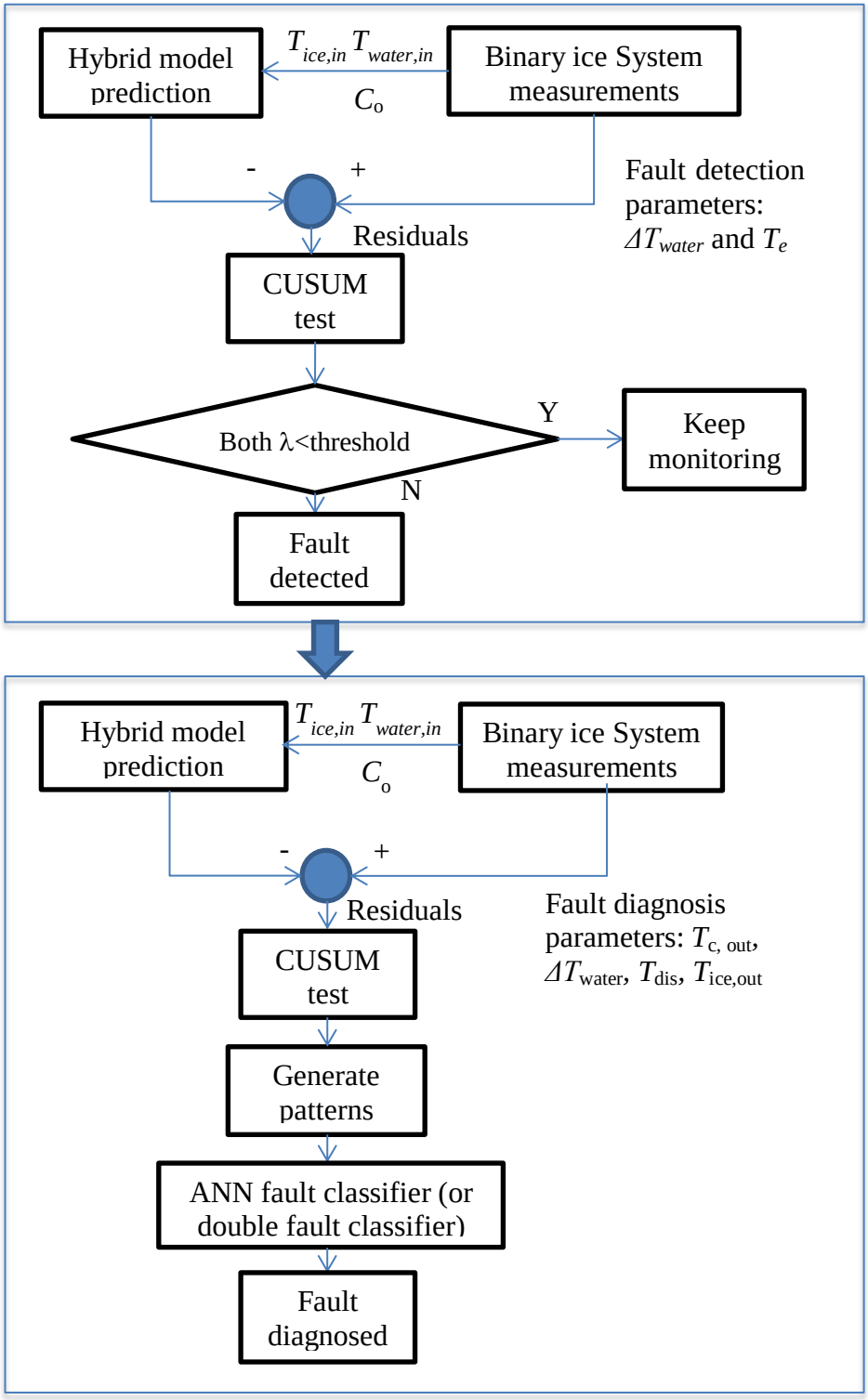

Figure 7.1 Overall FDD implementation procedure

7.2 Results

Evaluations of the FDD performance and/or reliability had been carried by previous researchers (e.g. (Comstock and Braun 1999; Reddy 2006). Reddy (2006) evaluated the fault detection and diagnosis separately. He used four different rates to assess the performance of the detection.

- False negative rate: the probability of diagnose a faulty process as fault free, i.e. missed diagnose;
- Correct fault-free detection rate: the probability of detecting a fault free process as fault free;
- False positive rate: the probability of detecting a fault-free process as faulty, i.e. false alarm;
- Correct fault detection rate: the probability of correctly detecting a fault.

The false negative rate can be in fact deduced from the correct fault detection rate, while the correct fault-free detection rate can also be deduced from the false alarm rate. The probabilities of each pair should add up to unity. Essentially, therefore only two rates, namely false alarm rate and correct fault detection rate, are needed.

Furthermore, Reddy divided the results of the fault diagnosis into four groups:

- Correct and unique diagnosis: the fault is correctly and clearly identified;
- Correct but non-unique: the diagnosis rules are unable to diagnose between more than one possible faults;
- Unable to diagnose: the fault patterns do not match with any predefined diagnosis rules;
- Incorrect diagnosis: a fault is wrongly diagnosed as another fault.

Correct and unique diagnosis is the desired results of a fault diagnosis procedure. The number of correct and unique diagnosis against the total number of diagnosis is used to measure the accuracy of the fault diagnosis method. For the current study, the correct but non-unique diagnosis is not applicable, as the diagnosis method is designed to identify a unique diagnosis pattern associated with each of the 5 chosen faults. The last two diagnosis results are both essentially non-correct diagnosis, and their combined rate can be deduced from the correct and unique diagnosis rate, as all the probabilities add up to unity.

In addition, for dynamic FDDs, one further factor needs to be considered, i.e. the speed of the detection. A faster or an earlier detection reduces the amount of time when the system is running under faulty conditions, thus cutting energy wastage and system downtime.

Therefore the overall performance analysis of the proposed FDD approach is based on the following performance indicators: (i) the false alarm rate, (ii) the correct fault detection rate, (iii) the fault detection speed, and (iv) the correct fault diagnosis rate. The FDD method was tested with experimental data and was evaluated based on the above four indicators. For each of the indicators of a particular fault, though data from 3 cycles were used for the overall assessment, only data from one cycle were presented for demonstration purpose, as shown in Figures 7.2 - 7.6. The overall results for all the tests are summarised in Tables 7.1 and 7.3

7.2.1 False alarm rate

False alarm is defined as the report of a fault during fault free conditions. Figure 7.2 and Figure 7.3 present the false alarm test results. The residuals of the fault detection parameter T_e and ΔT_{water} taken from a fault free test are shown respectively in Figures 7.2a and 7.3a. Five data points before and after the compressor on/off switching moments have been set to zero to reduce the influences of the modelling inaccuracy, as discussed in the previous chapter. The corresponding CUSUM test results are presented in Figure 7.2b for T_e, and Figure 7.3b for ΔT_{water}. The thresholds δ are set to the standard deviation of the fault free residual sets, which are 0.07 and 0.01 for T_e and ΔT_{water} respectively and the dynamic threshold λ is set to 4, as previously stated. Though many residual data points fall outside the ranges of ± 0.035 and ± 0.005 respectively, none of the CUSUM test results goes beyond the pre-set λ, suggesting that there is no fault present during the assessment period.

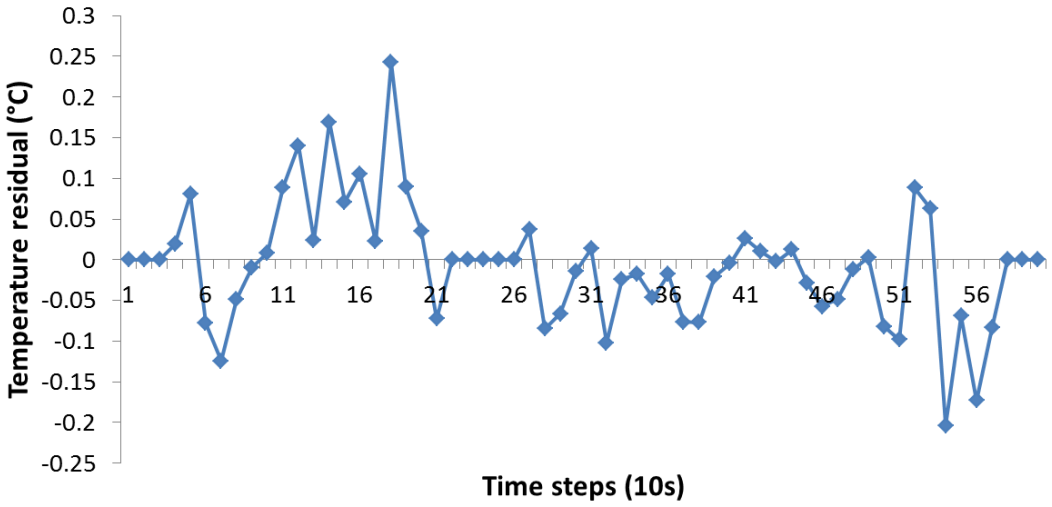

(a)

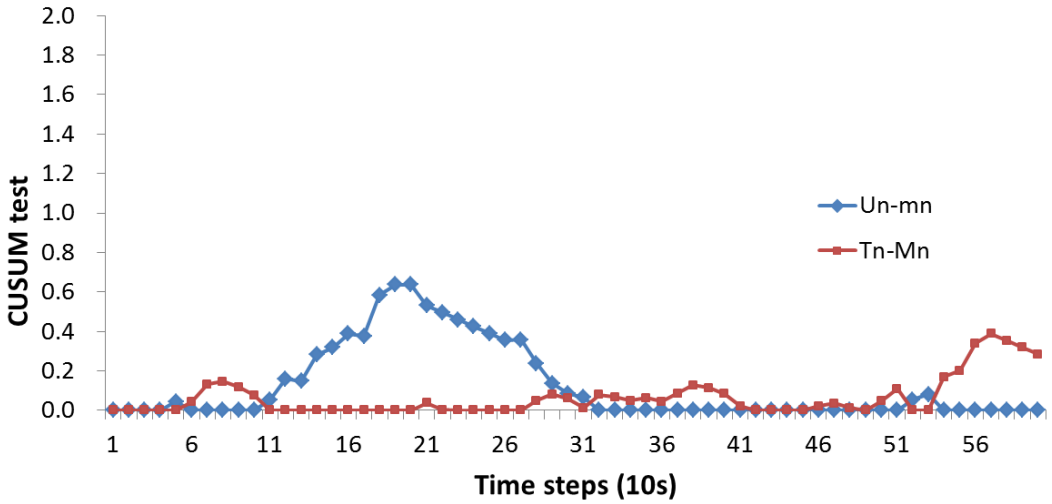

(b)

Figure 7.2 False alarm test under fault free condition for T_e, (a) residual of T_e, (b) CUSUM test for Residual of T_e.

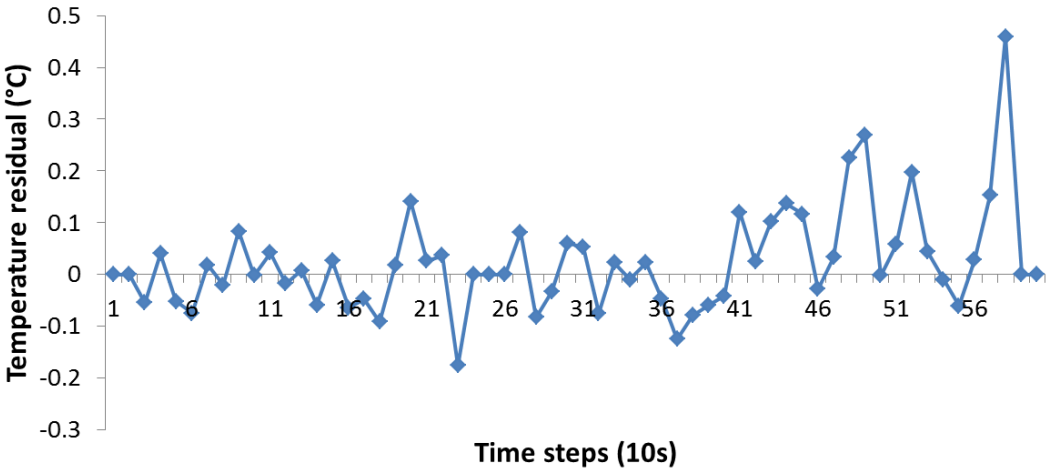

(a)

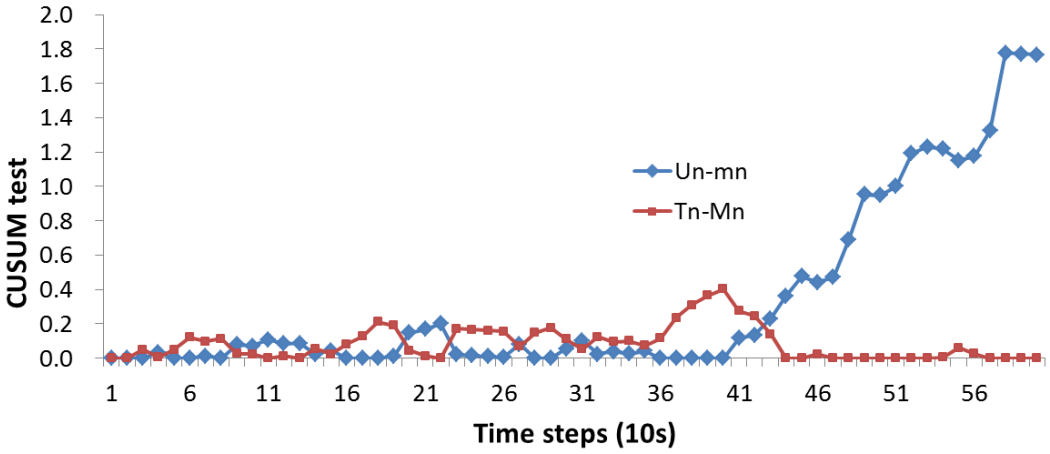

(b)

Figure 7.3 False alarm test under fault free condition for ΔT_{water}. (a) residual of ΔT_{water}, (b) CUSUM test for the residuals of ΔT_{water}.

Further tests regarding the false alarm had been performed on 318 data points from 5 different complete compressor cycles under fault free condition. No false alarm was reported during all the tests. Therefore it can be concluded that the procedure of setting the residual data points near the compressor switching moments to zero and the application CUSUM test eliminated the false alarm effectively. Based on the observation, it is possible to set a λ value as small as 2 without raising a false alarm, but to improve detection speed by approximately 1 to 3 minutes.

7.2.2 The correct fault detection rate and detection speed

The correct fault detection rate stands for the probability/percentage of a fault being detected. The speed of the fault detection is measured by the time delay between the occurrence of a fault and the detection of it. These two performance

indicators are addressed together because the detection speed will only apply when a fault is being detected. Figure 7.4 demonstrates the detection procedure of the binary ice flowrate reduction. The residual data sets of T_e and ΔT_{water} in Figure 7.4a is taken from a complete cycle when the binary ice flowrate reduction fault is at severity level 3. Figure 7.4b and 7.4c are the CUSUM test results for ΔT_{water} and T_e respectively. The thresholds are selected as specified in Chapter 6. In Figure 7.4b, the CUSUM tests for ΔT_{water} stay within the limit throughout the test. However, the CUSUM test T_n-M_n for T_e exceeds the threshold λ at time step 47 (time step 1 is defined as the beginning of the compressor off cycle), therefore a fault is detected and this case is count as a valid fault detection.

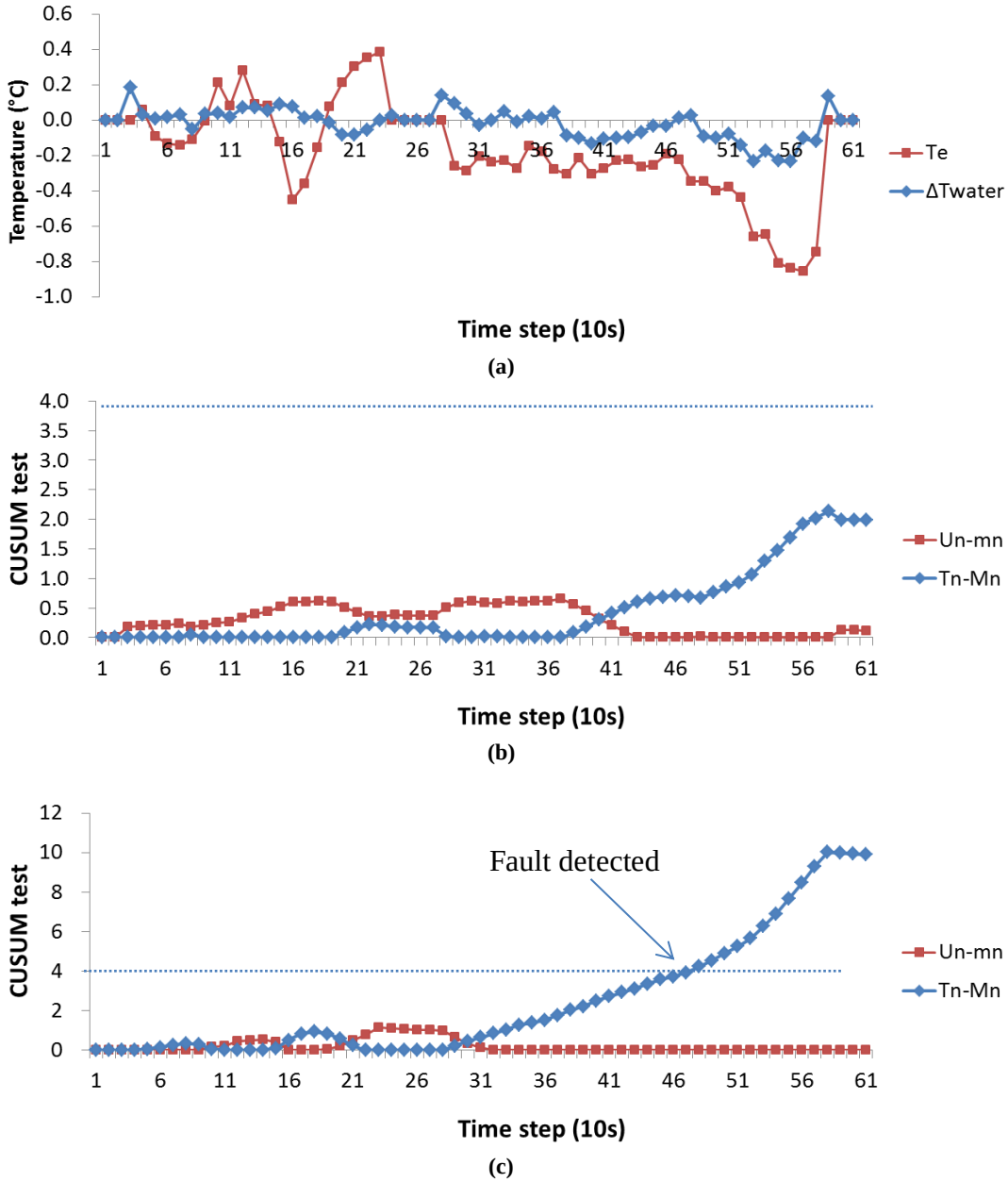

Figure 7.4 Fault detection test for binary ice flowrate reduction, (a) residuals of ΔT_{water} and T_e, (b) CUSUM test for ΔT_{water} and (c) CUSUM test for T_e

Similar tests were carried out for all the selected faults under all severity levels. For each severity level of each fault, three sets of measured faulty data, each from a compressor off/on cycle, were used. The testing results are shown in Table 7.1. The correct detection is the number of times (out of 3) when the detection is successful. The detection speed is regarded as the average time from the beginning of the compressor off-cycle to when the fault is first reported by the CUSUM test.

Table 7.1 The results of fault detection test.

Fault	Cooling water flow reduction			Binary ice flow reduction			Concentration increase		Concentration decrease		SSIG faulty blade	SSIG blade motor failure
Level	1	2	3	1	2	3	1	2	1	2		
Number of detection (out of a total of three)	2	3	3	1	2	3	3	3	3	3	2	3
Time step when the fault is first reported	48	42	39	52	47	41	43	35	42	37	40	18

As expected, the numbers of detection increase with the increasing fault severity level. Success rate is 100% for all the Level 3 faults, though at lower severity levels the detection rates drop, especially for the binary ice flow reduction fault as the present of the ice particle makes the changes of the parameters less obvious. The detection speed also increases (i.e. a shorter detection time) with the severity level, as the residuals become larger at higher fault severity levels. Once again, the detection speed for the binary ice flow reduction fault is poorest. 5 out of the 6 specified faults cannot be detected during the compressor off cycle because many of the parameters tend to stay relatively unaffected by the fault when the compressor is not running. However, the SSIG blade motor failure can be detected very early following the occurrence of the fault, causing T_e to increase rapidly, regardless whether the compressor is running or not, though it a faster detection can be achieved when the compressor is on.

7.2.3 The correct diagnosis accuracy

When a fault is detected, the fault diagnosis module is activated. The residuals of the fault diagnosis parameters listed in Table 6.9 are presented in Figures 7.5 for ΔT_{water}, $T_{ice,\ out}$, $T_{c,\ out}$, T_{dis}, using the same binary ice flow reduction data as used in Figure 7.4. The CUSUM test results for these parameters reveal that Figures 7.6a-d. ΔT_{water} (Figure 7.6a) and $T_{c,\ out}$ (Figure 7.6c) stay within the threshold of 4 all the time. The *Un-mn* value of the discharge temperature (Figure 7.6d) and the *Tn-Mn* values for $T_{ice,\ out}$ (Figure 7.6b) are higher than the thresholds. The CUSUM test results are then converted into patterns as shown in Table 7.2. Essentially, an increase in Un-mn above the threshold will return a +1 and an increase in Tn-Mn above the threshold

will return an -1. By using the ANN fault classifier, the pattern in Table 7.2 is identified as binary ice flow reduction fault.

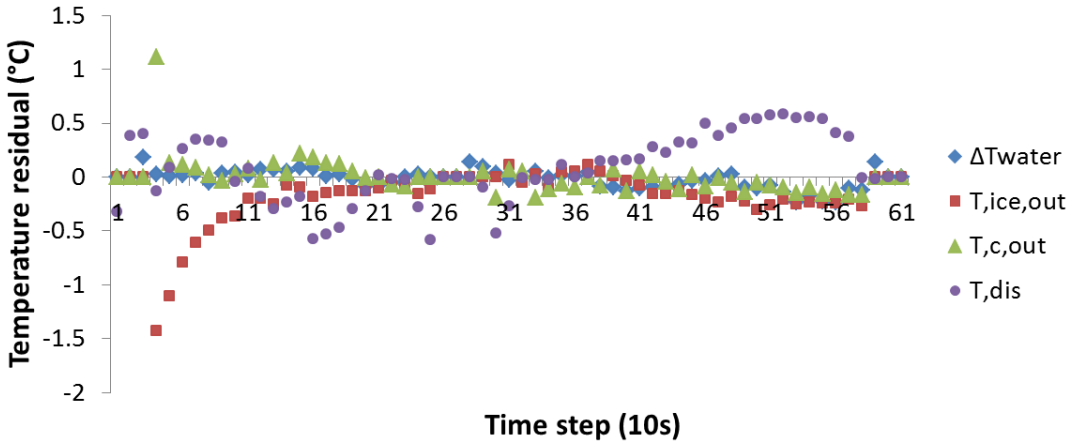

Figure 7.5 residuals of the fault diagnosis parameters.

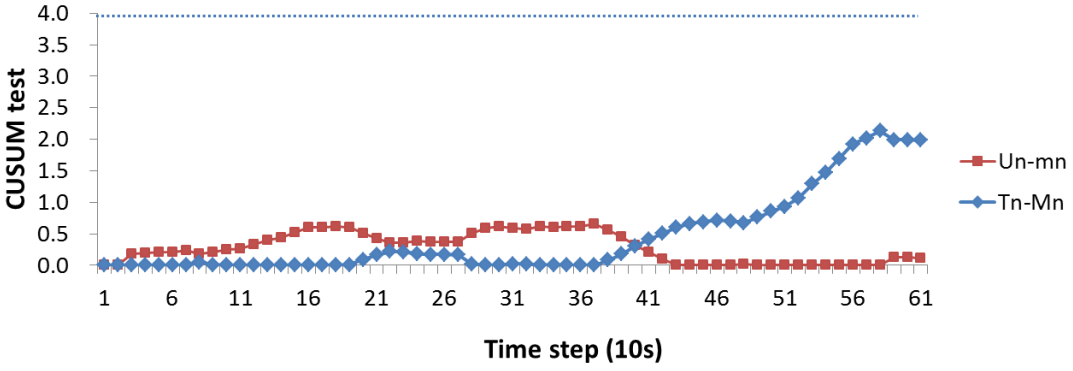

(a) ΔT_{water}

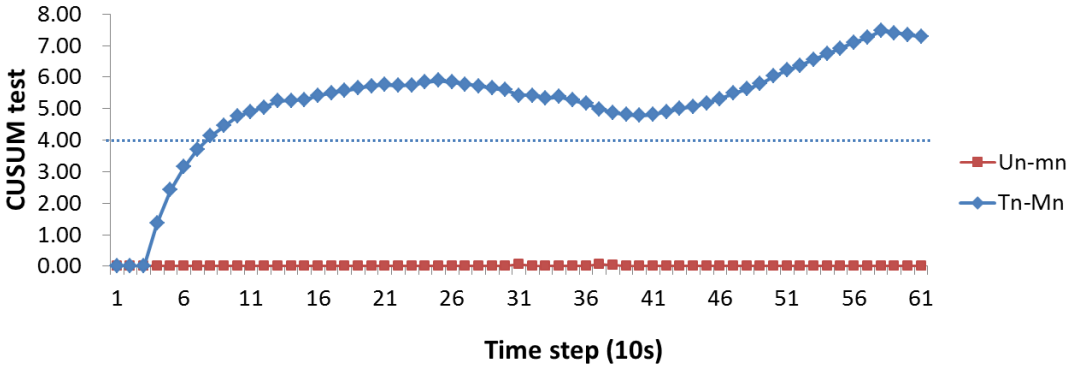

(b) $T_{ice,\ out}$

Figure 7.6 CUSUM tests for fault diagnosis parameters
(a) ΔT_{water}, (b) $T_{ice,\ out}$

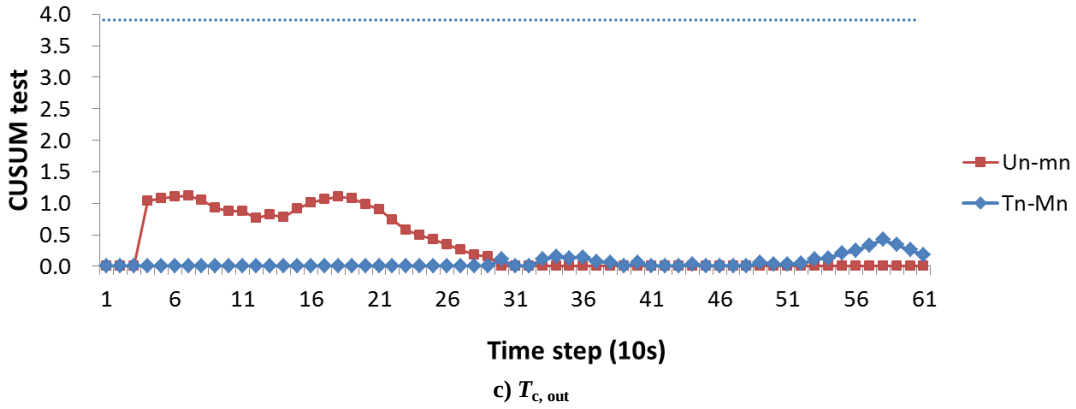

c) $T_{c,\,out}$

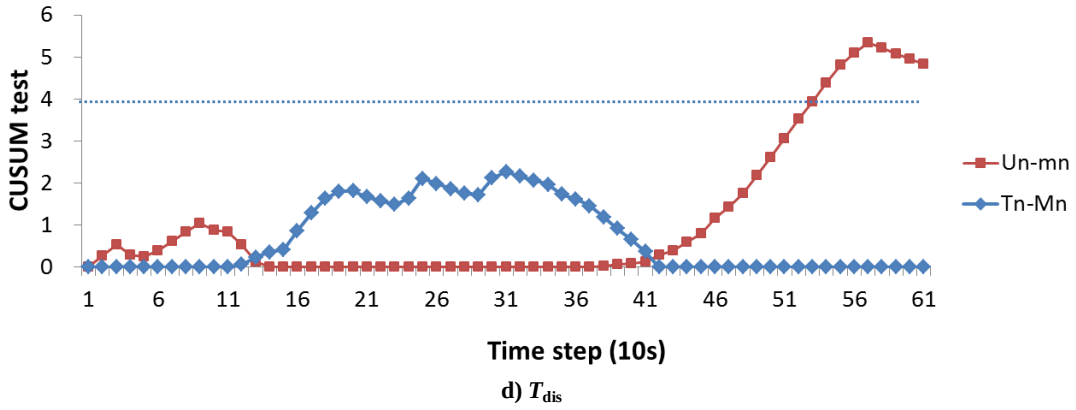

d) T_{dis}

Figure 7.6 CUSUM tests for fault diagnosis parameters (continued) (c) $T_{c,\,out}$, and d) T_{dis}

Table 7.2 fault diagnosis pattern for the parameters in Figure 7.5

$T_{c,\,out}$	ΔT_{water}	T_{dis}	$T_{ice,\,out}$
0	0	1	-1

Table 7.3 Fault diagnosis results

Fault	Cooling water flow reduction			Binary ice flow reduction			Concentration increase		Concentration decrease		SSIG faulty blade	SSIG blade motor failure
Level	1	2	3	1	2	3	1	2	1	2		
Correct diagnose	1/2	3/3	3/3	0/1	1/2	3/3	2/3	3/3	3/3	3/3	2/2	3/3

Table 7.3 shows the number of correct diagnoses based on a successful detection. The diagnosis of binary ice flow reduction once again has the poorest

accuracy. At the severity level 1, among the three faulty data sets, only one was detected successfully, as shown in Table 7.1, but the FDD failed to diagnose it. For level 2, only one of the two detected faults was correctly diagnosed. But as the fault becoming more severe the diagnose method shows a better performance with a 100% success rate.

Another two incorrect diagnoses are found in level 1 for cooling water flow reduction (only one of the two detected faults was identified correctly) and level 1 for concentration increase (with 66.6% success rate). In both cases the FDD was unable to diagnose which should not be confused with mis-diagnosis. The last three faults in Table 7.3 were found to have 100% diagnosis rate.

Tests for double fault FDD detection were also carried. Similar to the previous tests, three data sets were applied, each contained one compressor off/on cycle. All the faults were taken at their highest severity levels. As previously discussed, the fault BR and SCI have a similar pattern, therefore the residuals of the FDD parameters become larger, making the detection easier. All three data sets were correctly detected. The detection speed was faster than both of the single fault detections. The detected faults were also diagnosed correctly, suggesting the residual rate method (Chapter 6) is capable of distinguishing between a double fault and a single fault with the same pattern.

For the CR+SCI fault, as they cancel the effect of each other, the detection is less accurate, only 2 of the 3 data sets were detected as faulty but both were diagnosed correctly. The detection of the double fault is relatively slower than the individual single faults, due to smaller residual involved.

The three sets of BR+BS faults were all detected and diagnosed successfully. As the two faults did not have much influence on each other, the detection speed of the double fault followed the faster one of the two single fault detections, which was at time step 40 for BS.

Table 7.4 Double fault detection and diagnosis results

Fault	BR+SCI	CR+SCI	BR+BS
Correct detection	3	2	3
Detection speed (time step)	32	42	40
Correct diagnose	3	2	3

7.3 Discussion

As the results of the hybrid model were discussed in Chapter 5, this discussion mainly focusses on the performance of the FDD.

With the use of the hybrid prediction model, it can be seen from the results that the proposed FDD approach is able to reliably detect and diagnosis most of the pre-selected faults, including both the faults that common to many other refrigeration systems and those unique to binary ice systems. The unique characterises of binary ice and features of the binary ice system necessitate the careful selection of the FDD parameters, especially the output parameters, also taking into consideration their sensitivities to the selected fault as well as their ability to form unique patterns for individual faults.

The binary ice test rig is incorporated a compressor on/off thermostat to control the binary ice temperature at the outlet of the tank (i.e. the inlet of SSIG). Though the hybrid model is capable of predicting the periodical variations of various parameters, large modelling errors were encountered during the on/off switching moments. It is possible to improve the accuracy by using more training data collected from the measurements.

As stated in the beginning of this thesis, the existing FDD approaches for conventional chillers are not suitable for binary ice system. This is proved later by noting the secondary flow temperature difference (ΔT_{ice}) having a small sensitivity factor, which was often used by the others for chillers faults. Therefore, new FDD parameters are needed. Unlike many other FDD techniques which normally used the same parameters for both fault detection and diagnosis, the proposed method uses two separate groups of parameters. For the specified faults, two parameters (T_e and ΔT_{water}) are found needed for the detection purposes and a minimum of 4 parameters (ΔT_{water}, $T_{ice,\,out}$, $T_{c,\,out}$, and T_{dis}) are needed for the diagnosis.

As only two parameters, compared to usually 4 or 5 used by the others, are needed for detection, accordingly there will be less chances of a false alarm, assuming only one of two is needed to trigger an alarm for a given fault, with an additional

benefit of having a reduced real-time monitoring resources requirement for the fault detection. However, if the FDD is designed in such a way that more than one parameter are needed simultaneously to trigger an alarm for the fault, then the false alarm rate should reduce with increasing number of parameters involved. In addition, the selected parameters only involved temperature measurements which are relatively easy to implement.

Beside the selection of the parameters, the performance of the FDD is mainly depended on the thresholds, in particular the value of λ used in the CUSUM test. The current setting of λ is capable of detecting and diagnosing the majority of faults. In this study, λ is kept at 4, though as previously stated, detection could have been made around 2 minutes early if a λ of 2 were, as a 2 minute delay is considered insignificant for binary ice system. The elimination of false alarm is considered more important. Furthermore, the reduction of λ do not help improve the accuracies of the detection or diagnosis in the current study.

Another way of selecting the threshold for dynamic FDD is to use adaptable threshold. The calculations of the adaptable threshold are usually complicated, relating to some specified parameters in a particular system, such as the modelling error and the heat load (Cui and Wang 2005; Estrada-Flores et al. 2006). It is difficult to adapt the threshold calculation method of one system to another. On the contrary, a CUSUM test is common to various systems and its application is much easier. As a result, CUSUM test is selected for this project instead of adaptable threshold.

As shown in Table 7.1 and 7.3, there are both mis-detections and mis-diagnosis. To improve the performance, one possibility is to incorporate additional parameters. The fault with the lowest detection and diagnosis rate is the binary ice flow reduction. It will be helpful if, say, the electrical conductivity of the solution is monitored in real time, though it was unlikely to be implemented in practice due to cost and maintenance issues.

Although all the mis-diagnosis encountered in the current study are reported as unable to determine, it is also possible that one fault can be mis-diagnosed as another one when the two faults shared a similar fault pattern. One example is the binary ice flow reduction (Fault 1) and the solution concentration increase (Fault 3). It is noted

from Table 6.9 that the two faults cause the same variations in two parameters (T_{dis} and $T_{ice,out}$), and the other two parameters ($T_{c,out}$ and ΔT_{water}) decrease under the latter fault but stay unchanged for the former. Also, the sensitivity factors of $T_{c,out}$ and ΔT_{water} in Table 6.3 for the Fault 3 during the compressor on cycle are relatively small (both were -1). Therefore, it is likely that this fault can be mis-diagnosed as Fault 1, especially when the fault severity level is low. In this situation, it might be necessary to identify additional diagnosis parameters. However, when considering Fault 5 (the broken scraper) and Fault 6 (scraper motor failure) which also have similar patterns, and could only be separated by one parameter (ΔT_{water}), it is believed that these two faults are less likely to be confused during diagnosis because change of ΔT_{water} when Fault 6 occurs is more prominent (sensitivity factor -2.5).

The proposed FDD approach at present is designed to tackle certain specified faults, assuming no other types of fault will occur in the system at the same time. However If a fault which is not considered in this study occurs in the system, it may be mis-diagnosed as one of the six faults or reported as not able to diagnose.

As mentioned before, the SSIG can work in three modes, namely no ice in and no ice out, no ice in but ice out, and no ice in and no ice out. The analytical SSIG model has been shown to be able to differentiate the individual modes, thus the hybrid model is also capable of FDD in any of the 3 modes. The results for second mode are extensively presented in previous chapters. Not much data on first mode was collected as it was very much similar to chiller operation. Again, no false alarm was flagged during the tests. A detection rate of 100% for all selected fault and a diagnosis rate of 66% was obtained based on the same 6 parameters above. Only a very limited number of tests were performed as it was considered unsafe to run the system with high ice concentration which could potentially break the blades or overload the motor.

Strictly speaking, the duration of a fault free cycle differs from that of a faulty cycle, and their differences vary with the type and severity of the fault. As the proposed hybrid model is not capable of predicting the cycle durations, in the current study, the fault free parameters predicted at a particular instant are calculated based on the inputs ($T_{ice,in}$ and $T_{water,in}$) measured at the same time, not knowing if the inputs are from a faulty or fault free condition. This is considered acceptable based on the following observation. The deviations between the measured data from a fault free

cycle and a faulty cycle (as seen in Tables 6.3 and 6.4) are compared to the deviations between fault free predicted data and measured faulty data. Almost identical patterns of variations are noted.

The proposed FDD method is able to diagnose three pairs of double fault. As summarised by Cho et al. (2005), there are three types of interaction between two faults. Their first type of interaction (i.e. the magnitude of residuals of the single faults are similar with the double fault) is not applicable as such behaviour was not seen in the current study. Instead, another type of interaction is noticed, where the double faults have opposite influences on the system and their residuals cancel out each other.

8. Conclusions

An approach to detect and diagnose certain pre-specified faults in a binary ice system has been proposed and developed. A number of single and double faults are considered in the study; most of them are unique to the binary ice system though a fault common to both conventional water-cooled chillers and binary ice system is also included. The fault detection and diagnosis is based on comparing the measurements from a re-commissioned test rig with the predictions from a simulation model specifically developed for this study. Both binary ice and binary ice system have unique and different characteristics when compared to convention secondary systems, and thus existing FDD techniques are considered not applicable. As far as the author is aware, this is the first time a FDD approach has been developed for a binary ice system.

A hybrid approach is used to construct the dynamic simulation model that is based on a novel coupling of an ANN model of the primary refrigeration circuit with an analytical model of the scraped surface ice generator. The NARX ANN model is essentially a neural network with a tapped-delay-line to simulate the dynamic behaviour. On the other hand, the analytical model is a quasi-steady state distributed model based on mass and energy balances.

Using a unique combination of three set-parameters (flowrates of the binary ice and the condenser cooling water, and the initial solution concentration) and two measured control variables (cooling water inlet temperate to the condenser and binary ice inlet temperature to the SSIG), as well as looping two ANN outputs (evaporating temperature and compressor power consumption) as inputs to the analytical model, the coupled hybrid model is capable of predicting a range of fault free parameters under transient conditions. Extensive validations have been carried out and it is found in general, the measurements agree well with the predictions.

A huge amount of data has been collected from the test rig and generated by the model. Observations based on the data enable the author to gain a better insight and understanding (an objective of this study) into the operation behaviour of the SSIG as well as the binary ice system as a whole, in particular how various

parameters, including unmeasured ones, vary under both fault free and faulty conditions.

Having carefully analysed the residuals of various parameters together with their sensitivities towards the specified faults, it is concluded that only two parameters are needed for detection. Unlike many conventional chiller FDDs that use the temperature difference of the secondary fluid across the chiller as a detection parameter, plus probably 3 or 4 more other parameters, the current approach only uses the evaporating temperature and the temperature difference of the cooling water instead; this again reflects the unique features of the binary system. No other measurements such as pressure and flowrate need to be monitored for the fault detection purpose; this should reduce instrumentation resources and simplify the implementation of the proposed approach.

Based on the changes of the residuals of the parameters under various faults, it is found that four parameters, namely the refrigerant temperature at the compressor discharge and condenser outlet, the temperature difference of the cooling water across the condenser and binary temperature at the SSIG outlet, are sufficient to identify all the individual faults, each has a unique pattern of their residual variations.

CUSUM test is successfully applied to monitor the time-variations of residuals of the selected parameters, enabling both detection and diagnosis be carried reliably at any instant without the need to acquire any steady state status. The influence of the thresholds are systematically examined and evaluated, and by carefully choosing an appropriate combination of the thresholds needed in the CUSUM test, it has been proved possible to eliminate any false alarm in the current study. A great deal of effort is devoted to understand the application and implementation of CUSUM test to ensure the transient results are interpreted correctly.

The FDD performances with respect to diagnosis accuracy are examined. Though the overall FDD performance is considered satisfactory, the accuracies for the diagnosis of the binary ice flow reduction fault are generally lower than other specified faults due to the fact that the chosen parameters are relatively less sensitive to this fault, suggesting that some additional parameters need to be identified to improve accuracy.

The developed FDD are used to diagnose 3 sets of specified double faults, i.e. when two single faults occur simultaneously. The interactions between two faults are examined in details and their fault patterns are analysed. In particular, when two single fault patterns are similar to that of the associated double fault, the concept of comparing the residual ratio of two chosen diagnosis parameters is used successfully to differentiate the single and the double fault. The study also includes a case when the two single faults have their influence cancelled out each other; to the author's knowledge this has not been done before by other researchers. However, there is one type of previously reported interaction that is not seen in the current study of the chosen faults, i.e. the magnitudes of residuals of the single faults are similar with the double fault.

Various obstacles and limitations have been encountered, some are related to the inherent characteristics of the test rig and some are related to the model's incapability to provide accurate predictions during compressor on-off moments. Measures and ideas are devised and implemented to resolve the issues, including, say, the generation of "artificial" data to "experimentally simulate" a broken blade, and designing the FDD in such a way that the COP and Q_e are not included as detection and diagnosis parameters since the test rig has not got a refrigerant mass flowrate meter. The idea of "removing" some of the residual data during compressor on-off switching moments is also found to be effective in eliminating the false alarm caused by the erroneous residuals.

Further works have been identified for improving the accuracy of the model and to expand the scope of the work.

The developed approach is directly applicable for real time FDD. It will be useful to see how the FDD performs for variable loads and ambient temperatures. The FDD approach can be further developed to tackle other faults. It would be interesting to see for example how the system behaviour evolves in transient manner under a refrigerant leakage fault. They could enable early detection before a substantial quantity of refrigerant is lost.

The analytical model can be improved by using a calculated heat transfer coefficient h_o based on the evaporating temperature and the refrigerant mass flowrate

instead of the assumed constant value. As the changes of h_o become more significant when the temperature of the secondary fluid changes (i.e. under variable loads or different initial solution concentrations), a pre-set h_o value may not be valid. The performance of the FDD could also be improved by using some additional sensors and parameters. One possible parameter is the compressor power consumption, if a better power transducer is available to provide more reliable readings.

In practice, it is not uncommon to see a thermal storage unit incorporated into a binary system; it would be useful to expand the project to include this type of secondary circuit. As various control mechanisms have been applied in HVAC systems in addition to the on/off control in this study, (e.g. variable speed fans, direct digital control, etc.) It would also be necessary to improve the FDD method so that it can be used for binary ice systems with different kind of controls.

The project aims to achieve the following three main objectives:

(i) To fully understand the operation (both steady and dynamic) and control characteristics of a binary ice system as well as the scraped surface ice generator, under both faulty and fault-free conditions.

(ii) To build a dynamic hybrid model to predict the behaviour of binary ice system by coupling an analytical model of the ice generator and a system level ANN model.

(iii) To develop a FDD approach that can be employed to detect several pre-defined single faults in a binary ice system. The approach should be capable of detecting the faults without a steady state detector, i.e. under transient conditions, and of identifying some pre-defined double faults.

Overall, it can be concluded that the set objectives are fulfilled satisfactory and the study was considered unique and novel. Six faults in the binary ice system, namely condensing water flow reduction, binary ice flow reduction, increase or decrease of solution concentrations, ice generator broken blade and motor failure, can be diagnosed reliably based on six temperature measurements.

References

Admiraal, D. M. and Bullard, C. (1993). "Heat transfer in refrigerator condensers and evaporators." Urbana **51**: 61801.

Albrecht, S., Busch, J., Kloppenburg, M., Metze, F. and Tavan, P. (2000). "Generalized radial basis function networks for classification and novelty detection: self-organization of optimal Bayesian decision." Neural Networks **13**(10): 1075-1093.

Arora, R. C. (2010). Refrigeration and air conditioning, PHI Learning Pvt. Ltd.

Assawamartbunlue, K. (2000). "Fault detection and diagnosis for refrigerant leakage in a distributed refrigeration system for supermarket applications."

Assawamartbunlue, K. and Brandemuehl, M. J. (2006). "Refrigerant leakage detection and diagnosis for a distributed refrigeration system." HVAC&R Research **12**(3): 389-405.

Ayel, V., Lottin, O. and Peerhossaini, H. (2003). "Rheology, flow behaviour and heat transfer of ice slurries: a review of the state of the art." International Journal of Refrigeration **26**(1): 95-107.

Bailey, M. B. and Kreider, J. F. (2003). "Creating an automated chiller fault detection and diagnostics tool using a data fault library." ISA transactions **42**(3): 485-495.

Bar-Yam, Y. (2003). "Dynamics of complex systems."

Barnard, E. and Cole, R. A. (1989). A neural-net training program based on conjugate-gradient optimization, Oregon Graduate Center.

Basseville, M. (1986). On-line detection of jumps in mean. Detection of abrupt changes in signals and dynamical systems, Springer**:** 9-26.

Basseville, M. and Benveniste, A. (1983). "Desgin and comparative study of some sequential jump detection algorithms for digital signals." Acoustics, Speech and Signal Processing, IEEE Transactions on **31**(3): 521-535.

Basseville, M. E. and Nikiforov, I. V. (1993). "Detection of abrupt changes: theory and application."

Bechtler, H., Browne, M., Bansal, P. and Kecman, V. (2001). "New approach to dynamic modelling of vapour-compression liquid chillers: artificial neural networks." Applied thermal engineering **21**(9): 941-953.

Becker, L., Kasza, K., Jayakar, D., Williams, U., Padrid, P., Idris, A. and Hoek, T. (2000). "Rapid induction of hypothermia using phase-change ice slurry: targeted cooling of the heart and brain during cardiac arrest." Circulation A **2769**.

Bellas, I. and Tassou, S. (2005). "Present and future applications of ice slurries." International Journal of Refrigeration **28**(1): 115-121.

Bendapudi, S., Braun, J. and Groll, E. (2002a). "A dynamic model of a vapor compression liquid chiller."

Bendapudi, S., Braun, J. E., American Society of Heating, R. and Engineers, A.-C. (2002b). A review of literature on dynamic models of vapor compression equipment.

Billings, S. A. (2013). Nonlinear system identification: NARMAX methods in the time, frequency, and spatio-temporal domains, John Wiley & Sons.

Bingham, E. C. (1917). An investigation of the laws of plastic flow, Govt. Print. Off.

Bishop, C. M. (2006). Pattern recognition and machine learning, springer New York.

Björck, Å. (1996). Numerical methods for least squares problems, Society for Industrial Mathematics.
Bongers, P. M. (2006). "A heat transfer model of a scraped surface heat exchanger for ice cream." Computer Aided Chemical Engineering **21**: 539-544.
Box, G. and Ramirez, J. (1992). "Cumulative score charts." Quality and Reliability Engineering International **8**(1): 17-27.
Braun, J. (2003). "Automated fault detection and diagnostics for vapor compression cooling equipment." Journal of solar energy engineering **125**: 266.
Braun, J. E. (1988). Methodologies for the design and control of central cooling plants, University of Wisconsin-Madison.
Braun, J. E. (1999). "LITERATURE REVIEW FOR APPLICATION OF FAULT DETECTION AND DIAGNOSTIC METHODS TO VAPOR COMPRESSION COOLING EQUIPMENT."
Breuker, M. and Braun, J. (1998a). "Common faults and their impacts for rooftop air conditioners." INTERNATIONAL JOURNAL OF HEATING VENTILATION AIR CONDITIONING AND REFRIGERATING RESEARCH **4**: 303-318.
Breuker, M. S. and Braun, J. E. (1998b). "Evaluating the performance of a fault detection and diagnostic system for vapor compression equipment." HVAC&R Research **4**(4): 401-425.
Brooker, R. F., Zvara, D. A., Velvis, H. and Prielipp, R. C. (1997). "Topical ice slurry prevents brain rewarming during deep hypothermic circulatory arrest in newborn sheep." Journal of cardiothoracic and vascular anesthesia **11**(5): 591-594.
Browne, M. and Bansal, P. (2000). "Modelling of in-situ liquid chillers."
Browne, M. and Bansal, P. (2002). "Transient simulation of vapour-compression packaged liquid chillers." International Journal of Refrigeration **25**(5): 597-610.
Bryson, A. E. and Ho, Y. C. (1975). Applied optimal control: optimization, estimation, and control, Hemisphere Pub.
Butcher, J. C. and Wiley, J. (2008). Numerical methods for ordinary differential equations, Wiley Online Library.
Byrd, L. and Mulligan, J. (1986). "A population balance approach to direct contact secondary refrigerant freezing." AIChE Journal **32**(11): 1881-1888.
Campos, C. A., Rodríguez, Ó., Losada, V., Aubourg, S. P. and Barros-Velázquez, J. (2005). "Effects of storage in ozonised slurry ice on the sensory and microbial quality of sardine (Sardina pilchardus)." International journal of food microbiology **103**(2): 121-130.
Castro, N. (2002). "Performance evaluation of a reciprocating chiller using experimental data and model predictions for fault detection and diagnosis." ASHRAE Transactions **108**(1): 889-903.
Chen, Y. and Lan, L. (2009). "A fault detection technique for air-source heat pump water chiller/heaters." Energy and Buildings **41**(8): 881-887.
Chetouani, Y. (2008). "A neural network approach for the real-time detection of faults." Stochastic Environmental Research and Risk Assessment **22**(3): 339-349.
Chiang, L. H., Braatz, R. D. and Russell, E. L. (2001). Fault detection and diagnosis in industrial systems, Springer.

Cho, S. H., Hong, Y. J., Kim, W. T. and Zaheer‐uddin, M. (2005). "Multi‐fault detection and diagnosis of HVAC systems: an experimental study." International journal of energy research **29**(6): 471-483.

Clifford, A. A. (1973). Multivariate error analysis: A handbook of error propagation and calculation in many-parameter systems, Applied Science Publishers.

Comstock, M. and Braun, J. (1999). "Development of analysis tools for the evaluation of fault detection and diagnostics in chillers." Report# HL99-20. Purdue University, Ray W. Herrick Laboratories, West Lafayette, IN.

Comstock, M., Braun, J. and Groll, E. (2002a). "The sensitivity of chiller performance to common faults." ASHRAE Transactions **108**(1): 467.

Comstock, M., Braun, J. and Groll, E. (2002b). "A survey of common faults for chillers." ASHRAE Transactions **108**(1): 819-825.

Cui, J. and Wang, S. (2005). "A model-based online fault detection and diagnosis strategy for centrifugal chiller systems." International Journal of Thermal Sciences **44**(10): 986-999.

Cybenko, G. (1989). "Approximation by superpositions of a sigmoidal function." Mathematics of control, signals and systems **2**(4): 303-314.

Darbouret, M., Cournil, M. and Herri, J.-M. (2005). "Rheological study of TBAB hydrate slurries as secondary two-phase refrigerants." International Journal of Refrigeration **28**(5): 663-671.

Davies, T. (2005). "Slurry ice as a heat transfer fluid with a large number of application domains." International Journal of Refrigeration **28**(1): 108-114.

Davies, T. and Lowes, A. (2002). A high efficiency refrigeration system. Proceedings of a Conference on New.

Dehghan, M., Mahmoudi, Y., Valipour, M. S. and Saedodin, S. (2015). "Combined conduction–convection–radiation heat transfer of slip flow inside a micro-channel filled with a porous material." Transport in Porous Media **108**(2): 413-436.

Ding, X., Cai, W., Jia, L. and Wen, C. (2009). "Evaporator modeling–A hybrid approach." Applied Energy **86**(1): 81-88.

Egolf, P. W. and Kauffeld, M. (2005). "From physical properties of ice slurries to industrial ice slurry applications." International Journal of Refrigeration **28**(1): 4-12.

Ertunc, H. and Hosoz, M. (2006). "Artificial neural network analysis of a refrigeration system with an evaporative condenser." Applied thermal engineering **26**(5-6): 627-635.

Estrada-Flores, S., Merts, I., De Ketelaere, B. and Lammertyn, J. (2006). "Development and validation of "grey-box" models for refrigeration applications: a review of key concepts." International Journal of Refrigeration **29**(6): 931-946.

Everitt, B. and Skrondal, A. (2002). The Cambridge dictionary of statistics, Cambridge University Press New York.

Frei, B. and Egolf, P. (2000). Viscometry applied to the Bingham substance ice slurry. 2nd Workshop on Ice Slurries, Paris, IIR Paris.

Fukusako, S., Kozawa, Y., Yamada, M. and Tanino, M. (1999). Research and development activities on ice slurries in Japan.

Ge, X. and Wang, X. (2009). "Calculations of Freezing Point Depression, Boiling Point Elevation, Vapor Pressure and Enthalpies of Vaporization of Electrolyte Solutions by a Modified Three-Characteristic Parameter Correlation Model." Journal of solution chemistry **38**(9): 1097-1117.

Gertler, J. (1998). Fault detection and diagnosis in engineering systems, CRC press.
Gladis, S. (1997). "Ice Slurry Thermal Energy Storage for Cheese Process Cooling." ASHRAE Transactions **103**(Part 2).
Glorot, X. and Bengio, Y. (2010). Understanding the difficulty of training deep feedforward neural networks. International Conference on Artificial Intelligence and Statistics.
Gordon, J. and Ng, K. (2000). Cool Thermodynamics, Cambridge Int, Science Publishers, Cambridge.
Grace, I., Datta, D. and Tassou, S. (2005). "Sensitivity of refrigeration system performance to charge levels and parameters for on-line leak detection." Applied thermal engineering **25**(4): 557-566.
Greco, A. and Vanoli, G. (2005). "Flow-boiling of R22, R134a, R507, R404A and R410A inside a smooth horizontal tube." International Journal of Refrigeration **28**(6): 872-880.
Groeneveld, R. A. and Meeden, G. (1984). "Measuring skewness and kurtosis." Journal of the Royal Statistical Society. Series D (The Statistician) **33**(4): 391-399.
Gross, K., Singer, R., Wegerich, S., Herzog, J., VanAlstine, R. and Bockhorst, F. (1997). Application of a model-based fault detection system to nuclear plant signals. Proc. 9th Intnl. Conf. On Intelligent Systems Applications to Power Systems.
Guilpart, J., Stamatiou, E. and Fournaison, L. (2005). "The control of ice slurry systems: an overview." International Journal of Refrigeration **28**(1): 98-107.
Hägg, C. (2005). "Ice slurry as secondary fluid in refrigeration systems." School of Industrial Engineering and Management, Licentiate Thesis, Stockholm.
Halm-Owoo, A. and Suen, K. (2002). "Applications of fault detection and diagnostic techniques for refrigeration and air conditioning: a review of basic principles." Proceedings of the Institution of Mechanical Engineers, Part E: Journal of Process Mechanical Engineering **216**(3): 121-132.
Harrou, F., Kadri, F. and Sun, Y. (2015). "Improved Principal Component Analysis for Anomaly Detection: Application to an Emergency Department." Computers & Industrial Engineering.
Haves, P. and Khalsa, S. (2000). "Model-based performance monitoring: Review of diagnostic methods and chiller case study." Lawrence Berkeley National Laboratory.
He, X. D., Liu, S. and Asada, H. H. (1997). "Modeling of vapor compression cycles for multivariable feedback control of HVAC systems." Journal of dynamic systems, measurement, and control **119**: 183.
Hinkley, D. V. (1971). "Inference about the change-point from cumulative sum tests." Biometrika **58**(3): 509-523.
House, J. M., Lee, W. Y. and Shin, D. R. (1999). "Classification techniques for fault detection and diagnosis of an air-handling unit." TRANSACTIONS-AMERICAN SOCIETY OF HEATING REFRIGERATING AND AIR CONDITIONING ENGINEERS **105**: 1087-1100.
Hu, Q., Li, K. and So, A. T. (2007). Two ANN-Based Models for a Real MVAC System. Wireless Communications, Networking and Mobile Computing, 2007. WiCom 2007. International Conference on, IEEE.
Ingrassia, S. and Morlini, I. (2007). Equivalent number of degrees of freedom for neural networks. Advances in Data Analysis, Springer**:** 229-236.

Isermann, R. (1997). "Supervision, fault-detection and fault-diagnosis methods—an introduction." Control engineering practice **5**(5): 639-652.
Isermann, R. (2005). "Model-based fault-detection and diagnosis–status and applications." Annual Reviews in control **29**(1): 71-85.
Jeffrey, D. (1973). "Conduction through a random suspension of spheres." Proceedings of the Royal Society of London. A. Mathematical and Physical Sciences **335**(1602): 355.
Jia, Y. and Reddy, T. (2003). "Characteristic physical parameter approach to modeling chillers suitable for fault detection, diagnosis, and evaluation." Journal of solar energy engineering **125**: 258.
Kaldorf, S. and Gruber, P. (2002). "Practical experiences from developing and implementing an expert system diagnostic tool/Discussion." ASHRAE Transactions **108**: 826.
Katipamula, S. and Brambley, M. (2005). "Methods for fault detection, diagnostics, and prognostics for building systems-A review, part I." HVAC&R Research **11**(1): 3-25.
Katipamula, S., Brambley, M. R. and Luskay, L. (2003). "Automated proactive techniques for commissioning air-handling units." Journal of solar energy engineering **125**(3): 282-291.
Kauffeld, M., Christensen, K. G., Lund, S. and Hansen, T. M. (1999). Experience with ice slurry.
Kauffeld, M., Kawaji, M. and Egolf, P. W. (2005). Handbook on Ice Slurries: Fundamentals and Engineering, Institut international du froid= International institute of refrigeration.
Kauffeld, M., Wang, M., Goldstein, V. and Kasza, K. (2010). "Ice Slurry Applications." International Journal of Refrigeration.
Kelso, R. M. and Wright, J. A. (2005). "Application of fault detection and diagnosis techniques to automated functional testing."
Kidd, J. (1995). "Slurry ice production in gold mining." SOUTH AFRICAN MECHANICAL ENGINEER **45**: 11-14.
Kim, M., Yoon, S. H., Payne, W. V. and Domanski, P. A. (2010). "Development of the reference model for a residential heat pump system for cooling mode fault detection and diagnosis." Journal of mechanical science and technology **24**(7): 1481-1489.
Klaren, D. and Van Der Meer, J. (1991). "A fluidized bed chiller: A new approach in making slush-ice."
Knodel, B., France, D., Choi, U. and Wambsganss, M. (2000). "Heat transfer and pressure drop in ice-water slurries." Applied thermal engineering **20**(7): 671-685.
Koury, R., Machado, L. and Ismail, K. (2001). "Numerical simulation of a variable speed refrigeration system." International Journal of Refrigeration **24**(2): 192-200.
Kubat, M. (1999). Neural networks: a comprehensive foundation, Cambridge Univ Press.
Kumano, H., Hirata, T., Shirakawa, M., Shouji, R. and Hagiwara, Y. (2010a). "Flow characteristics of ice slurry in narrow tubes." International Journal of Refrigeration **33**(8): 1513-1522.
Kumano, H., Hirata, T., Shouji, R. and Shirakawa, M. (2010b). "Experimental study on heat transfer characteristics of ice slurry." International Journal of Refrigeration **33**(8): 1540-1549.

Lakhdar, M. B., Cerecero, R., Alvarez, G., Guilpart, J., Flick, D. and Lallemand, A. (2005). "Heat transfer with freezing in a scraped surface heat exchanger." Applied thermal engineering **25**(1): 45-60.

Laven, B. A., Kasza, K. E., Rapp, D. E., Orvieto, M. A., Lyon, M. B., Oras, J. J., Beiser, D. G., Vanden Hoek, T. L., Son, H. and Shalhav, A. L. (2007). "A pilot study of ice‐slurry application for inducing laparoscopic renal hypothermia." BJU international **99**(1): 166-170.

Lee, D. W., Yoon, E. S., Joo, M. C. and Sharma, A. (2006). "Heat transfer characteristics of the ice slurry at melting process in a tube flow." International Journal of Refrigeration **29**(3): 451-455.

Lee, T. (2004). "Thermodynamic Modeling and Experimental Validation of Screw Liquid Chillers." TRANSACTIONS-AMERICAN SOCIETY OF HEATING REFRIGERATING AND AIR CONDITIONING ENGINEERS **110**(1): 206-216.

Lowes, A. (2002). Fire-fighting apparatus and a method of fighting fire.

Lu, P., Van Eykeren, L., van Kampen, E.-J., de Visser, C. and Chu, Q. (2015). "Double-model adaptive fault detection and diagnosis applied to real flight data." Control engineering practice **36**: 39-57.

Lueders, D. (1999). Application of ice slurry/TES technology to supermarkets using ammonia refrigeration. Proceedings of the 21st Annual Meeting of the International Meeting of Ammonia Refrigeration.

MacQueen, J. (1967). Some methods for classification and analysis of multivariate observations. Proceedings of the fifth Berkeley symposium on mathematical statistics and probability, California, USA.

Marcos, A., Ganguli, S. and Balas, G. J. (2005). "An application of H∞ fault detection and isolation to a transport aircraft." Control engineering practice **13**(1): 105-119.

McIntosh, I., Mitchell, J. and Beckman, W. (2000). "Fault detection and diagnosis in chillers-Part I: Model development and application." TRANSACTIONS-AMERICAN SOCIETY OF HEATING REFRIGERATING AND AIR CONDITIONING ENGINEERS **106**(2): 268-282.

Melinder, A. (1997). "Thermophysical properties of liquid secondary refrigerants; Proprietes thermophysiques des frigoporteurs liquides."

Melinder, Å. (2007). Thermophysical properties of aqueous solutions used as secondary working fluids, KTH.

Mito, D., Kozawa, Y., Tanino, M. and Inada, T. (2000). "Development of Active Control Method for Supercooling Releasing of Water." Transactions **17**(2): 191-201.

Navarro-Esbrį J., Berbegall, V., Verdu, G., Cabello, R. and Llopis, R. (2007). "A low data requirement model of a variable-speed vapour compression refrigeration system based on neural networks." International Journal of Refrigeration **30**(8): 1452-1459.

Navarro-Esbrį J., Torrella, E. and Cabello, R. (2006). "A vapour compression chiller fault detection technique based on adaptative algorithms. Application to on-line refrigerant leakage detection." International Journal of Refrigeration **29**(5): 716-723.

Ng, J. S. K. C. (2008). "Predictive and Diagnostic Methods for Centrifugal Chillers." ASHRAE Transactions **114**(1): 6.

Nyers, J. and Stoyan, G. (1994). "A dynamical model adequate for controlling the evaporator of a heat pump." International Journal of Refrigeration **17**(2): 101-108.
Oakland, J. S. (2008). Statistical process control, Routledge.
Page, E. (1954). "Continuous inspection schemes." Biometrika **41**(1/2): 100-115.
Paul, J. (1992). Binary ice-technologies for the production of pumpable ice-slurries.
Paul, J. J., E; Lausen, D (1996). Cooling of mines with vacuum ice. Proceedings of the FRIGAIR'96 Conference. Johannesburg, South Africa.
Peitsman, H. and Bakker, V. (1996). "Application of black-box models to HVAC systems for fault detection." TRANSACTIONS-AMERICAN SOCIETY OF HEATING REFRIGERATING AND AIR CONDITIONING ENGINEERS **102**: 628-640.
Platt, J. (1999). "Probabilistic outputs for support vector machines and comparisons to regularized likelihood methods."
Qin, F., Chen, X. D., Ramachandra, S. and Free, K. (2006). "Heat transfer and power consumption in a scraped-surface heat exchanger while freezing aqueous solutions." Separation and Purification Technology **48**(2): 150-158.
Qin, F. G. F., Chen, X. D. and Russell, A. B. (2003). "Heat transfer at the subcooled©\scraped surface with/without phase change." AIChE Journal **49**(8): 1947-1955.
Rao, C. S. and Hartel, R. W. (2006). "Scraped surface heat exchangers." Critical reviews in food science and nutrition **46**(3): 207-219.
Rasmussen, B. D. and Jakobsen, A. (2000). "Review of compressor models and performance characterizing variables."
Reddy, T. (2006). "Evaluation and assessment of fault detection and diagnostic methods for centrifugal chillers-phase II." ASHRAE Research Project RP-127.
Reddy, T. (2007a). "Development and Evaluation of a Simple Model-Based Automated Fault Detection and Diagnosis (FDD) Method Suitable for Process Faults of Large Chillers." TRANSACTIONS-AMERICAN SOCIETY OF HEATING REFRIGERATING AND AIR CONDITIONING ENGINEERS **113**(2): 27.
Reddy, T. (2007b). "LB-07-036 Formulation of a Generic Methodology for Assessing FDD Methods and Its Specific Adoption to Large Chillers (RP-1275)." ASHRAE Transactions **113**(2): 334-342.
Riemer, P. L., Mitchell, J. W. and Beckman, W. (2002). "The use of time series analysis in fault detection and diagnosis methodologies." ASHRAE Transactions **108**(2): 384-394.
Riffat, S., Afonso, C., Oliveira, A. and Reay, D. (1997). "Natural refrigerants for refrigeration and air-conditioning systems." Applied thermal engineering **17**(1): 33-42.
Rivet, P. (2009). Overview of PCM applications around the world -Regional overview Europe. 8th IIR Conference on Phase Change Materials and Slurries for Refrigeration and Air Conditioning. Karlsruhe.
Rossi, T. M. (1995). "Detection, diagnosis, and evaluation of faults in vapor compression equipment."
Rossi, T. M. and Braun, J. E. (1997). "A statistical, rule-based fault detection and diagnostic method for vapor compression air conditioners." HVAC&R Research **3**(1): 19-37.

Rueda, E., Tassou, S. and Grace, I. (2005). "Fault detection and diagnosis in liquid chillers." Proceedings of the Institution of Mechanical Engineers, Part E: Journal of Process Mechanical Engineering **219**(2): 117-125.

Rumelhart, D. E., Hintont, G. E. and Williams, R. J. (1986). "Learning representations by back-propagating errors." Nature **323**(6088): 533-536.

Salsbury, T. and Diamond, R. (2001). "Fault detection in HVAC systems using model-based feedforward control." Energy and Buildings **33**(4): 403-415.

Saththasivam, J. and Ng, K. (2008). "Predictive and diagnostic methods for centrifugal chillers." ASHRAE Trans **114**(1): 282-287.

Schein, J. and Bushby, S. T. (2006). "A hierarchical rule-based fault detection and diagnostic method for HVAC systems." HVAC&R Research **12**(1): 111-125.

Schein, J. and House, J. M. (2003). "Application of control charts for detecting faults in variable-air-volume boxes." TRANSACTIONS-AMERICAN SOCIETY OF HEATING REFRIGERATING AND AIR CONDITIONING ENGINEERS **109**(2): 671-682.

Schwartzberg, H. and Liu, Y. (1990). Ice crystal growth on chilled scraped surfaces.

Seeniraj, R. and Hari, G. S. (2008). "Transient freezing of liquids in forced flow inside convectively cooled tubes." International Communications in Heat and Mass Transfer **35**(6): 786-792.

Sekiya, A. and Misaki, S. (2000). "The potential of hydrofluoroethers to replace CFCs, HCFCs and PFCs." Journal of Fluorine Chemistry **101**(2): 215-221.

Sen, A. and Srivastava, M. S. (1990). Regression analysis: theory, methods, and applications, Springer.

Sharma, A., Tyagi, V., Chen, C. and Buddhi, D. (2009). "Review on thermal energy storage with phase change materials and applications." Renewable and Sustainable Energy Reviews **13**(2): 318-345.

Snoek, C. (1993). The design and operation of ice-slurry based district cooling systems, Netherlands Agency for Energy and the Environment.

Soyguder, S. and Alli, H. (2009). "An expert system for the humidity and temperature control in HVAC systems using ANFIS and optimization with Fuzzy Modeling Approach." Energy and Buildings **41**(8): 814-822.

Spatz, M. W. and Yana Motta, S. F. (2004). "An evaluation of options for replacing HCFC-22 in medium temperature refrigeration systems." International Journal of Refrigeration **27**(5): 475-483.

Sreedharan, P. and Haves, P. (2001). Comparison of chiller models for use in model-based fault detection, Citeseer.

Stamatiou, E., Meewisse, J. and Kawaji, M. (2005). "Ice slurry generation involving moving parts." International Journal of Refrigeration **28**(1): 60-72.

Steel, R. G. D. and Torrie, J. H. (1960). "Principles and procedures of statistics." Principles and procedures of statistics.

Stouppe, D. and Lau, Y. (1989). "Air conditioning and refrigeration equipment failures." National Engineer **93**(9): 14-17.

Stylianou, M. (1997). "Application of classification functions to chiller fault detection and diagnosis." TRANSACTIONS-AMERICAN SOCIETY OF HEATING REFRIGERATING AND AIR CONDITIONING ENGINEERS **103**: 645-656.

Swider, D. (2003). "A comparison of empirically based steady-state models for vapor-compression liquid chillers." Applied thermal engineering **23**(5): 539-556.

Swider, D., Browne, M., Bansal, P. and Kecman, V. (2001). "Modelling of vapour-compression liquid chillers with neural networks." Applied thermal engineering **21**(3): 311-329.

Tamasauskas, J., Poirier, M., Zmeureanu, R. and Suny é, R. (2012). "Modeling and optimization of a solar assisted heat pump using ice slurry as a latent storage material." Solar Energy **86**(11): 3316-3325.

Tan, S. C. and Lim, C. P. (2004). "Application of an adaptive neural network with symbolic rule extraction to fault detection and diagnosis in a power generation plant." Energy Conversion, IEEE Transactions on **19**(2): 369-377.

The MathWorks, I. (2010). Matlab neural network toolbox, The MathWorks, Inc.

Thomas, D. G. (1965). "Transport characteristics of suspension: VIII. A note on the viscosity of Newtonian suspensions of uniform spherical particles* 1." Journal of Colloid Science **20**(3): 267-277.

Venkatasubramanian, V., Rengaswamy, R., Yin, K. and Kavuri, S. N. (2003). "A review of process fault detection and diagnosis:: Part I: Quantitative model-based methods." Computers & Chemical Engineering **27**(3): 293-311.

Viser, J., Vaezi-Nejad, H. and Corrales, P. (1999). "A fault detection tool for school buildings." TRANSACTIONS-AMERICAN SOCIETY OF HEATING REFRIGERATING AND AIR CONDITIONING ENGINEERS **105**: 543-554.

Wang, M., Hansen, T., Kauffeld, M., Christensen, K. and Goldstein, V. (1999). Application of ice slurry technology in fishery. Proceedings of the 20th International Congress of Refrigeration, IIF/IIR.

Wang, M. and Kusumoto, N. (2001). "Ice slurry based thermal storage in multifunctional buildings." Heat and Mass Transfer **37**(6): 597-604.

Wang, S.-w., Wang, J. and Burnett, J. (2000). "Mechanistic model of centrifugal chillers for HVAC system dynamics simulation." Building services engineering research and technology **21**(2): 73-83.

Wang, S. and Cui, J. (2005). "Sensor-fault detection, diagnosis and estimation for centrifugal chiller systems using principal-component analysis method." Applied Energy **82**(3): 197-213.

Wang, Z., Liu, Y. and Griffin, P. J. (1998). "A combined ANN and expert system tool for transformer fault diagnosis." Power Delivery, IEEE Transactions on **13**(4): 1224-1229.

Werbos, P. (1974). "Beyond regression: New tools for prediction and analysis in the behavioral sciences."

Willsky, A. and Jones, H. (1976). "A generalized likelihood ratio approach to the detection and estimation of jumps in linear systems." Automatic Control, IEEE Transactions on **21**(1): 108-112.

Yegnanarayana, B. (2004). Artificial neural networks, PHI Learning Pvt. Ltd.

Yegnanarayana, B. (2009). Artificial neural networks, PHI Learning Pvt. Ltd.

Yeo, Z., Fan, P., Nio, A., Byrne, C. and Lee, J. (2012). "Ice slurry on outdoor running performance in heat." International journal of sports medicine **33**(11): 859.

Yik, F. W. and Lam, V. K. (1998). "Chiller models for plant design studies." Building services engineering research and technology **19**(4): 233-241.

Yoon, Y.-J. and Lee, M. H. (2010). "Dynamic simulation of vapor-compression cycle using neural networks." International Journal of Control, Automation and Systems **8**(6): 1241-1249.

Zalba, B., Mar ń, J. M., Cabeza, L. F. and Mehling, H. (2003). "Review on thermal energy storage with phase change: materials, heat transfer analysis and applications." Applied Thermal Engineering **23**(3): 251-283.

Zwieg, T. (2002). Ice nucleating non-stick coating, Google Patents.
ZWIEG, T., CUCARELLA, V. and KAUFFELD, M. (2007). "Novel biomimetically based ice-nucleating coatings." International journal of materials research **98**(7): 597-602.

Appendix

A. Calculation of properties of ethanol solution

The properties of ethanol-water solution under different temperature and concentration can be calculated by the following equation from *Thermophysical Properties of Liquid Secondary Refrigerant* (Melinder 1997).

$$\begin{aligned} f = {} & C_{00} + C_{01}(y-y_m) + C_{02}(y-y_m)^2 + C_{03}(y-y_m)^3 + \\ & + C_{10}(x-x_m) + C_{11}(x-x_m)(y-y_m) + C_{12}(x-x_m)(y-y_m)^2 + C_{13}(x-x_m)(y-y_m)^3 + \\ & + C_{20}(x-x_m)^2 + C_{21}(x-x_m)^2(y-y_m) + C_{22}(x-x_m)^2(y-y_m)^2 + C_{23}(x-x_m)^2(y-y_m)^3 + \\ & + C_{30}(x-x_m)^3 + C_{31}(x-x_m)^3(y-y_m) + C_{32}(x-x_m)^3(y-y_m)^2 + \\ & + C_{40}(x-x_m)^4 + C_{41}(x-x_m)^4(y-y_m) + \\ & + C_{50}(x-x_m)^5 \end{aligned} \qquad \text{A.1}$$

where f represents the properties that can be calculated including freezing point temperature T_f, density ρ, specific heat capacity C_p, thermal conductivity k and dynamic viscosity μ. For a given solution concentration (x, %) and fluid temperature (y, ℃), the properties can be determined using the coefficients x_m, y_m and C_{ij}, all determined by experiments, given below in Table A.1.

Table A.1 Coefficients for property calculation of ethanol-water solution with known solution concentration and temperature (Melinder 1997)

x_m = 38.9250, validity limits: 11% ≤ x ≤ 60% y_m = -4.9038, validity limits: T_f ≤ y ≤ 20 ℃						
i	j	T_f	ρ	C_p	k	μ
0	0	-2.842e+001	9.544e+002	3.925e+003	3.545e-001	2.214e+000
0	1	9.753e-006	-6.416e-001	3.876e+000	4.421e-004	-5.710e-002
0	2	-1.236e-005	-2.495e-003	2.300e-004	-2.942e-007	4.679e-004
0	3	6.378e-007	1.729e-005	1.322e-005	-1.115e-008	-1.374e-006
1	0	-8.563e-001	-1.729e+000	-2.795e+001	-4.334e-003	8.025e-004
1	1	5.274e-005	-1.824e-002	1.773e-001	-2.021e-005	2.618e-004
1	2	1.843e-006	3.116e-004	4.769e-005	-4.865e-009	-8.472e-006
1	3	-1.428e-007	-6.425e-007	3.008e-006	2.972e-010	1.478e-007
2	0	4.050e-003	-2.193e-002	-9.620e-002	3.021e-005	-7.330e-004
2	1	-3.058e-006	5.847e-004	-3.908e-003	4.239e-007	7.056e-006
2	2	-1.531e-007	-2.517e-006	1.951e-005	1.007e-009	2.473e-007
2	3	5.543e-009	-2.875e-008	3.366e-008	-7.325e-012	-1.329e-008
3	0	-1.179e-004	6.217e-004	7.580e-003	6.904e-007	4.285e-007
3	1	-9.416e-008	4.208e-006	2.283e-005	-3.203e-009	3.239e-007
3	2	4.676e-009	-3.460e-007	-9.149e-007	-1.439e-011	-1.234e-008
4	0	-1.992e-006	2.288e-006	-1.213e-004	-1.512e-008	4.313e-008
4	1	5.409e-009	-4.141e-007	2.545e-006	-3.486e-010	8.582e-009
5	0	2.951e-007	-6.412e-007	2.235e-007	-1.012e-009	7.654e-009

On the other hand, when the solution temperature and its freezing point are known, the above equation can be used to determine the solution concentration *C,* density ρ, specific heat conductivity C_p, thermal conductivity k and dynamic viscosity μ using the coefficients in Table A.2. Table A.1 and Table A.2 are used in Chapter 4 for the modelling of the SSIG

Table A.2 Coefficients for solution concentration and property calculation of ethanol-water solution when its temperature and freezing point are specified

x = T_f (℃); x_m = -27.8846, validity limits: -45 °C ≤ x ≤ -5 ℃ y = T (℃); y_m = -4.9038, validity limits: x ≤ y ≤ 20 °C						
i	j	C	ρ	C_p	k	μ
0	0	3.830e+001	9.554e+002	3.940e+003	3.573e-001	2.211e+000
0	1	1.853e-004	-6.281e-001	3.745e+000	4.570e-004	-5.724e-002
0	2	-6.849e-006	-2.644e-003	8.054e-004	-2.695e-007	4.705e-004
0	3	1.566e-007	1.597e-005	-5.778e-006	-1.221e-008	-1.358e-006
1	0	-1.174e+000	1.988e+000	3.195e+001	5.161e-003	-2.923e-003
1	1	-3.691e-005	2.195e-002	-2.061e-001	2.287e-005	-2.696e-004
1	2	-2.130e-007	-3.693e-004	-3.060e-005	1.768e-009	9.900e-006
1	3	7.393e-008	-4.714e-007	1.413e-006	-5.937e-010	-2.024e-007
2	0	5.947e-003	-3.759e-002	-2.548e-001	1.297e-005	-9.079e-004
2	1	-4.386e-006	6.311e-004	-3.510e-003	3.639e-007	9.402e-006
2	2	-8.485e-008	-5.612e-007	1.084e-005	1.651e-009	3.813e-007
2	3	4.058e-009	-1.174e-007	4.766e-007	-2.258e-011	-2.138e-008
3	0	3.233e-004	-1.040e-003	-8.398e-003	-3.327e-006	2.378e-005
3	1	8.389e-008	-1.117e-005	-3.151e-005	8.246e-009	-8.056e-007
3	2	-6.145e-009	7.605e-007	5.825e-007	5.777e-011	2.577e-008
4	0	-9.750e-007	-2.033e-006	-2.319e-004	-1.514e-008	-2.184e-007
4	1	9.984e-009	-5.091e-007	2.082e-006	-2.981e-010	2.584e-008
5	0	-1.143e-006	2.597e-006	1.964e-006	8.600e-009	-6.136e-008

B. **Binary ice property calculation**

The thermo-physical properties of the binary ice at certain temperature *T*, carrier fluid concentration C_{cf} and ice concentration C_{ice} can be obtained by combining the properties of the ice and the solution. The subscript *bi* represents the properties for the binary ice, *cf* is for the carrier fluid and *ice* is for the properties of ice. All calculations can be found in *Handbook on Ice Slurries* (Kauffeld et al. 2005)

- **Specific Enthalpy**

Specific enthalpy of binary ice at a given temperature *T* (℃) is determined by

$$h_{bi} = h_{ice}C_{ice} + h_{cf}(1 - C_{ice}) \quad \text{B.1}$$

where h_{ice} is the specific enthalpy of ice

$$h_{ice} = -332.4 + T(2.12 + 0.008T) \quad \text{B.2}$$

and h_{cf} is the specific enthalpy of the carrier fluid at the same temperature

$$h_{cf} = c_{p,cf}T \quad \text{B.3}$$

$c_{p,cf}$ is the specific heat of the carrier fluid which can be calculated by Equation A.1 and the coefficients in Table A.1

- **Density**

Density of binary ice is derived from the density of ice and carrier fluid as well.

$$\rho_{bi} = \rho_{ice}C_{ice} + \rho_{cf}(1 - C_{ice}) \quad \text{B.4}$$

Density of ice is a function of temperature *T* (℃)

$$\rho_{ice} = 917 - 0.13T \quad \text{B.5}$$

The ice concentration C_{ice} can be calculated by Equation 1.1 in Chapter 1.

- **Viscosity**

The correlation from Thomas (1965) will be applied to calculate the viscosity of binary ice.

$$\mu_{bi} = \mu_{cf}\left(1 + 2.5C_{v,ice} + 10.05{C_{v,ice}}^2 + 0.00273e^{16.6C_{v,ice}}\right) \quad \text{B.6}$$

where $C_{v,ice}$ is the ice concentration by volume,

$$C_{v,ice} = \frac{C_{ice}}{C_{ice} + \frac{(1-C_{ice})\rho_{ice}}{\rho_{cf}}} \quad \text{B.7}$$

Equation B.7 is valid when the ice concentration by volume is smaller than 62.5%.

Thermal conductivity

The calculation of thermal conductivity is based on the equation from Jeffrey (Jeffrey 1973).

$$k_{bi} = k_{cf}\left(1 + 3C_{v,ice} + 3{C_{v,ice}}^2\beta^2\chi\right) \quad \text{B.8}$$

where

$$\alpha = k_{ice}/k_{cf} \quad \text{B.9}$$

$$\beta = \frac{\alpha-1}{\alpha+2} \quad \text{B.10}$$

$$\chi = 1 + \frac{\beta}{4} + \frac{3\beta}{16}\frac{\alpha+2}{2\alpha+3} \quad \text{B.11}$$

and the thermal conductivity of ice at temperature T (℃) is obtained by the following equation

$$k_{ice} = 2.21 - 0.012T \quad \text{B.12}$$

C. Process chiller temperature controller

The control of the cooling water temperature to the condenser is carried out by a CAREL µC2 controller. It takes analogue input from a Negative Temperature Coefficient (NTC) temperature probe, which is installed inside the cooling water tank inside the chiller.

Figure C.1 Control panel of CAREL µC2 controller

Adjusting the set point and the temperature differential:

1. Press and hold "*Sel*" button for 5 seconds, until - r - is displayed.
2. Press "▼" button twice to select the control setting (r) parameter group, and then press "*Sel*".
3. Select parameter r01 (cooling set point) by pressing "*Sel*". Use "▲" or "▼" to change its value. Press "*Sel*" to confirm the change.
4. Press "▼" and "*Sel*" to select parameter r02 (cooling differential). Use "▲" or "▼" to change its value. Press "*Sel*" to confirm the change.
5. Press "*Prg*" repeatedly until returning to the main menu to save all the changes.

Operation of the process chiller:

1. To start the cooling unit, switch on the main power supply. Then press and hold "▲". The cooling water pump will start first, followed by the compressor.

2 To stop the cooling unit, press and hold "▲" when the compressor is not running. Then switch off the main power.

D. **Thermodynamic properties of R507**

Table D.1 R507 saturation properties - temperature

Temp	Pressure (kPa)		Density (kg/m³)		Volume (m³/kg)		Enthalpy (kJ/kg)			Entropy (kJ/K-kg)	
(°C)	Liquid	Vapor	Liquid	Vapor	Liquid	Vapor	Liquid	Latent	Vapor	Liquid	Vapor
–100	3.1	3.1	1471.0	0.215	0.0007	4.659	77.3	225.8	303.1	0.4469	1.7510
–99	3.4	3.4	1469.0	0.233	0.0007	4.284	78.4	225.2	303.6	0.4533	1.7470
–98	3.7	3.7	1466.0	0.254	0.0007	3.944	79.5	224.7	304.2	0.4597	1.7430
–97	4.1	4.1	1463.0	0.275	0.0007	3.635	80.7	224.2	304.8	0.4661	1.7390
–96	4.4	4.4	1460.0	0.298	0.0007	3.354	81.8	223.6	305.4	0.4725	1.7350
–95	4.8	4.8	1458.0	0.323	0.0007	3.098	82.9	223.1	306.0	0.4788	1.7310
–94	5.2	5.2	1455.0	0.349	0.0007	2.865	84.0	222.6	306.6	0.4851	1.7280
–93	5.7	5.7	1452.0	0.377	0.0007	2.652	85.2	222.1	307.2	0.4914	1.7240
–92	6.2	6.2	1449.0	0.407	0.0007	2.457	86.3	221.5	307.8	0.4976	1.7210
–91	6.7	6.7	1447.0	0.439	0.0007	2.279	87.4	221.0	308.4	0.5039	1.7170
–90	7.2	7.2	1444.0	0.473	0.0007	2.116	88.6	220.5	309.0	0.5101	1.7140
–89	7.8	7.8	1441.0	0.509	0.0007	1.966	89.7	219.9	309.6	0.5163	1.7110
–88	8.5	8.4	1438.0	0.547	0.0007	1.829	90.8	219.5	310.3	0.5224	1.7080
–87	9.1	9.1	1436.0	0.587	0.0007	1.703	92.0	218.9	310.9	0.5286	1.7040
–86	9.8	9.8	1433.0	0.630	0.0007	1.587	93.1	218.4	311.5	0.5347	1.7010
–85	10.6	10.6	1430.0	0.675	0.0007	1.481	94.3	217.8	312.1	0.5408	1.6980
–84	11.4	11.4	1427.0	0.723	0.0007	1.382	95.4	217.3	312.7	0.5469	1.6960
–83	12.3	12.3	1424.0	0.774	0.0007	1.292	96.6	216.8	313.3	0.5529	1.6930
–82	13.2	13.2	1422.0	0.828	0.0007	1.208	97.7	216.2	313.9	0.5590	1.6900
–81	14.1	14.1	1419.0	0.884	0.0007	1.131	98.9	215.7	314.5	0.5650	1.6870
–80	15.2	15.2	1416.0	0.944	0.0007	1.059	100.0	215.1	315.1	0.5710	1.6850
–79	16.2	16.2	1413.0	1.007	0.0007	0.993	101.2	214.5	315.7	0.5769	1.6820
–78	17.4	17.4	1410.0	1.073	0.0007	0.932	102.3	214.0	316.3	0.5829	1.6800
–77	18.6	18.6	1407.0	1.143	0.0007	0.875	103.5	213.4	316.9	0.5888	1.6770
–76	19.9	19.9	1405.0	1.216	0.0007	0.822	104.6	213.0	317.6	0.5947	1.6750
–75	21.2	21.2	1402.0	1.293	0.0007	0.773	105.8	212.4	318.2	0.6006	1.6720
–74	22.7	22.7	1399.0	1.374	0.0007	0.728	107.0	211.8	318.8	0.6065	1.6700
–73	24.2	24.2	1396.0	1.459	0.0007	0.685	108.1	211.3	319.4	0.6123	1.6680
–72	25.7	25.7	1393.0	1.548	0.0007	0.646	109.3	210.7	320.0	0.6181	1.6660
–71	27.4	27.4	1390.0	1.642	0.0007	0.609	110.5	210.1	320.6	0.6239	1.6630
–70	29.2	29.2	1387.0	1.740	0.0007	0.575	111.7	209.5	321.2	0.6297	1.6610
–69	31.0	31.0	1384.0	1.842	0.0007	0.543	112.8	209.0	321.8	0.6355	1.6590
–68	32.9	32.9	1381.0	1.950	0.0007	0.513	114.0	208.5	322.5	0.6412	1.6570
–67	35.0	35.0	1379.0	2.062	0.0007	0.485	115.2	207.9	323.1	0.6470	1.6550
–66	37.1	37.1	1376.0	2.179	0.0007	0.459	116.4	207.3	323.7	0.6527	1.6530
–65	39.3	39.3	1373.0	2.302	0.0007	0.434	117.6	206.7	324.3	0.6584	1.6520
–64	41.7	41.7	1370.0	2.430	0.0007	0.412	118.7	206.2	324.9	0.6640	1.6500
–63	44.1	44.1	1367.0	2.563	0.0007	0.390	119.9	205.6	325.5	0.6697	1.6480
–62	46.7	46.7	1364.0	2.703	0.0007	0.370	121.1	205.0	326.1	0.6753	1.6460
–61	49.4	49.4	1361.0	2.848	0.0007	0.351	122.3	204.4	326.7	0.6809	1.6450
–60	52.2	52.2	1358.0	2.999	0.0007	0.333	123.5	203.8	327.3	0.6865	1.6430
–59	55.1	55.1	1355.0	3.157	0.0007	0.317	124.7	203.3	328.0	0.6921	1.6410
–58	58.2	58.2	1352.0	3.321	0.0007	0.301	125.9	202.7	328.6	0.6977	1.6400
–57	61.4	61.4	1349.0	3.492	0.0007	0.286	127.1	202.1	329.2	0.7033	1.6380
–56	64.8	64.8	1346.0	3.670	0.0007	0.273	128.3	201.5	329.8	0.7088	1.6370
–55	68.3	68.2	1343.0	3.855	0.0007	0.259	129.5	200.9	330.4	0.7143	1.6350
–54	71.9	71.9	1340.0	4.047	0.0008	0.247	130.7	200.3	331.0	0.7198	1.6340
–53	75.7	75.7	1337.0	4.246	0.0008	0.236	131.9	199.7	331.6	0.7253	1.6320
–52	79.6	79.6	1334.0	4.453	0.0008	0.225	133.1	199.1	332.2	0.7308	1.6310
–51	83.7	83.7	1331.0	4.669	0.0008	0.214	134.3	198.5	332.8	0.7363	1.6300

Table D.1 R507 saturation properties - temperature (continued)

Temp	Pressure (kPa)		Density (kg/m³)		Volume (m³/kg)		Enthalpy (kJ/kg)			Entropy (kJ/K-kg)	
(°C)	Liquid	Vapor	Liquid	Vapor	Liquid	Vapor	Liquid	Latent	Vapor	Liquid	Vapor
−50	88.0	88.0	1328.0	4.892	0.0008	0.204	135.6	197.8	333.4	0.7417	1.6280
−49	92.4	92.4	1325.0	5.123	0.0008	0.195	136.8	197.2	334.0	0.7472	1.6270
−48	97.0	97.0	1322.0	5.363	0.0008	0.187	138.0	196.6	334.6	0.7526	1.6260
−47	101.8	101.8	1319.0	5.612	0.0008	0.178	139.2	196.0	335.2	0.7580	1.6250
−46	106.8	106.8	1315.0	5.870	0.0008	0.170	140.5	195.3	335.8	0.7634	1.6230
−45	112.0	112.0	1312.0	6.137	0.0008	0.163	141.7	194.7	336.4	0.7687	1.6220
−44	117.3	117.3	1309.0	6.413	0.0008	0.156	142.9	194.1	337.0	0.7741	1.6210
−43	122.9	122.9	1306.0	6.699	0.0008	0.149	144.1	193.5	337.6	0.7795	1.6200
−42	128.7	128.6	1303.0	6.995	0.0008	0.143	145.4	192.8	338.2	0.7848	1.6190
−41	134.6	134.6	1300.0	7.301	0.0008	0.137	146.6	192.2	338.8	0.7901	1.6180
−40	140.8	140.8	1297.0	7.618	0.0008	0.131	147.9	191.5	339.4	0.7954	1.6170
−39	147.2	147.2	1293.0	7.945	0.0008	0.126	149.1	190.9	340.0	0.8007	1.6160
−38	153.9	153.8	1290.0	8.283	0.0008	0.121	150.3	190.3	340.6	0.8060	1.6150
−37	160.7	160.7	1287.0	8.633	0.0008	0.116	151.6	189.6	341.2	0.8113	1.6140
−36	167.8	167.8	1284.0	8.994	0.0008	0.111	152.8	189.0	341.8	0.8166	1.6130
−35	175.2	175.1	1281.0	9.366	0.0008	0.107	154.1	188.2	342.3	0.8218	1.6120
−34	182.8	182.7	1277.0	9.751	0.0008	0.103	155.4	187.5	342.9	0.8271	1.6110
−33	190.6	190.5	1274.0	10.150	0.0008	0.099	156.6	186.9	343.5	0.8323	1.6110
−32	198.7	198.6	1271.0	10.560	0.0008	0.095	157.9	186.2	344.1	0.8375	1.6100
−31	207.1	207.0	1268.0	10.980	0.0008	0.091	159.1	185.6	344.7	0.8427	1.6090
−30	215.7	215.6	1264.0	11.420	0.0008	0.088	160.4	184.9	345.3	0.8479	1.6080
−29	224.6	224.5	1261.0	11.870	0.0008	0.084	161.7	184.1	345.8	0.8531	1.6070
−28	233.8	233.7	1258.0	12.330	0.0008	0.081	163.0	183.4	346.4	0.8583	1.6070
−27	243.2	243.1	1254.0	12.810	0.0008	0.078	164.2	182.8	347.0	0.8635	1.6060
−26	253.0	252.9	1251.0	13.300	0.0008	0.075	165.5	182.0	347.5	0.8686	1.6050
−25	263.1	262.9	1248.0	13.800	0.0008	0.072	166.8	181.3	348.1	0.8738	1.6040
−24	273.4	273.3	1244.0	14.330	0.0008	0.070	168.1	180.6	348.7	0.8789	1.6040
−23	284.1	283.9	1241.0	14.860	0.0008	0.067	169.4	179.8	349.2	0.8840	1.6030
−22	295.1	294.9	1237.0	15.420	0.0008	0.065	170.7	179.1	349.8	0.8892	1.6020
−21	306.4	306.2	1234.0	15.990	0.0008	0.063	172.0	178.4	350.4	0.8943	1.6020
−20	318.0	317.8	1231.0	16.570	0.0008	0.060	173.3	177.6	350.9	0.8994	1.6010
−19	330.0	329.8	1227.0	17.180	0.0008	0.058	174.6	176.9	351.5	0.9045	1.6010
−18	342.3	342.1	1224.0	17.800	0.0008	0.056	175.9	176.1	352.0	0.9096	1.6000
−17	354.9	354.7	1220.0	18.430	0.0008	0.054	177.2	175.4	352.6	0.9146	1.5990
−16	367.9	367.7	1217.0	19.090	0.0008	0.052	178.5	174.6	353.1	0.9197	1.5990
−15	381.3	381.0	1213.0	19.770	0.0008	0.051	179.8	173.9	353.7	0.9248	1.5980
−14	395.0	394.8	1209.0	20.460	0.0008	0.049	181.1	173.1	354.2	0.9298	1.5980
−13	409.1	408.9	1206.0	21.170	0.0008	0.047	182.5	172.3	354.8	0.9349	1.5970
−12	423.6	423.3	1202.0	21.910	0.0008	0.046	183.8	171.5	355.3	0.9399	1.5970
−11	438.5	438.2	1199.0	22.660	0.0008	0.044	185.1	170.7	355.8	0.9450	1.5960
−10	453.7	453.4	1195.0	23.440	0.0008	0.043	186.4	170.0	356.4	0.9500	1.5960
−9	469.4	469.0	1191.0	24.230	0.0008	0.041	187.8	169.1	356.9	0.9550	1.5950
−8	485.4	485.1	1188.0	25.050	0.0008	0.040	189.1	168.3	357.4	0.9600	1.5950
−7	501.9	501.5	1184.0	25.890	0.0008	0.039	190.5	167.4	357.9	0.9651	1.5940
−6	518.8	518.4	1180.0	26.760	0.0009	0.037	191.8	166.7	358.5	0.9701	1.5940
−5	536.1	535.7	1176.0	27.650	0.0009	0.036	193.2	165.8	359.0	0.9751	1.5930
−4	553.8	553.4	1173.0	28.560	0.0009	0.035	194.5	165.0	359.5	0.9801	1.5930
−3	572.0	571.6	1169.0	29.490	0.0009	0.034	195.9	164.1	360.0	0.9851	1.5930
−2	590.6	590.2	1165.0	30.460	0.0009	0.033	197.3	163.2	360.5	0.9900	1.5920
−1	609.7	609.2	1161.0	31.440	0.0009	0.032	198.6	162.4	361.0	0.9950	1.5920

Table D.1 R507 saturation properties - temperature (continued)

Temp	Pressure (kPa)		Density (kg/m³)		Volume (m³/kg)		Enthalpy (kJ/kg)			Entropy (kJ/K-kg)	
(°C)	Liquid	Vapor	Liquid	Vapor	Liquid	Vapor	Liquid	Latent	Vapor	Liquid	Vapor
0	629.3	628.7	1157.0	32.460	0.0009	0.031	200.0	161.5	361.5	1.0000	1.5910
1	649.3	648.7	1153.0	33.500	0.0009	0.030	201.4	160.6	362.0	1.0050	1.5910
2	669.7	669.1	1150.0	34.570	0.0009	0.029	202.8	159.7	362.5	1.0100	1.5900
3	690.7	690.1	1146.0	35.670	0.0009	0.028	204.1	158.9	363.0	1.0150	1.5900
4	712.1	711.5	1142.0	36.800	0.0009	0.027	205.5	157.9	363.4	1.0200	1.5900
5	734.0	733.4	1138.0	37.950	0.0009	0.026	206.9	157.0	363.9	1.0250	1.5890
6	756.5	755.8	1133.0	39.140	0.0009	0.026	208.3	156.1	364.4	1.0300	1.5890
7	779.4	778.7	1129.0	40.360	0.0009	0.025	209.7	155.2	364.9	1.0350	1.5880
8	802.9	802.2	1125.0	41.620	0.0009	0.024	211.2	154.1	365.3	1.0400	1.5880
9	826.9	826.1	1121.0	42.910	0.0009	0.023	212.6	153.2	365.8	1.0450	1.5880
10	851.4	850.6	1117.0	44.230	0.0009	0.023	214.0	152.2	366.2	1.0500	1.5870
11	876.4	875.6	1113.0	45.580	0.0009	0.022	215.4	151.3	366.7	1.0550	1.5870
12	902.0	901.2	1108.0	46.980	0.0009	0.021	216.9	150.2	367.1	1.0600	1.5860
13	928.2	927.3	1104.0	48.410	0.0009	0.021	218.3	149.2	367.5	1.0640	1.5860
14	954.9	954.0	1100.0	49.880	0.0009	0.020	219.7	148.3	368.0	1.0690	1.5860
15	982.2	981.3	1095.0	51.390	0.0009	0.019	221.2	147.2	368.4	1.0740	1.5850
16	1010.0	1009.0	1091.0	52.940	0.0009	0.019	222.6	146.2	368.8	1.0790	1.5850
17	1039.0	1038.0	1086.0	54.540	0.0009	0.018	224.1	145.1	369.2	1.0840	1.5840
18	1068.0	1067.0	1082.0	56.170	0.0009	0.018	225.6	144.0	369.6	1.0890	1.5840
19	1097.0	1096.0	1077.0	57.850	0.0009	0.017	227.1	142.9	370.0	1.0940	1.5840
20	1127.0	1126.0	1073.0	59.580	0.0009	0.017	228.5	141.9	370.4	1.0990	1.5830
21	1158.0	1157.0	1068.0	61.360	0.0009	0.016	230.0	140.8	370.8	1.1040	1.5830
22	1190.0	1189.0	1063.0	63.190	0.0009	0.016	231.5	139.7	371.2	1.1090	1.5820
23	1222.0	1221.0	1059.0	65.060	0.0009	0.015	233.0	138.5	371.5	1.1140	1.5820
24	1255.0	1254.0	1054.0	66.990	0.0010	0.015	234.5	137.4	371.9	1.1190	1.5810
25	1288.0	1287.0	1049.0	68.980	0.0010	0.015	236.0	136.2	372.2	1.1240	1.5810
26	1322.0	1321.0	1044.0	71.020	0.0010	0.014	237.6	135.0	372.6	1.1290	1.5800
27	1357.0	1356.0	1039.0	73.120	0.0010	0.014	239.1	133.8	372.9	1.1340	1.5800
28	1392.0	1391.0	1034.0	75.280	0.0010	0.013	240.6	132.6	373.2	1.1390	1.5790
29	1429.0	1427.0	1029.0	77.510	0.0010	0.013	242.2	131.3	373.5	1.1440	1.5790
30	1465.0	1464.0	1024.0	79.800	0.0010	0.013	243.7	130.2	373.9	1.1490	1.5780
31	1503.0	1502.0	1018.0	82.160	0.0010	0.012	245.3	128.8	374.1	1.1540	1.5780
32	1541.0	1540.0	1013.0	84.590	0.0010	0.012	246.9	127.5	374.4	1.1590	1.5770
33	1580.0	1579.0	1008.0	87.090	0.0010	0.011	248.5	126.2	374.7	1.1640	1.5770
34	1620.0	1618.0	1002.0	89.670	0.0010	0.011	250.0	125.0	375.0	1.1690	1.5760
35	1660.0	1659.0	996.5	92.340	0.0010	0.011	251.7	123.5	375.2	1.1740	1.5750
36	1702.0	1700.0	990.9	95.090	0.0010	0.011	253.3	122.1	375.4	1.1790	1.5750
37	1744.0	1742.0	985.1	97.920	0.0010	0.010	254.9	120.7	375.6	1.1850	1.5740
38	1786.0	1785.0	979.3	100.900	0.0010	0.010	256.5	119.4	375.9	1.1900	1.5730
39	1830.0	1828.0	973.3	103.900	0.0010	0.010	258.2	117.8	376.0	1.1950	1.5720
40	1874.0	1873.0	967.2	107.000	0.0010	0.009	259.8	116.4	376.2	1.2000	1.5720
41	1919.0	1918.0	961.1	110.200	0.0010	0.009	261.5	114.9	376.4	1.2050	1.5710
42	1965.0	1964.0	954.8	113.600	0.0011	0.009	263.2	113.3	376.5	1.2100	1.5700
43	2012.0	2011.0	948.4	117.100	0.0011	0.009	264.9	111.7	376.6	1.2160	1.5690
44	2060.0	2058.0	941.8	120.700	0.0011	0.008	266.6	110.1	376.7	1.2210	1.5680
45	2109.0	2107.0	935.2	124.400	0.0011	0.008	268.3	108.5	376.8	1.2260	1.5670
46	2158.0	2156.0	928.3	128.300	0.0011	0.008	270.1	106.8	376.9	1.2310	1.5660
47	2208.0	2206.0	921.4	132.300	0.0011	0.008	271.8	105.1	376.9	1.2370	1.5650
48	2259.0	2258.0	914.2	136.500	0.0011	0.007	273.6	103.3	376.9	1.2420	1.5640
49	2312.0	2310.0	906.9	140.900	0.0011	0.007	275.4	101.5	376.9	1.2480	1.5630

E. **Binary ice temperature control**

The capacity control of the ice generator is implemented by monitoring the binary ice temperature at the outlet of the tank (i.e. the inlet to the ice generator) with a Positive Temperature Coefficient (PTC) 1.5M -50/140 Silicon thermocouple connected to a EWPC 901/N temperature controller from Eliwell

The EWPC 901/N is an one-intervention point electronic temperature controller specifically designed for refrigeration applications. It can cut off the compressor at the set-point temperature and restart the compressor at the set-point temperature plus a positive differential.

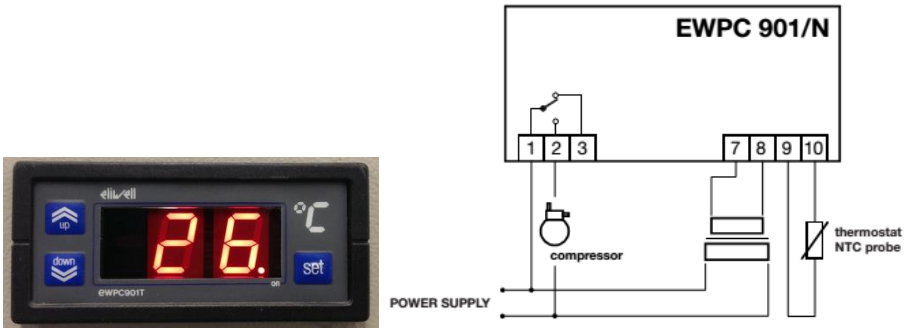

(a) (b)

Figure E.1 (a) the front view of the EWPC 901/N control panel and (b) wiring diagram

Control setting of the binary ice temperature outlet of the load tank:

- Change of set-point

1. Press and release "**Set**" button to display the current set-point temperature.

2. The set-point can then be changed within 15 seconds with the "**UP**" or "**DOWN**" button and the new value is automatically stored after 15 seconds.

- Parameter programming

Programming is accessed by holding the "**SET**" button down for more than 5 seconds. Various parameters, including the positive temperature differential, can be accessed with the "**UP**" and "**DOWN**" button. Pressing the "**SET**" button will display current setting of the parameter. The "**UP**" or "**DOWN**" key allows this setting to be changed; the new value is stored automatically when no further key is pressed within 15 seconds.

F. **Wiring diagram of Multitek M100-WA2 power transducer**

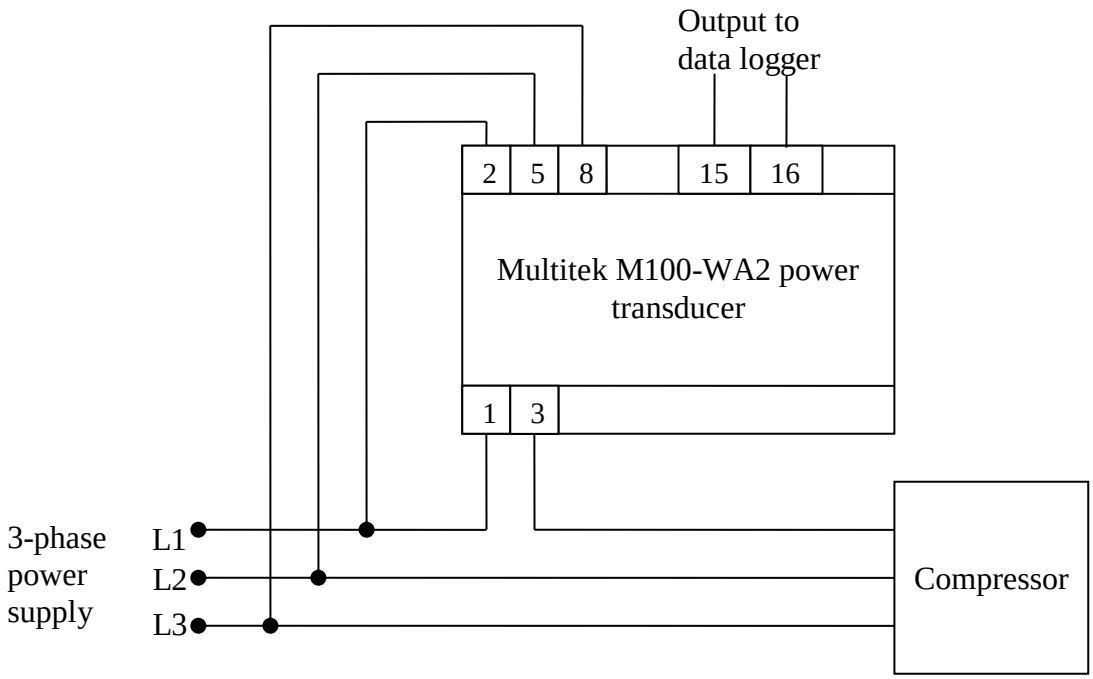

Figure F.1 Wiring diagram of Multitek M100-WA2 power transducer

G. Binary ice flow meter Omega FPR302 and the counter

The flowrate of the binary ice is measured by an Omega FPR302 Low-Flow Meter. Its electrical current sinking pulse output is measured by an Omega DPF75-A Rate Meter which needs to be programmed to display the corresponding flowrate in litre/min. The rate meter has two input channels, A and B. The output of the flowmeter is only connected to channel A, leaving Channel B empty.

Figure G.1 Omega FPR302 Low-Flow Meter,

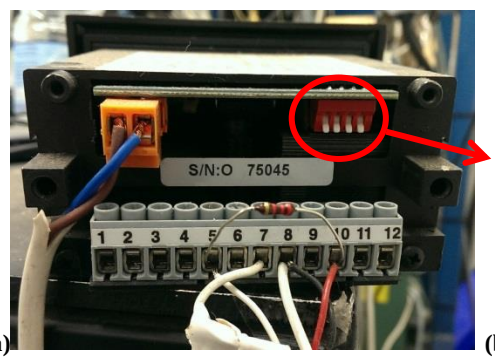

(a)

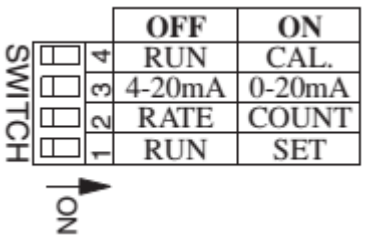

(b)

Figure G.2 Omega DPF75-A Rate Meter (a) front view and (b) back view and the setup switches

There are four setup switches on the back of the ratemeter as shown in Figure E.2.

Switch 1: View or change set values (normally off)

- OFF: the rate meter is set to the run mode. The front display panel will show the flowrate.
- ON: allow setting the "low" and/or "high" flowrate values corresponding to the limits of output current.

Switch 2: Select output for rate or total (normally off)

- OFF: the pulse rate (1 pulse per rotation of the rotor) is displayed.
- ON: the total count of the pulse number.

Switch 3: Select output signal range (normally off).

- OFF: 4-20 mA
- ON: 0-20 mA

Switch 4: Unit calibration (normally off)

The ratemeter is pre-calibrated by the manufacturer, thus Switch 4 should always be left at the OFF position during the test.

The rate meter needs to be programmed so that the pulse rate can be converted to flowrate accurately. This requires inputting the scaling factor, selecting the units for the flowrate and matching the current output limits with the flowrate range.

1. Inputting Scaling factor.

- Press "PRGM".
- Press "ENTER" to set the position of the decimal point for the scaling factor of channel A. Press the arrow key under the digit where the decimal is desired. To clear the decimal, press "PRGM".
- Press "ENTER" to input the scaling factor of channel A. Press the arrow key under the digits to change the number. The scaling factor which is the *K* factor of the flowmeter, i.e. 164.8 pulses per litre provided by the manufacturer of the flowmeter.
- Press "ENTER" repeatedly to save the setting and return to the run mode.

2. Selecting the units for the flowrate

- Press "PRGM" three times.
- Press "ENTER" to choose RPS (rate per second) or SCALE (RPM, RPH). Press "PRGM" to select SCALE.
- Press "ENTER". Press PRGM to choose ÷60 (RPM) or ÷3600 (RPH).
- Press "ENTER" repeatedly to save the setting and return to the run mode.

3. Turn Switch 1 to ON position.

4. Matching the current output limits with the flowrate range

- LOW SETTING can be changed by pressing PRE A. Press buttons A through E to step to the desired value and press ENTER, e.g. setting 0.5 l/min to correspond to 4mA output.
- HIGH SETTING can be changed by pressing PRE B. Press buttons A through E to step to the desired value and press ENTER, e.g. setting 15 l/min to correspond to 20mA output.

H. **Data acquisition software *Dalite***

A software package *Dalite* for Windows is the used with the Datascan data acquisition modules. It allows real time processing and display of the logged data. A brief instruction of this software is given here.

- Communication configuration

This step connects the Datascan modules to the computer. To specify the PC communication port for the Datascan modules, choose the *Communication* from the *Configure* menu, then select the correct baud rate and the communication port as shown in Figure H.1.

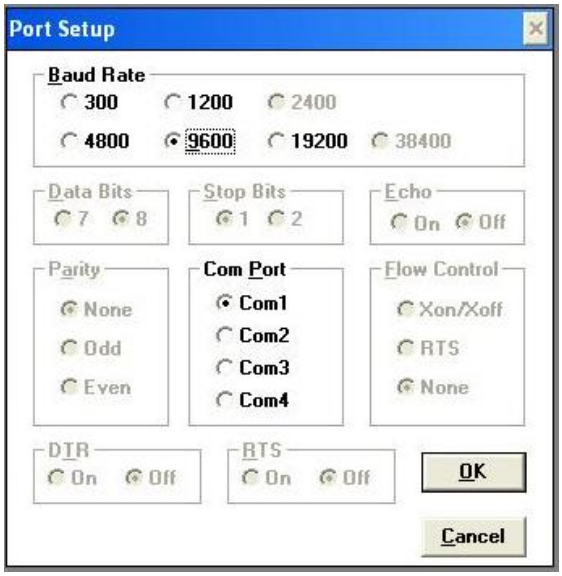

Figure H.1 Communication setup dialogue box

◆ Data scan module configuration

Next step is to configure the Datascan modules and their channels. Choose *Channels* under the *Configure* menu. A Datascan module dialogue box will pop up as shown in Figure H.2.

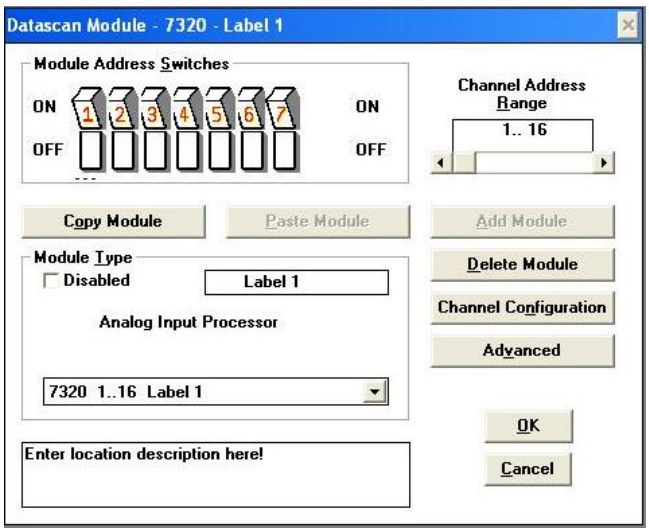

Figure H.2 Datascan module configuration dialogue box

First is to choose the module type from the drop down menu on the lower left half of the box (Models 7320 and 7020 are used in this case). Then, match the module address switches on the dialogue box with the switches on the actual Datascan module. Next is to set the channel address range using the scroll bar on the right. Both modules 7320 and 7020 are 16 channel-modules and their ranges are set to 1-16 and 17-32 respectively, though not all of them will be used during the study. To configure any newly added modules, click *Add Module* button and repeat the above procedure.

◆ Data scan channel configuration

To configure each individual channel, click *Channel Configuration* button and a dialog box as shown in Figure H.3 will appear. This box allows the user to select the type of the sensor connected to the channel, the sensor output signal type and the measured parameter range.

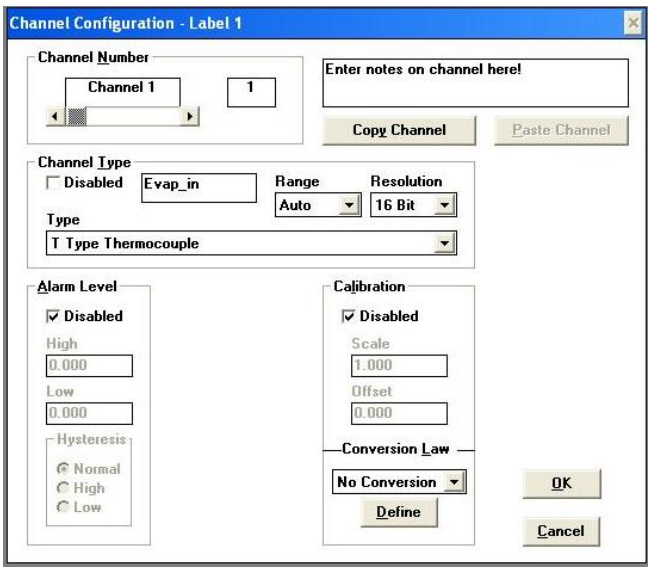

Figure H.3 Analogue input channel configuration dialogue box

First is to select the channel number which the sensor connected to using the scroll bar in the upper loft corner. Then choose the right channel type to match with the sensor

◆ Monitor page configuration

The monitor page provides the user real time readings of the sensors. After all the sensors are configured, click *Monitor* from the *configure* menu, the monitor configuration window will appear.

The frist step is to configure the layout of the monitor page. Click *Grid* in the menu bar to show the grid adjust dialogue box. It allows the user to choose the numbers of row and column for the monitor page.

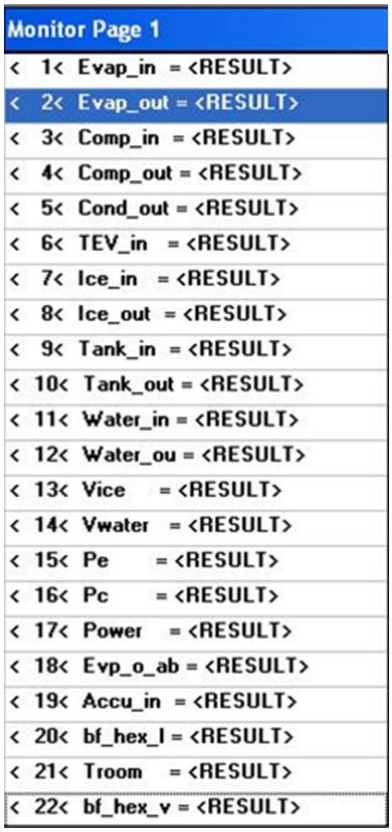

Figure H.4 Monitor Page

Figure H.5 Selecting Channels to Monitor

A monitor page dialog box as in Figure H.4 will pop up after the layout is set. The next step it to configure channels to the page. Select *Channels* from the menu bar in the monitor configuration window to show a select channel to monitor dialog box (Figure H.5). From the drop down list of this box, all channels that have been configured in the previous step can be found. Copy the selected channel, and paste it to the cell in the monitor page. The number and the description of the channel will be

shown in the cell. When the configuration is finished, choose *File* and *Save* from the menu bar, and then *Exit*.

◆ Logger configuration

A logger is the computer file where all the monitored sensor readings are recorded. To configure the logger, click *Configure* from the menu bar in the main window and selecte *Logger*. The configure logger window is shown in Figure H.6

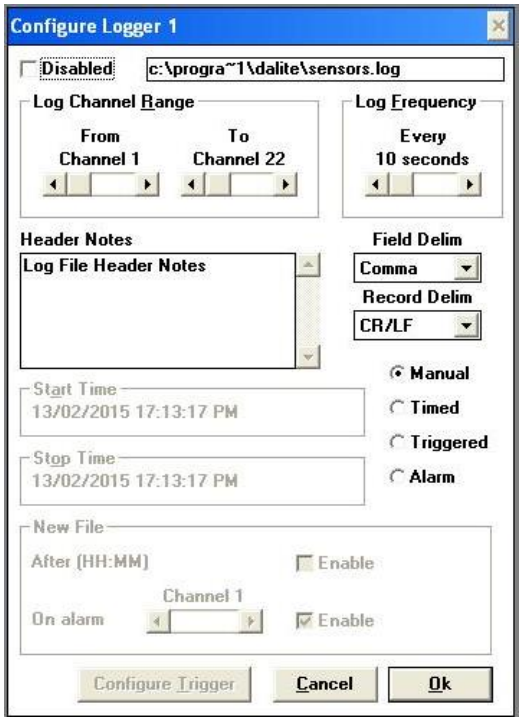

Figure H.6 Logger configuration window

Unclick the *Disabled* box from the upper left corner to active the logger. The Log Channel Range section allows the user to choose the channels to be recorded. The sampling interval can be adjusted in the Log Frequency section. Choose *Manual* to let the log start when *Dalite* starts to monitor the sensors.